A FRAMEWORK FOR ESTIMATING THE DYNAMIC RESPONSE OF STRUCTURES SUBJECT TO THUNDERSTORM DOWNBURSTS



By

JING SONG

A thesis submitted to the University of Birmingham

For the degree of DOCTOR OF PHILOSOPHY

Department of Civil Engineering
School of Engineering
University of Birmingham
January 2022

UNIVERSITY OF
BIRMINGHAM

University of Birmingham Research Archive

e-theses repository

This unpublished thesis/dissertation is copyright of the author and/or third parties. The intellectual property rights of the author or third parties in respect of this work are as defined by The Copyright Designs and Patents Act 1988 or as modified by any successor legislation.

Any use made of information contained in this thesis/dissertation must be in accordance with that legislation and must be properly acknowledged. Further distribution or reproduction in any format is prohibited without the permission of the copyright holder.

UNIVERSITY OF BIRMINGHAM

University of Birmingham Research Archive

e-theses repository

This unpublished thesis/dissertation is copyright of the author and/or third parties. The intellectual property rights of the author or third parties in respect of this work are as defined by The Copyright Designs and Patents Act 1988 or as modified by any successor legislation.

Any use made of information contained in this thesis/dissertation must be in accordance with that legislation and must be properly acknowledged. Further distribution or reproduction in any format is prohibited without the permission of the copyright holder.

ABSTRACT

Thunderstorm (TS) downburst is a type of extreme wind event that are statistically non-stationary with rapid variation in time. Therefore, they cannot be regarded as the same as the stationary boundary layer wind for the purposes of engineering design. In this research, a framework to evaluate the influence of TS downburst wind load on structures has been established. Firstly, a theoretical model, named the vortex model, is introduced and shown to be capable of simulating the process of six full-scale TS downburst events. These six sets of full-scale TS downburst data were recorded by the Texas Tech University Wind Engineering Research Field Laboratory (WERFL) and the Joint Airport Weather Study (JAWS). The simulations of the vertical distribution of horizontal wind speed are validated with the data from WERFL and JAWS and demonstrate good consistency. Secondly, a combination of the quasi-steady (QS) theory and concepts from the partial turbulence simulation (PTS) method has been applied to estimate the wind load on generic building shapes arising from downburst types of events. Using this approach, the wind-induced pressures arising from an isolated downburst-like flow on the building surface can be estimated by the dynamic pressures of a specific downburst event and a database of pressure coefficients for wind flows with a range of azimuths, elevation angles and turbulence intensities; the latter was measured during the experimental part of this study, using a standard, atmospheric boundary layer wind tunnel (WT). In these experiments, the building models were positioned on a rotational support in uniform flow which was produced by a passive turbulence generator located at different upstream positions to obtain different turbulence intensities. As preliminary validation of the technique, velocity data from the University of Birmingham Transient Wind Simulator (TWS) has been combined with these pressure coefficients to predict the wind pressure time series, which is compared to those

measured directly in the TWS. The results demonstrate that the predicted pressure time series have a similar tendency compared with the TWS measurements; and the root-mean-square (RMS) errors of pressure time series between these are less than 50 Pa which is less than one-third of the maximum pressure of TWS. Thirdly, the concept of the design spectrum is adopted subject to thunderstorm downburst. The present investigation builds on previous research to develop wind design spectra (WDS), addressing the potential occurrence of TS downbursts and their effect on structures. This algorithm revisits random vibration theory for assessing the dynamic response of the oscillators that filters input acceleration induced by wind, to then conform design spectra of structures exposed to TS downbursts. A parametric analysis was completed to establish the variability of outflow velocity, structural dimensions, mass, and natural frequency, and their influence on the design spectra, in addition to variations induced by different damping ratios and terrain categories. The outcome of the referred spectral technique is then used to estimate the dynamic performance of a benchmark building. The results are further validated by comparing them with their equivalent calculation based on numerical integration methods, fed with simulated wind time series. The simulated wind field is also applied to the benchmark building whose modelling enhances with finite element software. The superiority of the characteristics of this technique enables the effective and rapid application for the engineering structural design with variable mechanical and aerodynamic properties. According to the built algorithm for the thunderstorm downburst wind design spectra (TWDS), the generalisation of the spectra is carried out through non-linear regression modelling, which can be regarded as an alternative to estimate the dynamic response of structures subjected to transient non-stationary winds. Finally, this research presents a computational method for investigating the ductility demands imposed by transient non-stationary wind loads induced by TS downburst to steel building structures that have been

previously damaged during natural hazard events (earthquakes, winds). The new numerical framework enables an inter-phase between the finite element (FE) analysis software ABAQUS and MATLAB reverse optimisation subroutines. A nonlinear static pushover analysis is initially performed to impose the ductility demands due to the primary hazard event. The relationship between the base shear force and lateral roof drift is obtained from the linear elastic range up to a target plastic deformation. The method uses the pushover analysis to bring the structure to any pre-defined ductility level, including the descending branch of the load-deformation curve, thus allowing for a better control on the initially imposed damage. Then, the transient wind loads can be subsequently applied as an externally applied dynamic loading and the new displacement ductility demand can be directly determined. Accordingly, the global plastic deformation mechanism that leads to collapse can be identified. The proposed computational algorithm is applied to a tall steel building structure subjected in its damaged stage to eleven downburst synthetic records. The results demonstrate the non-negligible effects of such wind events on the ductility demands.

ACKNOWLEDGEMENTS

I am very grateful to my supervisor, Dr. Pedro Martinez-Vazquez, whose wisdom and leadership guided me to finish my PhD research work step-by-step, and I am thankful to his admirable viewpoints on my research topic and dedication. I am very grateful to my co-supervisor Dr. Konstantinos Skalomenos. His patient guidance and brilliant ideas over these years was a great support and inspiration for me. His passionate and earnest attitude towards research always encouraged me to obtain better research outcomes. I am thankful to my former supervisors, Dr. Mike Jesson and Prof. Mark Sterling, who helped me a lot during my first two years of research work and guided me to complete the contents of Chapter 3-4 of this thesis. I appreciate their detailed feedback on my reports and their excellent suggestions for improving my research.

I am also thankful to Dr. Franklin T. Lombardo from the University of Illinois, Urbana-Champaign for providing the field measurement data of thunderstorm downbursts. I am grateful to professional technicians Mr. Mohammed Aslam and Mr. Mark Carter, and Wind Tunnel Systems Engineer Dr. Frederick Bourriez, who gave me insightful technical assistance for the setup of wind tunnel experiments. I am grateful to Dr. Wenda Li from University College London and to my colleagues at the University of Birmingham, Visiting Professor Qiang Gao, Post-Doctoral research fellows Dr. Zhenru Shu and Dr. Genora Joseph, and PhD student Miss Pelagia Kastiza for their support during my project and all of my friends who encouraged my efforts.

Finally, I am very grateful to my dear mum and dad, grandma and grandpa, and my whole family for giving me huge encouragement and support during my PhD period.

TABLE OF CONTENTS

ABSTRACT **I**

ACKNOWLEDGEMENTS **IV**

LIST OF FIGURES **X**

LIST OF TABLES **XVIII**

NOMENCLATURE **XX**

Notation **XX**

Abbreviations **XXVII**

Glossary **XXIX**

Chapter 1 Introduction and Literature review **1**

1.1 Wind catergories **1**

1.1.1 Atmospheric boundary layer winds 1

1.1.2 Extreme winds 8

1.2 Thunderstorm downburst **12**

1.2.1 Formation 12

1.2.2 Microburst characteristics 13

1.2.3 Identification 17

1.2.4 Wind velocity 18

1.2.5 Non-stationary analysis methods 27

1.3 Simulation methods of TS downburst wind field **33**

1.3.1 Full-scale measurement 33

1.3.2 Physical experiment 36

1.3.3 Numerical simulation 42

1.3.4 Theoretical modelling 45

1.4 Downburst wind loading **52**

1.4.1 Aerodynamic property 52

1.4.2 Quasi-steady theory 53

1.4.3 Partial turbulence simulation 57

1.4.4 Prediction of downburst wind loading 58

1.5 Dynamic response on structures **60**

1.6 Sequential multi-hazard analysis **63**

1.7 Summary **66**

1.7.1 Motivation for this study 66

1.7.2 Limitations of previous research 67

1.7.3 Research aim and objectives 68

1.7.4 Structure of thesis 69

Chapter 2 Methodology **72**

2.1 Modelling procedure setup for full-scale downburst events **73**

2.2 Experiment setup **74**

2.2.1 UoB-WT facility and measurement apparatus 75

2.2.2 Scaling and Reynolds number 76

2.2.3 Building models and support design 78

2.2.4 Passive turbulence generator design 81

2.3 Theoretical setup of TWDS **90**

2.3.1 Point-like SDOF system 90

2.3.2 Area-like MDOF system 93

2.3.3 Modal analysis 97

2.4 Computational procedure setup for sequential multi-hazard analysis **99**

2.4.1 Introduction of theory 100

2.4.2 Multi-hazard analysis framework 101

2.5 Summary **105**

Chapter 3 Results and discussion of TS theoretical model **106**

3.1 Validation with laboratory-scale experiments **106**

3.2 Model full-scale downbursts using vortex model **111**

3.2.1 CASE 1 112

3.2.2 CASE 2 115

3.2.3 CASE 3 119

3.2.4 CASE 4 121

3.2.5 CASE 5 123

3.2.6 CASE 6 125

3.2.7 Discussion 127

3.3 Summary **129**

Chapter 4 Results and discussion of downburst wind loading on generic buildings **131**

4.1 UoB-WT experiments for the database of pressure coefficients **131**

4.1.1 Normalised peak pressure coefficient 132

4.1.2 Individual point on cube building model 137

4.1.3 Individual point on portal framed building model 142

4.1.4 Separate areas on cube building model 143

4.1.5 Separate areas on portal framed building model 146

4.2 Preliminary validation **148**

4.2.1 Data analysis for non-stationary time series 148

4.2.2 Cube building model - Individual point 153

4.2.3 Portal framed building model - Individual point 157

4.2.4 Cube building model - Areas 162

4.2.5 Portal framed building model- Areas 168

4.3 Summary **171**

Chapter 5 Results and discussion of TWDS **175**

5.1 Scrutinising of controlling parameters of TWDS **176**

5.2 Description of CAARC benchmark tall building **179**

5.3 Validation of WDS for synoptic wind **180**

5.4 Validation of TWDS for TS downburst wind **182**

5.4.1 Application of TWDS 182

5.4.2 Simulation of downburst wind field 185

5.4.3 Validation Stage 1: Based on Numerical Integration 189

5.4.4 Validation Stage 2: Based on FEM Modelling 189

5.5 Summary **194**

Chapter 6 Results and discussion of Generalisation of TWDS **197**

6.1 Investigation of input parameters **197**

6.2 Three-dimensional non-linear regression model **199**

6.2.1 Introduction 199

6.2.2 Validation of non-linear regression model 202

6.2.3 Application on CAARC benchmark tall building 207

6.3 Summary **209**

Chapter 7 Results and discussion of ductility demands for damaged tall steel structures under downburst wind loading **210**

7.1 Introduction of tall steel building **211**

7.2 Model analysis **213**

7.3 Simulation of downburst wind field **216**

7.4 Results and discussion **220**

7.4.1 TS downburst wind load only 220

7.4.2 Primary and secondary multi-hazard analysis 222

7.5 Summary **236**

Chapter 8 Conclusions and Further work **239**

8.1 Introduction **239**

8.1.1 Objective 1 239

8.1.2 Objective 2 240

8.1.3 Objective 3 240

8.1.4 Objective 4 241

8.2 Notable Findings **241**

8.2.1 Objective 1 241

8.2.2 Objective 2 242

8.2.3 Objective 3 244

8.2.4 Objective 4 246

8.3 Recommendations for further work **247**

Reference **249**

Appendix A Database of the pressure coefficients **264**

Appendix B Surface roughness categories from ASCE **277**

Appendix C Terrain categories from Eurocode 1-4 **278**

Appendix D Publications **279**

LIST OF FIGURES

Figure 1-1. Turbulence intensities for an empty linear wind tunnel. 6

Figure 1-2. Andrews Air Force Base (AAFB) microburst (The peak wind speed reached approximately 130 kt (67 m/s) at 1410:45 EDT on 1st August 1983) (Fujita, 1985b). 10

Figure 1-3. Life cycle of a single microburst (Hjelmfelt, 1988). 15

Figure 1-4. Wind velocity decomposition of a TS recorded at 158 m on May 21, 2008, at the WERFL field: (a) Recorded velocity time history; (b) 40 s moving average mean velocity; (c) Residual turbulent fluctuation; (d) Slowly varying standard deviation of u'; (e) Time varying turbulence intensity; (f) Rapidly varying turbulent fluctuation. 19

Figure 1-5. Comparison of velocity profiles: (a) Vertical profiles of horizontal winds for TS downburst and synoptic wind ($^{z}\bar{U}_{max}$ denotes the height of $\bar{U}_{max}$ for TS downburst wind; ϵ is the exponent of power-law for ABL wind (see Eq. (5.1)); (b) Simulated velocity time history and time function. 21

Figure 1-6. The layout of the storm location relative to observed position (Holmes and Oliver, 2000). 23

Figure 1-7. Comparison of different normalised PSD functions of longitudinal velocity. 26

Figure 1-8. Horizontal radial velocity profiles (Holmes and Oliver, 2000). 47

Figure 1-9. Schematic for the position of primary and secondary vortices. 49

Figure 1-10. Local polar coordinate system for elliptical vortices with calculations. 50

Figure 1-11. Velocity profiles of TS downburst and synoptic wind. 67

Figure 2-1. Methodology map. 72

Figure 2-2. Pressure tapping positions and numbering, and the coordinate system at zero azimuth and zero elevation angle: (a) 60 mm cube; (b) 240 × 130 × 53 mm (42 mm) portal frame. 78

Figure 2-3. Layout of the azimuth and elevation angles. 79

Figure 2-4. Velocity and turbulence intensity profiles in the empty wind tunnel: (a) Velocity profiles along heights in u-v-w directions; (b) Vertical turbulence intensity profiles in u-v-w directions. 80

Figure 2-5. Layout of the wind tunnel: (a) The plan of the wind tunnel; (b) The cross-section of the wind tunnel. M is the distance between adjacent central lines of bar. b is the bar width.84

Figure 2-6. Variation of the magnitude of turbulence intensities with mesh size and x_d. Units of M and b are metres. 84

Figure 2-7. The integral length scales with varying turbulence intensities. Units of M and b are metres. 85

Figure 2-8. Design of edge bars: (a) Vertical distribution of velocity profile; (b) Vertical distribution of turbulence intensity profile. 86

Figure 2-9. Experimental scene diagrams with different x_d. 88

Figure 2-10. Turbulence intensities (left) and vertical profiles of velocity (right) with variable grid distance (x_d). 89

Figure 2-11. Transfer function. 93

Figure 2-12. The first modal amplitude with varying exponent ψ (Eurocode, 2010). 99

Figure 2-13. Diagram of the computational procedure for the sequential restart analysis.101

Figure 3-1. Velocity and pressure time-series from experimental data. 107

Figure 3-2. Velocity comparison between the results from the vortex model and UoB-TWS data. Blue line represents vortex model data; Orange line represents the UoB-TWS data. 109

Figure 3-3. Pressure comparison between the results from the vortex model and UoB-TWS. Blue line represents the vortex model data; Orange line represents the UoB-TWS data. 111

Figure 3-4. Velocity profiles comparison: (a) Profile of normalised maximum horizontal velocity with height. Velocity is normalised to the maximum velocity (u_{max}). Height scaled to the height of maximum velocity (z_{vmax}); (b) Profiles of normalised radial velocity along azimuth of maximum velocity and scaled radius from microburst centre at $t=t_m$. Velocity is normalised to the maximum velocity (u_{max}). Radius is scaled to the radius of the maximum velocity (r_{vmax}). "VM" represents the vortex model. x_m represents the radial position when the maximum velocity occurs. t_m is the time when the maximum velocity occurs. Upper bound represents the maximum velocity at each vertical position. Lower limit and upper limit come from the 26 JAWS events. 115

Figure 3-5. Velocity profiles comparison for case two: (a) Vertical distribution of horizontal velocity profiles of horizontal winds; (b) Velocity time series for the position of maximum velocity. "VM" represents the vortex model. x_m represents the radial position at the time of maximum velocity. 118

Figure 3-6. Comparison of the vertical distribution of horizontal velocity profiles at different times between the vortex model and full-scale data: (a) Prior to ramp-up; (b) During ramp-up; (c) At the time of maximum velocity; (d) During ramp-down. "VM" represents the vortex model. 119

Figure 3-7. Velocity profiles comparison for case three: (a) Vertical distribution of horizontal velocity profiles of horizontal winds; (b) Velocity time series for the position of maximum

velocity. “VM” represents the vortex model. x_m represents the radial position when the maximum velocity occurs. 121

Figure 3-8. Velocity profiles comparison for case four: (a) Vertical distribution of horizontal velocity profiles of horizontal winds; (b) Velocity time series for the position of maximum velocity. “VM” represents the vortex model. x_m represents the radial position when the maximum velocity occurs. 123

Figure 3-9. Velocity profiles comparison for case five: (a) Vertical distribution of horizontal velocity profiles of horizontal winds; (b) Velocity time series for the position of maximum velocity. “VM” represents the vortex model. x_m represents the radial position when the maximum velocity occurs. 125

Figure 3-10. Velocity profiles comparison for case six: (a) Vertical distribution of horizontal velocity profiles of horizontal winds; (b) Velocity time series for the position of maximum velocity. “VM” represents the vortex model. x_m represents the radial position when the maximum velocity occurs. 126

Figure 3-11. Profiles of normalised radial velocity along azimuth of maximum velocity and scaled radius from microburst centre at $t=t_m$. t_m is the time when the maximum velocity occurs. Velocity is normalised to the maximum velocity (u_{max}). Radius is scaled to the radius of the maximum velocity (r_{vmax}). 128

Figure 4-1. The dividing areas on the roof. 133

Figure 4-2. Mean and standard deviation of pressure for subsets of measurements spanning the range (A.M.S., 2018) at 45° azimuth, 0° elevation angle, TI=19.4% (TI5). 134

Figure 4-3. The points on the roof for cube building model (axis origin is in the centre of the building but shifted for clarity). 138

Figure 4-4. Mean pressure coefficients with six different turbulence intensities (TI) for cube building at locations: (a) P51, (b) P71, (c) P91, (d) P73, (e) P55, (f) P95, with variable elevation angles when the azimuthal angle is zero degrees (TI0=1.7%; TI1=3.9%; TI2=6.6%; TI3=10.9%; TI4=14.8%; TI5=19.4%). 139

Figure 4-5. Peak pressure coefficients with six different turbulence intensities for cube building at locations: (a) P51, (b) P71, (c) P91, (d) P73, (e) P55, (f) P95, with variable elevation angles when the azimuthal angle is zero degrees (TI0=1.7%; TI1=3.9%; TI2=6.6%; TI3=10.9%; TI4=14.8%; TI5=19.4%). 141

Figure 4-6. The points on the roof for the portal building model and axis definition (axis origin is in the centre of the building but shifted for clarity). 142

Figure 4-7. Peak pressure coefficients with six different turbulence intensities for portal building at locations: (a) P51, (b) P71, (c) P91, (d) P73, (e) P55, (f) P95, with variable elevation angles when the azimuthal angle is zero degrees (TI0=1.6%; TI1=3.8%; TI2=6.4%; TI3=11.3%; TI4=15.3%; TI5=19.8%). 143

Figure 4-8. The layout of the areas on the roof for cube building model (axes shifted for clarity; origin is in the centre of the building). 145

Figure 4-9. Peak pressure coefficients for cube building with six different turbulence intensities at locations: (a) A1, (b) A2, (c) A3, (d) A4, (e) A5, (f) A6, (g) A7, (h) A8, with variable elevation angles when the azimuthal angle is zero degrees (TI0=1.7%; TI1=3.9%; TI2=6.6%; TI3=10.9%; TI4=14.8%; TI5=19.4%). 145

Figure 4-10. The layout of the areas on the roof for portal building model (axes shifted for clarity; origin is in the centre of the building). 147

Figure 4-11. Peak pressure coefficients for portal building with six different turbulence intensities at locations: (a) A1, (b) A2, (c) A3, (d) A4, (e) A5, (f) A6, (g) A7, (h) A8, with variable elevation angles when the azimuthal angle is zero degrees (TI0=1.6%; TI1=3.8%; TI2=6.4%; TI3=11.3%; TI4=15.3%; TI5=19.8%). 147

Figure 4-12. Construction of the predicted pressure coefficient time-series. Red rhombic boxes contain the inputs. Purple rectangular boxes with rounded corners contain the outputs. Black rectangular boxes and blue rectangular boxes with rounded corners are the calculation processes. 150

Figure 4-13. Wavelet decomposition of velocity time series at height 60 mm. Blue line is the TI time series. Orange line is the horizontal velocity time series. Black line is 50 points moving average TI time series. For clarity, TI is only shown when $u > u_{mean}$. Red dashed lines represent the 0.4s range used for comparison with full-scale data. 151

Figure 4-14. Wavelet decomposition of velocity time series at height 60mm. Blue line is the TI time series. Orange line is the horizontal velocity time series. Black line is 50 points moving average TI time series. For clarity, TI is only shown when $u > u_{mean}$. 152

Figure 4-15. Basic information of downburst simulation for P51, P71, P91, P73, P55 and P95 on the roof of the cube building: (a) Pressures on different positions; (b) Velocity time series in three directions; (c) Variation of the angles; (d) C_p time series. 153

Figure 4-16. Comparison of peak pressure coefficient for cube building: (a) P51; (b) P71; (c) P91; (d) P73; (e) P55; (f) P95. WT represents the estimated values. Fitting curves are based on the orange squares. Filtered TI represents database C_p values extracted using the 50 points moving averaged TI. Relative error is the ratio of the values to the maximum magnitude of C_p measured in the TWS. The design C_p comes from Eurocode 1-4. 155

Figure 4-17. Comparison of pressures for cube building: (a) P51; (b) P71; (c) P91; (d) P73; (e) P55; (f) P95. Relative error is the ratio of the values to the maximum magnitude of pressure measured in the TWS. 156

Figure 4-18. Basic information of downburst simulation for P51, P71, P91, P73, P55 and P95 on the roof of the portal building: (a) Pressures on different positions; (b) C_p time series.158

Figure 4-19. Comparison of pressure coefficient for portal building: (a) P51; (b) P71; (c) P91; (d) P73; (e) P55; (f) P95. WT represents the estimated values. Fitting curves are based on the orange squares. Filtered TI represents database C_p values extracted using the 50 points moving

averaged TI. Relative error is the ratio of the values to the maximum magnitude of C_p measured in the TWS. The design C_p comes from Eurocode 1-4. 160

Figure 4-20. Comparison of pressure for portal building: (a) P51; (b) P71; (c) P91; (d) P73; (e) P55; (f) P95. Relative error is the ratio of the values to the maximum magnitude of pressure measured in the TWS. 161

Figure 4-21. Basic information about UoB-TWS for A1, A2, A3, A4, A5, A6, A7 and A8 on the roof of the cube building: (a) Pressures on different positions; (b) Velocity time series in three directions; (c) Variation of the angles; (d) C_p time series. 162

Figure 4-22. Comparison of C_p for cube building: (a) A1; (b) A2; (c) A3; (d) A4; (e) A5; (f) A6; (g) A7; (h) A8. WT represents the estimated values. Filtered TI represents database C_p values extracted using the 50 points moving averaged TI. Relative error is the ratio of the values to the maximum magnitude of C_p measured in the TWS. The design C_p comes from Eurocode 1-4. 164

Figure 4-23. Comparison of pressure for cube building: (a) A1; (b) A2; (c) A3; (d) A4; (e) A5; (f) A6; (g) A7; (h) A8. Relative error is the ratio of the values to the maximum magnitude of pressure measured in the TWS. 165

Figure 4-24. Comparison of pressure for cube building: (a) A1; (b) A2; (c) A3; (d) A4; (e) A5; (f) A6; (g) A7; (h) A8. Relative error is the ratio of the values to the maximum magnitude of pressure measured in the TWS. 167

Figure 4-25. Basic information about UoB-TWS for A1, A2, A3, A4, A5, A6, A7 and A8 on the roof of the portal building: (a) Pressures on different positions; (b) C_p time series. 168

Figure 4-26. Comparison of C_p for portal building: (a) A1; (b) A2; (c) A3; (d) A4; (e) A5; (f) A6; (g) A7; (h) A8. WT represents the estimated values. Filtered TI represents database C_p values extracted using the 50 points moving averaged TI. Relative error is the ratio of the values to the maximum magnitude of C_p measured in the TWS. The design C_p comes from Eurocode. 169

Figure 4-27. Comparison of pressures for portal building: (a) A1; (b) A2; (c) A3; (d) A4; (e) A5; (f) A6; (g) A7; (h) A8. Relative error is the ratio of the values to the maximum magnitude of pressure measured in the TWS. 170

Figure 5-1. Design spectra of output acceleration with variable parameters based on basic properties (Default values: $\bar{U}_{max,10}$=25 m/s, W=20 m, H/W=10, L/W =1, ξ =0.025, $z_{\bar{U}_{max}}$=50 m and Terrain exposure B): (a) Resonant component; (b) Background component; (c) $\bar{U}_{max,10}$; (d) H/W; (e) L/W; (f) ξ; (g) $z_{\bar{U}_{max}}$; (h) Terrain exposure. 178

Figure 5-2. The CAARC benchmark building: (a) The dimensions; (b) The simplified modelling. 180

Figure 5-3. Comparison of the displacements at the top of the CAARC building model: (a) β=0°; (b) β=90°. 182

Figure 5-4. Reduced lateral displacements with varying heights: (a) In x-direction; (b) In y-direction. 185

Figure 5-5. (a) PSD function at different levels; (b) Coherence function between any two vertical points. 186

Figure 5-6. Simulated velocity time series of horizontal wind at top of the building. 187

Figure 5-7. Comparison of the PSD function between the simulated time history and the target. 188

Figure 5-8. Comparison of the cross-correlation function between the simulated time history and the target. 188

Figure 5-9. The layout of each storey for CAARC benchmark building: (a) Building plan; (b) Elevation section in x-direction; (c) Elevation section in y-direction. 190

Figure 6-1. TWDS of output acceleration with varying input parameters (Default values: $\bar{U}$max,10=25 m/s, W=20 m, H=200 m, L=20 m, ξ=0.025, $z_{\bar{U}_{max}}$=50 m, Terrain exposure B, m_v=384 kg/m3, c_d=1 and ψ=1.5) (Song et al., 2021b). 198

Figure 6-2. Comparison between the real and simulated values of TWDS with varying T and $\bar{U}_{max}$ (Song et al., 2021b). 200

Figure 6-3. Comparison between the normalised TWDS and normalised non-linear regression model for varying input parameters: (a) $\bar{U}_{max}$; (b) Structural width exposed to wind action; (c) H/W; (d) L/W. 202

Figure 6-4. Comparison between the scaled TWDS and scaled non-linear regression model for varying input parameters: (a) $z_{\bar{U}_{max}}$; (b) Damping ratio; (c) Terrain categories; (d) ψ; (e) m_v; (f) c_d. 203

Figure 6-5. Comparison between the real and simulated TWDS considering local variations of input parameters: (a) $\bar{U}_{max}$; (b) W; (c) H/W; (d) L/W (Song et al., 2021b). 204

Figure 6-6. Comparison between the real and simulated TWDS for varying input parameters: (a) $z_{\bar{U}_{max}}$; (b) Damping ratio; (c) Terrain categories; (d) ψ; (e) m_v; (f) c_d. 204

Figure 6-7. Comparison of real and simulated design spectra for scenarios (Song et al., 2021b). 207

Figure 6-8. Comparisons for the lateral displacements with varying heights: (a) In x-direction; (b) In y-direction. 208

Figure 7-1. Basic information of frames for the 20-storey steel building, * represents weak axis orientation (Hall, 2017). 212

Figure 7-2. Displacement distribution: (a) Gravity load; (b) Frequency analysis. 214

Figure 7-3. Pushover curves (base shear force at the ground level is normalised by the frame weight; roof drift represents the roof displacement divided by the overall height of the building): (a) entire frame model; (b) each column. 215

Figure 7-4. Time history of the simulated transient winds when $z_{\bar{U}_{max}}$ = 30 m: (a) Simulated velocity time history; (b) Downburst wind loading on each storey. 217

Figure 7-5. Time history of the simulated transient winds when $z_{\bar{U}_{max}}$ = 50 m: (a) Simulated velocity time history; (b) Downburst wind loading on each storey. 217

Figure 7-6. Time history of the simulated transient winds when $z_{\bar{U}_{max}}$=70 m: (a) Simulated velocity time history; (b) Downburst wind loading on each storey. 218

Figure 7-7. Horizontal and vertical profiles of downburst velocity: (a) Horizontal velocity time history at the height of maximum velocity; (b) Peak velocity at each storey with varying $z_{\bar{U}_{max}}$; (c) Peak velocity at each storey with varying vertical profiles of I_u; (d) Peak velocity at each storey with varying U_{max}. 219

Figure 7-8. Pushover curves of the building frame under different downburst profiles (Grey dash line represents the pushover curves as shown in Figure 7-3). 221

Figure 7-9. (a) Peak SDR and (b) Peak displacement of the building frame for each storey under the downburst wind fields. 221

Figure 7-10. Global stress distribution at the time of maximum displacement under the downburst wind profile 1, 2, and 3. 222

Figure 7-11. Pushover curves of the damaged building under secondary downburst wind hazard with varying $z_{\bar{U}_{max}}$: (a) DL1-Downburst wind; (b) DL2-Downburst; (c) DL3-Downburst; (d) DL4-Downburst; (e) DL5-Downburst; (f) DL6-Downburst (Grey dash line represents the pushover curves as shown in Figure 7-3; Red dash line represents the maximum displacement after the primary and secondary hazards separately). 226

Figure 7-12. Global Stress distribution at maximum displacement for profiles 1, 2, and 3, (a) DL1-Downburst; (b) DL2-Downburst; (c) DL3-Downburst; (d) DL4-Downburst; (e) DL5-Downburst; (f) DL6-Downburst. 227

Figure 7-13. Pushover curves of the damaged building under secondary downburst wind hazard with varying vertical profiles of I_u from variable terrain types (0, I, II, III, IV), (Grey dash line represents the pushover curves as shown in Figure 7-3; Red dash line represents the maximum displacement after the primary and secondary hazards separately). 230

Figure 7-14. Global Stress distribution at maximum displacement for profile 4, 5, 6, 7, and 8: (a) DL1-Downburst; (b) DL2-Downburst; (c) DL3-Downburst; (d) DL4-Downburst; (e) DL5-Downburst; (f) DL6-Downburst. 231

Figure 7-15. Pushover curves of the damaged building under secondary downburst wind hazard with varying U_{max} (Grey dash line represents the pushover curves as shown in Figure 7-3; Red

dash line represents the maximum displacement after the primary and secondary hazards separately). 233

Figure 7-16. Peak SDR for each storey: (a) DL1-Downburst; (b) DL2-Downburst; (c) DL3-Downburst; (d) DL4-Downburst; (e) DL5-Downburst; (f) DL6-Downburst (H1 denotes the primary hazard alone). 235

Figure 7-17. Peak displacement for each storey: (a) DL1-Downburst; (b) DL2-Downburst; (c) DL3-Downburst; (d) DL4-Downburst; (e) DL5-Downburst; (f) DL6-Downburst (H1 denotes the primary hazard alone). 236

LIST OF TABLES

Table 1-1. Microburst Characteristics (Hjelmfelt, 1988). 15

Table 1-2. Parameters for time function. 23

Table 1-3. Summarised profile for five full-scale downburst events. 35

Table 2-1. Summary of the TI and velocity profiles. 89

Table 2-2. Comparison of the design spectra between TS downburst wind and ABL wind.96

Table 3-1. Summary of the input data of vortex modelling. 114

Table 3-2. Full-scale event data for Case 2. 116

Table 3-3. Full-scale event data for Case 3. 120

Table 3-4. Summary of the correlation coefficients for the comparison for five sets of data. 121

Table 3-5. Full-scale event data for Case 4. 122

Table 3-6. Full-scale event data for Case 5. 123

Table 3-7. Full-scale event data for Case 6. 126

Table 3-8. Comparison with microburst characteristics. 129

Table 4-1. Corresponded peak pressure coefficients calculated from design codes. 136

Table 4-2. Pressure coefficients with varying azimuthal angles for tap V7 (Richards and Hoxey, 2012a). 137

Table 4-3. Summary of RMS errors of Cp and pressures for cube building. 157

Table 4-4. Comparison of the peak pressures on the roof for cube building. 166

Table 5-1. Static and dynamic displacements (m) at the top of the building. 181

Table 5-2. The static and dynamic lateral displacements. 184

Table 5-3. Design and modal properties. 190

Table 5-4. Natural period, frequency, modal mass participate factor for the first ten modes.191

Table 5-5. Lateral displacements on each storey from modal integration by linear add (Unit, Meter). 193

Table 6-1. Scaling factors for three-dimensional NLRM of the TWDS and normalised TWDS. 201

Table 6-2. RMSE for varying parameters - Part 1 (Song et al., 2021b). 205

Table 6-3. RMSE for varying parameters - Part 2 (Song et al., 2021b). 206

Table 6-4. RMSE for varying parameters - Part 3 (Song et al., 2021b). 206

Table 6-5. Lateral displacements at the structural roof level. 208

Table 7-1. The dimensions for the column and beam elements of 20-storey frame building in Figure 7-1 (Hall, 2017). 212

Table 7-2. Summarised ductility demand (maximum roof drift) for eleven downburst wind profiles (Profile 1-3 for varying $z_{\bar{U}_{max}}$; Profile 4-8 for varying I_u; Profile 9-11 for varying U_{max}). 225

NOMENCLATURE

Notation and abbreviations are defined within the thesis. The following lists are not intended to be exhaustive but cover the frequently used terms.

Notation

a	Scale factor; wavelet scale; Major radius of the ellipse (m)
A	Area of the structures exposed to wind (m^2)
b	Localised time translation parameter; Bar width; Minor radius of the ellipse (m)
c	Location factor; Damping coefficient
c_d	Grid drag; Drag coefficient
C_F	Force coefficient
C_D	Drag coefficient
C_L	Lift coefficient
C_p	Pressure coefficient
$\hat{C}_p$	Peak pressure coefficient
$\bar{C}_p$	Mean pressure coefficient
$C_{p_{inst}}$	Instantaneous pressure coefficient
$C_{p_{TWS}}$	Pressure coefficients from transient wind simulation
$C_{p_{database}}$	Estimated pressure coefficients from wind tunnel database
C_{pe}	Design pressure coefficient
C_y	Decay constant in horizontal y direction, taken as 10
C_z	Decay constant in vertical z direction, taken as 10

D	Impinging jet diameter; Distance between the maximum radial velocities (m)
E	Leading edges of the outflow (m)
f	Frequency (Hz or s^{-1}); Total horizontal force (N)
$\bar{f}$	Slowly varying mean component (N)
f'	Residual fluctuating component (N)
f_c	Cut-off frequency (Hz or s^{-1})
f_s	Sample frequency (Hz or s^{-1})
F	Resultant wind force (N)
F_D	Drag force (N)
F_L	Lift force (N)
$J(n)$	Transfer function
H	Building height (m); Outflow depth (m)
I_u	Turbulence intensity in horizontal direction
I_v	Turbulence intensity in lateral direction
I_w	Turbulence intensity in vertical direction
$\bar{I}_u$	Slowly varying mean turbulence intensity
k	von Karmen's constant, standard value 0.4 used in this thesis
K	Shape factor, standard value 0.1 used in this thesis
L_1	First modal mass (kg)
L	Width of the test section (m)
L_u	Integral length scale (m)
L_x	Integral length scale in x direction, x includes horizontal, lateral, vertical (m)
m	Mass of the structure excited by the wind force (kg)
m_1	First modal mass per unit height (kg/m)
m_l	Structural mass per unit height (kg/m)

M	Mesh size, the distance between the centres of two bars (m)
n	The natural frequency of gust wind (Hz or s^{-1})
n_0	The natural frequency of structures (Hz or s^{-1})
n_1	First natural frequency of structures (Hz or s^{-1})
N	The length of the signal
p	Pressure (Pa or Nm^{-2})
$\bar{p}$	Mean pressure (Pa or Nm^{-2})
$\hat{p}$	Peak pressure (Pa or Nm^{-2})
p_{ref}	Reference pressure, usually taken atmospheric pressure (Pa or Nm^{-2})
p_{atm}	Atmospheric pressure (Pa or Nm^{-2})
r_{max} or $r_{V_{max}}$	Radius of the maximum horizontal wind speed (m)
r	Radial distance to the central point of the vortex "core" (m)
R	Radius of the circle (m)
Re	Reynolds number
S_a	Thunderstorm downburst wind design spectrum (ms^{-2})
S_A	Spectrum of input acceleration (ms^{-2})
$S_{A_{ij}}$	Cross spectrum of input acceleration (ms^{-2})
S_{cu}	Generalised cross-spectrum of input acceleration (ms^{-2})
S_u	Power spectrum of the horizontal wind speed (WHz^{-1})
$S_{\tilde{u}'}$	Wind velocity power spectrum for reduced horizontal fluctuating velocity component $\tilde{u}'$ (WHz^{-1})
S_{C_pQS}	Auto-spectra of QS-predicted pressure ($Js^{-1}Hz^{-1}$)
S_{C_pM}	Auto-spectra of measured pressure ($Js^{-1}Hz^{-1}$)
S_{C_pQS,C_pM}	Cross-spectra between measured and predicted pressure ($Js^{-1}Hz^{-1}$)

S_F	Force spectrum (N)
t	Time (s)
t_m	Time of the maximum velocity (s)
Δt	Time interval (s)
T	Temperature (°C); Total time (s)
$u\ or\ V$	Instantaneous longitudinal (streamwise, horizontal, radial) velocity at a time (ms^{-1})
u'	Residual fluctuating velocity (ms^{-1})
$\tilde{u}'$	Reduced turbulent fluctuation (ms^{-1})
u_{max}	Maximum horizontal velocity (ms^{-1})
u_*	Friction velocity (ms^{-1})
u_L	Low-frequency fluctuating velocity (ms^{-1})
u_H	High-frequency fluctuating velocity (ms^{-1})
u_R	Mean value of the adopted non-stationary velocity time series (ms^{-1})
$\bar{u}$	Mean horizontal velocity (ms^{-1})
U	The instantaneous resultant velocity at a position given by the coordinates x, y and z (ms^{-1})
$\overline{U}$	Mean velocity, the running mean velocity or the slowly varying mean velocity (ms^{-1})
$\overline{U}_{10}$	Mean velocity at 10 m height (ms^{-1})
U_{ref}	Reference velocity (mean velocity or running mean velocity) (ms^{-1})
$\overline{U}_{max}$	Maximum slowly varying mean velocity (ms^{-1})
$\overline{U}_{max,10}$	Maximum running mean velocity at 10 m height (ms^{-1})
v	Instantaneous transverse velocity at a time (ms^{-1})
V_r	Radial (horizontal, longitudinal) velocity (ms^{-1})

$V_{r,max}$ *or* V_{max}	Maximum radial (horizontal, longitudinal) velocity (ms^{-1})
$\bar{V}_{max}$	Mean value for the maximum horizontal velocity of different full-scale records (ms^{-1})
V_{jet}	Velocity of the impinging jet (ms^{-1})
ΔV	Maximum radial velocity at height when the maximum velocity occurs (m)
w	Instantaneous vertical velocity at a time (ms^{-1})
x	Distance between the radial position and centre of downdraft (m)
x_d	Distance between the grid and building models (m)
X_r	The distance between the release position of the platform and the centreline of the jet (m)
X_R	Horizontal position for the point on the elliptical vortex in local polar coordinate system (m)
Z_R	Vertical position for the point on the elliptical vortex in local polar coordinate system (m)
z	Height above the ground (m)
z_0	Ground roughness length (m)
z_{ref}	Reference height above the ground (m)
z_m *or* $z_{v_{max}}$	Height above the ground corresponding to the maximum wind speed (Height of maximum velocity) (m)
$\bar{z}_{v_{max}}$	Mean value for the maximum velocity heights of several full-scale downburst records (m)
Z	Height of the support (m)
α or ϵ	Exponent of power-law
β	Instantaneous elevation angle of velocity (°)
$\bar{\beta}$	Mean elevation angle of velocity (°)
β'	Fluctuating elevation angle of velocity (°)

$\beta_{porosity}$	The porosity of the grid
Γ	Circulation ($m^2 s^{-1}$)
δ	Boundary layer thickness (m)
θ	Instantaneous azimuthal angle of velocity (°)
$\bar{\theta}$	Mean wind direction in the horizontal plane (°)
ϕ_1	First modal shape
μ	Sample mean of velocity (ms^{-1})
ν	Kinetic viscosity ($m^2 s^{-1}$)
ρ	Air density (kgm^{-3})
σ	Standard deviation of velocity (ms^{-1})
σ_u	Standard deviation of velocity time series in longitudinal direction or slowly varying standard deviation (ms^{-1})
σ_v	Standard deviation of velocity time series in transverse direction (ms^{-1})
σ_w	Standard deviation of velocity time series in vertical direction (ms^{-1})
σ_a	Dynamic response (ms^{-2})
$\sigma_{a,b}$	Background dynamic response (ms^{-2})
$\sigma_{a,r}$	Resonant dynamic response (ms^{-2})
τ	Time offset (s)
τ_0	Shear stress for force per unit area (Nm^{-2})
ω	Angular frequency ($rads^{-1}$)
ω_0	Non-dimensional frequency ($rads^{-1}$)
Re	Reynolds number
ψ	Modal shape factor
$\psi(i)$	Wavelet function, $i = u, v, w$
χ	Aerodynamic admittance

Δ_y	The horizontal distances between two points, i, j, located at coordinates $\{y_i, z_i\}$ and $\{y_j, z_j\}$
Δ_z	The vertical distances between two points, i, j, located at coordinates $\{y_i, z_i\}$ and $\{y_j, z_j\}$
ξ	Damping ratio

Abbreviations

TS	Thunderstorm
AAFB	Andrews Air Force Base
ABL	Atmospheric boundary layer
ASCE	American Society of Civil Engineers
BLWT II	Boundary Layer Wind Tunnel II
CPDF	Cumulative probability distribution function
CFD	Computational fluid dynamics
CWT	Continuous Wavelet Transform
DL	Ductility level
DPMS	Digital pressure measurement system
ECN	Energy Research Centre of the Netherlands
EPSD	Evolutionary power spectral density
EF	Enhanced Fujita scale
FFT	Fast Fourier Transform
GEV	Generalised extreme value
HSLE	High-speed and large-Elevation
JAWS	Joint Airport Weather Study
MIST	Microburst and Severe Thunderstorm
MDOF	Multi-Degree-Of-Freedom
NIMROD	Northern Illinois Meteorological Research on Outflows
NLRM	Non-linear regression model
PTS	Partial turbulence simulation
PSD	Power spectral density

QS Quasi-steady theory

RMS Root mean square

STFT Short-time Fourier Transform

SDOF Single-Degree-Of-Freedom

TFI Turbulent Flow Instrumentation

TI Turbulence intensity

UoB-TWS University of Birmingham transient wind simulator

UoB-WT University of Birmingham wind tunnel

UWO University of Western Ontario

VM Vortex model

WERFL Wind Engineering Research Field Laboratory

WT Wind tunnel

WDS Wind design spectra

TWDS Thunderstorm downburst wind design spectra

Glossary

Stationary flow	Statistical properties are constant with respect to time.
Non-stationary flow	Statistical properties vary with respect to time.
Uniform flow	The streamwise velocity does not vary with the flow path.
Non-uniform flow	The streamwise velocity varies from point to point along the flow path.
Steady flow	No variations in flow parameters with respect to time for any points.
Unsteady flow	Flow parameters for one point vary with respect to time.
Stable flow	The air flow will return to its initial state after the initial disturbance.
Unstable flow	The disturbance has noticeable effects on the state of the air flow and the air flow progressively departs from the initial state due to the disturbance.
Homogeneous	Statistical parameters for any points in space are the same. The statistical parameters include fluctuating parameters, turbulence intensity and turbulence kinetic energy.
Isotropic	Variation (if any) of statistical parameters in different directions is the same. The statistical parameters include fluctuating parameters, turbulence intensity and turbulence kinetic energy.
Peak velocity	The maximum velocity of the time series.
Maximum velocity	The maximum velocity in the domain, including time and space.

Chapter 1 Introduction and Literature review

This chapter is divided into seven sections, including wind categories, characteristics of TS downburst, simulation methods, downburst wind loading, dynamic response of buildings subject to downburst induced wind loading, and influence of downburst wind loading on damaged buildings. The final section of this chapter summarises the motivation for this study, limitations of previous research, research aim and objectives, and the structure of this thesis.

1.1 Wind catergories

1.1.1 Atmospheric boundary layer winds

The layer of air near the ground surface that is influenced by ground friction is defined as the atmospheric boundary layer (ABL). It can extend up to 500-1000 m in height for large storms whose horizontal dimensions can generally extend to over 1000 km, such as extra-tropical depressions (Holmes, 2018). For small-scale storms whose horizontal dimensions are usually approximately 1000 m, such as downbursts, the height influenced by the ground friction is much smaller and may be less than 100 m (Holmes, 2018). There are mainly two types of surface-air interactions: mechanical and thermal. The mechanical interactions are induced by the friction between the wind and the ground surface, which can result in wind shear and in turn can generate turbulence (Roisin, 2019). The thermal effects result from the differential heating of the atmosphere and can be characterised as the stability of the atmosphere. The stability of the

air in the atmosphere depends on the temperature of the rising air relative to the temperature of the stationary surrounding air when this rising air passes through (Machine, 2008). The atmospheric stability has three situations, including stable, neutral, and unstable, which can be judged by the atmospheric temperature gradient. Due to the compressibility of the air, the neutral stability happens when the measured vertical temperature gradient (the lapse rate) is equal to the adiabatic lapse rate, which is characterised as no heat exchange occurring between the rising air and its surrounding air (Hemond and Fechner, 2014). The adiabatic lapse rate for a dry atmosphere, which may contain water vapour but without liquid moisture in the form of fog, droplets, or clouds, is approximately 9.8 °C/km. With every increasing height of 1 km, the temperature decreases by 9.8 °C (Hemond and Fechner, 2014). The adiabatic lapse rate for a wet atmosphere, which contains clouds or other visible forms of moisture, is approximately in the range of 3.6 °C/km and 5.5 °C/km, dependent on the temperature and pressure. The temperature gradient above the adiabatic lapse rate is classified as unstable, and the temperature gradient less than the adiabatic lapse rate is considered as stable (Hemond and Fechner, 2014). In a stable atmosphere, the warmer air parcel with lower density is pushed upward and then becomes cooler and denser at a higher altitude, and finally, it sinks back down. The higher altitude tends to suppress vertical mixing. In an unstable atmosphere, when this warmer air parcel reaches a higher altitude, as the surrounding temperature decreases more rapidly with elevation than the adiabatic rate, it is pushed up further by buoyancy. This vertical mixing is thereby promoted by unstable conditions.

In neutral conditions, the ABL can be regarded to be neutral and the velocity profiles varying with the height above the ground can be characterised to follow the “logarithmic law” and “power law”. The logarithmic law is originally derived from the turbulence boundary layer (Holmes, 2018). However, it is generally accepted that the logarithmic law is the most accurate

method to describe the wind speed profile in the ABL for strong wind conditions (Holmes, 2018). The roughness of the ground and the viscosity of the air can induce wind shear in ABL. However, due to the turbulent nature of flow in an ABL, the influence of the molecular viscosity can be neglected. The wind shear caused by the ground roughness is defined as the rate of change of mean speed with height. The non-dimensional equation for wind shear is shown in Eq. (1.1) (Holmes, 2018).

$$wind\ shear\ = \frac{dU}{dz} z \sqrt{\frac{\rho}{\tau_0}} \tag{1.1}$$

where $\overline{U}$ is the mean velocity, z is the height above the ground, τ_0 is the shear stress for force per unit area and ρ is the air density. The friction velocity, u_* (defined in Eq. (1.2)), can be included in Eq. (1.1), and Eq. (1.1) can be considered to be equal to a constant as shown in Eq. (1.3) (Holmes, 2018). Integrating Eq. (1.3), $\int_0^U d\overline{U} = \frac{u_*}{k}\int_{z_0}^{z} z^{-1} dz$, the equation of the logarithmic law can be obtained as shown in Eq. (1.4).

$$\sqrt{\frac{\tau_0}{\rho}} = u_* \tag{1.2}$$

$$\frac{dU}{dz}\frac{z}{u_*} = \frac{1}{k} \tag{1.3}$$

$$\overline{U}(z) = \frac{u_*}{k} \ln(\frac{z}{z_0}) \tag{1.4}$$

where k is von Kármán's constant and has a value of 0.4 found in the experiment (Holmes, 2018), z_0 is the ground roughness length depending on the terrain categories (Holmes, 2018). For urban areas and forests with very rough terrain, the height z in Eq. (1.4) is often replaced by an effective height, $(z - z_h)$, where z_h is a "zero-plane displacement" and can be taken as

3/4 times of rooftop height (Holmes, 2018). Then, the Eq. (1.4) will be replaced by $\overline{U}(z) = \frac{u_*}{k}\ln(\frac{z-z_h}{z_0})$. When the effective height $(z - z_h)$ is less than the roughness length z_0, the wind speed becomes a negative number, which is meaningless for the specific mathematical properties of the logarithms. In order to avoid this problem, the power law is introduced.

The power law is an empirical equation. The equation for connecting the mean wind speed at any height with that at 10 m is shown in Eq. (1.5).

$$\overline{U}(z) = \overline{U}_{10}(\frac{z}{10})^{\alpha} \tag{1.5}$$

$\overline{U}_{10}$ is the mean velocity at a height of 10 m. α is related to the terrain roughness and the reference height, as shown in Eq. (1.6).

$$\alpha = (\frac{1}{\ln(z_{ref}/z_0)}) \tag{1.6}$$

The z_{ref} is a reference height at which the two "laws" are matched and can be taken as the average height in the range over which matching is required or half the maximum height over which the matching is required.

There are a variety of classification systems that have been used to describe the wind, the Beaufort scale, the Enhanced Fujita (EF) scale, and the Saffir-Simpson Hurricane scale. The Beaufort scale is based on the observation of wave heights at sea and the condition of the sea. In America and Canada, the EF scale was adopted to classify the wind speed of tornados. The damage indicators (e.g., the types of structures that have been damaged) are mainly adopted in determining the tornado intensity. For example, when the wind speed is more than 65 mph or 105 km/h in the EF scale, there is minor damage. The Saffir-Simpson Hurricane Wind Scale is used to classify the hurricanes in the Atlantic Ocean and Northeast Pacific with an average

speed in 1-minute at 10 m height. The World Meteorological Organization (WMO) standard takes 10-minute at 10 m height for mean wind speed. The National Hurricane Centre in the US takes 1-minute for mean wind speed (Kareem and Tamura, 2013).

The main features of the velocity time history can be obtained by applying a moving-average filter, which is also called "running mean" or "slowly varying mean". Subtracting the filtered velocity time history from the original velocity time history, the residual time history can be described as "turbulence" (Holmes, 2018). The turbulence can be quantified by turbulence intensity (Holmes, 2018). The turbulence intensity of stationary winds is the ratio of the standard deviation of the velocity components (u, v, w), Eq. (1.7), to the mean streamwise velocity, $\overline{U}$. The measurement of the turbulence intensity in the University of Birmingham Wind Tunnel (UoB-WT) without roughness elements is shown in Figure 1-1. When the range of the height is 0.3 m to 0 m, the turbulence intensity is between 2% and 19%. Eq. (1.8), Eq. (1.9) and Eq. (1.10) are the turbulence intensities in longitudinal, lateral, and vertical directions.

$$\sigma_u = \left\{\frac{1}{T}\int_0^T [U(t) - \overline{U}]^2 dt\right\}^{1/2} \tag{1.7}$$

$$I_u = \frac{\sigma_u}{U} \quad (longitudinal) \tag{1.8}$$

$$I_v = \frac{\sigma_v}{U} \quad (lateral) \tag{1.9}$$

$$I_w = \frac{\sigma_w}{U} \quad (vertical) \tag{1.10}$$

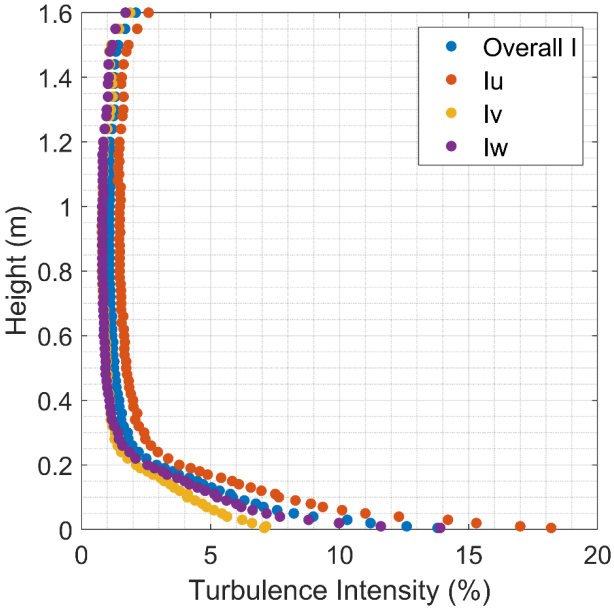


Figure 1-1. Turbulence intensities for an empty linear wind tunnel.

Considering the measurement near the ground, it has been found that the standard deviation in the longitudinal direction is approximately equal to $2.5u_*$ (Holmes, 2018), shown in Eq. (1.11). Eq. (1.11) - Eq. (1.13) show that the turbulence intensity is determined by the roughness length.

$$I_u = \frac{2.5u_*}{(u_*/0.4)log_e(z/z_0)} = \frac{1}{In(z/z_0)} \tag{1.11}$$

$$I_v \cong \frac{0.88}{\ln(z/z_0)} \tag{1.12}$$

$$I_w \cong \frac{0.55}{\ln(z/z_0)} \tag{1.13}$$

The maximum size of vortices in the wind is defined as the integral length scale. The integral length scale is shown in Eq. (1.14) for the original velocity time series which can be calculated as the integral of the autocorrelation function, $A_x(\tau)$ ($x = u, v, w$; τ is the time offset) as shown in Eq. (1.15) within the range of $0 \leq \tau \leq \tau_0$ (τ_0 is the first time at which $A_x(\tau) \leq 0$), multiplying u_R. The velocity scale, u_R is defined as the mean value of the adopted non-stationary velocity time series by Taylor's hypothesis (Batchelor, 1953).

$$L_x = u_R \int_{\tau=0}^{\tau=\tau_0} A_x(\tau) d\tau \quad (1.14)$$

$$A_x(\tau) = \frac{1}{\sigma_x^2} \int_{t=0}^{t=T} x(t)x(t-\tau)dt \quad (1.15)$$

Considering the flow field around a bluff body due to ABL type flow, the stagnation point is the position where the streamwise velocity is reduced to zero and static pressure increases to a maximum as a result, which typically results from Bernoulli's equation that is valid for inviscid, incompressible, steady flow conditions and follows the streamline (Holmes, 2018). The wind flow near the top of the building moves up and passes the edge into another side of the building and separates from the leading edges due to the adverse pressure gradient near the edges (Wu, 2000). This region is called the separation region which has also been demonstrated on two sides of the building. Due to the large vortices induced by the separated shear layer, suction pressures are large as the wind flow passes through the sharp edge of the building. For the low-rise building structures, the damage on the windward side of the roof would be extremely high caused by the separation bubble and conical vortices (Wu, 2000). A separation bubble is produced along the edge of the roof when the wind is normal to the edge. The conical vortices are usually generated in pairs, and they are near the corners along both roof edges when the wind attacks at an angle. Moreover, the low-rise buildings are situated at lower part of the ABL and the high suction pressures on the low-rise building roofs may also be induced by additional factors, such as terrain roughness. The rougher the terrain, the larger magnitudes of the suction pressure, particularly the peak suction pressure, occur on the low-rise building roof (Wu, 2000), which results from the higher turbulence intensities of the rougher terrain. The turbulence near a building can arise from two different sources - the turbulence inherent in the streamwise wind and the local turbulence produced by the interaction between the approaching wind and the building (Wu, 2000). According to different turbulence intensities of the upstream wind and the

dimension of the building, the flow may reattach to the roof or to the regions on the backward of the two sides of the building, which is categorised as reattachment region. The suction pressure declines in this region. As the flow starts to leave the building, a non-stable region happens caused by the shear layer between the high-speed flow and the static flow at the leeward side of the building, which is the reason for the flow rolling up into vortices, known as the wake region.

For an idealised indication of the flow over an idealised building, several vortices are indicated, largely due to flow separation (Cook, 1986). As a result, the pressure over the cube can vary which in turn can influence the flow field. The bottom half of the flow on the windward wall tends to roll up forming a formation known as a "horseshoe vortex". On both sides of the building, the mean flow transports these vortices parallel to the separation region, and these vortices are entrained into ABL.

The conical vortices can be generated when the wind attacks the structures with an angle (Wu, 2000). When the wind angles towards the building's corner are approximately 30°, the production of conical vortices on the roof is more likely (Wu, 2000). The reason is that the remaining horizontal momentum of the flow is transformed by the momentum of the flow separating into two sides of the building over the roof when the flow impinges the building. This reaction can produce high vorticity and cause vortices to rotate at an angle of 10° and 20° from the roof edge commonly along two sides of the building (Wu, 2000).

1.1.2 Extreme winds

There are two types of classical large-scale wind storms whose horizontal dimensions can reach up to over 1000 km: tropical cyclones and extratropical cyclones. Tropical cyclones are strong

rotating systems which encircle the intense low-pressure regions (Holmes, 2018). There are different names for tropical cyclones in different locations or for different strengths, which mainly include typhoons in Asia and Australia, and hurricanes in the USA for the maximum sustained surface winds (one-minute average) of 74 mph or greater, tropical depressions for the maximum sustained surface winds of 38 mph or less, and tropical storms for the maximum sustained surface winds ranging from 39-73 mph. When the temperature in tropical regions increases over 26 °C due to solar radiation, the air moves upward saturated with water. When the air reaches higher latitude and encounters cool air at higher elevations, part of the surrounding air falls as rain. During the process of liquidation, latent heat is released and further promotes the upward movement of the dominant air. This upward moving air is dominated by Coriolis forces (caused by the rotation of the earth) and starts to rotate in an anti-clockwise direction in the northern hemisphere and a clockwise direction in the southern hemisphere (Holmes, 2018). The extra-tropical cyclones are caused by the large-scale instabilities of atmospheric boundaries between different climate zones and happen at mid-latitudes of the earth (Holmes, 2018).

For small-scale windstorms, such as tornadoes and downbursts, horizontal dimensions can reach up to one kilometre. Tornadoes are upward swirling moving air. The moist air rises and becomes trapped under a colder and drier air cumulonimbus cloud. This produces a strong downdraft in the centre of these clouds. This two-way air flow strengthens the rotational flow and produces high rotational wind speeds with a central updraft. The length scale of tornadoes varies from 10 m to 1000 m, and the wind speeds can reach up to 200 km/h to 300 km/h. The strength of tornadoes is generally categorised by the EF scale, which is a scale based on the observations of building damage rather than on actual wind speed measurements. The scale of the EF changes from EF0 for the minor damage to EF5 for the incredible damage (McDonald

and Mehta, 2006). Gust speed generally represents the increase of wind speed within 20 seconds to the peak wind speed of at least 8.23 m/s (A.M.S., 2018).

A downburst is characterised as when the powerful downdraft reaches the ground, the flow direction diverges, resulting in an outburst of damaging wind. There are two types of downbursts: macrobursts and microbursts. The macroburst ranges in scale from 4 km to 400 km. The microburst ranges in scale from 40 m to 4 km (Fujita, 1985b). From Figure 1-2, the wind speeds increase to very high values over a period of a few minutes. Considering the small size of the buildings compared with the downburst and higher intensity of microburst than macroburst, the term "downburst" refers to microburst in this thesis. The formation of the downburst is shown in Section 1.2.1.

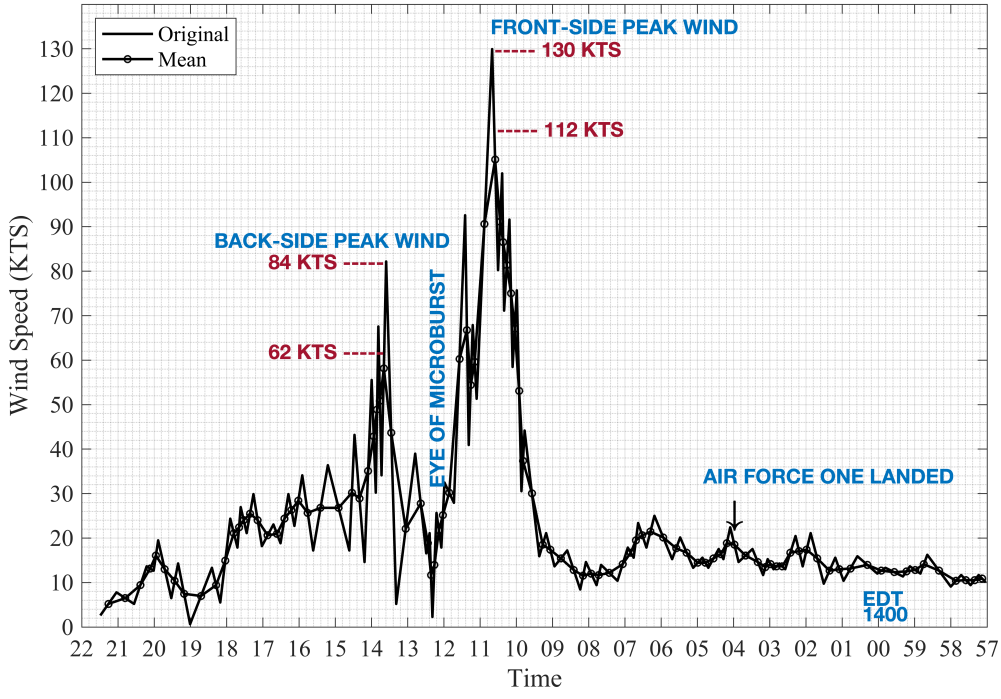


Figure 1-2. Andrews Air Force Base (AAFB) microburst (The peak wind speed reached approximately 130 kt (67 m/s) at 1410:45 EDT on 1st August 1983) (Fujita, 1985b).

In order to obtain the design wind loads for structures under the effects of extreme wind events, such as TS downbursts, the statistical analysis of recorded velocity time history is crucial and extreme value analysis was generally adopted to predict the appropriate design wind speeds (Holmes, 2018). Jenkinson (1955) proposed a generalised extreme value (GEV) distribution, which combines Frechet Distribution, Weibull Distribution, and Gumbel Distribution into one mathematical form (Eq. (1.16)) (Holmes, 2018).

$$P_{CPDF}(U) = exp\{-[1 - K(U - c)/a]^{1/K}\} \tag{1.16}$$

where K is a shape factor, a is a scale factor and c is a location parameter. K is usually around 0.1 (Holmes, 2018).

$$a \cong \left(\frac{\sqrt{6}}{\pi}\right)\sigma \tag{1.17}$$

$$c \cong \mu - 0.5772a \tag{1.18}$$

σ is the standard deviation of the velocity time series and μ is the sample mean.

When $K < 0$, GEV is known as the Type II Extreme Value (Frechet) Distribution

When $K > 0$, GEV is a Type III Extreme Value (Weibull) Distribution

When K tends to 0, the Eq. (1.16) becomes Eq. (1.19) which is the Type I Extreme Value (Gumbel) Distribution.

$$P_{CPDF}(U) = exp\{-exp[-(U - c)/a]\} \tag{1.19}$$

The return period of the annual maximum wind speed is in Eq. (1.20). A 50-year return period wind speed has a probability of exceedance of 0.02 in any one year.

$$R = \frac{1}{Probability\ of\ exceedence} = \frac{1}{(1-P_{CPDF}(U))} \quad (1.20)$$

1.2 Thunderstorm downburst

1.2.1 Formation

Fujita (1976) defined that,

"A downburst is a strong downdraft which induces an outburst of damaging winds on or near the ground".

Firstly, the warmer and moist air flow moves upward, caused by the buoyancy (Chay and Letchford, 2002). The downburst starts with the occurrence of a thunderstorm and the water droplets or hailstones being suspended within the updraft. Due to this strong updraft, it suspends large amounts of these droplets and hailstones in the upper portions of the updraft. When this air flow reaches higher elevations, the moisture in this air flow becomes colder and starts to become condensed. As the rain evaporates and hailstone melts, the heat is constantly being taken out of the air. The upward movement halts and the density of air rises. Because of gravity, this denser airflow starts to accelerate downward forming a strong downdraft (Straka and Anderson, 1993). From the angle of the first law of thermodynamics, the kinetic energy transfers to potential energy during the process of upward movement and the stored potential energy transfers to kinetic energy during the process of downward movement.

Secondly, when this downdraft flow reaches the ground, the velocity in the impingement point decreases to zero and the stagnation pressure reaches its maximum (known as high-pressure "dome" in the middle) which pushes the downdraft flow to spread out, producing a radiating accelerated outflow near the ground (known as low-pressure rings when it reaches the

maximum) accompanied by a vortex ring in front of the outflow (Fujita, 1985b). Based on the summary of the Doppler radar observations from 26 JAWS microburst cases (Hjelmfelt, 1988), the height of the maximum velocity occurred in the range of 50 m to 100 m and the maximum height of the vortices could reach up to 700 m-1000 m.

Thirdly, during the process of the downdraft and outflow, there are two types of vortices that appear - a primary vortex and a secondary vortex. At the edge of the downdraft, because of the unstable shear layer between the downward airflow and quiescent environment, the primary vortices are produced and this phenomenon has been illustrated by both impinging jet simulation and the cooling source method (Kim and Hangan, 2007; Lin et al., 2007; Mason et al., 2005; McConville et al., 2009). As the flow spreads outwards from the impingement point, the primary vortex is also convected radially outwards and starts to deform. The secondary vortices are formed because of the interaction of the unsteady separation of the boundary layer on the ground triggered by the primary vortex and the flow reattachment due to the ground roughness, and these move radially until dissipation (Kim and Hangan, 2007). However, there is no evidence that the secondary vortex formed within the downdraft state, which represents that the secondary vortex is formed at the outflow region (Kim and Hangan, 2007; Mason et al., 2009b). The position of the secondary vortex is located at the base of the primary vortex, which is also the reason for a nose-shaped velocity profile near the ground (Jesson et al., 2015b; Kim and Hangan, 2007; Lin et al., 2007; Mason et al., 2009a; Mason et al., 2009b; McConville et al., 2009).

1.2.2 Microburst characteristics

The summary of the Doppler radar observations from 26 JAWS full-scale microburst cases is presented in Table 1-1 (Hjelmfelt, 1988). The average maximum radial velocity is 24 m/s and

the diameter between maximum velocities is 3.1 km as shown in Table 1-1. The outflow depth varies with the location and for most of the time is less than 1 km. The average outflow depth from the recorded data of JAWS is 0.7 km. According to Figure 1-3, the average total period of a downburst is around 13 minutes. Initially, there is no observable wind shear in the first stage and no obviously horizontal diverging outflow in the second stage – see Figure 1-3. When the leading edge of the downdraft flow touches the ground, the divergently horizontal flow starts to be observed by Doppler radar and this period is usually less than 1 minute. Then, the shear increases to microburst intensity in the third stage. The time duration between the outflow starting to be divergent and maximum velocity is around 7.5 minutes. The time duration between the wind shear reaching microburst intensity and the maximum intensity is 5 minutes. At the time of maximum velocity, the distance between the leading edges of the outflow is, in general, twice the distance between maximum intensity (Hjelmfelt, 1988). Each downburst is unique, and the precise process of downbursts is different from each other. The outflow reaches its maximum intensity and presents similar structures as wall jet after the third stage as shown in Figure 1-3 (Hjelmfelt, 1988). As the primary vortex moves away from the downdraft centre, the outflow intensity starts to decrease. The fully developed vortex becomes obvious in stage five. The average decay period starting from maximum radial velocity is around 8 minutes.

Table 1-1. Microburst Characteristics (Hjelmfelt, 1988).

Microburst	Time of MAX (MDT)	Initial		First Alarm		Max		Decay			Depth at MAX (km)	Diameter (km)
		Δt to MAX (min)	ΔV/D (m/s/km)	Δt to MAX (min)	ΔV/D (m/s/km)	ΔV/D (m/s/km)	E at MAX (km)	Δt to MAX (min)	ΔV/D (m/s/km)	Expansion after MAX		
23 May A2	14:26	-5:00	14/1 6	-5:00	14/1 6	24/2 5	4 9	-	-	-	0 8	-
22 June 1	15:50	-16:00	4/1 0	-	-	18/3 0	4 3	+14:00	-	Yes	0 6	-
22 June 2	16:09	-4:00	12/2 5	-4:00	12/2 5	14/2 5	4 8	+5:00	6/3	No	0 8	-
22 June 3	16:14	-10:00	4/2 0	-3:31	15/2 0	18/2 5	6	+6:27	12/3	No	1 1	1 2
22 June 4	16:16	-6:00	9/3 0	-4:19	12/2 0	12/2 0	3 2	+2:10	6/4	No	0 4	1 6
22 June 5	16:23	-9:00	12/1 3	-9:00	12/1 3	16/2 3	5	+15:00	6/5	Yes	0 6	1 4
22 June 6	16:25	-10:00	4/1 0	-7:00	11/3 0	22/4 0	4 8	+15:00	9/6	Yes	0 9	1 4
23 June A	16:53	-9:00	6/1 8	-	-	20/2 5	6	+7:00	-	Yes	0 9	-
29 June G	16:05:59	-5:58	12/2 0	-5:58	12/2 0	24/4 0	6 5	+5:56	9/4	No	0 9	2 1
29 June C	15:51:15	-3:04	9/2 0	-1:16	27/3 0	27/3 0	5	+5:02	9/4	No	0 8	-
30 June A2	18:26:15	-	-	-	-	30/6 0	7	+9:20	21/14	Yes	0 5	2 1
8 July C	13:51:15	-14:59	6/1 0	-12:46	12/1 0	21/3 0	5	+16:23	9/8	Yes	0 9	1 4
14 July A	14:45:15	-	-	-	-	42/5 0	5 6	+9:27	9/4	No	0 9	-
14 July C1	14:53:36	-5:16	12/3 0	-5:12	18/2 0	24/4 0	5 1	+5:08	18/7	Yes	0 6	2 2
14 July C2	15:13	-7:00	12/2 0	-	-	16/3 0	-	+8:00	-	No	0 5	-
14 July D	16:47	-7:00	12/2 0	-4:03	18/3 0	24/4 0	3 5	+6:00	9/3	No	0 3	3 1
20 July A12	18:16:15	-7:15	9/1 0	-2:58	18/5 0	21/4 0	6 3	+5:00	12/3	No	1 1	1 8
5 Aug B1	18:31:15	-8:00	12/4 0	-8:00	12/4 0	27/7 0	9	+5:00	-	Yes	0 4	-
5 Aug B2	18:29:43	-8:00	6/2 0	-6:00	12/2 0	24/4 0	3 6	+2:00	9/3	Yes	0 9	-
5 Aug B3	18:48	-10:00	14/1 2	-	-	30/2 5	4	+13:00	-	No	0 5	2 0
5 Aug B4	18:48	-2:00	16/0 8	-2:00	16/0 8	18/2 0	2 7	+8:00	8/1	No	0 4	-
5 Aug C	18:34	-	-	-	-	26/3 0	5	+7:00	9/1	No	0 4	-
6 Aug A1	17:28:36	-8:34	6/2 0	-2:21	20/2 0	22/2 5	6	+3:09	18/4 5	Yes	1 1	-
6 Aug A2	17:22:13	-	-	-	-	24/2 0	9	-	-	No	0 6	-
6 Aug A34	17:41:15	-	-	-	-	36/2 0	9	+9:10	9/1 0	No	0 5	-
6 Aug A5	17:52:44	-	-	-	-	30/2 0	8 5	+5:32	18/7 0	Yes	1 2	-
12 Aug A	14:34:20	-	-	-2:10	18/2 5	24/4 0	5 7	+5:25	27/7 0	Yes	0 9	-
		-7:48	9/1 9	5:00	15/2 3	24/3 1	5 4	+8:13	12/4 5	12 yes/14 no	0 7	1 8

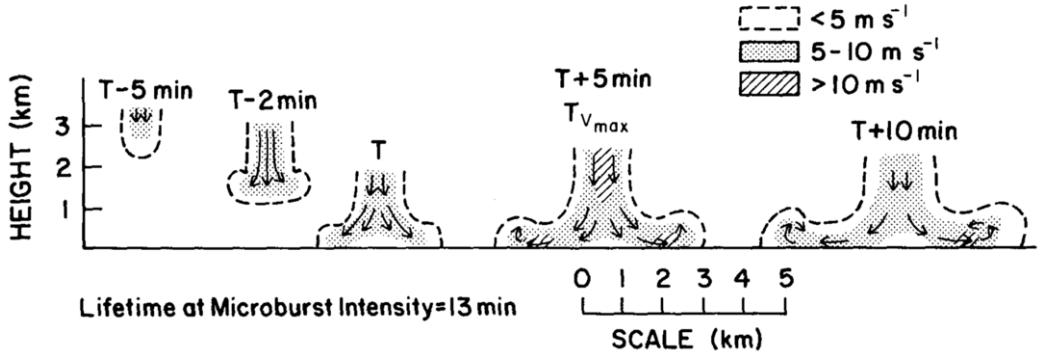


Figure 1-3. Life cycle of a single microburst (Hjelmfelt, 1988).

Generally, the downdraft diameter of a microburst is approximately 1 km, and the period of extreme wind speed lasts around 5 minutes (Fujita and Wakimoto, 1981; Holmes et al., 2008; Jesson et al., 2019). The AAFB downdraft had a ramp-up period lasting approximately 90-100 seconds (Fujita, 1990). Holmes et al. (2008) found that using a moving average time of less than 100 seconds leads to the turbulence component with a near-zero mean. The peak velocity

time period of the recorded rear-flank downburst can last around 120 s to 180 s (Gast and Schroeder, 2003; Kwon and Kareem, 2009). One recorded strong TS downburst at Nanyang Technological University (NTU) station on 22nd May 2001, whose high wind speed period lasted approximately 120 s to 180 s and the total period was 20 minutes (Choi and Hidayat, 2002b). Lombardo et al. (2014) advised that the appropriate time period or time segments for the analysis of the TS downburst time series is around 60 s to 240 s. Durañona et al. (2007) discovered that the increasing velocity time period varied from 2 to 6 minutes, the decreasing velocity time period of these non-stationary events lasted between 5 and 6 minutes and the overall time period for these events was approximately 5 to 20 minutes, based on the analysis of 11 extreme non-stationary velocity time series measured in Northern Europe (Alsvik (1), Cabauw (3), Energy Research Centre of the Netherlands (ECN) (2) and Sletringen (5)). Solari et al. (2015) analysed that the period of the most intense part of the measured TS downburst events from the "Wind and Ports" project lasted around 248 s, including the ramp-up period of 116 s and the decreasing period of 27 s. Romanic et al. (2020a) proposed a new method of segmentation for picking up the duration of the TS downburst and velocity peak based on the isolated segments using statistical mean and standard deviation, which has been applied on 41 instantaneous velocity time histories of 19 downburst events from Europe (9), the United States (9) and Australia (1). Romanic et al. (2020a) stated that the TS peak can be larger than 2-4 times of mean wind speed before the TS based on the analysis of the velocity records from Europe and the duration of the TS peak is 2-5 minutes which occupied 2/3 of these records using the statistical mean method and 5-10 minutes using the standard derivation method.

1.2.3 Identification

A number of features of the velocity time history for translational full-scale downburst events were summarised from the downburst occurring at Lubbock, Texas, 2002 recorded by Gast and Schroeder (2003).

- An initial nearly constant wind speed over 10 m/s.
- A rapid acceleration to peak wind speed over 25 m/s.
- A sharp decrease as the centre of the downburst with stagnation zone passes over the measurement equipment.
- A "back-side" peak as the downburst begins to move away from the measurement equipment.

De Gaetano et al. (2014) classified the raw velocity records by these key parameters (i.e. non-stationary and non-Gaussian events, which have high peak velocities and gust factors while its mean velocities are relatively low) for each subsequent 10 minutes period within 1 hour as thunderstorms, which includes,

- Mean velocity, $\overline{U}_{10min} > 10$ m/s and $\overline{U}_{1hour}$.
- One-second Gust peak, $\widehat{U}_{10min} > 15$ m/s and gust factor, $G_{10min} = \widehat{U}_{10min}/\overline{U}_{10min}(G_{10min}/G_{10\text{min_ref}} > 1.25)$; $G_{1hour} = \widehat{U}_{10min}/\overline{U}_{1hour}$.

  $G_{10\text{min_ref}}$ is the reference gust factor (see (ESDU, 1993))
- Turbulence intensity, I_{10min} and I_{1hour}.
- Skewness, γ_{10min} and γ_{1hour} and Kurtosis, κ_{10min} and κ_{1hour}.

1.2.4 Wind velocity

The main characteristics of the downburst outflow have been studied in the past based on full-scale measurements (Burlando et al., 2017; Chen and Letchford, 2007; Gunter and Schroeder, 2015; Holmes et al., 2008; Lombardo et al., 2014; Romanic, 2021; Romanic et al., 2020a; Solari et al., 2015; Zhang et al., 2018). The recorded velocity time history of such events can be considered as the sum of the slowly varying mean wind velocity related to the low-frequency component and a residual fluctuating turbulence associated with the high-frequency component, which is regarded as a non-stationary random process. The fluctuation caused by small-scale turbulence is dealt with as the product of its slowly varying standard deviation by a rapidly varying stationary Gaussian random process with zero mean and unit standard deviation (Chen and Letchford, 2007; Solari, 2016), which resembles processes that characterise high-frequency fluctuating components of stationary winds (see Figure 1-4). Accordingly, the total instantaneous horizontal velocity time history and the residual fluctuating velocity are shown in Eq. (1.21) and Eq. (1.22) separately, where the flow field is height dependent.

For instance, Figure 1-4 (a) is one recorded time history of a downburst at 158 m height from the Texas Tech University Wind Engineering Field Research Laboratory (WERFL). The main feature of this time history obtained by applying a moving-average filter in a 40 s moving is shown in Figure 1-4 (b), which is also called slowly varying mean velocity. Subtracting the filtered history from the original time history, the residual time history as shown in Figure 1-4 (c) can be described as fluctuating turbulence.

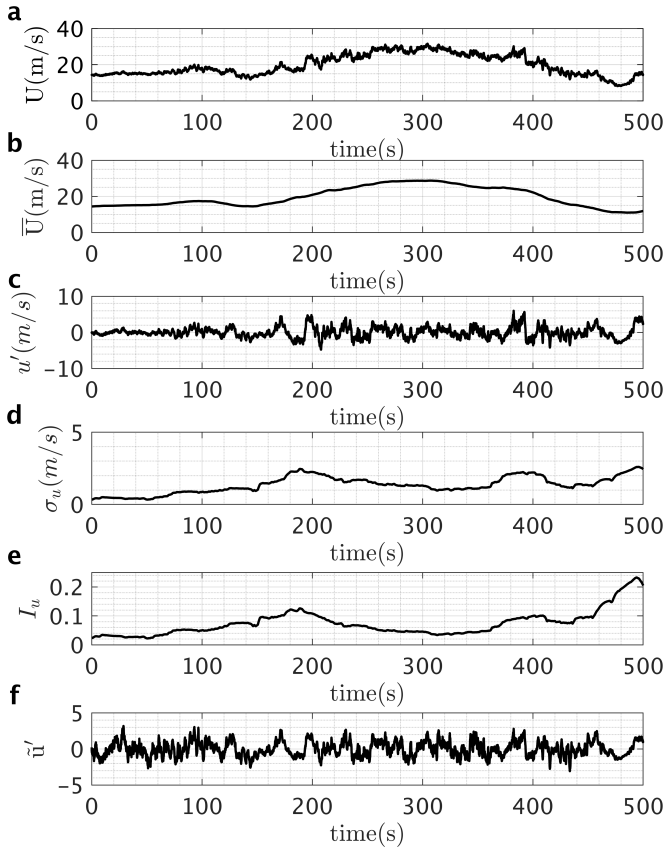


Figure 1-4. Wind velocity decomposition of a TS recorded at 158 m on May 21, 2008, at the WERFL field: (a) Recorded velocity time history; (b) 40 s moving average mean velocity; (c) Residual turbulent fluctuation; (d) Slowly varying standard deviation of u'; (e) Time varying turbulence intensity; (f) Rapidly varying turbulent fluctuation.

$$U(z,t) = \overline{U}(z,t) + u'(z,t) \tag{1.21}$$

$$u'(z,t) = \sigma_u(z,t)\tilde{u}'(z,t) \tag{1.22}$$

In these equations, $\overline{U}$ is the slowly varying mean wind velocity to low-frequency components, yields from the running mean or moving average technique, introduced by Holmes et al. (2008); z is the varying height above the ground; u' is the residual fluctuating velocity to high-frequency components (Hjelmfelt, 1988; Holmes et al., 2008; Lombardo et al., 2014; Solari et al., 2015). Furthermore, σ_u is the slowly varying standard deviation, often expressed in terms of the slowly varying mean wind velocity on a large scale and the corresponding turbulence

intensity, I_u, i.e. $\sigma_u = I_u \overline{U}$; $\tilde{u}'$ is the reduced turbulent fluctuation, dealt with as a rapidly varying stationary Gaussian random field. In Chapter 5 and 7, the residual turbulent fluctuation has been assumed to be modulated uniformly regardless of the time function for the turbulence intensity. This hypothesis is also consistent with the analysis results among the 129 recorded TS events by Roncallo and Solari (2020).

Then, Eq. (1.21) can be substituted by Eq. (1.23).

$$U(z,t) = \overline{U}(z,t)[1 + I_u(z,t)\tilde{u}'(z,t)] \tag{1.23}$$

To simplify these equations, a non-dimensional vertical shape function of horizontal wind $\alpha(z) = \overline{U}_{max}(z)/\overline{U}_{max}(r)$, as well as a non-dimensional time function of horizontal wind $\gamma(t) = \overline{U}(z,t)/\overline{U}_{max}(z)$ are defined. In these expressions, $\overline{U}_{max}$ is the maximum slowly varying mean wind velocity and r is the reference height. In doing so, the slowly varying mean velocity can be expressed by Eq. (1.24) (Solari, 2016).

$$\overline{U}(z,t) = \overline{U}_{max}(r)\alpha(z)\gamma(t) \tag{1.24}$$

Given the "nose" shaped profile of TS outflow, the original algorithm for the ABL becomes redundant. For this reason, analytical models to describe the vertical profile of horizontal velocity in TS outflow have been proposed (Abd-Elaal et al., 2013; Abd-Elaal et al., 2014; Li et al., 2012; Wood et al., 2001). In Chapter 5, the suggested shape function for the vertical velocity profile of horizontal wind proposed by Wood et al. (2001) is adopted, given by Eq. (1.25).

$$\overline{U}(z,t) = \overline{U}_{max}(r) \times \left(\frac{z}{r}\right)^{\frac{1}{6}} \left[\frac{1-\mathrm{erf}\left(0.7\frac{z}{\delta}\right)}{1-\mathrm{erf}\left(0.7\frac{r}{\delta}\right)}\right] \times \gamma(t) \tag{1.25}$$

In this equation, δ is the height where the velocity is equal to half its maximum value along with the height, i.e. $\overline{U}_{max}(\delta) = 0.5\overline{U}_{max}(z_{U_{max}})$, erf is the error function. The method uses a value of δ equal to $6z_{U_{max}}$, where $z_{U_{max}}$ is the height for the maximum value of the slowly varying mean velocity along z.

The comparisons of horizontal wind velocity profiles between the TS downburst and synoptic wind are demonstrated in Figure 1-5 (a), assuming that their maximum velocity matches. The synoptic wind profile was built based on the power-law model. In this case, ϵ represents the exponents of power-law. This particular case is representative of real scenarios in the sense that, the horizontal wind velocity induced by downburst outflow exceeds that produced by boundary layer wind near the ground.

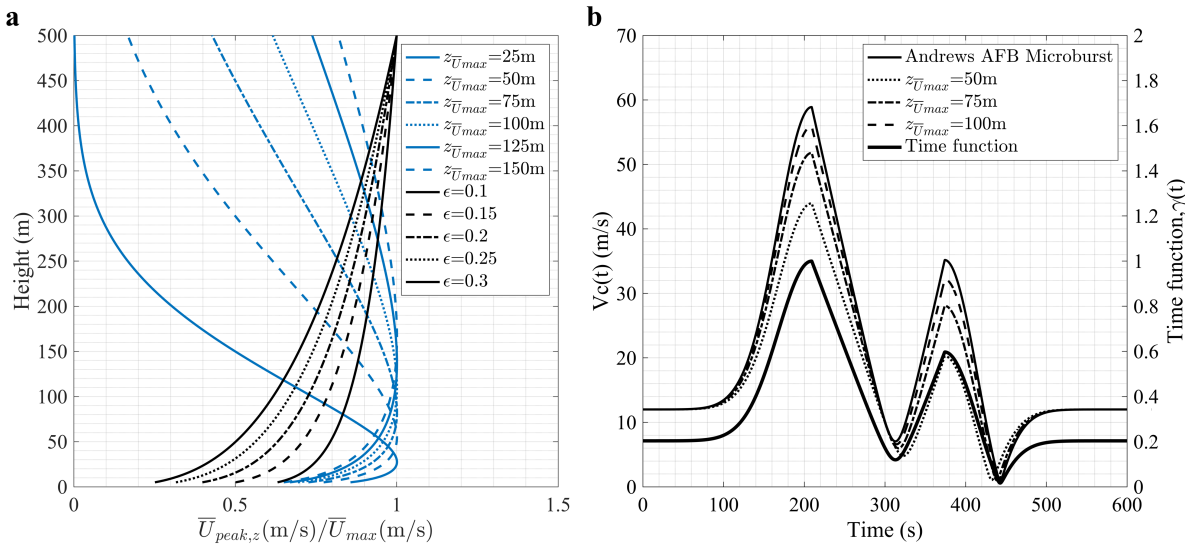


Figure 1-5. Comparison of velocity profiles: (a) Vertical profiles of horizontal winds for TS downburst and synoptic wind ($z_{\overline{U}_{max}}$ denotes the height of $\overline{U}_{max}$ for TS downburst wind; ϵ is the exponent of power-law for ABL wind (see Eq. (5.1)); (b) Simulated velocity time history and time function.

The radial velocity profile of horizontal wind suggested by Holmes and Oliver (2000) is described and given in Eq. (1.26). The model assumes that the resultant velocity V_c at the

observation point P with an offset distance, e, can then be expressed as Eq. (1.27) - where the angle between the translation velocity V_t and the radial velocity V_r is defined as θ-see Eq. (1.28), described in Figure 1-6.

$$\begin{cases} V_r(x) = \overline{U}_{r,max} \times \left(\frac{x}{r_{max}}\right) & x \le r_{max} \\ V_r(x) = \overline{U}_{r,max} \times exp\left\{-\left[\frac{x-r_{max}}{R}\right]^2\right\} & x > r_{max} \end{cases} \tag{1.26}$$

$$V_c^2 = V_r^2 + V_t^2 - 2V_rV_t\cos(180° - \theta) = V_r^2 + V_t^2 + 2V_rV_t\cos(\theta) \tag{1.27}$$

$$\theta = \begin{cases} \text{atan}\left(\frac{e}{d}\right) & 0° < \theta < 90° \\ 180° - \text{atan}\left(\frac{e}{d}\right) & 90° < \theta < 180° \end{cases} \tag{1.28}$$

In these equations, R is the radial length scale defined as the distance from the "low pressure ring" (r_{max}) to the "high-pressure ring" (Fujita, 1985b); x is the radial distance from the storm centre, defined as $x = (d^2 + e^2)^{1/2}$; r_{max} is the radius at which the maximum horizontal wind velocity occurs. Then, the $\gamma(t)$ can be represented by $\frac{|V_c(t)|}{\max|V_c(t)|}$. The simulated time history of the slowly varying mean wind velocity, including the AAFB Microburst event mentioned in Figure 1-2 and simulated random TS downburst events with varying $z_{U_{max}}$, as well as the time function are illustrated in Figure 1-5 (b), for the parameterisation listed in Table 1-2. f_s is the sampling frequency of the simulated fluctuation which corresponds to the simulated wind field mentioned in Section 5.4.2. The higher resultant velocity in Figure 1-5 (b) is induced by the increasing value of $\overline{U}_{r,max}$ at the assumed reference height of 183 m, since $z_{U_{max}}$ increases (see Table 1-2). It needs to note that this time function is built based on one typical recorded time history of a downburst event. Based on the improved analytical model detailed by Xhelaj et al. (2020), more representative time history records of the downburst outflow can be attempted.

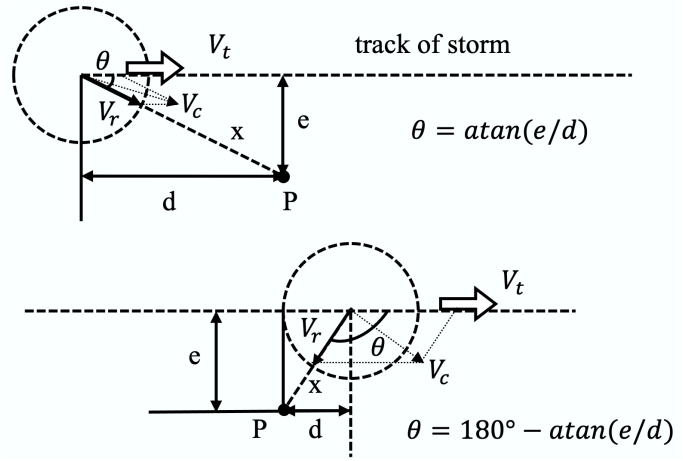


Figure 1-6. The layout of the storm location relative to observed position (Holmes and Oliver, 2000).

Table 1-2. Parameters for time function.

Parameters	Value
r_{max} (m)	1000
$z_{U_{peak}}$ (m)	4.9, 50, 75, 100
$\overline{U}_{r,max}$ (m/s)	47, 32.06, 39.89, 44.01
R (m)	700
e (m)	150
V_t (m/s)	12
$P_{initial}$ (m)	3500
f_s (Hz)	2.56

The effect of terrain roughness on turbulence intensities has been extensively researched in the past based on full-scale measurements of downburst events (Aboshosha et al., 2015; Burlando et al., 2017; Choi, 2004; Durañona et al., 2007; Hjelmfelt, 1988; Kwon and Kareem, 2009; Lombardo et al., 2014; Orwig and Schroeder, 2007; Romanic et al., 2020a; Solari et al., 2015). Accordingly, these studies partially support the result that the turbulence intensity of the wind field is not affected by the terrain roughness during the time evolution of the TS downburst due to its transient properties. In Section 2.3 and Chapter 5, $I(z,t)$ is assumed to be time-independent, i.e. $I(z,t) = I(z)$ (Burlando et al., 2017; Chay et al., 2006; Choi, 2004; Durañona et al., 2007; Holmes et al., 2008; Orwig and Schroeder, 2007; Romanic et al., 2020a; Solari et al., 2015; Solari et al., 2017). The vertical distribution of the turbulence intensity is assumed to

be independent of height by many researchers (Chay and Albermani, 2005; Chay et al., 2006; Chen and Letchford, 2004a; Chen and Letchford, 2006). Ample discussions addressing this consideration for different terrain categories can be found at (Kwon and Kareem, 2009; Solari et al., 2015). Since the empirically vertical shape function of I_u under non-stationary wind events needs further investigation, the turbulence intensity for boundary layer wind proposed in ASCE7 (2013) is adopted in Section 2.3 and Chapter 5 and $I(z) = \mathrm{c} \times (r/z)^{1/6}$. In this case, r is often taken as 10 m and c (the turbulence intensity factor) is assumed as 0.3, 0.2 and 0.15, for exposures B, C and D - as defined by ASCE7 (2013).

In addition, extensive work on the power spectral density (PSD) functions of horizontal fluctuating components under stationary wind has been reported by Simiu and Scanlan (1996). That work was extended to the non-stationary wind by Chen and Letchford (2007), Choi and Hidayat (2002a), Holmes et al. (2008), Lombardo et al. (2014), Solari et al. (2015) and Roncallo and Solari (2020) to mention some. The analysis of the wind turbulence of the recorded TS downburst by Holmes et al. (2008) demonstrated that the high-frequency spectral density of downburst outflow is similar to that of ABL winds. The most common non-dimensional expression of the PSD function of rapidly varying turbulent fluctuation $\tilde{u}'$ (parallel to the slowly varying mean wind direction) is the von Kármán spectra (von Kármán, 1948), shown in Eq. (1.29a), which has been adopted by the ASCE7 (2013). Considering the variation of the PSD function with height, an extended form was proposed by Solari and Piccardo (2001) as given in Eq. (1.29b). Based on the mean value of the PSD of the rapidly varying turbulent fluctuation of all the TS records detected by the "Wind and Ports" project, a close match with Eq. (1.29b) can be found when $f_m = 0.055$ (Solari et al., 2015). This evidence underpins the assumed form of PSD of $\tilde{u}'$, based on 93 TS downburst records, given in Eq. (1.29c). It is worthwhile to highlight that Eq. (1.29d) provides an alternative expression to produce the PSD

and this approach was proposed by Kaimal et al. (1972). The difference between these is that Eq. (1.29a) is defined by the integral length scale while the rest of these (i.e. Eq. (1.29b) - (1.29d)) demonstrate the pertinence of the height above the ground. For the former application, Zhang et al. (2018) and Roncallo and Solari (2020) have illustrated that the PSD of the reduced turbulent fluctuations has higher peaks with varying running-mean time intervals (Δt) while the latter has lower peaks and larger span ranges of the scaled frequency $nz/\overline{U}_{max}(z)$ with different Δt. Therefore, the importance is to confirm the PSD peak located in the low-frequency range with different PSD models.

$$\frac{nS_{\tilde{u}'}(n)}{{\sigma_u}^2} = \frac{4(\frac{nL_u}{U})}{\left[1+70.8(\frac{nL_u}{U})^2\right]^{5/6}} \tag{1.29a}$$

$$\frac{nS_{\tilde{u}'}(z,n)}{{\sigma_u}^2(z)} = \frac{f/f_m}{[1+1.5f/f_m]^{5/3}} \tag{1.29b}$$

$$\frac{nS_{\tilde{u}'}(z,n)}{{\sigma_u}^2(z)} = \frac{18f}{[1+27f]^{5/3}} \tag{1.29c}$$

$$\frac{nS(z,n)}{u_*^2} = \frac{200f}{(1+50f)^{5/3}} \tag{1.29d}$$

In these equations, n is the frequency of gust wind; L_u is the turbulence integral length scale, defined as $L_u = \overline{U}\int_0^\infty \rho(\tau)d\tau$, where $\rho(\tau)$ is the autocorrelation function that changes with the time delay (τ); $f = nz/\overline{U}_{max}(z)$, $f_m = 0.1456z/L_u$ when $nS_{\tilde{u}'}$ is maximum; u_* is the friction velocity. In Section 2.3, the $L_u(z) = l(z/r)^\alpha$ for ABL winds is adopted, where l and α are integral length scale factor and exposure constant, respectively, 98 m and 1/3 for exposure B, 152 m and 1/5 for exposure C, 198 m and 1/8 for exposure D (ASCE7, 2013).

Figure 1-7 shows the comparison of the PSD models. This comparison assumes that the height of peak velocity is located at 50 m above ground; the reference height and reference velocity

are 10 m and 50 m/s respectively, while the power spectral densities describe wind regimes at a height of 100 m. According to Figure 1-7, the von Kármán model reports higher energy within turbulence than the others. In Section 2.3 and Chapter 5, the PSD function suggested by Solari and Piccardo (2001) with unit standard deviation will be adopted for the TWDS and wind field simulation.

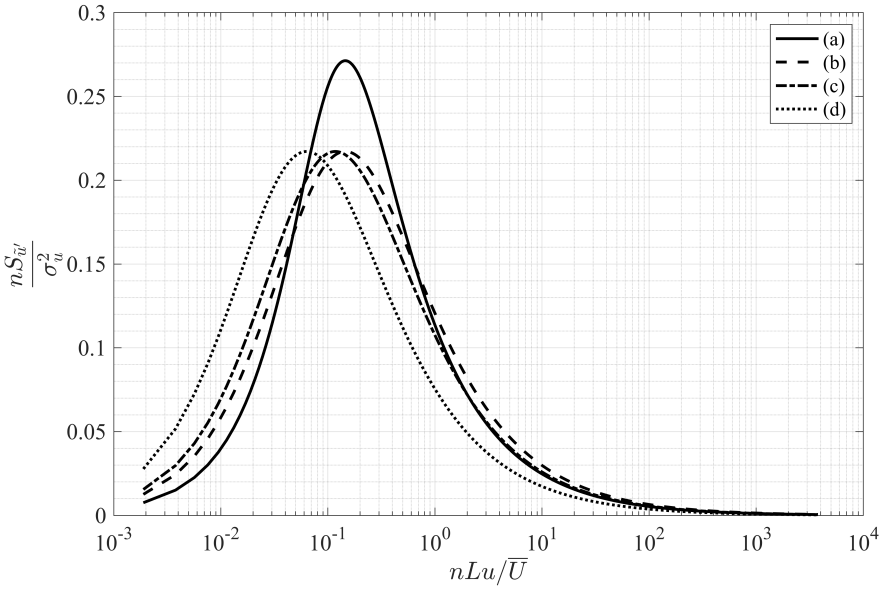


Figure 1-7. Comparison of different normalised PSD functions of longitudinal velocity.

To solve the complex characteristics of the structural coherence for the fluctuating turbulence flow induced by the divergent rotating vortices during the movement of the impinging point, Hangan et al. (2019) suggested the modal decomposition approach for the fluctuating velocity field, which can be used for further investigation. In Section 2.3 and Chapter 5, there is an assumption for this simplification that the horizontal velocity is built based on the steady structure of the TS outflow since the modulus factor i.e. the component of the turbulence intensity involved in the slowly varying standard deviation is regarded as time-independent for the velocity decomposition.

1.2.5 Non-stationary analysis methods

Downburst wind events are typically non-stationary and as such the methods used to analyse stationary data are not necessarily applicable. There are three methods discussed in this section, frequency-domain analysis, N-point moving averaging and wavelet analysis method. The frequency-domain analysis is only suitable for stationary wind analysis. N-point moving averaging and wavelet analysis method are used for non-stationary wind analysis. Wavelet analysis method is adopted in this research work that also has been adopted by many other researchers (Haines et al., 2013; Jesson et al., 2015a; Jesson et al., 2015b; Lombardo, 2009; Wang, 2008).

1.2.5.1 Frequency-domain analysis

Two types of frequency-domain analysis methods are discussed in this section, Fast Fourier Transform (FFT) and Short-time Fourier Transform (STFT). Fast Fourier transform (FFT) is characterised as converting a signal from the time-domain into frequency-domain as shown in Eq. (1.30).

$$FFT(f) = \int_{-\infty}^{\infty} x(t) e^{-i2\pi f t} dt \tag{1.30}$$

In this equation, f is the frequency, t is the time and $x(t)$ is the periodic function of t.

When the time-series of the wind load is known, the PSD can be obtained through square of the FFT. The PSD represents the distribution of turbulence with frequency (see Figure 1-7 (a)). The standard deviation of velocity can be obtained by integrating the power spectrum function over all frequency domain as shown in Eq. (1.31). The calculation of the PSD with specific turbulence frequency is shown in Eq. (1.32).

$$\sigma_u{}^2 = \int S_u(n) dn \tag{1.31}$$

$$S_u(n) = \frac{1}{fN}|\hat{x}_{fN}(n)|^2 \quad (1.32)$$

In this equation, S_u is the power spectrum of the horizontal wind velocity, N is the length of the signal, n is frequency and $\hat{x}_{fN}(\omega)$ is the Fourier transform of the horizontal wind speed in the frequency domain and represents the power per unit frequency contained in the signal at the frequency f (Haines, 2015).

However, the FFT can only illustrate the amplitude of frequency and cannot illustrate the information about the frequency variation in time. The velocity time series for downburst is non-stationary and a mushrooming velocity time series occurs during the process of downburst. The peaks characteristics are the most important for downburst data analysis. Moreover, different non-stationary time series may produce similar results in the frequency domain. Therefore, the FFT cannot effectively demonstrate the characteristics of the non-stationary time series.

An improved method based on Fast Fourier transform is put forward by adding different window sizes and this method is named Short-time Fourier Transform (STFT) (Allen, 1977) and is shown in Eq. (1.33).

$$STFT(f) = \int_{-\infty}^{\infty} W(t-\tau)x(\tau)e^{-i2\pi f\tau}d\tau \quad (1.33)$$

where W is the window function and τ is the time offset (s). The STFT method divides the time-series into infinite small time-series uniformly and then use the FFT method. The length of these small time-series is defined as window size. If the window size is too small, the time domain resolution would be high, and the frequency domain resolution would be poor. Or if the window size is too large, the results would be opposite. As for the non-stationary wind signals, high-frequency needs small window size and low-frequency needs large window size. However,

the window size cannot change with frequency in STFT, which means that STFT also not quite suitable for non-stationary signal analysis.

1.2.5.2 N-point moving average

N-point moving average decomposition aims to use the moving average filters to decompose the time series into slowly-varying (low-frequency) component and residual turbulence component (high-frequency) (Holmes et al., 2008). As for the choice of the moving average time, a lower moving-average time can lose some residual turbulence components and higher moving-average time can lose the characteristics of the large-scale storm (Holmes et al., 2008). The basic rule for choosing the suitable averaging time is that the residual turbulence components that remain after subtracting the filtered time series from the original velocity time series should have a near-zero mean value. The residual turbulence components should have similar properties to the high-frequency components in atmospheric boundary wind. What needs to be noted is that the high amplitudes of turbulence correspond to the high running mean values of the time series (Holmes et al., 2008) for non-stationary downburst events. The turbulence intensity, in this case, is the ratio of the root-mean-square (RMS) turbulence obtained from a moving average filter to the running-mean velocity as shown in Eq. (1.34).

$$I_u(t) = \frac{\sqrt{(U(t)-U(t))^2}}{U(t)} \tag{1.34}$$

where U is the instantaneous resultant velocity and $\overline{U}$ is the moving average velocity.

The effective cut-off frequency, f_c, of the time series sampled as a frequency of f_s, over a time interval of Δt, is estimated by Eq. (1.35) (Mooneghi et al., 2016), which determines the limitation between the low-frequency and high-frequency components.

$$f_c = \frac{0.45}{\Delta t} = \frac{0.45}{N/f_s} \tag{1.35}$$

1.2.5.3 Wavelet analysis method

The wavelet transform consists of wavelet decomposition and wavelet reconstruction. The wavelet decomposition is to decompose the one-dimensional non-stationary time-series into the two-dimensional time-frequency domain with a series of wavelets through the translation and dilation of the parent wavelet (Torrence and Compo, 1998). There are many types of parent wavelets that should have the zero-mean property in time and frequency domain (Torrence and Compo, 1998). The parent wavelet is the wavelet basis function that can generate a series of continuously translated and dilated wavelets. The dilation parameters correspond to the width of the wavelet and the translation parameters correspond to the actual position of the wavelet in physical space (Farge, 1992).

The Continuous Wavelet Transform (CWT) algorithm outputs the 2-D matrix of wavelet coefficients related to the original signal $f(x)$ and demonstrates both the amplitude of any characteristics (velocity and frequency) against the scale and how this amplitude varies with time (Torrence and Compo, 1998). The small wavelet scales represent the narrow wavelet which can demonstrate the details of the high-frequency components and vice versa. The wavelet reconstruction renamed the inverse CWT algorithm (Erickson, 2016) is applied to obtain the velocity time-series due to certain ranges of the frequency components. The cut-off wavelet scales divided by an appropriate velocity scale give the cut-off frequencies. The scales larger than the cut-off length scales correspond to the low-frequency turbulence. The scales that are smaller than the cut-off length scales correspond to the high-frequency turbulence.

The Continuous Wavelet Transform of a discrete sequence x_n (with equal time spacing and $n = 0, \dots, N-1$) is defined as the convolution of x_n with a scaled and translated version of

$\psi_0(x)$, where a is the wavelet scale, b is the localised time translation parameter and δt is the time spacing (Torrence and Compo, 1998) - see Eq. (1.36). The (*) in Eq. (1.36) indicates the complex conjugate. In order to close to continuous sequence, the convolution in Eq. (1.36) should be repeated N times for each scale, where N is the number of points in velocity time series. As a result, the wavelet coefficients correspond to the power spectrum densities (Torrence and Compo, 1998).

$$WT_n(a) = \sum_{n=0}^{N-1} x_n \psi^*[\frac{(n-b)\delta t}{a}] \tag{1.36}$$

The Morlet wavelet is adopted here due to its modulated sinusoid wave shape which can demonstrate the non-stationary time series effectively. Eq. (1.37) is the time domain Morlet wavelet function consisting of a plane wave modified by the Gaussian envelope of unit width (Torrence and Compo, 1998).

$$\psi_0(x) = \pi^{-1/4} e^{i\omega_0 x} e^{-(x^2/2)} \tag{1.37}$$

where ω_0 is the non-dimensional frequency and taken as 6 to satisfy the admissibility condition, detailed in Lee and Yamamoto (1994). This function must have zero mean and be localised in both time and frequency space.

In the analysis of building aerodynamics under non-stationary downburst events, the wavelet scales are limited by the cut-off wavelet scale, matching the 5×H length scale, certified by Wu and Kopp (2018) where H is the height of the building. The chosen "5×H" is based on the smallest length scale of the turbulence for which the effects of the pressure fluctuations can be explained by the QS model (Wu and Kopp, 2018). Based on the coherence function between the QS-predicted and measured pressures, the coherence is going to zero when the length scale is less than 5×H, which demonstrates that the QS model can only explain the effects of large-

scale turbulence on the roof surface pressure fluctuation (i.e. length scale larger than 5×H) (Wu and Kopp, 2018). Therefore, the effects of the small-scale turbulence (i.e. length scale smaller than 5×H) on the roof surface pressure fluctuation are studied in this research.

After the wavelet analysis, the velocity time series can be divided into a running mean velocity time series (low-frequency velocity time series) and fluctuating velocity time series (high-frequency velocity time series) by the cut-off frequency. The turbulence intensity of this non-stationary signal is calculated by Eq. (1.38).

$$I_u(t) = \frac{\sigma_u(t)}{u(t)} \tag{1.38}$$

Generally, the velocity is only considered in the streamwise direction as shown in Eq. (1.38). However, this is invalid for downburst wind fields as the vertical and lateral components induced by the large vortices (primary vortex and secondary vortex) are significant (Fujita, 1985b; Jesson et al., 2019; Mason et al., 2009b). Therefore, the turbulence intensity should be calculated using the overall wind speed (Jesson et al., 2019) seen in Eq. (1.39).

$$I_u(t) = \frac{\sigma_u(t)}{U(t)} \tag{1.39}$$

where U is the instantaneous resultant wind speed (Eq. (1.40)).

$$U(t) = \sqrt{u^2(t) + v^2(t) + w^2(t)} \tag{1.40}$$

In Quasi-steady theory (defined in Section 1.4.2), there is an assumption that the turbulence components in lateral (I_v) and vertical (I_w) directions are small enough to be negligible.

1.3 Simulation methods of TS downburst wind field

The characteristics of the TS downburst have been discovered by different methods, including full-scale downburst measurements, physical experiments of microburst, numerical simulations for the downburst flow field, and the theoretical models for microburst velocity profiles, and the velocity profiles of the TS downburst have also been analysed based on different types of methods (Solari, 2020; Solari et al., 2020).

1.3.1 Full-scale measurement

There were three historic projects related to the characteristics of the TS downbursts, which have been discussed by Wilson and Wakimoto (2001). These were NIMROD (Northern Illinois Meteorological Research on Outflows) near Chicago, Illinois in 1978, JAWS (Joint Airport Weather Studies) near Denver, Colorado in 1982 (discussed in Section 1.2.2) and MIST (Microburst and Severe Thunderstorm) near Alabama airport, Huntsville in 1986 (Fujita, 1990). Several microbursts were recorded by ground-based anemometers and Doppler radars. The maximum horizontal velocity was 31 m/s and was located less than 100 m above the ground though the maximum vertical velocity was situated at over 800 m. Obvious wind shear can be observed at around 1000 m. As defined in Section 1.2.1, when the downdraft flow reaches the ground surface, the wind starts to be divergent in different directions and the maximum diameter of the outflow can extend to approximately 4 km.

In 2002, a severe downdraft was recorded at Reese-Lubbock by the Wind Science and Engineering Research Centre of Texas Tech University (Gast and Schroeder, 2003; Holmes et al., 2008). The unfiltered maximum wind gust of this downburst was slightly over 40 m/s recorded at 10 m height at tower 3 and the recorded peak speeds are slightly lower for tower 4,

5 and 6 compared with the peak speed from tower 3. Six anemometer towers are at a spacing of 263 m. The time duration of wind speeds of over 25 m/s lasted approximately 120 s to 180s.

Even though many full-scale downburst events have been recorded by the previous projects, there is still a lack of reliable and sufficient detailed full-scale downburst data on buildings. The uncertainty of where and when a downburst will impinge on the ground as well as the small dimensions of buildings relative to the downburst enlarge the difficulty of the full-scale downburst measurement over the building. However, a few identified downburst events measured by anemometers on the tower located at different heights at the Texas Tech University Wind Engineering Field Research Laboratory (WERFL) were captured successfully, along with the measured pressures over the surface of a 9 m height × 14 m length × 4 m width WERFL building by pressure transducers (Lombardo, 2009; Lombardo et al., 2018; Lombardo et al., 2014).

Horizontal and vertical wind speed data for full-scale downbursts have been recorded at the WERFL field site during five downburst events. Details of the site measurements and transient wind record have been given by Lombardo (2009) and Lombardo et al. (2014). Initially, a 50-metre anemometer tower was used for velocity measurements. In early 2006, a new 200-metre anemometer tower was built at a new site. Anemometer heights are given in Table 1-3. All anemometers were sampled at a frequency of 30 Hz. The velocities mentioned in Table 1-3 are 3-second filtered data to correspond to the 3 s gust wind in ASCE7 (2013). The roughness length for these sites is around 0.015 m which can be regarded as smooth terrain type. Peak maximum velocity and the height of peak velocity for each event are given in Table 1-3. Each event was measured at different heights and the height of the peak velocities for each event was different.

Table 1-3. Summarised profile for five full-scale downburst events.

Date	Tower Height (m)	Peak velocity (m/s)	Height of peak velocity (m/s)	Measured Height Z (m)									
June 19, 2003	50	24.41	4		2.4	4	10	21	50				
May 21, 2008	200	30.67	158	1	2	4	10				116	158	200
June 19, 2008	200	28.32	158	1	2	4	10				116	158	200
August 13, 2008	200	26.29	116	1	2	4	10				116	158	200
March 08, 2010	200	34.40	75			4	10	17	47	75	116	158	200

The maximum magnitude of suction pressure coefficients can reach over 1 at the corner of the building roof, which is induced by conical vortices, and this result is consistent with the discussion in Section 1.1.1. Although the downburst wind loads have been successfully recorded by Lombardo (2009), this recorded data can only represent one type of building.

According to the European project of "Wind and Ports", the main characteristics of the detected TS records have been analysed by Solari et al. (2015). This consists of 64 TS events and 93 TS records at five ports including Genoa, Savona, La Spezia, Livorno and Bastia. Romanic (2021) analysed a nocturnal downburst event measured on a 213 m Cabauw tower in the Netherlands and four ultrasonic 10 Hz anemometers are located at 3, 60, 100, and 180 m above the ground. Its maximum velocity can reach up to 34 m/s at 180 m with a one-second moving average. Romanic (2021) also summarised the measurements of the TS winds at tall meteorological towers which are over 150 m above the ground, while the anemometer sampling frequency for the TS measurements before 2000 was lower than 10 Hz which seriously limits the investigation of the turbulent and transient properties of the downburst records. Burlando et al. (2017) investigated one record of a downburst event that occurred at Livorno, Italy on October 1, 2012, and this detection is part of the European "Wind and Ports" and "Wind, Ports and Sea" projects. This investigation compared the records of three anemometers with those of the Livorno site under this downburst event.

In summary, although field measurements are more realistic than the other approaches outlined below, this method is limited by the instantaneous nature of a downburst and the type of buildings. It is difficult to predict when and where such flows will occur and the distance between the centre of the downburst and the anemometer is uncertain, which may result in the whole process of the measurements being expensive and requiring long-term measurement campaigns. Therefore, a number of physical simulations have been carried out, which make it easier to model different types and styles of structures.

1.3.2 Physical experiment

Due to the uncertainty and associated costs of full-scale measurements, physical simulations have been used to determine the downburst wind loadings on different types of buildings. Physical experiments have the advantage of being relatively easy to control. Therefore, many researchers undertook a variety of physical experiments to simulate the laboratory-scale downburst wind loads on different types of structures, which demonstrated good agreement on downburst simulations.

Lundgren et al. (1992) modelled a microburst by releasing high-density fluid into low-density fluid which resulted in a vortex generating between the two sides of this falling fluid until striking the ground. This process has been compared with the full-scale microbursts recorded by Wilson et al. (1984) through a scaling law that demonstrated an agreement on the general characteristics, such as the ratio of the peak outflow velocity to the peak downdraft velocity and the radial position of the peak outflow velocity. However, there are a few limitations to these experiments: The momentum induced by the gravitational acceleration cannot support the acceleration of the heavier flow for the whole descending process and the heavier flow is submerged at a nearly constant velocity before it is close to the ground, which is inconsistent

with the mechanism of the downdraft flow; A too small cylindrical container (45 mm diameter × 45 mm height; with salt-water in it) for the microburst simulation can lead to an extremely small diameter of downdraft flow, which results in a particularly large length scale between the full-scale downburst and the simulated downburst (e.g. a full-scale downdraft with a diameter of 1.8 km leads to a length scale of 40000:1).

In order to better understand the characteristics of the microburst flow field, many researchers simulated the gust fronts of the outflow, including wall slot jets from the University of Western Ontario (Lin et al., 2007; Lin and Savory, 2006; Lin, 2010), large vortex generators (Sarkar et al., 2006), a flat plate gust front simulator (Butler and Kareem, 2007), and multi-fan wind tunnels (Butler et al., 2010). Additionally, for the purpose of better simulating the process of downburst flow, more researchers concentrated on the impinging jets including air impinging jet (Holmes, 1999), a static continuous impinging jet (Wood et al., 2001), travelling jet wind tunnel (Chay and Letchford, 2002; Letchford and Chay, 2002), circular pipe impinging jet (Choi, 2004), the pulsed wall jet (Mason et al., 2005), the transient wind simulator (1 m diameter impinging jet) from the University of Birmingham for the downburst velocity field (McConville et al., 2009), an impinging jet microburst simulator from the Iowa State University (Zhang et al., 2013), steady impinging jet (Zhang et al., 2014), the transient wind simulator from the University of Birmingham for high rise buildings (Haines et al., 2013; Haines, 2015) and the impinging jet simulation from University of Birmingham for the aerodynamic forces on buildings (Jesson et al., 2015a; Jesson et al., 2015b).

Six distances between the measured positions and the jet axis, and three different types of ground roughness, including smooth (plywood board), rough (carpet), and very rough (coarse grain particles) were considered in the impinging jet experiments carried out by Choi (2004), which found that the height of the peak wind speed increased with the increasing distance from

the jet axis as well as the increasing ground roughness. Furthermore, Choi (2004) fitted the power-law profile to the vertical distribution of velocity profiles when the height was lower than peak wind speed. The calculated power exponents can also illustrate that higher power exponents correspond to rougher surfaces and a larger distance between the centre of the simulated downdraft and the measurement position where the influence of ground roughness becomes dominant. However, the diameter of a downburst generally is approximately 1000 m and the diameter of this impinging jet is 100 mm, which leads to a large length scale. Moreover, whether the transient features of the downburst can be simulated is uncertain due to the limited description of this experiment.

McConville et al. (2009) built a TS downburst generator at the University of Birmingham to simulate the transient downburst events. This downburst simulator is based on the previous impinging wall jet downburst simulation, but instead of buoyancy-driven flow, fan-driven flow is adopted. The simulated velocity time history of a transient downburst has been compared with the data from a full-scale downburst event recorded at AAFB near Washington, which demonstrated a good agreement. However, the large length scale of 1:700 to 1:1000 can be limiting for engineering design, which normally uses models at a scale of 1:300 to 1:400 (McConville, 2008). The lower turbulence intensity occurred during the acceleration process of the flow from the centre of the jet to the position of peak maximum velocity compared with the full-scale downburst event recorded in Reese, 2002 and mentioned by Holmes et al. (2008). One limitation of the pressure measurements is the influence of the length of the small diameter tube connecting the tappings inside of the cube model and the transducers. Due to the limitations of the measurement technique, an 80 mm length of tube was chosen, though the measured peak pressure was underestimated by 40% and the mean pressure was underestimated by 13% compared with the data for the tube length which is smaller than 40 mm. Furthermore, even

though the peak and mean pressure coefficients have been obtained, the dynamic pressure is calculated based on the constant jet velocity or mean peak gust velocity of ten runs at eave height. Firstly, with the increase of radial positions of cube models, the velocity experienced by the cube is variable, and the constant jet velocity may overestimate or underestimate the true pressure coefficients on the cube surface. Secondly, the mean peak gust velocity at eave height can solve the problem induced by the first method, while this method may underestimate the pressure coefficients over the time series. A synchronous pressure and velocity time series may be a better method for the calculation of pressure coefficients.

Haines (2015) improved the transient wind simulator described by McConville et al. (2009) using the pulsed vortex technique but not the translating platform technique, which aims to reduce the vibration induced by the unsmooth movement of the platform. A Commonwealth Advisory Aeronautical Research Council (CAARC) building model (30 mm length, 46 mm depth, 183 mm elevation) with a 1:1000 length scale was adopted and measured in this experiment. The maximum pressure coefficients on this single building model under simulated downburst flow were higher than the data in ABL when the azimuthal angle was 0° or 90°, while the comparison of maximum pressure coefficients on the buildings was similar under simulated downburst and ABL when the azimuth was 45°. The interference effects between two high-rise buildings were also discussed by Haines (2015). When the distance between buildings was within the range of around 5 mm and 70 mm, the pressure field had an obvious difference compared with a single building. Another interesting result from Haines (2015)'s work is that the interference effects from a downburst event are lower than those from ABL flow due to the large scale vortices. However, the downburst simulations carried out by Haines (2015) also have many limitations. The velocities near the ground (below 5 mm) cannot be measured by the cobra probe, and the information about the nose shape may be missing. This

downburst simulation was still a stationary microburst, and many researchers suggested to add an ABL flow field aiming to simulate a travelling microburst.

The pressure distributions on different types of building models (cube building and portal building) were first carried out by Jesson et al. (2015b) using UoB-TWS. However, this experiment is also limited to stationary downburst simulation. The reference velocity adopted for the calculation of the pressure coefficient is the peak maximum velocity at eave height. The maximum velocity of the measured extreme microburst events, AAFB (Fujita, 1985a), was approximately 67 ms^{-1} which was used for velocity scale estimation. The mean value of the full-scale event is 6 ms^{-1} and is subtracted from the maximum velocity of the AAFB time series, which gives a maximum full-scale velocity of 61 ms^{-1}, as the full-scale microburst does not start from zero. The ratio of the maximum radial velocity to the downdraft velocity, U_{max}/V_j =1.7 is assumed in Jesson et al. (2015b). The calculated downdraft velocity for a full-scale microburst is 35.88 ms^{-1}. The velocity scale is obtained from the ratio of the downdraft velocity from physical simulations (13.7 ms^{-1}) and the downdraft velocity from the AAFB full-scale downburst (35.88 ms^{-1}). The estimated scales of the transient wind simulations based on the experimental work are 1:1600, 1:2.6, and 1:600 for length, velocity, and time, respectively (Jesson et al., 2015b). The length scale, 1:1600, comes from the assumption of a 1600 m diameter downdraft flow, and the diameter of the impinging jet is 1 m. Based on this scaling method, if a typical low-rise building of 10 m in height was measured, the height of the physical model should be approximately 6.25 mm, which is too small to obtain any reliable data from physical measurements. In this experiment, the height of the cube model is 60 mm corresponding to a 96 m height building in full-scale, which is a relatively large building. Many researchers (e.g. (Haines, 2015; McConville et al., 2009)) also adopted time scaling to fit partial velocity time history or entire velocity time history. The pressures were measured over the

surface of the cube building model with a 500 Hz, bespoke, 64-channel digital pressure measurement system (DPMS) and the duration of pressure measurement was 8 s. The sampling frequency of pressure measurement is 500 Hz. The time scale (1:600) in this experiment corresponds to 1.2 seconds of full-scale sampling time, which is within the 3-second gust wind. Therefore, this frequency of 500 Hz can be regarded as a reasonable value. The pressure time series are smoothed by a three-point moving average based on the time scale to correspond to the approximately 3 s duration of full-scale gusts ($\frac{3}{600}/(\frac{1}{500})$). The overall duration of the TS downburst is around 20 minutes (see Section 1.2.2). Based on the time scale (1:600) used by Jesson et al. (2015b), the whole recorded duration (3.28 s) can reach up to 32.8 minutes, which is inconsistent with the characteristics of the downburst duration.

More recently, Asano et al. (2019) further investigated the downburst wind loads on a low-rise building with a dimension of 80 m × 80 m × 40 m according to the newly developed downburst simulator which can generate a pulsed jet and a moving downdraft air flow separately or simultaneously. In this simulator, the diameter of the blower is 600 mm with a 1/2000 geometric scale. The velocity scale is approximately 1/5 since the wind velocity at the roof height of H is assumed as 35 m/s at full scale, which results in a time scale of approximately 1/400. The downdraft velocity, V_j, is 7.17 m/s with a turbulence intensity of 3.1%, measured at 100 mm above the simulator outlet. At the meantime, the downburst simulation experiments were also carried out by Junayed et al. (2019) in the Wind Engineering, Energy and Environment (WindEEE) Dome at Western University, which investigated the key characteristics of the generated downbursts with varying height to downdraft jet diameter ratios (i.e. H/D=0.8 and 1.2, with varying jet diameters of 3.2 m and 4.5 m) and Reynolds number (1.82×10^6 to 4.24×10^6). Consistency with previous research can be observed. However, this experiment is concentrated on the stationary TS downburst, and the scaling factors are not considered.

In experiments, the proper geometric (dimensions) and kinematic (velocity) scaling are important factors to simulate the downburst outflow to be equivalent to full-scale downburst events. Recently, Romanic et al. (2020b) proposed a new scaling method to solve this issue based on the decomposition of the velocity records and validated between 17 full-scale downburst events from the "Wind and Ports" and "Wind, Ports and Sea" projects in the period of 2009 to 2015 in the Mediterranean (Repetto et al., 2018; Solari et al., 2012) and 1400 experimentally simulated downbursts from the WindEEE Dome in Canada (Hangan et al., 2017). The comparison between the results from the experiments and full-scale measurements for the normalised slowly varying mean velocity demonstrated its efficiency to some extent. However, they also admitted that this method did not consider the existing ABL since non-interference environments are produced in the experiments. Furthermore, this method is limited to the specific measured points for the locations of the cobra probes but not the whole flow field.

The scaling law is important for the accuracy of the results, while a standardised method for the scaling of downburst events is needed. Even though a variety of structures can be measured in wind tunnel experiments, the investigations into the main features of the complicated, translating downburst events acting on the structures are still limited. Moreover, the influence of terrain and ground roughness on the downburst events is also important, as the maximum velocity caused by the combination of the primary vortex and the secondary vortex is affected by these factors. Physical experiments can be an effective method for varying types of buildings and are the basis for further theoretical calculations of the structural design.

1.3.3 Numerical simulation

In order to better understand the characteristics of the microburst, many numerical simulations (Abd-Elaal et al., 2018; Butler and Kareem, 2007; Chay et al., 2006; Chen and Letchford, 2007;

Haines and Taylor, 2018; Kim and Hangan, 2006; Mason et al., 2009a; Mason et al., 2009b; Selvam and Holmes, 1992) were carried out and verified with the full-scale field measurements data, physical experimental data, or theoretical models. These mainly were numerical simulation of gust front (Butler and Kareem, 2007), the combination of the non-turbulent downburst wind numerical simulation with an analytical model originally created for predicting wind shear and an auto-regressive moving average (ARMA) method aiming to adding turbulence (Chay et al., 2006), an axisymmetric, dry, non-hydrostatic numerical sub-cloud model to simulate an intense stationary downburst wind flow (Mason et al., 2009b), a movable downburst simulated by a three-dimensional, dry, non-hydrostatic, numerical sub-cloud atmospheric model (Mason et al., 2010), an unsteady Reynolds Averaged Navier-Stokes (RANS) simulation to simulate the downburst velocity time series and fitted to the full-scale rear-front downburst (RFD) data (Kim and Hangan, 2006; Kim and Hangan, 2007), Large eddy simulation (LES) to simulate the transient lift and drag coefficients around a cube and portal building (Haines and Taylor, 2018) with the same length scale as the experiments from Jesson et al. (2015b).

Numerical simulations can provide a visible platform for deeply understanding the formation of primary and secondary vortices as well as the flow characteristics around a building, such as the conical vortices, vortices on the roof and rear face of the building and vortex shedding. According to the simulation driven by Kim and Hangan (2007), it can be observed that the primary vortex is generated near the edge of the downdraft flow. Accompanying the primary vortex spreading out radially, a counter-rotating secondary vortex is formed beneath the primary vortex due to the unsteady separation-reattachment of the boundary layer. What needs to be noticed is that the secondary vortex moves upward along the edge of the primary vortex and then a new counter-rotating vortex is produced beneath the primary vortex. These two

counter-rotating vortices can also generate a region of intense stretching in between them, which accelerates the local flow separation as well. Kim and Hangan (2007) also demonstrated that the formation of the vortices was related to the Reynolds number, where the second counter-rotating vortex would not form when the Reynolds number was reduced from 100,000 to 20,000. Therefore, Kim and Hangan (2007) illustrated that higher Reynolds numbers can lead to more organised and periodic flow.

Following Kim and Hangan (2007)'s work, Mason et al. (2009b) also demonstrated a lifting secondary vortex during the outflow simulation process, while this secondary vortex formed at greater elevations compared with the simulations by Kim and Hangan (2007). The occurrence of the secondary vortex at high elevations indicates that the high velocity regions produced by the combination of vortices at high elevations can produce a significant change in flow directions, i.e. significant vertical velocity components.

Compared with the flow separation on the roof of the building in ABL flow, Haines and Taylor (2018) demonstrated that the primary vortex can keep its vortex-like structure jumping over the building roof with the vortex core at a higher elevation. Two separation bubbles can be observed, which led to the double peaks in the maximum lift coefficients on the roof of the building. The Reynolds number in this numerical simulation is 8×10^4. Two separation bubbles are formed on the two sides of the buildings as well, and the vortices are shed from alternate sides of the buildings. The differences with buildings in the ABL are that the second separation bubbles on the sides of the buildings are produced due to the primary vortex of the downburst flow and the duration of this phenomenon is short-lived due to the transient flow characteristics.

In contrast with different methods of downburst generators in experiments, Mason et al. (2010) proposed a simplified imposed cooling source technique to accelerate the downdraft, which can

effectively simulate the evaporative processes. With the variations of the translational speeds, the heights of the maximum velocities remain relatively constant. Mason et al. (2010) also stated the importance of the sub-cloud environmental wind field, i.e. the boundary layer flow with surface roughness and a log-law velocity profile. However, Mason et al. (2010) demonstrated that with the increase of the translational speed, the development of the primary vortex was reduced, and the intensity of the primary vortex did not relate to the environmental winds. Moreover, the secondary vortex did not occur in these non-stationary simulations and the explanation for this was that, when the downbursts descended into disturbed environments, the development of the secondary vortex lifting high wind speeds to large elevations was limited (Mason et al., 2010). The absence of the secondary vortex in movable downburst simulations shows that the height of the maximum horizontal velocity is lower than the data from stationary downburst simulations (Mason et al., 2010).

Even though numerical simulation is a feasible method, this method can be computationally expensive.

1.3.4 Theoretical modelling

Analytical modelling includes three types: theoretical modelling, semi-empirical and empirical modelling. In a theoretical model, it is relatively easy to change the important parameters of the downburst, e.g. height, size, shape, scale, intensity, location, and time, and it is thus an efficient way of understanding the importance of various variables. The theoretical analysis can be used to guide wind tunnel experiments and field measurements as well and can also be regarded as a basis for CFD simulations. Initially, a small number of downburst models were successfully built to simulate the major flow patterns of the wind shear for aeronautical applications (e.g. (Ivan, 1986; Zhu and Etkin, 1985)) and the influence of the ground roughness and the vortices

near the ground was not considered. In these downburst models, the velocity profiles are focused on one point. However, the buildings cannot be regarded as one point in the downburst flow field because the pressure distributions on the different sides of buildings induced by the downburst flow are quite different. The secondary vortex induced by the primary vortex and ground roughness is also important.

Furthermore, many researchers were interested in the radial velocity profiles and vertical distribution of the horizontal downburst wind speed profiles (Abd-Elaal et al., 2013; Abd-Elaal et al., 2014; Holmes and Oliver, 2000; Li et al., 2012; Sengupta and Sarkar, 2008; Wood and Kwok, 1998; Wood et al., 2001). These empirical downburst shape functions were obtained from the analysis of the full-scale downburst velocity profiles, the measured data from the downburst physical simulations, or the computational downburst wind simulations, which can potentially be used for the civil engineering structural design induced by the downburst wind flow.

Holmes and Oliver (2000) put forward an empirical downburst model to obtain the distribution of horizontal wind speed in each radial direction. This model divided the velocity profile for the points in the flow field into two parts: inside the stagnation region and outside the stagnation region. The application of this model is detailed in Section 1.2.4 and is shown in Figure 1-8, where V_r is the radial velocity; $V_{r,max}$ is the maximum horizontal velocity; x is the radial distance from the storm centre; r_{max} is the radius of the maximum horizontal wind speed; R is the radial length scale. When R is taken as $0.5\times r_{max}$, the velocity profile fits the radar recorded data of Hjelmfelt (1988). This downburst model can obtain the horizontal velocity at a different distance from the stagnation point at a fixed height of 10 metres. The limitation of this model is the lack of vertical distribution of the horizontal velocity profile.

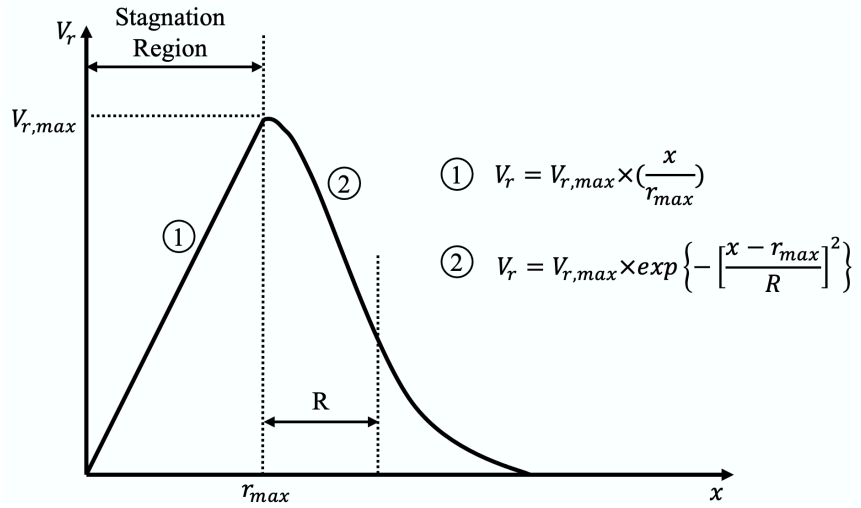


Figure 1-8. Horizontal radial velocity profiles (Holmes and Oliver, 2000).

Based on a series of impinging jet simulations of downburst flow, an empirical equation was put forward to accurately estimate the vertical distribution of horizontal velocity profiles (Wood and Kwok, 1998). These physical simulations have been compared with previously published data, which demonstrates a good agreement. The empirical equation is shown in Eq. (1.41). The application of this model is detailed in Section 1.2.4.

$$u(z) = A\,(\frac{z}{z^*})^B \left[1 - erf\left(C\,\frac{z}{z^*}\right)\right] \tag{1.41}$$

where "erf" is the error function, the parameters A, B, and C are 1.55, 1/6, and 0.7 respectively. z^* is the height at which the magnitude of horizontal speed is half the maximum speed. Sengupta and Sarkar (2008) improved parameters A, B, and C to 1.52, 1/6.5, and 0.68 separately based on the horizontal velocity profiles from impinging jet experiments, which showed a quite similar tendency to Rajaratnam (1976) and Wood and Kwok (1998)'s empirical profiles as well as Cooper et al. (1993) and Chay and Letchford (2002)'s experimental work.

More recently, Jesson and Sterling (2018) put forward a theoretical model named the "vortex model" that consists of three independent velocity fields, as shown in Figure 1-9. These are the outflow from the impingement point due to the relatively high pressure at this location, the

primary vortex due to the shear layer of the downdraft, and the secondary vortex due to the interaction of the ground roughness and the higher velocity of outflow and primary vortex as shown in Figure 1-9. The generation of the shear layer is due to the existence of the velocity gradient, which is induced by two types of situations. The first situation is the influence of the wall roughness, which is the reason for the secondary vortex. The second situation is when two adjacent air flows in the same direction with a large speed difference, which is the reason for the primary vortex. There are two types of typical vortices: irrotational vortices and rotational vortices (Acheson, 1991). Irrotational vortices demonstrate that there are no extra forces. The superposition of these flow fields is the application of the plane potential flow technique, which is a reliable method to estimate the flow structures theoretically. This potential flow technique demonstrates that one complicated two-dimensional flow movement for irrotational flows or inviscid potential flows can be superimposed and decomposed, because the function of this method, Laplace's equation, is a linear function (Wang, 2018). Therefore, the superposition of the velocities of these flow fields is the result of the whole flow field. However, the potential flow technique can not deal with the boundary condition because the potential flow is inviscid. Therefore, the mirroring method is adopted to satisfy the zero flow across the ground plane. The mirror vortices can also accelerate the radial flow close to the ground as the continuous rotational flow is contracted by the ground plane (Jesson and Sterling, 2018). The inviscid flow field also demonstrates that this is not the no-slip boundary condition (Jesson and Sterling, 2018). The no-slip boundary condition demonstrates that there is no relative movement between the air flow layer and the ground boundary (Acheson, 1991). Li et al. (2012) demonstrated that the boundary layer characteristic thickness is the height of half the maximum velocity of the downburst wind flow.

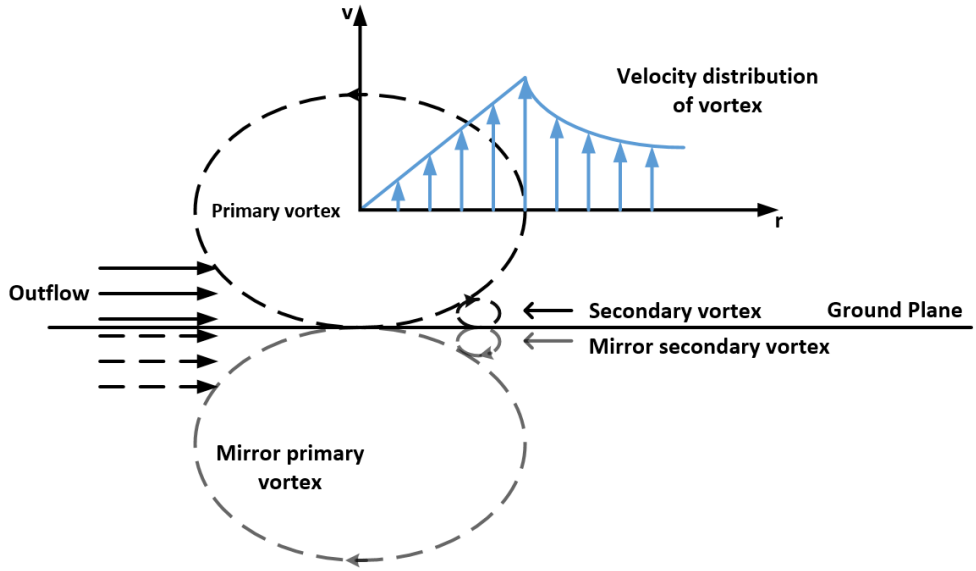


Figure 1-9. Schematic for the position of primary and secondary vortices.

Each vortex in the vortex model is modelled as a Rankine vortex, which is a simple mathematical model for a real vortex (Acheson, 1991). The real vortex is typically characterised by a small vortex "core" and defines that the flow within this vortex core is rotational flow with a velocity gradient and that the flow outside of this vortex core without external force is irrotational flow (Acheson, 1991). The vortex core is not always the exactly circular, and the Rankine vortex equations for the circular vortex core are shown in Eq. (1.42).

$$u_\theta(r) = \begin{cases} \frac{\Gamma r}{2\pi R^2} = \frac{\Gamma\sqrt{X^2+Z^2}}{2\pi(X_R^2+Z_R^2)} & for \quad r \le R\,; \\ \frac{\Gamma}{2\pi r} = \frac{\Gamma}{2\pi\sqrt{X^2+Z^2}} & for \quad r > R; \end{cases} \tag{1.42}$$

$$R = \sqrt{X_R^2 + Z_R^2} \tag{1.43}$$

$$r = \sqrt{X^2 + Z^2} \tag{1.44}$$

where u_θ is the tangential velocity of Rankine vortices relative to the centre point of each vortex "core" and r is the radial distance between the central point of the vortex "core" and any point in the flow domain. R is the radius of the circle and Γ is the circulation defined by the line

integral of a closed curve of the velocity field (Kuethe et al., 1986). (X, Z) are general points in the domain of the Cartesian coordinate system. (X_R, Z_R) are the points on the boundary of the vortex "core".

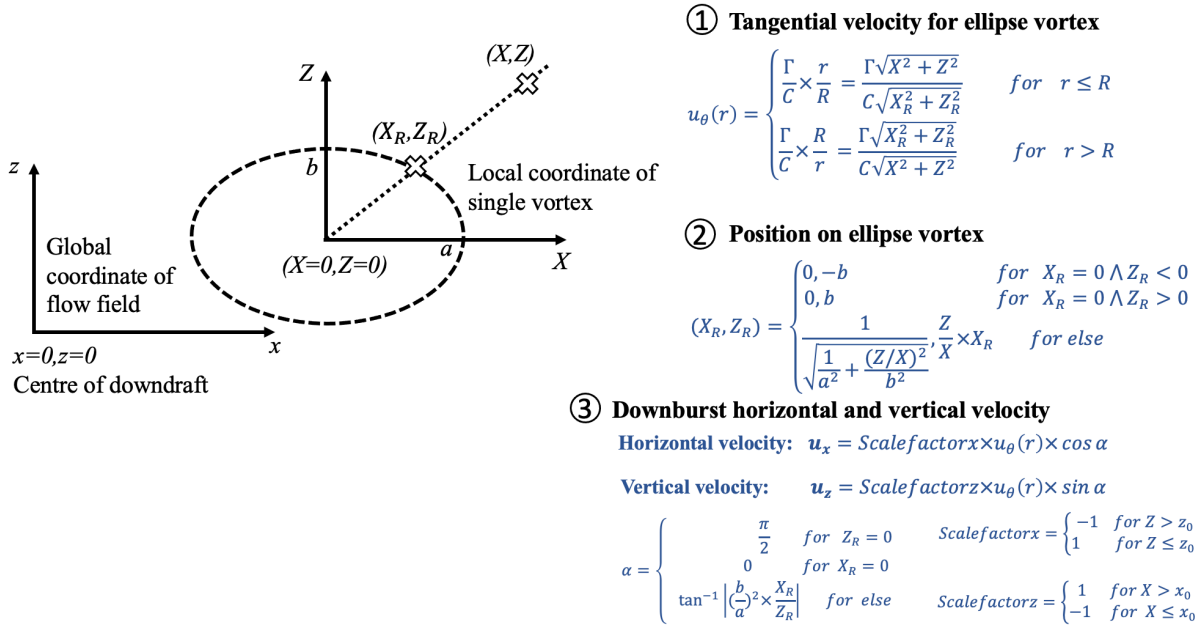


Figure 1-10. Local polar coordinate system for elliptical vortices with calculations.

Considering the evolution of the vortex shapes in a downburst, as for each Rankine vortex in the model, the shape of the vortex changes from a circle to an ellipse by specifying the rate of change of the length of the ellipse axes. Figure 1-10 is the local polar coordinate system for elliptical vortices with the application of Rankine vortex equations for the elliptical vortex. The standard equation of the ellipse is $\frac{X_R^2}{a^2} + \frac{Z_R^2}{b^2} = 1$. a is the major radius of the ellipse, which is characterised as being parallel to the x-axis (parallel with the ground surface) in the Cartesian coordinate system. b is the minor radius of the ellipse, which is characterised as being parallel to the z-axis (perpendicular to the ground surface).

The velocity distribution for each vortex is shown in Figure 1-9 and the maximum velocity occurs on the edge of the ellipse, which means that the maximum velocity occurs at the tangency

point between the primary vortex and the secondary vortex. The outflow velocity increases linearly from zero to final outflow velocity in a time of 1.6 times the secondary vortex half-life, which has resulted in the outflow velocity reaching its maximum as the rear of the vortex passes x_m. The factor of 1.6 is suggested by Jesson and Sterling (2018). This vortex model can obtain the velocity at any time and any position during the simulation of the downburst. More details about the application of this vortex model are discussed in Chapter 3.

Extending from the records of the full-scale TS downburst detection, the wind field of these typical characteristics has been simulated through hybrid models, such as those reported in Chen and Letchford (2004a), Chen (2008), and Solari et al. (2017) based on the theoretical velocity profile (Abd-Elaal et al., 2013; Abd-Elaal et al., 2014; Holmes and Oliver, 2000; Li et al., 2012; Oseguera and Bowles, 1988; Vicroy, 1992; Wood et al., 2001). In line with that, Chen and Letchford (2004a) suggested a hybrid model adopting the superposition of a deterministic mean and a stochastic fluctuation that yields a uniformly modulated evolutionary power spectral density (EPSD) function with an assumed stationary Gaussian distribution (Shinozuka and Deodatis, 1991). Solari et al. (2017) proposed a separate hybrid simulation technique using a Monte Carlo algorithm merged with full-scale downburst records. The state of the art is therefore limited to specific yet dispersed techniques to estimate the wind loading of TS downbursts. This evidence the further investigations of the potential effect that TS wind regimes could have on civil engineering infrastructure are needed.

1.4 Downburst wind loading

1.4.1 Aerodynamic property

Aerodynamic forces are generally resolved into two orthogonal directions, which are parallel and perpendicular to the wind direction, named drag force and lift force respectively in two-dimensional space (Holmes, 2018). Extending to three-dimensional space, the lateral force of the two sides of the building can be induced by vortex shedding. The generic definition of a force coefficient is shown in Eq. (1.45) and the drag coefficient and lift coefficient are defined in Eq. (1.46) and Eq. (1.47) respectively.

$$C_F = \frac{F}{\frac{1}{2}\rho U_{ref}^2 A} \tag{1.45}$$

$$C_D = \frac{F_D}{\frac{1}{2}\rho U_{ref}^2 A} \tag{1.46}$$

$$C_L = \frac{F_L}{\frac{1}{2}\rho U_{ref}^2 A} \tag{1.47}$$

In these equations, A is the area, U_{ref} is the reference velocity, F_D is the drag force and F_L is the lift force. One dimensionless pressure parameter, named pressure coefficient, is defined in Eq. (1.48).

$$C_p = \frac{p - p_{ref}}{\frac{1}{2}\rho U_{ref}^2} \tag{1.48}$$

In this equation, p_{ref} is the reference pressure, usually regarded as atmospheric pressure or the pressure of the surrounding environment for the wind tunnel design. U_{ref} is the reference velocity near the measured building while far enough away to not be influenced by the measured buildings. Generally, the reference velocity is characterised as the velocity time series

at eaves height where the maximum velocity occurs on the building according to the ABL wind velocity profile. The eave height represents the average of the roof eave height and the height to the highest point on the roof surface for the roof angles of less than or equal to 10 degrees (ASCE7, 2013). Jesson et al. (2015b) selected the peak maximum velocity of the measured downburst wind on the windward side as reference velocity. The height of this maximum velocity may be below the eaves height for high-rise building whose height is over 50 m because the downburst vertical distribution of horizontal velocity profile is different from the ABL vertical distribution of horizontal velocity profile. Wu and Kopp (2018) adopted the reference velocity measured at twice the building height and the selection of this position is a representative of the roof top flow and it is a negotiation between the minimal interference and being close enough to the roof. Mooneghi et al. (2016) chose the upstream approach flow velocity at cube height as reference velocity.

1.4.2 Quasi-steady theory

Letchford et al. (1993) stated that,

"In the Quasi-steady theory, the surface pressures generated on a building respond to atmospheric turbulence directly as if they were changes in mean wind speed and direction. Thus, pressure variations correspond exactly to wind fluctuations."

Under this assumption, the instantaneous pressure, $p\ (t)$, can be expressed as,

$$p\ (t) = \frac{1}{2}\rho U^2(t)\bar{C}_p(\theta(t)) \tag{1.49}$$

where $U(t)$ is the magnitude of instantaneous wind velocity (see Eq. (1.50)) and is composed of three components, longitudinal velocity, u, transverse velocity, v, and vertical velocity, w.

$\bar{C}_p(\theta(t))$ is the mean (with respect to time) pressure coefficient for the instantaneous wind direction $\theta(t)$.

$$U^2(t) = u^2 + v^2 + w^2 \tag{1.50}$$

The fluctuating wind direction in the horizontal plane is defined as,

$$\theta(t) = \bar{\theta} + \theta \tag{1.51}$$

where $\bar{\theta}$ is the mean wind direction in the horizontal plane and the fluctuating wind direction in horizontal plane, θ, also named azimuth angle is defined in Eq. (1.52) according to geometry. The vertical fluctuating component or elevation angle are defined in Eq. (1.53).

$$\theta = tan^{-1}\left(\frac{v}{u}\right) \tag{1.52}$$

$$\beta = tan^{-1}\left(\frac{w}{\sqrt{u^2+v^2}}\right) \tag{1.53}$$

where the azimuth θ is the angle between wind direction and "north" (perpendicular to the front face of the building) in the horizontal plane. The elevation angle β is the angle between wind direction and horizontal in the vertical plane.

The fluctuating wind directions are assumed linear for small v and w relative to u and the mean pressure coefficient corresponding to the instantaneous azimuthal angle can be expressed as (Letchford et al., 1993):

$$\bar{C}_p(\theta(t)) = \bar{C}_p(\bar{\theta}) + \left(\frac{v}{U}\right)\frac{dC_p(\theta)}{d\theta} + \left(\frac{w}{U}\right)\frac{dC_p(\theta)}{d\beta} \tag{1.54}$$

where, for angles, overbars demonstrate the mean wind direction. $\bar{C}_p(\bar{\theta})$ represents the mean (with respect to time) pressure coefficient for the mean wind direction, $\bar{\theta}$. $\overline{U}$ is the mean velocity of the time series. v is the transverse velocity and w is the vertical velocity.

Richards et al. (1995) indicated that the variation of the 10-minute mean pressure coefficient with 10-minute mean wind direction can be fitted by a Fourier series from the full-scale measurements of the Silsoe Structure Building. The estimation of this method did not consider the influence of the elevation angle due to the influence of ground limiting the obvious elevation angle for low-rise buildings.

Accordingly, Richards et al. (1995) assumed that the mean pressure coefficient with instantaneous wind direction may also be fitted by a similar Fourier series,

$$\bar{C}_P(\theta) = \sum_{k=0}^{N} a_k \cos(k\theta) + b_k \sin(k\theta) \tag{1.55}$$

where a_k and b_k are the k-th order Fourier coefficients which can be obtained by a least-squares method of fitting and N is the required maximum order. Without the consideration of the variation of elevation angle, the instantaneous pressure coefficient with instantaneous azimuthal angle is shown in Eq. (1.56).

$$C_{Pinst}(\theta) = \sum_{k=0}^{N_1} a_{1k} \cos(k\theta) + b_{1k} \sin(k\theta) \tag{1.56}$$

In fact, the influence of elevation angles is significant for the instantaneous aerodynamic pressure coefficients on the roof (Letchford and Marwood, 1997; Richards et al., 1995; Sharma and Richards, 1999). Due to the near-zero correlations between the fluctuating azimuth and fluctuating elevation angles, $\overline{v'w'} \approx 0$, for a given instantaneous azimuth, the gradient of the

instantaneous pressure coefficient to the fluctuating elevation angles is assumed to be linear (Wu and Kopp, 2016):

$$B(\theta) = \left(\frac{\partial C_{p_{inst}}}{\partial \beta'}\right)_{\theta} = \sum_{k=1}^{N_2} a_{2k}\cos(k\theta) + b_{2k}\sin(k\theta) \quad (1.57)$$

where a_{2k} and b_{2k} are the k-th order Fourier coefficients and N_2 is the maximum order. β' is equal to the instantaneous elevation angle minus mean elevation angle ($\beta' = \beta - \bar{\beta}$).

The final form of the instantaneous pressure coefficient is given by,

$$C_{p_{inst}}(\theta, \beta) = C_{p_{inst}}\left(\theta, \bar{\beta}\right) + B(\theta)\beta' \quad (1.58)$$

The peak and fluctuating wind loads on the building surface depend on the ABL turbulence (turbulence intensity and turbulence integral scale) directly (Tieleman, 2003) in the ABL wind. The assumption of the Quasi-Steady (QS) theory states that the fluctuating pressure on one point or an averaged area of the building surface depends on the fluctuating longitudinal wind speed (Letchford et al., 1993). However, Letchford et al. (1993) also demonstrated that the quasi-steady theory can overestimate the high-frequency pressure fluctuations. Wu and Kopp (2016) put forward a "quasi-steady vector model" to predict the pressure time series on the building surface and the coherence function $\left(\frac{Re\sqrt{(S_{C_pQS,C_pM}(n))^2}}{\sqrt{S_{C_pQS}(n)}\times\sqrt{S_{C_pM}(n)}}\right)$ between the measured pressures obtained from the experiments in the Boundary Layer Wind Tunnel II (BLWT II) at the University of Western Ontario (UWO) performed by Wu and Kopp (2018) and the QS-predicted pressures demonstrated that the QS vector model can accurately predict the pressure fluctuations on the roof surface for the large-scale turbulence (>100×H, H is the building height) and was not suitable for the circumstances when the turbulence scale is smaller than 5×H. S_{C_pQS}

and S_{C_pM} represent the auto-spectra of the QS-predicted pressures and measured pressures respectively. S_{C_pQS,C_pM} represents the cross-spectra between measured and predicted pressures. Label "Re" represents the real part of the cross-spectra.

1.4.3 Partial turbulence simulation

Mooneghi et al. (2016) put forward that the aerodynamic characteristics of small length scale turbulence which can be measured by experimental simulation directly, independently of the large-scale turbulence. The large-scale energy can be assessed effectively by quasi-steady (QS) theory. Both high-frequency turbulence and low-frequency turbulence have been considered, and this theory is defined as partial turbulence simulation (PTS). The assumed probability distribution (i.e. Gaussian) was adopted for obtaining low-frequency component for ABL flow (Mooneghi et al., 2016).

In the method of partial turbulence simulation (Mooneghi et al., 2016), the total velocity U is written as Eq. (1.59).

$$U = (\overline{U} + u_L) + u_H \tag{1.59}$$

where u_L is the low-frequency fluctuating velocity and u_H is the high-frequency fluctuating velocity. The combination of $\overline{U} + u_L$ is the running mean velocity and the longitudinal turbulence intensity in partial turbulence simulation is:

$$I_{uH} = \frac{\sqrt{u_H^2}}{U+u_L} = \frac{\sigma_{uH}}{U+u_L} \tag{1.60}$$

where the overbar denotes the mean values and σ_{uH} is the high-frequency fluctuation.

Additionally, in partial turbulence simulation, the time series is divided into subintervals and the duration needs to cover the peak values for each period, which may be regarded as independent events (Mooneghi et al., 2016). The peak pressure, $\hat{p}$, in each subinterval is given by Eq. (1.61). The duration of each subinterval should exceed Δt ($\Delta t = 0.45/f_c$, f_c is the cut-off frequency), which is the moving average time, in order to avoid excessive correlation between adjacent subintervals (Mooneghi et al., 2016).

$$\hat{p} = \frac{1}{2}\rho U^2 \hat{C}(\theta, \beta) \tag{1.61}$$

$$U^2 = (\overline{U} + u_L)^2 + v_L^2 + w_L^2 \tag{1.62}$$

where $\hat{C}(\theta, \beta)$ is the peak pressure coefficient during the subinterval and v_L, w_L are the low-frequency turbulence velocity in transverse and vertical directions. The final peak pressure coefficient function over all subintervals is defined by:

$$\hat{C}_p = \langle (1 + 2\eta)\hat{C}(\theta, \beta) \rangle_{max} \tag{1.63}$$

where $\eta = \frac{u_L}{U}$, and the notation $<>_{max}$ denotes the maximum value of all subintervals. u_L is regarded as constant during the subinterval.

1.4.4 Prediction of downburst wind loading

For the TS downburst wind flow, the downdraft flow becomes divergent when it strikes the ground surface. The divergent movements of the outflows and vortices, coupled with the translation of the impinging point, results in the variation of the orientation of the wind flow with respect to the building. This occurs both in terms of the azimuthal angles and elevation angles. Based on an analysis of five sets of data from full-scale downburst events measured at

Texas Tech University WERFL field site, it has been shown that the velocity can reach up to approximately 46% of peak horizontal velocity at an elevation angle as extreme as -50° or 50° (Jesson et al., 2019), which was defined as "High-Speed, Large-Elevation" (HSLE) periods (Jesson et al., 2019). Even though the downburst simulations have been carried out by many researchers (discussed in Section 1.3), all of these studies focus on the horizontal velocity components and only a few of these considered the influence of azimuthal angles (Haines et al., 2013; Jesson et al., 2015a; Jesson et al., 2015b; Zhang et al., 2013) and none of them considered the influence of vertical velocity components. Considering the expensive experimental equipment of downburst generator, the slow experimental process, the precision of probe locations, Jesson et al. (2019) postulated that the wind loads on buildings can be determined through the combination of the pressure coefficients obtained from the linear wind tunnel for small-scale turbulence and the velocity profiles from the full-scale downburst events by the application of the quasi-steady theory for large-scale turbulence.

The process for the application of this method put forward by Jesson et al. (2019) is expressed as follows:

Step 1: The variable azimuth, elevation angles and turbulence intensity can be calculated from the recorded full-scale velocity time history of downburst events.

Step 2: The pressure coefficients with variable azimuth, elevation angles and turbulence intensity w.r.t. raw recorded data can be selected from the pressure coefficient database measured in a linear wind tunnel.

Step 3: If the building height less than 50 m, the building can be characterised as a low-rise building. If the building height over 50 m, the building is regarded as a high-rise building (Jesson et al., 2019). The low-rise building below 50 m has similar wind characteristics as ABL

wind load, and the wind load can be regarded as an approximately horizontal wind load on the buildings. The high-rise building needs to be calculated above 50 m and below 50 m separately. The high-rise building below 50 m can be treated the same as a low-rise building. The difference is that the vertical component needs to be taken account for the high-rise building above 50 m. The "High-Speed, Large-Elevation" situation is more likely to occur when the height is higher than 49 m which means that when the height over 50 m, "HSLE" situation is needed to be considered. The wind speed, elevation angle, the duration of the high speed and duration of the large elevation are needed to be evaluated.

Step 4: The wind load can be obtained by combining the aerodynamic pressure coefficients from the pressure coefficients database acquired from linear wind tunnel experiments and the velocities of the specific downburst events.

The application of this method is different for low-rise buildings and high-rise buildings as the HSLE is more likely to occur on high rise building.

1.5 Dynamic response on structures

Various researchers in the past have discussed the downburst wind load and the dynamic response of structures, see for example (Chay and Albermani, 2005; Chen and Letchford, 2004a; Chen, 2008; Choi and Hidayat, 2002a; Holmes et al., 2005; Solari, 2016). However, they acknowledge that the transient properties and relatively limited records of this complex phenomenon make their study uncertain and challenging to some extent, starting from the characterisation of the unsteady wind load. Choi and Hidayat (2002a) put forward a revised gust response factor method that, combined with a running-mean filter technique of the measured velocity time history, enabled them to predict the dynamic responses of a Single-

Degree-Of-Freedom (SDOF) system under non-stationary wind. Chen and Letchford (2004b) proposed a maximum dynamic magnification factor as a function of the maximum dynamic response in the time domain and the natural circular frequency to estimate the maximum displacement at the top of tall buildings. Furthermore, Holmes et al. (2005) estimated a series of dynamic response factors with varying structural parameters for one typical TS record, which extended from the traditional analysis theory for transient earthquake load, whereas Chay and Albermani (2005) also adopted dynamic response factors to investigate the dynamic response of a SDOF system with a variety of aerodynamic properties and structural mechanical properties.

More recently, Chen (2008) addressed the time-varying mean and RMS displacement responses using the linear acceleration step-by-step integration method with the developed transient wind time history built in the frequency domain. Solari (2015) and Solari (2016) constructed a TS spectra technique in the time-frequency domain derived from the traditional response spectra technique to earthquakes for fully correlated SDOF systems and partially coherent MDOF systems separately. Kareem et al. (2019) suggested a generalised nonstationary wind loading chain framework which extended the Davenport's chain that was originally for synoptic wind (Dyrbye and Hansen, 1997) through the representations of the EPSD and wavelet analysis, to address the relationship of wind-force-response in the time-frequency domain. Further work by Peng et al. (2018) focused on the effects of the time-varying coherence of the non-stationary wind on the dynamic response of structures, which poses some differences with the time-invariant coherence function used for various studies by Chen and Letchford (2004a), and Solari (2016). Le and Caracoglia (2017) also formulated a numerical model to investigate the dynamic response of a tall building considering the buffeting effects induced by transverse wind. Kwon and Kareem (2019) put forward a new approach to the gust-front factor for the codification of

design wind loading induced by the TS downburst events. This method considered the effects of the typical vertical velocity profile and the non-stationary and transient aerodynamic characteristics of such wind events with four factors, i.e. kinematic effects factor, pulse dynamics factor, structural dynamic factor, and potential load modification factor (detailed in Kwon and Kareem (2009)). This suggested framework is also implemented at http://gff.ce.nd.edu.

Martinez-Vazquez (2016) and Martinez-Vazquez (2020) dealt with the WDS for regular prismatic buildings subjected to stationary wind. The method requires the generalisation of force exerted by wind, structural mass, and stiffness, which enabled mapping aerodynamics of MDOF systems to their equivalent SDOF systems, and then applying classic techniques used in earthquake engineering for generating WDS. Notwithstanding, the use of design spectra could be adopted to analyse MDOF systems via modal analysis, which unfolds the response of the oscillators (implicit in the design spectra) to capture the contribution of higher-order modes. Accordingly, the short duration and instantaneous properties of the downburst outflows lead to similarities with earthquake loads, which are generally evaluated by the response spectra technique (Housner et al., 1953; Serras et al., 2021; Skalomenos et al., 2015) - widely used in the past to deal with random vibrations, where the structural performance was combined with the inter-storey displacement and roof displacement ductility of the buildings. In Section 2.3, the proposed TWDS technique merges the response spectral technique applied in earthquake engineering with a refined characterisation of wind loads (Simiu and Scanlan, 1996; Solari, 1989), as a basis that is also an extension of the originally developed wind design spectra (WDS) (Martinez-Vazquez, 2016; Martinez-Vazquez, 2020) for the structural vibrations of regular buildings from synoptic wind to TS downburst winds. In contrast to the previous research work (Kareem et al., 2019; Solari, 2016), this proposed technique in Chapter 2 is developed in the

time-frequency domain and the TWDS technique starts from the consideration of the PSD of the reduced turbulent fluctuations instead of the reduced turbulent fluctuating velocity. This assumes that the time function of the turbulence intensity is constant in the applied decomposition algorithm of the wind velocity, and this hypothesis is also discussed in Roncallo and Solari (2020). Here the spatial cross-coherence of the turbulent fluctuations is reflected by the defined interrelated distances. The merit of this technique can directly demonstrate the structural performance from the perspective of the mechanical properties of the buildings and the aerodynamic properties of the downburst outflow. The detailed methodology of the TWDS is demonstrated in Section 2.3.

1.6 Sequential multi-hazard analysis

The increased frequency of severe thunderstorms observed over recent decades, like TS downbursts, has motivated researchers to study this complex natural phenomenon (Brooks, 2013; Rädler et al., 2019). Factual evidence shows that structures that have been damaged during previous hazard events (earthquakes, strong winds) are prone to secondary damage induced by subsequent hazards, such as TS downbursts (ABCNEWS, 2017; NEWS, 2021). This may increase post-disaster damage and eventually cause the collapse of structures that remained exposed after the primary event. Slender steel structures are vulnerable to damaging vibrations, such as earthquakes and microbursts, and current design guidelines ignore these multi-hazard effects that are likely to occur within the lifespan of a structure.

Previous researchers have highlighted the risk associated with the collapse mechanism of tall structures under TS downbursts (Loredo-Souza et al., 2019; Tilloy et al., 2019). The state of the art still identifies important knowledge gaps spanning from the design aspects to the

development of contingency plans and strategies to increase structural resilience. The current design guidance (ASCE7, 2013) evidences such limitations, as it disregards the joint occurrence of natural events, such as earthquakes and extreme winds, within the design life of a structure. When compared to regions governed by a single hazard, the risk of exceeding the limit states can be twice as high in regions with significant wind and seismic hazard events, while the seismic performance of buildings designed to primary withstand wind loads can be very poor even under low-amplitude events (Aly and Abburu, 2015; Duthinh and Potra, 2011; Duthinh and Simiu, 2010; Kim et al., 2022; Thilakarathna et al., 2018).

Recent researchers have utilised probability-based techniques for multi-hazard structural analysis to understand the impact of wind-earthquake vibrations on structural performance. Martinez-Vazquez (2017) and Martinez-Vazquez et al. (2019) stressed the necessity of consideration for the combined effect of earthquakes and strong winds, since this may drive the structures into their inelastic response obviously increasing ductility demands. Martin et al. (2019) proposed fragility surfaces for multi-hazard analysis and assessment of suspension bridges under earthquakes and microbursts. Roy et al. (2021) developed a multi-hazard framework for investigating high-rise base-isolated buildings under sequential multiple earthquakes and long-duration winds likely to occur in the design life of a structure. Kwag et al. (2021) transferred a probabilistic risk-assessment framework into a deterministic performance-based framework to consider multiple hazards in structural design. Further studies have focused on the development of vibration control systems for tall buildings to reduce multi-hazard vibrations (Elias et al., 2019; Taha, 2021).

Most of the studies above have mainly focused either on generating multi-hazard scenarios or assessing structural performance under multiple hazards by applying each hazard separately,

thus ignoring possible sequential effects (e.g., damage accumulation, fatigue, strength, and stiffness deterioration). There are a few studies that account for sequential multi-hazard effects (Li et al., 2014; Rossetto et al., 2019; Roy et al., 2021), but their proposed analysis frameworks require the execution of all hazard analysis in a series which is time-consuming and may induce uncertainties by the selection of each event. A more direct analysis framework that builds upon the existing well-established knowledge of single-hazard analysis without requesting its repetition would allow for a more rapid transition from the single-hazard design to a multi-hazard design that reflects the previous knowledge. This novel approach can be possible if the secondary hazard analysis can be applied directly to structural models that include the response information induced by the major event. By driving, therefore, a structure to a certain deformation level through a controlled analysis method (major event), and then, by performing a restart sequential analysis of the deformed structure under various secondary hazard events can allow the direct quantification of the additional design requirements instructed by secondary hazard events alone.

The above methodological approach promotes the studies to develop a generalised multi-hazard analysis framework for evaluating the impact of TS downburst events to structures damaged by major events, as demonstrated in Chapter 7. The present work investigates for a first time the effects of TS downbursts on earthquake-damaged tall steel buildings giving an emphasis on assessing the revised combined earthquake-wind ductility demands.

1.7 Summary

1.7.1 Motivation for this study

Extreme winds are important when considering the design of buildings and facilities, since they can result in infrastructural damage, serious injury, and loss of life. For example, one microburst event occurred at Mesa, Arizona on August 23, 2014, that ripped the roof off of half a building and shed, slightly damaging the surrounding buildings; another microburst event happened at the area of Spotsylvania County, Virginia on July 9, 2012, resulting in severe damage to two buildings, with two serious injuries reported (Wtopnews, 2012). In most cases, buildings are designed assuming the wind is homogeneous and (in a statistical sense) stationary. However, a TS downburst is one type of extreme wind which is non-stationary over a relatively short period of time and where the velocities can reach up to 150 mph (Fujita, 1985b). Current wind loading design codes are based on ABL theory and tend to only consider the wind velocity profile in the lower part of the boundary layer (i.e. less than 200 m above the ground (Eurocode, 2010)), thus a logarithmic profile is typically assumed where the wind speed increases with height above the ground. However, for transient TS downburst winds, a "nose" profile has been observed where the streamwise velocity peaks between 30 m-100 m height above the ground (Figure 1-11). During such flows, it is likely that the wind loading on a building can differ from that resulting from an ABL flow. Figure 1-11 illustrates the velocity time history for a TS downburst wind, which highlights the differences with respect to time. Understanding the differences between ABL and downburst flows, and the wind loading which arises from each, is important for the safe design of buildings and infrastructure.

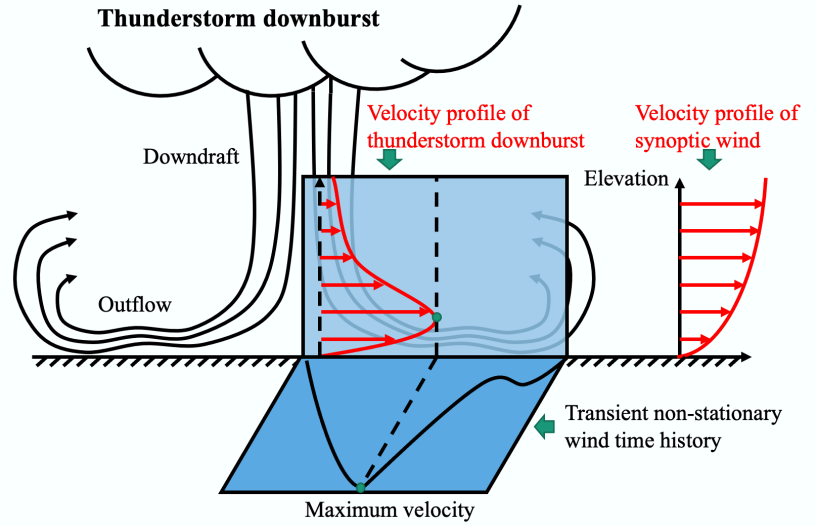


Figure 1-11. Velocity profiles of TS downburst and synoptic wind.

1.7.2 Limitations of previous research

The characteristics and velocity profiles of the TS downburst have been investigated by various methods, including full-scale measurements, physical experiments, theoretical models, and numerical simulations. However, research into the aerodynamic influence of such wind events on structural buildings is limited. The high cost and complexity of the full-scale measurements, as well as the uncertain reality of scaling methods subjected to TS downbursts in lab experiments, prompt the researchers to propose a number of theoretical models. The most effective theoretical models to simulate the process of the downburst outflows are still undergoing testing. Additionally, the importance of the vertical velocity components of the downburst outflow on the structural design has been stressed by many researchers, while a limited number of studies have considered this factor and most of the studies have only concentrated on the horizontal wind. Following that, previous studies of downburst-induced dynamic responses on buildings were only reflected by the velocity time history in the time-domain and lack of detailed consideration of the turbulent correlations of the outflow wind on the front surface of the building. Finally, the assessments for damage or collapse mechanisms

of the structural buildings directly or indirectly induced by TS downburst are quite limited, and it is necessary to understand their structural performance under the impact of this hazard wind event for the purpose of better structural design.

1.7.3 Research aim and objectives

The aim of this research is to investigate the impact of TS downburst type events on buildings and to evaluate if the structural dynamic response induced by such wind loading can be represented using thunderstorm downburst wind design spectra (TWDS). Related to this aim were four objectives:

- To understand the TS downburst wind field through an analytical model of an idealised downburst using potential flow theory and to compare the results from this model with full-scale data.
- To understand the TS downburst wind loading on the roof by evaluating if a standard ABL wind tunnel can be used effectively to represent the wind loading arising from a TS downburst.
- To construct a newly framework named “thunderstorm downburst wind design spectra” to evaluate the deformation of high-rise buildings under the effects of non-stationary winds
- To develop a novel computational procedure to assess the ductility demands and collapse mechanisms for the damaged steel structures under non-stationary wind hazards.

1.7.4 Structure of thesis

Chapter 1 provides the relevant background information, including an introduction to ABL theory and the concept of extreme winds, and the formation and characteristics of TS downburst events. In addition, a literature review relevant to the research is divided into four subsections: a section introducing full-scale downburst field measurements, a section outlining different physical experiments of the downburst type flow, in particular the University of Birmingham Transient Wind Simulation (UoB-TWS), a section summarising the computational simulations relating to downburst type flow, a section introducing the theoretical models, in particular a vortex model developed by Jesson and Sterling (2018). Furthermore, one method combining the QS theory with PTS to estimate the downburst wind loading on buildings is described. Moreover, a section presenting a review of the approaches to evaluating the structural dynamic response subjected to downburst outflow and a section stressing the risk of damaged steel buildings induced by a secondary TS downburst wind hazard are introduced separately. According to the previous sections, the final part encompasses the motivation of this research, the limitations of previous research, research aim and objectives, and the structure of the thesis.

Chapter 2 establishes the research methodology framework, which includes one vortex-based modelling procedure of full-scale downburst events; WT experiments for a database of pressure coefficients with variable azimuthal angles, elevation angles, and turbulence intensities; one theoretical algorithm, named TWDS, to estimate the dynamic responses of point-like SDOF and area-like MDOF systems; and one computational procedure to determine the damage and collapse mechanisms of the damaged steel structures subjected to secondary TS downburst induced wind hazard.

Chapter 3 solves Objective 1, which relates to the application of an analytical model describing the TS downburst flow, including the comparison of velocity time series with laboratory-scale experiments, the estimated results of full-scale downburst wind fields using this model, and comparisons with full-scale data from WERFL and Joint Airport Weather Study (JAWS).

Chapter 4 is for Objective 2, which concerns the physical wind tunnel experiments for evaluation of the aerodynamic properties on the buildings. This chapter includes a discussion (point analysis and area analysis) of the acquired database of pressure coefficients with variable turbulence intensities, azimuths, and elevation angles, a comparison between the predicted pressure time series and the data from the UoB-TWS on two generic buildings, a cube building and a portal framed building. The pressure time series for the different points and for the different areas on the roof are discussed.

Chapter 5 addresses Objective 3 by first discussing the controlling parameters of the TWDS. This framework is tested on a benchmark tall building, and its findings are discussed and then validated by comparisons with the results from numerical integration and FEM modelling subjected to one simulated downburst wind field.

Chapter 6 extends Objective 3, which refines the design spectra tailored to TS downburst through the generalisation of the spectra, via non-linear regression modelling. A multi-factorial polynomial equation is introduced to capture the influence of controlling parameters that determine the corresponding wind-structure interaction. The effectiveness of the simulated design spectra was validated through comparison with results obtained for the CAARC benchmark tall building when using the non-synthetic design spectra.

Chapter 7 implements Objective 4, which applies an innovative computational technique to a 20-storey steel building designed according to the Uniform Building Code (1994), and its

ductility demands and collapse mechanisms under the impact of TS downburst wind loading are discussed.

Finally, Chapter 8 outlines the conclusions of the research and suggests additional work that can be undertaken in the future.

Chapter 2 Methodology

In this study, the influence of TS downburst wind loading is assessed by two methods, including a framework of the TWDS for evaluating the downburst induced dynamic response of point-like SDOF and area-like MDOF systems, and a novel computational procedure for further assessing the ductility demands and collapse mechanisms for the damaged buildings subjected to transient non-stationary winds. Before the construction of these two algorithms, one analytical model of an idealised outflow wind field to deeply understand this complex phenomenon and a PTS method combined with the QS theory to estimate the downburst induced wind loading on non-structural components, i.e. roof, were introduced and discussed. The overall methodology map is shown in Figure 2-1.

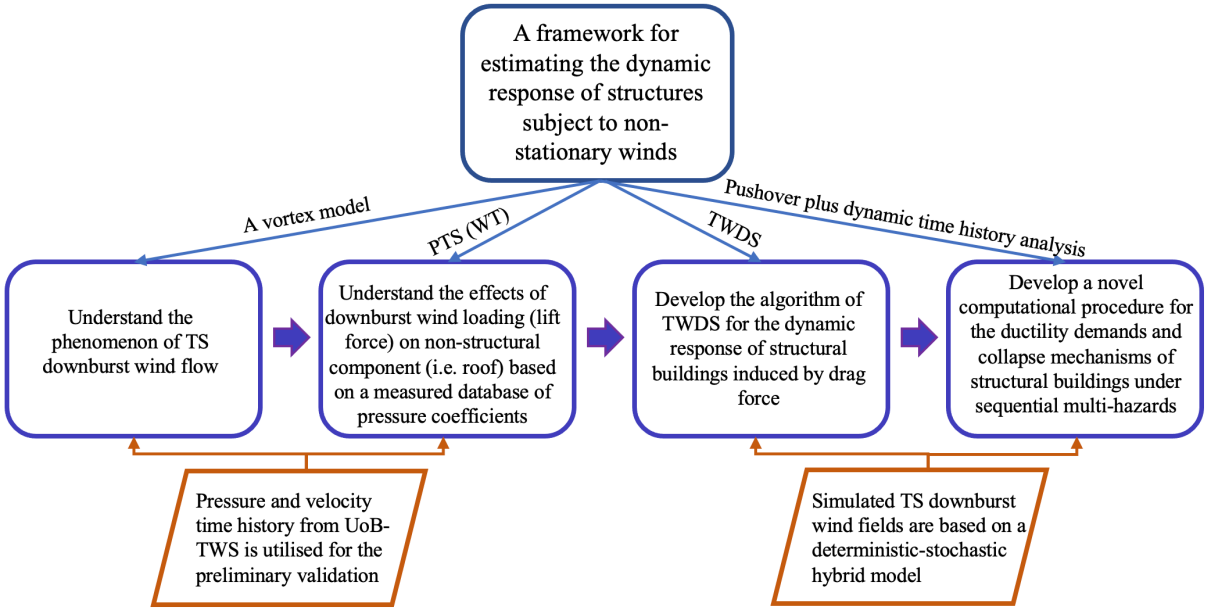


Figure 2-1. Methodology map.

2.1 Modelling procedure setup for full-scale downburst events

According to the introduction of the vortex model originally used for laboratory-scale downburst wind fields (see Section 1.3.4), one modelling procedure for full-scale downburst events is further constructed as follows:

Step one: Select an appropriate duration for the downburst to be simulated. The duration should be of a sufficient length in order to simulate the whole non-stationary event. This includes the periods of the rapid increase of velocity to its maximum value and the subsequent decay. One assumption is that the chosen duration of velocity is the most appropriate to a characteristic downburst (see Section 1.2.3 suggested by Gast and Schroeder (2003)).

Step two: Calculate the initial velocity of the simulated downburst and the final outflow velocity. Generally, the initial velocity is the mean value of the velocity time series before the ramp-up period, and the final outflow velocity is assumed as the average value after the decay period and before the "back-side" peak (see Section 1.2.3). As the initial velocities of the secondary vortex and the outflow are zero, the initial velocity of the simulated downburst is, in fact, the initial velocity of the primary vortex. The duration of the secondary vortex circulation from zero to its maximum value depends on the time of maximum velocity. The circulation of the secondary vortex increases to a maximum at the time of peak velocity.

Step three: Vary each of the input parameters in order to evaluate their relative importance and to generate a family of downburst simulations. There are six unknown input parameters which include the primary vortex radii a and b (a: semi-major axis of ellipse; b: semi-minor axis of the ellipse), the secondary vortex radii a and b, the rate of change of primary major radius and the rate of change of secondary major radius. The values for these parameters were estimated

from the work of Hjelmfelt (1988), Jesson et al. (2015b) and Lombardo et al. (2014) and varied over a range of values also matching the known ranges from full-scale studies. From this parametric study, the best-fit values were identified.

Step four: Change these three circulation-related parameters separately, including the "factor a" representing the change of the initial circulation of the primary vortex, the "factor b" representing the rate of change of circulation of the primary vortex and the "factor c" representing the rate of change of circulation of the secondary vortex, aiming to create a series of downburst simulations. A variety of values for these three parameters have been combined randomly, aiming to obtain the best fit.

Based on the above modelling procedure, the horizontal and vertical velocity time history for the positions (e.g. the position of maximum velocity) in the wind field and the vertical distributions of horizontal velocity at any time (e.g. at the time of maximum velocity) can be obtained.

2.2 Experiment setup

A combination of quasi-steady (QS) theory and concepts from the PTS method has been applied to estimate the microburst wind load on generic building shapes (discussed in Section 1.4). In this approach, the pressures induced by the large-scale flow structures of an isolated microburst are calculated from the velocities of the specific downburst events and a database of pressure coefficients for winds from a range of azimuthal angles, elevation angles and turbulence intensities. The latter were measured during the experimental part of this study, using a standard, linear wind tunnel (WT). These experiments used building models supported on an angled stand, along with a passive turbulence generator, to obtain the required pressure coefficient data. This

section contains four parts: the introduction of the University of Birmingham Wind Tunnel (UoB-WT) facility and measurement apparatus, the consideration of the related scaling factors, details of the cube and portal building models and support design, and information relating to the passive turbulence generator design.

2.2.1 UoB-WT facility and measurement apparatus

The University of Birmingham Wind Tunnel facility is an open-circuit wind tunnel with a 2 m × 2 m working cross-section and a 14 m fetch. Forty-nine 0.85 m^2 cross-section axial flow fans drive the flow, giving a maximum freestream wind speed (when the wind tunnel is empty) of approximately 12 ms^{-1}. Although generally used as an ABL tunnel with spires and blocks to generate an ABL velocity and turbulence profiles, for this work these features were removed in order to create a uniform flow. Uniform flow is required following the method suggested by Jesson et al. (2019), in which pressure coefficients are obtained for a range of independent parameters, including azimuthal angles, elevation angles and turbulence intensities; non-uniformity and directional effects are incorporated when the pressure coefficients are applied to a predicted velocity field (see Section 1.4.4).

The velocity measurements in this experiment were made using Series 100 Cobra Probes manufactured by Turbulent Flow Instrumentation (TFI), and the velocity was sampled at a rate of 5 kHz for a duration of 40 s. The cut-off frequency is 2 kHz, above which the signal is attenuated while the higher frequency obtains the more accurate velocity time series during a short period. According to the Nyquist sampling theorem (The Nyquist sampling theorem states that a signal can be exactly reproduced if it is sampled at a frequency that is greater than twice the maximum frequency of the signal (Zawistowski and Shah, 2010)), the sampling frequency should be at least twice the frequency of the highest frequency of interest. Therefore, 5 kHz,

which is larger than twice of the cut-off frequency was chosen. The Cobra Probe can measure flow fields within a range of ±45° at frequencies greater than 2 kHz. The accuracy of the Cobra Probe is ±0.3 m/s (T.F.I., 2017), with a range from 2 m/s to 100 m/s, and ±1.0° for speed and direction respectively.

The pressures over the building models were recorded by a bespoke 64-channel digital pressure measurement system (DPMS) at a rate of 500 Hz. The DPMS was designed and manufactured by Solutions for Research Ltd. and is based around 64 Sensor-Technics HCLA12×5DB differential pressure transducers. The range of the transducers is ±1250 Pa, and the accuracy is ±3 Pa (SensorTechnics, 2014). Eight transducers were fixed in one Multi-Channel Pressure Logger (MCPL) box. Eight MCPLs were connected to the building pressure tappings through 1.35 mm (inside diameter) tubes. The reference pressure ports of the transducers were connected to a tube running to a partially sealed box outside the wind tunnel, unaffected by the flow field from the tunnel.

2.2.2 Scaling and Reynolds number

Before the construction of buildings, understanding the aerodynamic properties on the buildings is important for the structural design purpose. In order to undertake wind tunnel experiments for unusual structures or unstable air flow events (e.g., TS downburst), the approaching flow and models used need to be appropriately scaled (e.g., velocity scale, time scale, length scale, Reynolds number). The building models in wind tunnel should exhibit similar natural characteristics as the building models under the full-scale wind load.

Due to the limitation of the wind tunnel dimensions, the large turbulence integral scale is difficult to obtain. The Partial Turbulence Simulation (PTS) method aims to simulate the wind

flow properties of the high-frequency turbulence which can represent the flow separation, reattachment and vortex shedding (Mooneghi et al., 2015). The wind flow in low-frequency turbulence mainly demonstrates the mean characteristics. In this research, the Reynolds number is an important scaling parameter, which must be considered. Reynolds number is the ratio of the inertial forces and viscous forces in wind flow, defined as,

$$Re = \frac{uL}{\nu} \tag{2.1}$$

where u is the longitudinal velocity, L is the windward dimension and ν is the air kinematic viscosity. Based on dimensional analysis, the geometric dimensions in full-scale events are much larger than the corresponding factors in small-scale wind tunnels and the velocity in the small-scale wind tunnel must be sufficiently large compared with the velocity in full-scale events to give an acceptable Reynolds number. Higher Reynolds number can result in higher level of flow separation with higher turbulence (Haines, 2015). If the Reynolds number is relatively high and the inertia force is dominant, the reattachment on the roof of the building can be replaced by the flow separation (Castro and Robins, 1977). However, Golden (1961) found that when the Reynolds number was larger than 10^4, the turbulence flow structures were similar and the inertial forces became dominant. In this situation, the system can be assumed to be Reynolds number independent. Scruton (1981) also found that the Reynolds number does not influence the drag coefficients when the bluff bodies have sharp-edged corners. However, Castro and Robins (1977) found that the Reynolds number independence cannot reach until 10^5 for a cube model in an ABL wind tunnel at 45 degrees. When the Reynolds number is small (<2100), which means that the viscous force is dominant, the flow becomes laminar flow due to molecular viscosity.

2.2.3 Building models and support design

Two 3-D printed building models were used in this study, a cubic building model and a portal building model (Figure 2-2). These are standard generic building shapes used in other studies (Jesson et al., 2015a; Jesson et al., 2015b; Levitan and Mehta, 1992; Lombardo et al., 2018; Mooneghi et al., 2016; Richards and Hoxey, 2012a; Richards and Hoxey, 2012b; Richards et al., 2007; Richards and Hoxey, 2004; Stenabaugh et al., 2015; Tieleman et al., 1996; Wu, 2017), and were the same building models used by Jesson et al. (2015b) in the UoB-TWS. The dimensions of the cube building model are 60 × 60 × 60 mm, and of the portal building model are 240 × 130 × 53 mm (42 mm), as shown in Figure 2-2. The maximum blockage ratio when these two building models are used in the wind tunnel is 0.32%, which is far smaller than the 5% limit for blockage correction (Takeda and Kato, 1992) and so no extra calibration has been applied. The azimuth and elevation angles in Figure 2-2 are defined in Eq. (1.52) and Eq. (1.53) separately.

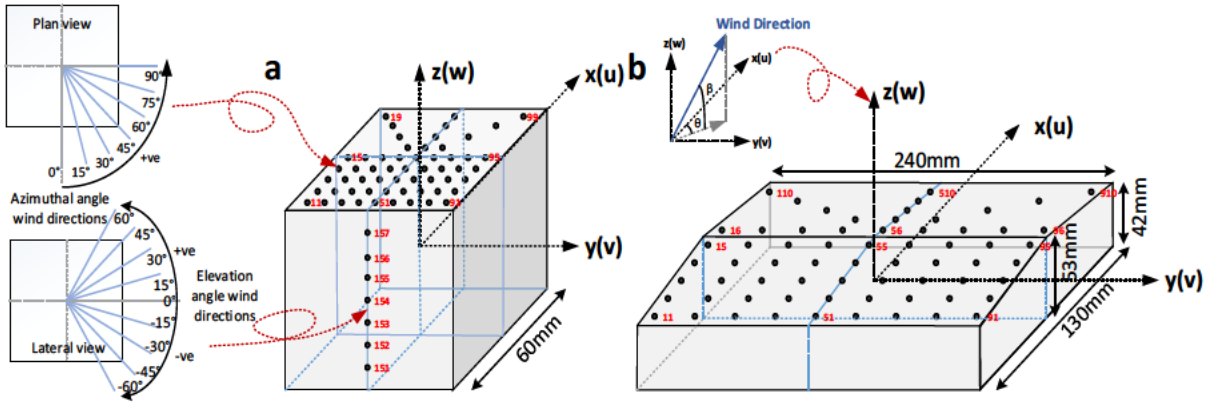


Figure 2-2. Pressure tapping positions and numbering, and the coordinate system at zero azimuth and zero elevation angle: (a) 60 mm cube; (b) 240 × 130 × 53 mm (42 mm) portal frame.

In order to ensure that the models lie within the region of uniform velocity and turbulence intensity (i.e. away from the thin boundary layers at the tunnel walls), the building models were placed on a support (Figure 2-3 (b)) which was fitted to a turntable in the wind tunnel. This

support allowed the elevation angle of the wind relative to the building to be altered, with the azimuthal angle varied using the turntable. The tubing required for the pressure tappings was passed through the support to secure them against flapping in the flow. The height of the support, Z, was 0.58 m, which was determined from the turbulence intensity profile (see Figure 2-4) of the empty UoB-WT. The width of the support is the same as the dimensions of the building models to keep the flow on the front surface of the building free of interference caused by the support.

The range of the azimuthal angles used was 0° to 90° in 15° increments (0°, 15°, 30°, 45°, 60°, 75°, 90°), and for elevation -60° to 60° at 15° increments (-60°, -45°, -30°, -15°, 0°, 15°, 30°, 45°, 60°). This is in accord with the analysis of full-scale downburst events by Jesson et al. (2019), which also found a variation in turbulence intensity with height above ground: I_u (z_{f_s}=1 m) ≅ 17% and I_u (z_{f_s}=200 m) ≅ 2% (z and subscript f_s represent the height and full-scale respectively). This I_u was calculated over the period of the peak wind speed using the wavelet analysis method applied by Jesson et al. (2019). Therefore, the required range of the turbulence intensities in this wind tunnel experiment varies from 2% to 20%.

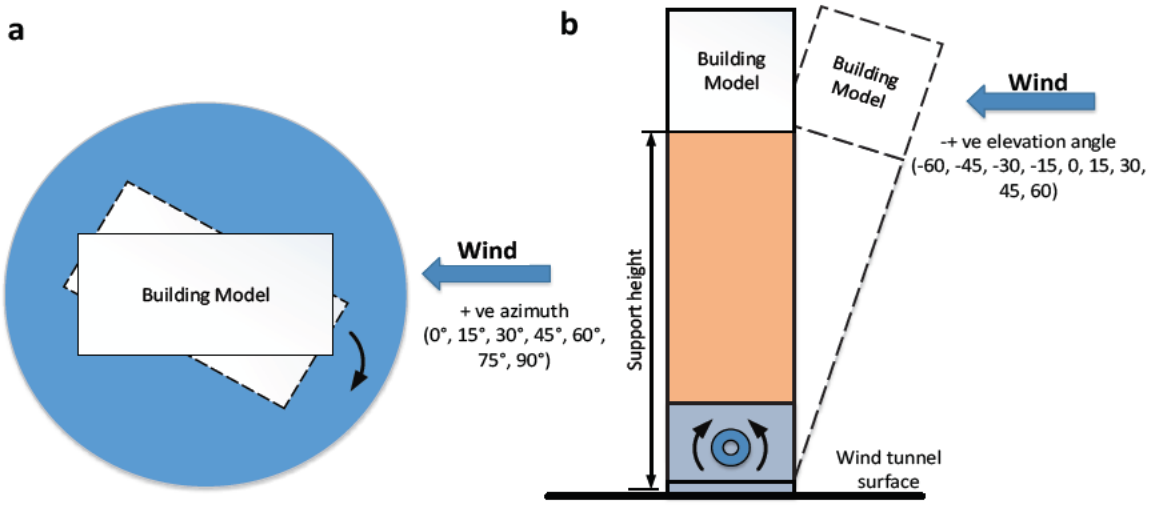


Figure 2-3. Layout of the azimuth and elevation angles.

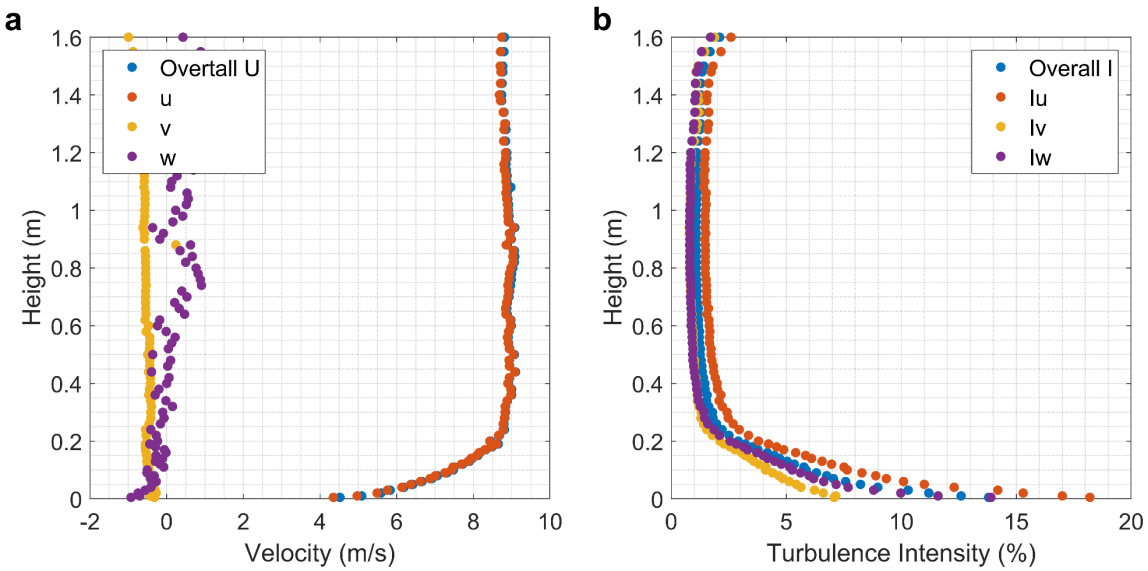


Figure 2-4. Velocity and turbulence intensity profiles in the empty wind tunnel: (a) Velocity profiles along heights in u-v-w directions; (b) Vertical turbulence intensity profiles in u-v-w directions.

The pressure coefficients measured in the linear wind tunnel are defined as:

$$C_p(\bar{\theta}, \bar{\beta}, I) = \frac{p - p_{ref}}{0.5\rho U^2} \tag{2.2}$$

where p is the absolute pressure, p_{ref} is the reference pressure, ρ is the air density and $\overline{U}$ is the mean velocity used to calculate a reference dynamic pressure for normalisation. $\bar{\theta}$, $\bar{\beta}$ and I are the pre-set azimuthal angle, elevation angle (defined in Figure 2-2) and turbulence intensity (generated by different positions of grid).

In order to obtain the database of pressure coefficients, the dynamic pressure (denominator part of Eq. (2.2)) is calculated from a reference velocity. Based on previous researchers' analysis (Mooneghi et al., 2016; Wu and Kopp, 2018), the position of the reference velocity measurement in this experiment is 2×H (H is the height of the building) above the building model (z-coordinate) and a lateral (y-direction) distance H to the side of the building model in order to reduce the influence of the model. The windward position of the reference velocity is

on the middle line of the building models in the streamwise (x) direction. The definition of the x, y, and z coordinate is shown in Figure 2-2 (a).

2.2.4 Passive turbulence generator design

In order to generate the appropriate flow within a wind tunnel, various methods can be used, and a typical method is adding honeycomb type grids for the purpose of obtaining uniform flow in wind tunnel and this honeycomb is placed downstream of the fans. The hexagonal honeycombs were chosen, as the shape of the hexagon is the most effective method for wind tunnel turbulence straightener (Welsh, 2013). The first aim of the honeycombs is to remove the swirling flow produced by the fans and redirect the flow to the horizontal flow. The second aim of the honeycombs is to reduce the turbulence scale. The second screen, a grid, positioned downstream of the wind tunnel's honeycomb screen, was used to obtain the different turbulence intensities and more uniform vertical distributions of velocity and turbulence intensity needed for this work. The grid turbulence is produced by vortex shedding from the downstream edge of the bars.

An expected design of passive turbulence generator requires to at least consider three important parameters, the distance between the grid and building models (x_d), the bar width (b), and the mesh size (M) (the distance between the centres of the two bars) (Figure 2-5). Baines and Peterson (1951) illustrated that the model should keep at least 5 mesh widths with the grid if the uniform flow was expected. Vickery (1965) suggested that the optimal mesh size should be one-eighth of the available width of the test section (L) (Eq. (2.3)), aiming to obtain the turbulence conditions being representative for atmospheric turbulence. For example, if the width of the wind tunnel test section is 2 m, the optimal mesh size is equal to approximately 0.25 m.

$$M = L/8 \tag{2.3}$$

The turbulence is produced by the rectangular bars on the grid. The design of the bar size depends on the blockage of the grid and the desired scale of turbulence (Laneville, 1973). A larger scale of turbulence requires larger bar width (Laneville, 1973). Hinze (1959) found that with the increase of bar width, the relationship between grid drag and the ratio of the bar width to mesh size can be illustrated in Eq. (2.4).

$$c_d = \frac{b/M(2-b/M)}{(1-b/M)^4} \tag{2.4}$$

When M/b is smaller than 4, the grid drag coefficient increases at a drastic rate (Laneville, 1973). Baines and Peterson (1951) suggested M/b should be greater than 3.4 while Vickery (1965) recommended M/b should be equal to 4 as the grid drag coefficient is around 1.4. However, this is for the circular rod design not for a rectangular bar.

Due to the bar size related to the blockage of the grid, one function (Eq. (2.5)) between the porosity ($\beta_{porosity}$) and the ratio of the square-mesh size and bar width was put forward by Roach (1987) according to large range of experiments on variable grid types and sizes.

$$\beta_{porosity} = (1 - b/M)^2 \tag{2.5}$$

Many researchers (Bearman and Morel, 1983; Nakamura et al., 1988; Roach, 1987) suggested the porosity should be greater than 0.5, while larger porosity (greater than 0.5) can result in smaller drag coefficients (smaller than 2). Generally, the drag coefficient of the bluff bodies is less than 2 (Vita et al., 2018). The longitudinal turbulence intensity (Eq. (2.6)) and integral length scale (Eq. (2.7)) generated by a grid had been given by the empirical expressions (Roach, 1987).

$$I_u = 1.13(x_d/b)^{-5/7} \quad (2.6)$$

$$L_u/b = 0.2(x_d/b)^{0.5} \quad (2.7)$$

The experiments were completed at a range of different turbulence levels, spanning the range seen during full-scale downbursts (2%~20%, see Jesson et al. (2019)). In order to obtain uniform turbulent flow in the wind tunnel, turbulence-generating grids were constructed to dimensions based on the theory discussed above. Eight grids were pre-designed, each with a different combination of mesh size and bar width. The predicted turbulence intensities with variable x_d for each of the different grids are shown in Figure 2-6. x_d is the distance between the grid and the building model. The most suitable choice is M=0.25 m, b=0.069 m (defined in Figure 2-5 (b)) as shown in the red line (Figure 2-6) whose range of turbulence intensity covers the required range (2% to 20%) and x_d varies between 12 m and 0.8 m. M represents the distance between adjacent bar centre lines and b is the bar width. In order to confirm whether the corresponding integral length scale with varying turbulence intensity (2% to 20%) is within the range of 5×H, the calculated results based on the wavelet analysis method is shown in Figure 2-7. The black line in Figure 2-7 is the variation of the integral length scales from the experimental measurements at 0.5 m height, and the maximum integral length scale is around 0.2 m. The cut-off integral length scale for building models is 5×H (discussed in Section 1.2.5.3), corresponding to 0.3 m for the cube and 0.265 m for the portal-framed building. Therefore, the integral length scale (0.2 m) generated from the design grid is approximately 30% smaller than the cut-off scale between quasi-steady and local aerodynamic effects. However, the influence of the integral length scale is quite small on the separation regions (Wu et al., 2017), and this integral length scale can represent the small-scale turbulence. Therefore, M=0.25 m, b=0.069 m has been chosen for the grid design (Figure 2-5 (b)). The calculated $\beta_{porosity}$ is around 0.52

and the grid drag is around 1.73. The thickness of the bars is 0.018 m which is the standard thickness of bars that the wood factory can provide. From the perspective of the author, the thickness of the bars does not have effects on the experiments.

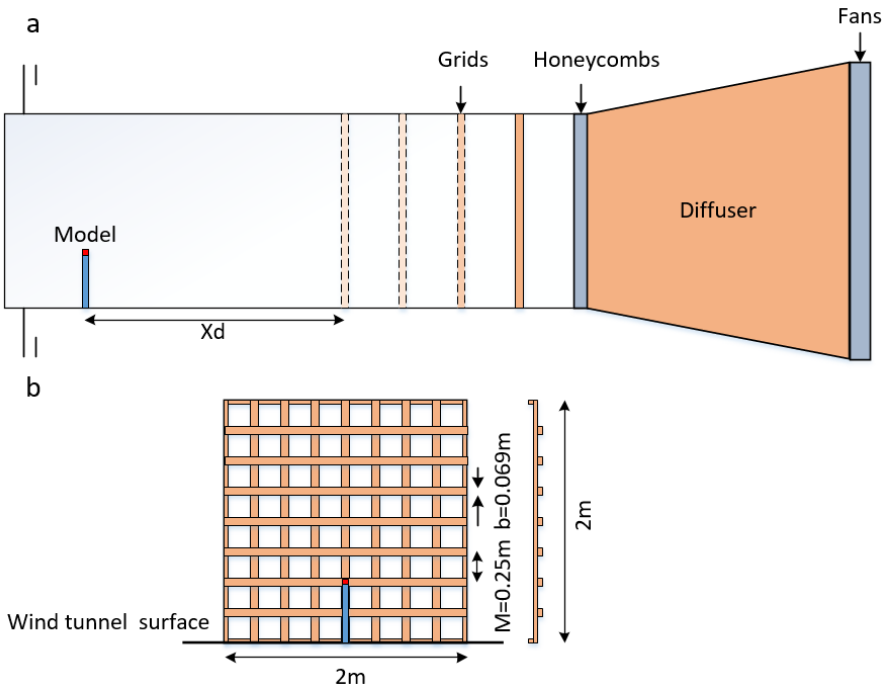


Figure 2-5. Layout of the wind tunnel: (a) The plan of the wind tunnel; (b) The cross-section of the wind tunnel. M is the distance between adjacent central lines of bar. b is the bar width.

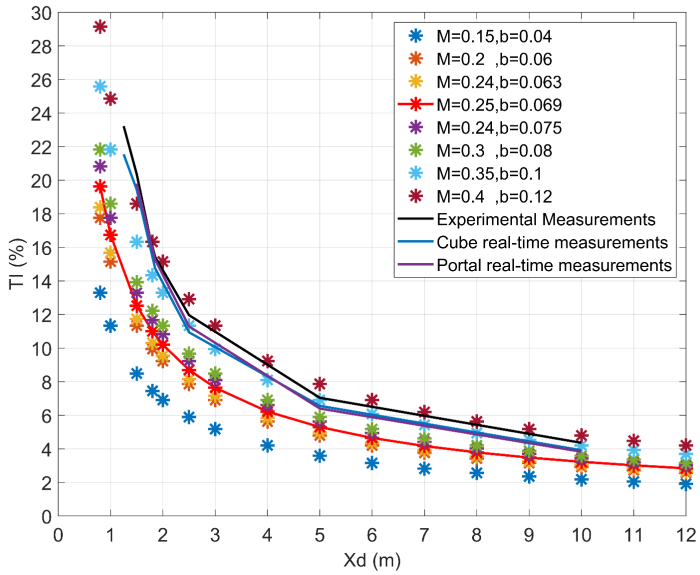


Figure 2-6. Variation of the magnitude of turbulence intensities with mesh size and x_d. Units of M and b are metres.

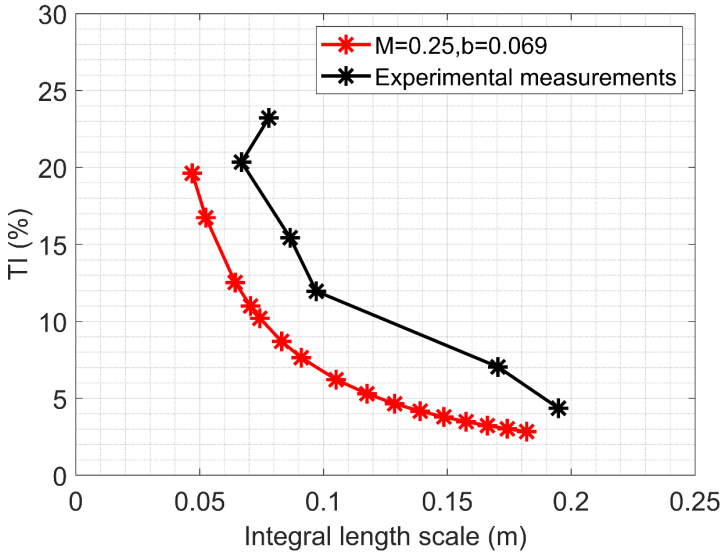


Figure 2-7. The integral length scales with varying turbulence intensities. Units of M and b are metres.

Three design methods for the edge bars (the bars around the perimeter of the tunnel) have been studied in this research, including (a) no edge bars, (b) the same width of other bars near the edges and (c) half-width of other bars near the edges (Figure 2-8). The vertical distributions of velocity and turbulence intensity profiles in these three situations demonstrate that if no edge bars are used then the velocity profiles near the edges were higher and the turbulence intensity profiles would be significantly lower. When the edge bars used had the same size as the rest of the grid bars then the velocity profiles near the edges were significantly lower and the turbulence intensity profiles were higher. With edge bars of half the width of the main bars, the velocity and turbulence intensity profiles were uniform near the four tunnel walls. Therefore, four thinner bars were added into the grid design along the edges, ensuring the production of uniform flow as near to the ground as practical. The width of the edges' bar is 0.0345 m as shown in Figure 2-5 (b).

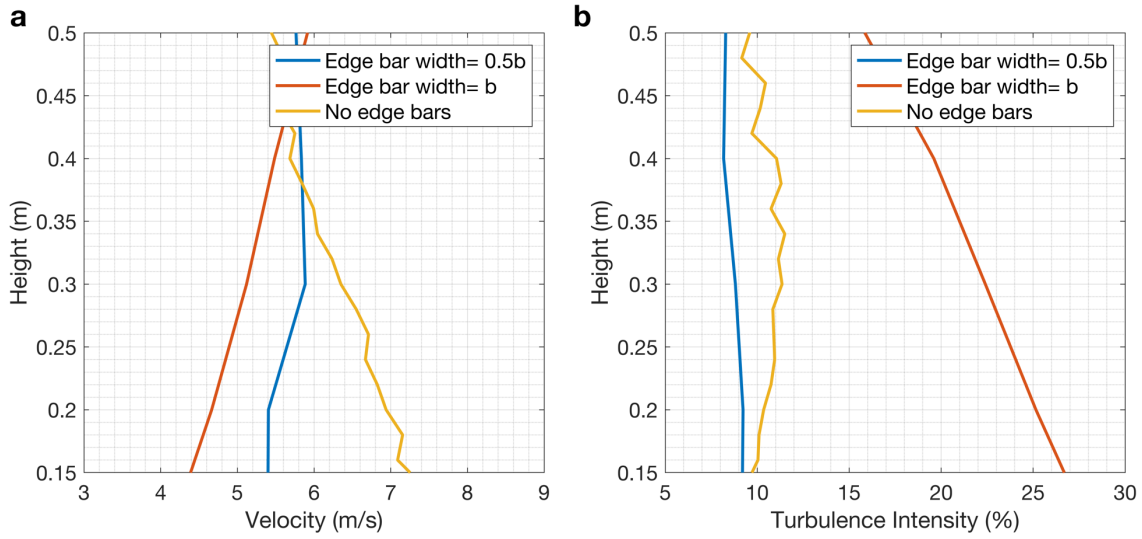


Figure 2-8. Design of edge bars: (a) Vertical distribution of velocity profile; (b) Vertical distribution of turbulence intensity profile.

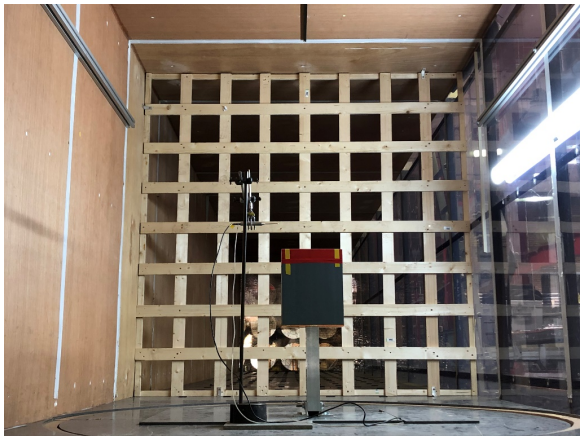
The experimental scene diagrams with different distances (1.25 m, 1.5 m, 1.85 m, 2.5 m, 5 m and 10 m) between the grid and the building models are shown in Figure 2-9. The experimental results (vertical distributions of velocity and turbulence intensity) of the designed grid are shown in Figure 2-10 and summarised in Table 2-1. Each turbulence intensity value used to plot the black line in Figure 2-6 is the mean turbulence intensity over the height ranging from 0.26 m (the height of the lowest point of the building model) to 0.64 m (the height of the highest point on the building model) for the corresponding x_d. The large range of heights occurs due to the variable angling of the support. The turbulence intensities in black line (see Figure 2-6) are slightly higher than the pre-estimated TI. The black line in Figure 2-6 represents the velocity measurements without a building model. The blue line and purple line are the mean turbulence intensity measured with the cube building model or portal building model in place respectively. The simultaneous (at the same time as the pressure measurements) TI measurements are slightly smaller than the measured TI without building models, though the difference is small (maximum approximately 10% of the TI value) and attributed to the measured positions. The position of the measured TI without building models was in the centre of the test section (Figure

2-3 (a)). In the simultaneous measurements, with the building models inside the wind tunnel, the position of the measured TI varies with the position of the building models. Furthermore, if the position of the measured TI is situated toward the bars, the turbulence intensity would be somewhat high. If the measured position is towards the centre of the gap between the bars, the turbulence intensity would be slightly smaller. However, the vertical distribution of turbulence intensities (Figure 2-10) shows that this effect can be negligible, discussed further in the following paragraph.

In order to quantify the uniformity of the flow, the standard deviations of the velocity and turbulence intensity measurements for each point spanning the range 0.26 m < Z < 0.64 m have been calculated, and standard deviations of the turbulence intensity are seen to vary from 0.1 to 0.54 and the standard deviations of the velocity change from 0.1 m/s to 0.3 m/s. This can be regarded as negligible, showing that velocity and TI are uniform over the region occupied by the building models. The grid also significantly reduces the mean flow speed, down to approximately 5.7 m/s, though this change is unimportant as it is reflected in the normalisation in the C_p calculation. The Reynolds number for the cube building model is 2.43×10^4 with the grid inside the wind tunnel and 4.32×10^4 without a grid. The Reynolds number for portal building model with the grid is 5.27×10^4 and 9.98×10^4 without a grid. Based on the discussions in Section 2.2.2, independence of Reynolds number can be assumed. The velocities and turbulence intensities for the simultaneous records in Table 2-1 are the mean values of recorded data with over all azimuths and elevation angles (63 runs) for each turbulence intensity. The velocities and turbulence intensities from the simultaneous record in Table 2-1 were adopted to calculate the pressure coefficients for the database and were used for the interpolation of the turbulence intensity time series in Chapter 4.



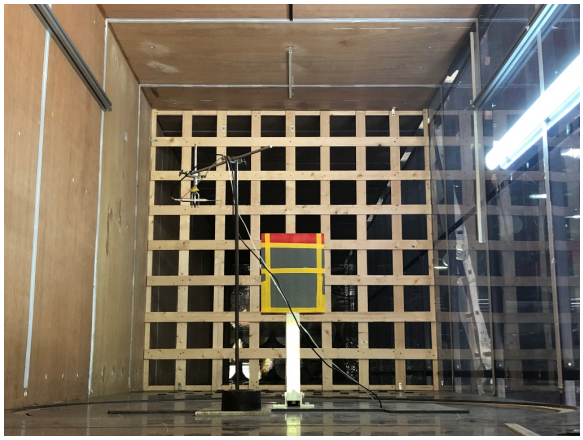
(a) 1.25 m



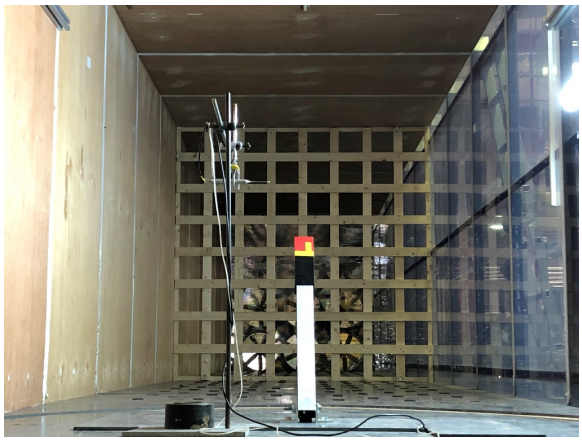
(b) 1.5 m



(c) 1.85 m



(d) 2.5 m



(e) 5 m



(f) 10 m

Figure 2-9. Experimental scene diagrams with different x_d.

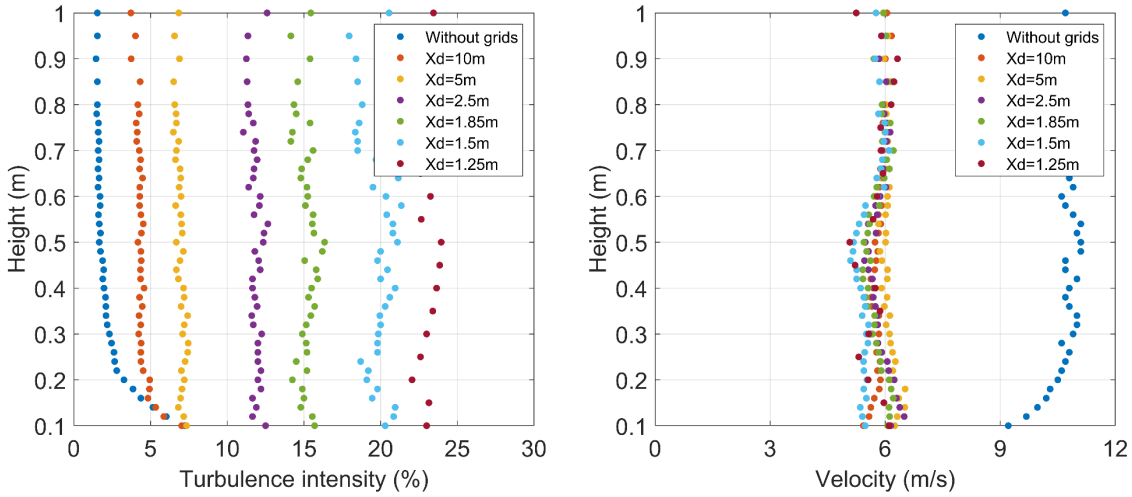


Figure 2-10. Turbulence intensities (left) and vertical profiles of velocity (right) with variable grid distance (x_d).

Table 2-1. Summary of the TI and velocity profiles.

Grid distance (m)		without grid	10	5	2.5	1.85	1.5	1.25
Label		TI0	TI1	TI2	TI3	TI4	TI5	TI6
Without buildings	u (m/s)	10.9	5.8	6.0	5.7	5.6	5.4	5.6
	Std of u (m/s)	0.2	0.1	0.1	0.2	0.2	0.2	0.3
	I_u (%)	1.9	4.4	7.0	12.0	15.4	20.4	23.2
	Std of I_u	0.3	0.1	0.2	0.3	0.4	0.5	0.5
Simultaneous record for cubic building	u (m/s)	10.7	6.2	6.0	6.0	6.0	5.9	6.0
	I_u (%)	1.7	3.9	6.6	11.0	14.8	19.4	21.5
Simultaneous record for portal building	u (m/s)	11.4	6.4	6.2	6.1	6.0	5.9	/
	I_u (%)	1.6	3.8	6.4	11.3	15.3	19.8	/

In summary, the designed bars near the edges of the grid are crucial for obtaining the uniform flow near the ground. The width of the bars near the edges of the grid needs to be chosen carefully. The passive turbulence generator can effectively produce the uniform velocity and turbulence intensity profiles along with the heights.

2.3 Theoretical setup of TWDS

Section 2.1 and 2.2 applied the existing methods for investigating the complexity of the downburst wind field and the downburst induced pressures on the roof surface of the building. Following that, Section 2.3 proposes a new non-stationary wind design spectral technique to estimate the structural deformation under the act of the downburst wind loads from the perspective of the structural design and it revisits well-established concepts drawn from random vibration theory to integrate the spatio-temporal description of turbulence induced by TS downbursts. This novel theoretical algorithm assesses the structural dynamic response on both point-like SDOF and area-like MDOF systems which can provide effective guidance for the engineering practice. Therefore, this section contains three parts: the TWDS for the SDOF system, the TWDS for the MDOF system, and the modal analysis based on the fundamental mode of vibration for obtaining the structural displacements subjected to TS downburst wind loading.

2.3.1 Point-like SDOF system

The following paragraphs describe the procedures to build the TWDS for SDOF systems (Song et al., 2021a).

Step 1: Wind force

For a point-like SDOF system, the total horizontal force on a structure can be given by Eq. (2.8a), and the slowly varying mean component $\bar{f}$ and residual fluctuating component f' are expressed as Eq. (2.8b) and Eq. (2.8c) respectively.

$$f(t) = \bar{f}(t) + f'(t) = c_D \times 0.5\rho A U^2(t) \tag{2.8a}$$

$$\bar{f}(t) = c_D \times 0.5\rho A\bar{U}^2(t) \quad (2.8b)$$

$$f'(t) = c_D\rho A\bar{U}^2(t)[1 + 0.5I_u(t)]I_u(t)\tilde{u}'(t) \quad (2.8c)$$

In these equations, c_D represents the drag coefficients, ρ is the air density, A is the structural surface exposed to wind. The second-order term of the fluctuating turbulence, u'^2, is replaced by $\sigma_u u'$ to simplify the calculation process, i.e. $2\bar{U}u' + u'^2 = (2\bar{U} + u')u' \approx (2\bar{U} + \sigma_u)\sigma_u\tilde{u}' \approx (2\bar{U} + I_u\bar{U})I_u\bar{U}\tilde{u}'$.

Step 2: Response acceleration of a point-like SDOF system

The method departs from establishing the physical relationship between force and acceleration as established by Newton's Second Law on a point-like structure - see Eq. (2.9) - (2.10). The relationship enables the spectra of the input acceleration induced by the wind on a SDOF system to be determined.

The force spectrum being the scaled wind power spectrum.

$$S_F(n) = q^2 S_{\tilde{u}'}(n) \quad (2.9)$$

$$S_A(n) = \left(\frac{q}{m}\right)^2 S_{\tilde{u}'}(n) \quad (2.10)$$

In these equations, S_F is the force spectra; S_A is the input acceleration spectra, i.e. the acceleration imparted by the wind to the structural system; $S_{\tilde{u}'}(n)$ is the PSD function for the reduced horizontal fluctuating velocity component $\tilde{u}'$; n is the frequency of gust wind; m is the mass of the structure excited by the wind force; q is a force factor, expressed as $q = c_D\rho A\bar{U}_{max}^2[1 + 0.5\bar{I}_u]\bar{I}_u$.

To quantify high-frequency velocity fluctuations, which remain partially correlated, the aerodynamic admittance, $\chi(n)$, is applied - here given by Eq. (2.11), as dictated by classical models such as in Vickery (1968).

$$|\chi(n)| = \frac{1}{1+\left(\frac{2n\sqrt{A}}{U_{max(t)}}\right)^{4/3}} \tag{2.11}$$

The variance of the output response acceleration for the SDOF oscillator is given by Eq. (2.12). In this model, the transfer function, $J(n)$- derived by Martinez-Vazquez (2016) for wind excitation given in units of acceleration is introduced. This sequence of steps follows spectral methods reported elsewhere, see for example (Holmes, 2018; Kareem and Tamura, 2013).

$$\sigma_a^2 = \int_0^\infty |J(n)|^2 |\chi(n)|^2 S_A(n) dn \tag{2.12}$$

$$J(n) = \frac{1}{\sqrt{[1-(n/n_0)^2]^2+4\xi^2(n/n_0)^2}} \tag{2.13}$$

In Eq. (2.13), n is the frequency of the gust wind; n_0 is the natural frequency of structures, which is reciprocal of the natural period of the structures, T; ξ is the damping ratio, expressed as $\xi = \frac{c}{2\sqrt{mk}} = \frac{c}{4m\pi n_0}$, where c is the damping coefficient; k is the structural stiffness. The transfer function with varying frequency ratio is shown in Figure 2-11.

Therefore, the TWDS of the output acceleration for SDOF systems can be defined as S_a in Eq. (2.14).

$$S_a = \sqrt{\sigma_a^2} \tag{2.14}$$

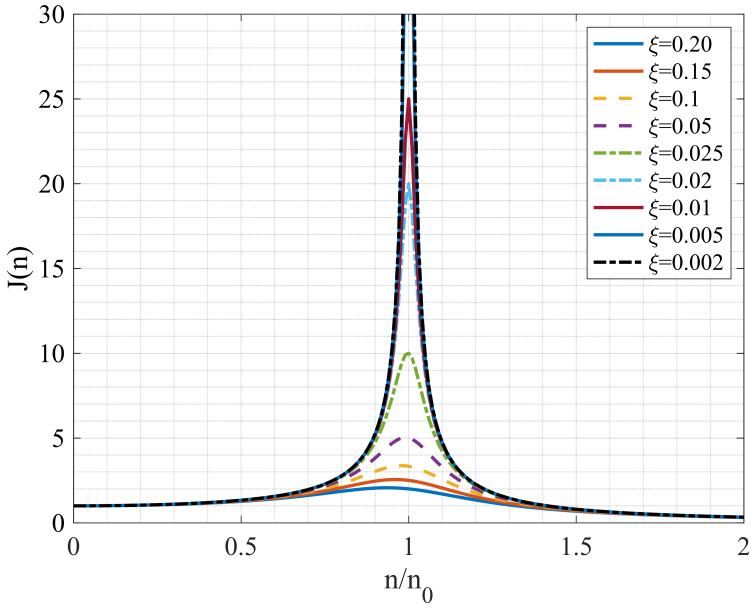


Figure 2-11. Transfer function.

2.3.2 Area-like MDOF system

The following paragraphs describe the processes to construct the TWDS for MDOF system (Song et al., 2021a).

Step 1: Wind force

For a vertical MDOF system, the drag force on structures induced by the downburst outflow can be expressed by Eq. (2.15), and the slowly varying mean component $\bar{f}$ and residual fluctuating component f' with varying height are given by Eq. (2.16) and Eq. (2.17), separately.

$$f(z,t) = \bar{f}(z,t) + f'(z,t) = c_D(z) \times 0.5\rho A(z) U^2(z,t) \tag{2.15}$$

$$\bar{f}(z,t) = c_D(z) \times 0.5\rho A(z) \bar{U}^2(z,t) \tag{2.16}$$

$$f'(z,t) = c_D(z)\rho A(z)\bar{U}^2(z,t)[1 + 0.5I_u(z,t)]I_u(z,t)\tilde{u}'(z,t) \tag{2.17}$$

Few studies have demonstrated the necessity to consider the variability of the direction of the wind flow (see Section 1.4.4), caused by the vortices coupled with the translation of the impinging point. Noting that, due to the insufficient research data related to the pressure coefficients on the front surface of the structures under non-stationary winds, the value of c_D is assumed constant along with the height of the building in the current research stage.

Step 2: Cross spectra of acceleration of a MDOF system

The spectral relationship established for SDOF systems explained above can be extended to determine the input acceleration of MDOF systems. This requires finding a series of SDOF systems equivalent to the MDOF system, considering the spatial correlation of wind gusts. This is done by bringing into the algorithm the normalised cross-spectra proposed by Davenport (1977) given by Eq. (2.18).

$$\chi(z,n) = exp\left\{-\frac{n}{1/2[U_{max}(z_i)+U_{max}(z_j)]}\sqrt{(C_y\Delta_y)^2+(C_z\Delta_z)^2}\right\} \tag{2.18}$$

In Eq. (2.18), Δ_y and Δ_z are the horizontal and vertical distances between two points, i, j, located at coordinates $\{y_i, z_i\}$ and $\{y_j, z_j\}$ respectively. C_y and C_z are non-dimensional decay constants along with the horizontal and vertical directions, in this case, assumed to be equal to 10. $\overline{U}_{max}(z_i)$ and $\overline{U}_{max}(z_j)$ represent the maximum value of the slowly varying mean wind velocity at height z_i and z_j, respectively.

It follows that, by combining the spectra of the input acceleration given in Eq. (2.10) with the cross spectra of the horizontal turbulence component given in Eq. (2.18), the cross-power spectra of the input acceleration can be obtained, see Eq. (2.19) where the force factor $q(z) = c_D(z)\rho A(z)\overline{U}^2_{max}(z)[1+0.5\bar{I}_u(z)]\bar{I}_u(z)$.

$$S_{A_{ij}}(z_i, z_j, n) = \frac{1}{m^2} q(z_i) q(z_j) \sqrt{S_{\tilde{u}'}(z_i, n) S_{\tilde{u}'}(z_j, n)} \frac{1}{A^2} \chi(z_i, z_j, n) \quad (2.19)$$

The integration of Eq. (2.19) across the area exposed to wind flow contributes to the PSD of the generalised input acceleration $S_{cu}(z_i, z_j, n)$, given in Eq. (2.20).

$$S_{cu}(z_i, z_j, n) = \iint_A \phi(z_i) \phi(z_j) S_{A_{ij}}(z_i, z_j, n) dy_i dy_j dz_i dz_j \quad (2.20)$$

where $\phi(z)$ represents the fundamental modal shape at height z above the ground.

Step 3: Response acceleration of an area-like MDOF system

As Eq. (2.20) provides the acceleration inputted to a system, the variance of the overall spectral response can be obtained by passing the signal through the transfer function (see Eq. (2.20)), as shown in Eq. (2.21a). The integration of this equation can be done in two parts, to separate the background and resonant response components. These are expressed in Eq. (2.21b) and Eq. (2.21c), where the algorithm can be found in Simiu and Scanlan (1996).

$$\sigma_a^2 = \int_0^\infty |J(n)|^2 S_{cu}(z_i, z_j, n) dn \quad (2.21a)$$

$$\sigma_{a,b}^2 = \int_0^\infty S_{cu}(z_i, z_j, n) dn \quad (2.21b)$$

$$\sigma_{a,r}^2 = S_{cu}(n_0) \int_0^\infty |J(n)|^2 dn \cong \frac{\pi n_0 S_{cu}(z_i, z_j, n_0)}{4\xi} \quad (2.21c)$$

Furthermore, the design spectra of the output acceleration can be evaluated by the square root of the sum of the background component and the resonant component (see Eq. (2.22)). Therefore, the design spectra for vertical MDOF systems are defined as Eq. (2.22). The summarised procedures for design spectra of TS downburst winds and ABL winds are shown in Table 2-2.

$$S_a = \sqrt{\sigma_a^2} = \sqrt{\sigma_{a,b}^2 + \sigma_{a,r}^2} \tag{2.22}$$

Table 2-2. Comparison of the design spectra between TS downburst wind and ABL wind.

Vertical MDOF system to ABL		Vertical MDOF system to TS downburst	
Equation		Equation	
$S_F(z,n) = q^2(z)S_{u'}(z,n)$	(1)[a]	$S_F(z,n) = q^2(z)S_{\tilde{u}'}(z,n)$	
$S_A(z,n) = \left(\frac{q(z)}{m}\right)^2 S_{u'}(z,n)$	(2)[a]	$S_A(z,n) = \left(\frac{q(z)}{m}\right)^2 S_{\tilde{u}'}(z,n)$	
$q(z) = c_D \times 0.5\rho A(2\bar{U}(z) + \sigma_u(z))$, $\bar{U}(z) = U_r(z/z_r)^{\alpha}$		$q(z) = c_D(z)\rho A(z)\bar{U}_{max}^2(z)[1 + 0.5\bar{I}_u(z)]\bar{I}_u(z)$	
$\chi(z_i, z_j, n) = exp\left\{-\frac{n}{1/2\ \bar{U}(z_i)+\bar{U}(z_j)}\sqrt{(C_y\Delta_y)^2 + (C_z\Delta_z)^2}\right\}$	(5)[a]	$\chi(z,n) = exp\left\{-\frac{n}{1/2[\bar{U}_{max}(z_i) + \bar{U}_{max}(z_j)]}\sqrt{(C_y\Delta_y)^2 + (C_z\Delta_z)^2}\right\}$	(2.18)
Point-like SDOF system to TS downburst Equation		$S_{A_{ij}}(z_i, z_j, n) = \frac{1}{m^2}q(z_i)q(z_j)\sqrt{S_{\tilde{u}'}(z_i,n)S_{\tilde{u}'}(z_j,n)}\frac{1}{A^2}\chi(z_i, z_j, n)$	(2.19)
$S_F(n) = q^2 S_{\tilde{u}'}(n)$	(2.9)		
$S_A(n) = \left(\frac{q}{m}\right)^2 S_{\tilde{u}'}(n)$	(2.10)	$S_{cu}(z_i, z_j, n) = \iint_A \phi(z_i)\phi(z_j)S_{A_{ij}}(z_i, z_j, n)dy_i dy_j dz_i dz_j$	(2.20)[b]
$q = c_D \times 0.5\rho A\bar{U}_{max}^2[2 + \bar{I}_u]\bar{I}_u$		$\sigma_{a,b}^2 = \int_0^{\infty} S_{cu}(z_i, z_j, n)dn$	(2.21b)[b]
$\lvert\chi(n)\rvert = \frac{1}{1+\left(\frac{2n\sqrt{A}}{U_{max}}\right)^{4/3}}$	(2.11)	$\sigma_{a,r}^2 = S_{cu}(z_i, z_j, n_0)\int_0^{\infty}\lvert J(n)\rvert^2 dn \cong \frac{\pi n_0 S_{cu}(z_i,z_j,n_0)}{4\xi}$	(2.21c)[b]
$\sigma_a^2 = \int_0^{\infty}\lvert J(n)\rvert^2\lvert\chi(n)\rvert^2 S_A(n)dn$	(2.12)	$\sigma_a^2 = \int_0^{\infty}\lvert J(n)\rvert^2 S_{cu}(z_i, z_j, n)dn$	(2.21a)[b]
$S_a = \sqrt{\sigma_a^2}$	(2.14)	$S_a = \sqrt{\sigma_a^2} = \sqrt{\sigma_{a,b}^2 + \sigma_{a,r}^2}$	(2.22)[b]

It is common practise for TS downbursts to be partially correlated with gusts through the equivalent coherence function of the fluctuating turbulence at $0.6 \times$ H (building height). However, the TWDS technique adopts the coherent function of the cross-spectra proposed by Davenport (1977) with defined distances of the separate points in the horizontal and vertical directions of the structural surface.

[a]Equation numbers for ABL wind refers to Martinez-Vazquez (2016).

[b]Universal procedures for ABL wind and TS downburst.

2.3.3 Modal analysis

When a vertical slender structure with linear elastic behaviour is considered, according to the modal analysis, assuming that natural frequencies are well-separated and the damping is small and proportional, the dynamic along-wind displacement of the structure is demonstrated as Eq. (2.23a) from the equation of motion-see Eq. (2.23b) (Simiu and Scanlan, 1986).

$$d(z,t) = \sum_q \phi_q(z) d_q(t) \tag{2.23a}$$

$$\ddot{d}_k(t) + (4\pi n_k \xi)\dot{d}_k(t) + (2\pi n_k)^2 d_k(t) = \frac{1}{m_k} f_k(t) \tag{2.23b}$$

In these equations, ϕ_k is the k-th mode shape, d_k is the k-th principal coordinate, n_k, m_k (Eq. (2.24a)) and f_k (Eq. (2.24b)) represent the k-th natural frequencies, modal mass, and modal force, respectively.

$$m_k = \int_0^H m_l(z)\phi_k^2(z)dz \tag{2.24a}$$

$$f_k = \int_0^H f(z,t)\phi_k(z)dz \tag{2.24b}$$

In Eq. (2.24a), m_l is the structural mass per unit length, $m_l = WLm_v$, where m_v is the mass per unit volume.

Since the assumption that the structural response to TS outflows is dominated by the fundamental mode of vibration and the fundamental modal shape can approximately take the form $\phi_1(z) = (z/H)^\psi$ $(k = 1)$ with H representing the vertical dimension of A and ψ taking a value within the range of 1-1.5 (Piccardo and Solari, 1998) as shown in Figure 2-12. $\phi_1(z)$ is the modal amplitude at height z. Then, the m in Eq. (2.24a) can be replaced by Eq. (2.24c) for $k = 1$.

$$m_1 = {}^{mH}/_{(2\psi+1)} \tag{2.24c}$$

The dynamic displacement response, σ_d (rms of dynamic displacement), can be obtained from the proposed design spectra using Eq. (2.25a) (Simiu and Scanlan, 1986).

$$\sigma_{1d}(z) = \phi_1(z)\frac{L_1 S_a}{m_1(2\pi n_1)^2} \tag{2.25a}$$

$$L_1 = \int_0^H m_l(z)\phi_1(z)dz \tag{2.25b}$$

In Eq. (2.25a), L_1 is the first modal excited mass expressed in Eq. (2.25b), n_1 represents the fundamental natural frequency and S_a is the design spectra of the output acceleration varying with the fundamental period (T_1).

The static displacement response of the structure can be obtained by Eq. (2.26a) which is the ratio of the maximum value of the first modal static force (Eq. (2.26b)) and the first modal stiffness (Eq. (2.26c)) (Simiu and Scanlan, 1986).

$$d_{1s}(z) = \frac{f_1(z)}{k_1} \tag{2.26a}$$

$$\bar{f}_1(z_i) = c_D \times 0.5\rho W(L)\bar{U}^2_{max}(z_i)\sum_1^i\left[\int_{z_i}^{z_{i+1}}\alpha^2(z)\phi_1(z)dz\right] \tag{2.26b}$$

$$K_1 = 4\pi^2 n_1^2 m_1 \tag{2.26c}$$

In Eq. (2.26b), c_D is the pressure coefficient, ρ is the air density, $W(L)$ represents the width (chord) of the building, i represents the i-th number of recorded velocity time history and $\alpha(z) = \bar{U}_{max}(z)/\bar{U}_{max}(z_i)$ which is the non-dimensional vertical shape profile of horizontal wind.

Therefore, the maximum displacement response can be expressed in Eq. (2.27).

$$d_{1T}(z) = d_{1s}(z) + \sigma_{1d}(z) \tag{2.27}$$

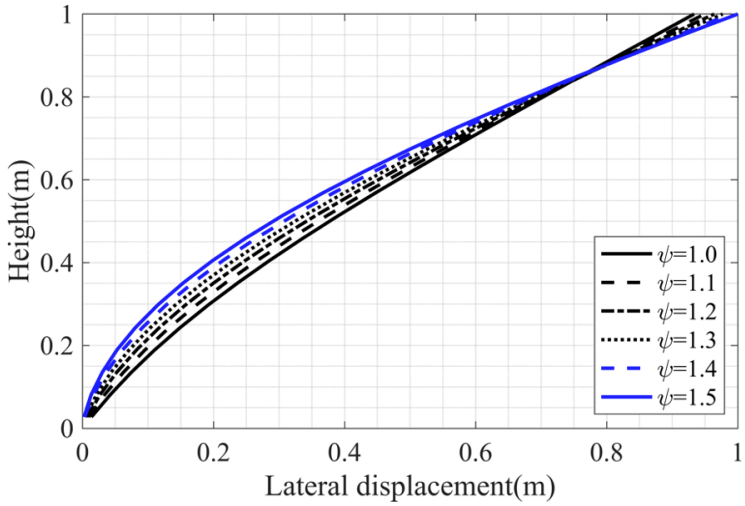


Figure 2-12. The first modal amplitude with varying exponent ψ (Eurocode, 2010).

2.4 Computational procedure setup for sequential multi-hazard analysis

The theoretical algorithm of TWDS established in Section 2.3 can determine the displacement of the buildings induced by downburst wind loads, which contributes to the author's proposing a computational procedure to quantify the roof displacement of the building or damaged buildings under the influence of TS downburst winds. Therefore, this section develops a novel computational algorithm to determine the ductility demands and collapse mechanisms of steel structures under sequential multi-hazard events, including primary hazard (e.g., earthquakes or strong winds) and secondary hazard, i.e. TS downburst wind hazards. This novel algorithm utilised the advanced finite element software ABAQUS (2020) and the advanced programming capabilities of Matlab MATLAB (2021).

2.4.1 Introduction of theory

The performance-based damage and collapse mechanisms of the structures induced by these hazard events can then be determined at progressive analysis steps. The proposed computational algorithm combines the non-linear step-by-step static pushover analysis induced by the seismic loads as the primary hazard event with the dynamic time history analysis caused by the downburst winds as the secondary hazard event. This analysis framework can effectively control the deformation of the buildings from the linear elastic range to a target plastic range, including the descending branch of the load-deformation curve, thus allowing for better control of the primary imposed damage and restart state of subsequential secondary hazards.

The proposed methodology combines the principles of the nonlinear adaptive static (pushover) analysis (Chopra and Goel, 2002), which aims to reproduce the damages induced by the major earthquake event, with the sequential dynamic time-history analysis, which aims to estimate the damages induced by the secondary hazard event, the TS downburst. The proposed multi-hazard analysis algorithm offers a robust implementation of pushover analysis and wind time-history analysis within a novel restart analysis framework that allows a parametric study to be performed focusing on the impact of the secondary hazard event by investigating various thunderstorm profiles, wind velocities and terrain types. The proposed analysis framework can produce superior numerical results especially for the deteriorating part of the inelastic response of the structure, as well as accurately identify the overall plastic deformation mechanism of the structure until global collapse triggered by the secondary hazard. The method accurately controls the damage level induced by the major event, thus eliminates uncertainties, and separately assesses secondary hazard effects which enables a direct quantification of the additional design requirements. This can provide effective guidance in the stage of structural

design or post-hazard assessment of new structures, as well as support repair procedures and decision-making frameworks for existing structures.

2.4.2 Multi-hazard analysis framework

Figure 2-13 schematically illustrates the overall concept of the proposed multi-hazard analysis framework. The computational procedure combines two classical analysis methods which are performed in two phases: (a) the pushover nonlinear analysis which is executed first in order to drive the structure in a target deformation state assumed to be induced by the primary hazard, followed by (b) a set of dynamic time history analysis which is performed within a restart analysis framework that allows for analysis repetition and random reloading of the previously deformed structure. This sequential multi-hazard analysis procedure is described by the following four steps:

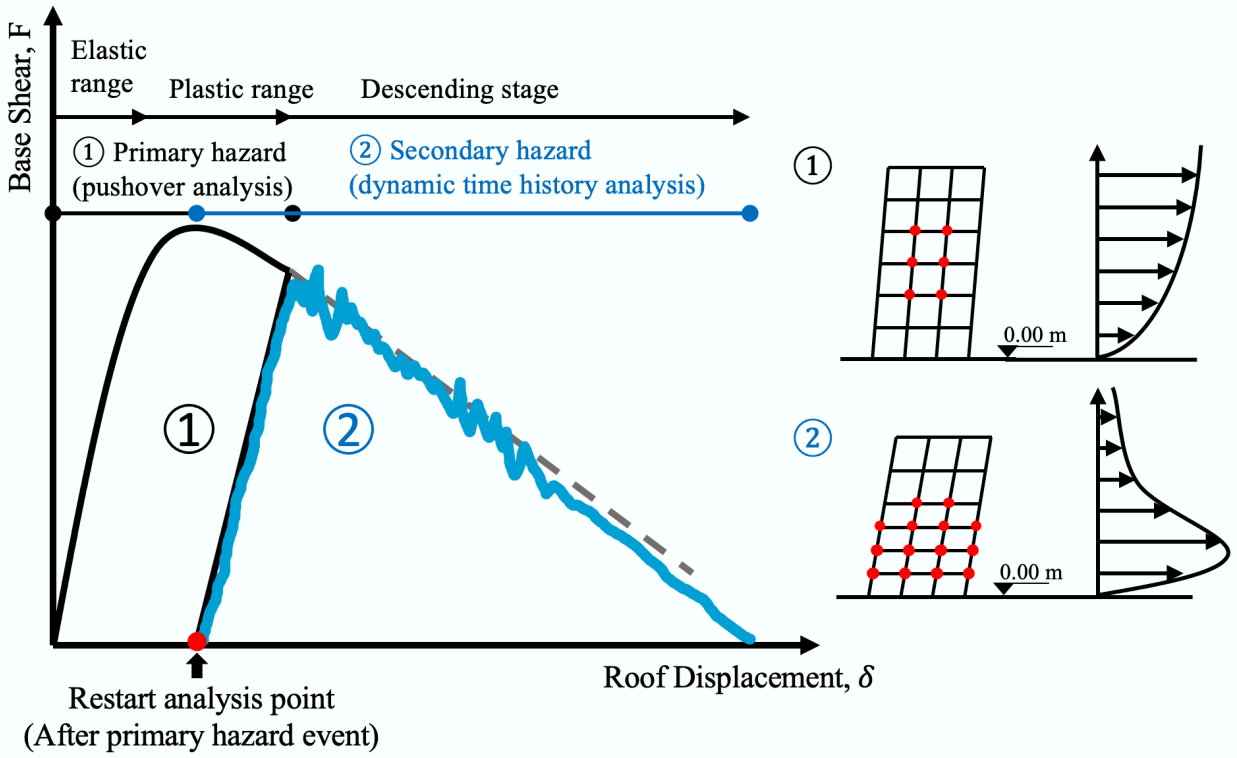


Figure 2-13. Diagram of the computational procedure for the sequential restart analysis.

Step 1: Apply axial loads.

Gravity and live loads are calculated and applied in the structure model using a general static analysis method of ABAQUS (2020). Appropriate modelling is considered to account for the P-Δ effects (second order effects) induced during the large displacement analysis.

Step 2: Perform frequency analysis for obtaining the fundamental mode shape.

During this step the modal shapes of the structure are obtained. According to Chopra and Goel (2002), the lateral force distribution across the height of the building can be determined using the mass matrix and the fundamental mode. Higher vibration modes can be combined by the square-root-of-sum-of-squares (SRSS) rule.

Step 3: Adaptive pushover analysis for the primary hazard event (see ① in Figure 2-13).

This step links ABAQUS (2020) pushover capabilities to MATLAB (2021) optimisation procedures to perform an adaptive pushover analysis based on (Skalomenos and Papazafeiropoulos, 2019) method. The advantage of their method is the utilisation of a novel mixed force/displacement optimisation control algorithm which can successfully trace the plastic range and descending branch of the structural response without obtaining the classical convergence errors. Note that ABAQUS (2020) has its own stabilisation algorithms or arc-length control (Riks) methods, but these are not sufficient for an adaptive pushover analysis. Static analysis with Riks can trace only a single loading path during the analysis and does not allow the user to control over the force distribution pattern during the pushover analysis.

In this step, the base shear - roof displacement relationship is obtained as schematically illustrated in Figure 2-13 (labelled with ①). The roof displacement can be controlled to reach a pre-defined ductility level caused by the primary hazard event. Abaqus2Matlab

(Papazafeiropoulos et al., 2017) is adopted as a post-processing tool to analyse the data. The load-displacement optimisation process is explained below (Skalomenos and Papazafeiropoulos, 2019):

Each increment (i) of the optimisation procedure maps the linear dependence between the real force distribution imposed on the building, $\{F_{r,i}\}$, and the target force distribution created by its fundamental eigenmode, $\{F_{t,i}\}$, using a load proportionality factor, λ_i, as implicit in Eq. (2.28).

$$F_{r,i}(n) = \lambda_i F_{t,i}(n), n = 1,2,\dots N \tag{2.28}$$

In this equation, N is the total number of storeys.

According to the controlled roof displacement and real force on the rest of the storeys, the reaction force at the roof level can be obtained to minimise the variance of the ratio between the real force array and the target force array (see Eq. (2.29)) within the loop until $d \cong 0$.

$$d = var(\{F_{r,i}\} / \{F_{t,i}\}) \tag{2.29}$$

Step 4: Transient non-stationary wind analysis of the secondary hazard event (see ② in Figure 2-13).

ABAQUS (2020) offers the capability of restart analysis which enables the user to stop the analysis at a desired time point and to restart at the same or another time point before (Skalomenos et al., 2018a; Skalomenos et al., 2018b). As a result, a subsequent hazard analysis can be performed by reading the output file of the previously deformed structure and subjecting the same structure to any type of loading. In the present multi-hazard framework, the subsequent analysis is a dynamic microburst analysis (secondary hazard event) imposed after the structure has reached a pre-defined ductility level representative to the primary hazard event. The restart

microburst analysis is a force control analysis using the direct-integration implicit dynamic algorithm available in ABAQUS (2020). The dynamic time history analysis begins after the adaptive non-linear pushover analysis has finished, meaning that the structure has returned to the zero-force equilibrium state (permanent plastic deformations), as shown in Figure 2-13 (labelled with ②). It is noted here that the stabilisation algorithms and arc-length control methods available in ABAQUS (2020) for pushover analysis have further limitations from those mentioned before. They can not distinguish between loading and unloading directions, and there is a possibility that the analysis starts from a point different from the last converged equilibrium point and applies the loading in a direction opposite to the one specified before. For this reason, the restart analysis in this study is used only with general static analysis controlled by MATLAB (2021) securing that the structure has returned to zero-force equilibrium and pushover analysis has terminated.

The application set of the sequential dynamic analysis is transient fidelity, where the Hilber-Hughes-Taylor integrators are $\alpha = -0.05$, $\beta = 0.27$, and $\gamma = 0.55$ (Hilber et al., 1977). The maximum increment size is consistent with the time step of the recorded wind load time history (i.e. 0.3068 of the simulated velocity time history of Section 7.3). The initial increment size to help convergence is 0.01. All the restart analytical steps are carried out in accordance with the analytical results of the previous phase based on the setting of FREQUENCY =1 in the input files opened by the restart analysis procedure. The proposed sequential multi-hazard analysis can directly control the non-linear analysis steps and randomly combine different type of loads induced by TS downburst events under various wind velocity patterns and terrain types.

2.5 Summary

The modelling procedure described in Section 2.1 is applied to simulate six full-scale downburst records, and the results are discussed in Chapter 3.

The pressure coefficient data obtained from the WT experiments built in Section 2.2 is discussed in Chapter 4. As preliminary validation of the technique, velocity data from the University of Birmingham Transient Wind Simulator (TWS) is combined with these pressure coefficients to predict pressure time series, which were compared to those measured directly in the TWS, as discussed in Section 4.2.

Based on the theoretical algorithm in Section 2.3, the so-called wind design spectra then undergo verification, including the scrutiny of their controlling parameters in Chapter 5. This enables us to identify the variability of design spectral ordinates with the outflow velocity, structural dimensions, mass, and terrain type. The spectral method validates through estimation of the dynamic performance of a benchmark building, via generalised techniques, as well as through numerical integration. Further validation takes the form of time step analysis based on a synthetic wind field that replicates TS downbursts, as discussed in Section 5.4.

The novel computational procedure built in Section 2.4 is applied to a tall steel building frame subjected to several primary damage states and eleven subsequent downburst synthetic records. The ductility demands and collapse mechanisms induced by the strong downburst on the damaged structures and the effectiveness of this computational procedure are discussed in Chapter 7.

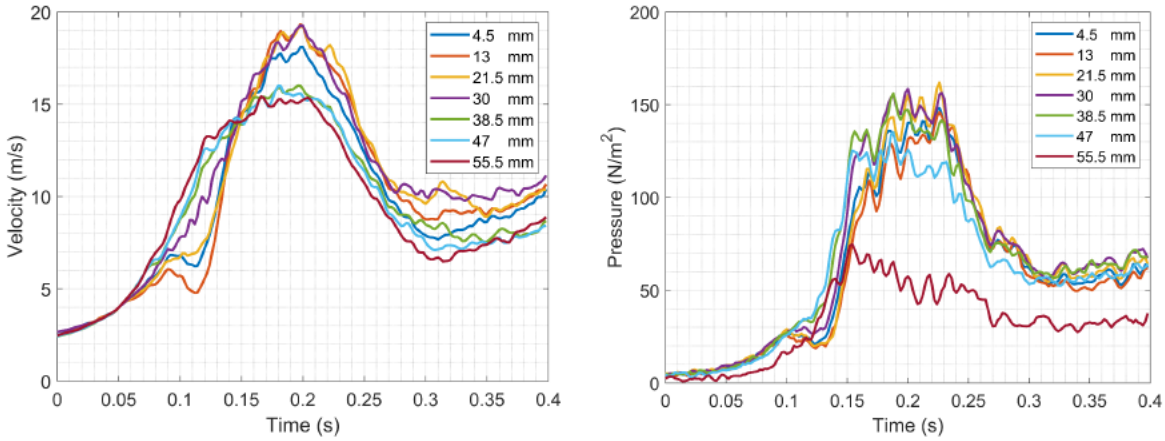
Chapter 3 Results and discussion of TS theoretical model

Chapter 3 concentrates on the analytical modelling of full-scale downburst events via the two-dimensional "vortex model" outlined in Section 1.3.4. The width of a building relative to the lateral dimensions of the main flow structures of a downburst is small, and so the wind may be considered horizontally uniform over the scale of a building. Therefore, the two-dimensional (streamwise and vertical) "vortex model" can be used to model a downburst effectively. Based on the original settings of the laboratory-scale modelling for the TWS obtained from Jesson and Sterling (2018), the boundary layer profile has been improved and the further comparisons of the velocity time series and pressure time series at different heights between the vortex model and TWS are illustrated in Section 3.1. The upgraded modelling procedure of this vortex model for full-scale downburst events is outlined in Section 2.1 based on the theory discussed in Section 1.3.4. The results and discussion of this vortex model to model the full-scale downburst events from JAWS and WERFL are demonstrated in Section 3.2.

3.1 Validation with laboratory-scale experiments

The variation of experimental velocity data against time at six elevations at the horizontal position of maximum velocity was calculated by interpolation method according to the original data, see Figure 3-1 (a). These six elevations are at 13 mm, 21.5 mm, 30 mm, 38.5 mm, 47 mm

and 55.5 mm, the same heights as the pressure taps on the model. The recorded pressure time series at six tapping heights from UoB-TWS is presented in Figure 3-1 (b).



(a) Velocity time-series (b) Pressure time-series

Figure 3-1. Velocity and pressure time-series from experimental data.

It has been verified that this vortex model can accurately model the laboratory-scale downburst by Jesson and Sterling (2018). In order to further validate the accuracy of this vortex model for laboratory-scale downburst simulations, the velocity time series acquired from the vortex model are compared with those from the UoB-TWS.

It should be emphasised that the original data for pressure and velocity time series from Jesson et al. (2015b) were measured separately, i.e. they were not obtained using simultaneous measurements, which given the variable nature of each downburst generated raises implications for the interpretation of the velocity field; thus, the pressure coefficients cannot be calculated from the velocity time history and pressure time history of TWS directly. Jesson et al. (2015b) adopted the maximum velocity as the reference velocity for the calculation of pressure coefficients, while this method could not reproduce the actual pressure coefficients time series (since the velocity also varies with respect to time). Therefore, in order to synchronise the velocity and pressure time series, the middle point (at z=30 mm) corresponding to the centreline of the front surface of the cube was used, assuming the stagnation pressure at this point is

proportional to the local velocity. Furthermore, it was assumed that the time of the maximum velocity also corresponds with the time of the maximum pressure. It has been shown from Figure 3-1 that the greatest pressure corresponds to the short period with peak velocity; thus only the duration of the downburst starting from the time of downdraft hitting the ground to twice the time of peak velocity is simulated by vortex model. Therefore, the period of 0.2 s before and after the time point of maximum velocity and maximum pressure at 30 mm height is selected for comparison with the data from the vortex model.

The comparisons between the experimental velocity time series and the model simulation (outlined in Section 1.3.4) are shown in Figure 3-2 for a period of 0.4 s. The trends of the velocity time series between the vortex model and experimental data are similar at different heights (see Figure 3-2) and the RMS errors (defined in Eq. 3.1) of velocity time series are 9.8%, 6.5%, 7.5%, 10.9%, 12.4%, 13.9% of the maximum velocity (19.4 ms^{-1}) for z = 13 mm, 21.5 mm, 30 mm, 38.5 mm, 47 mm and 55.5 mm respectively, thus, demonstrating a good consistency between the simulated and experimental data.

$$RMS_{error} = \sqrt{\frac{1}{T}\sum_0^t (A(t) - B(t))^2} \tag{3.1}$$

In Eq. (3.1), $A(t)$ and $B(t)$ are two different time histories, (i.e. the simulated and experimental). t is the instantaneous time and T is the total time.

From Figure 3-2, it can be observed that when z = 21.5 mm, the maximum velocities corresponding to both the simulated and experiments are identical. The largest difference in terms of simulated and experimental maximum values is approximately 3 ms^{-1} and occurs at 13 mm. One possible explanation for this difference could be due to the relative position of the primary and secondary vortices and the secondary vortex is always tangential to the ground

surface since only the simplified pattern of vortices is considered in the current vortex model. The time-lag of the peak velocities at heights 38.5 mm, 47 mm and 55.5 mm may be due to the influence of the fixed pattern of variable sizes of the primary and secondary vortices in the current vortex model, i.e. the major radius of primary vortex increases with time, accompanying the decrease of minor radius of primary vortex, and the minor radius of secondary vortex grows with time. In the experimental transient simulation, the variable sizes of the vortices and the relative position between the primary vortex and secondary vortex are more complicated than the setting in vortex model. In addition, predicting the exact relative movement of the primary vortex and secondary vortex is challenging. However, based on the observation of the velocity comparison in Figure 3-2, the current patterns of the vortex model, i.e. the relative position of the primary and secondary vortex, the varying sizes of vortices, can effectively illustrate the main features of the downburst. After 0.2 s, more accurate settings of vortex model are needed, while in this case, the vortex model focuses on peak velocities due to its transient characteristic.

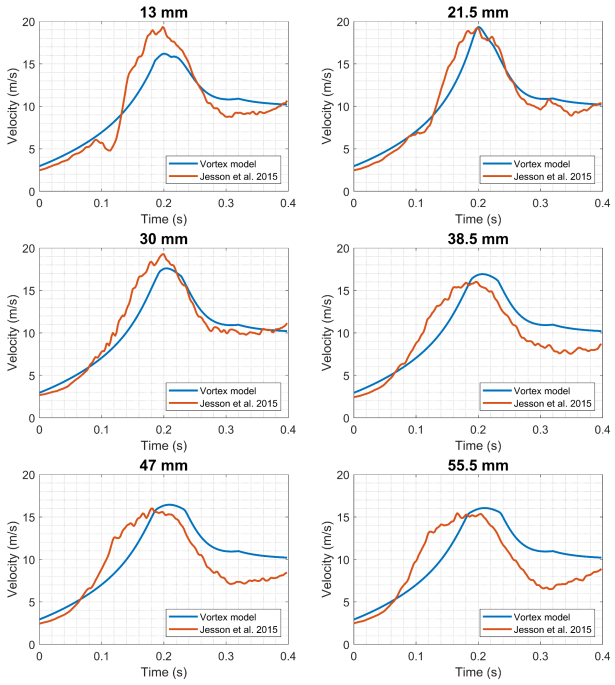


Figure 3-2. Velocity comparison between the results from the vortex model and UoB-TWS data. Blue line represents vortex model data; Orange line represents the UoB-TWS data.

Additionally, the pressures calculated from the velocity time series of the vortex model and the pressure coefficients from the UoB-TWS are compared with the pressures recorded from UoB-TWS. In this case, the velocity time series at the height of the tapping is taken as the time-varying reference velocity for that point on the front surface of the cube building model. Therefore, the pressure coefficient time series for each point on the front surface from the UoB-TWS can be calculated by Eq. (1.48). Combining the experimental pressure coefficient time series at different points on the front surface with the velocity time series at different heights from the vortex model, the estimated pressure time series from vortex model has been calculated based on Eq. (1.48). The pressure comparisons between the vortex model and UoB-TWS at different heights are shown in Figure 3-3. These heights correspond to the tapping heights on the front surface of the buildings. Except at height 55.5 mm, the overall trends between the estimated pressure time series from vortex model and the measured pressure time series on the cube building model are quite similar and the RMS errors of pressure time series are 21 Pa, 14 Pa, 18 Pa, 34 Pa, 37 Pa, 26 Pa for z = 13 mm, 21.5 mm, 30 mm, 38.5 mm, 47 mm and 55.5 mm respectively. The relative higher RMS errors (>25 Pa) at $z \geq 38.5$ mm may be due to the flow separations as the streamwise flow on the front surface is deflected onto and over the roof.

The time-lag for the peak pressures at height 38.5 mm, 47 mm and 55.5 mm increases with heights which results from the unpredictable variable sizes of primary and secondary vortices and the relative positions of primary and secondary vortices. The maximum velocities in the vortex model are induced by the superposition of the primary vortex, secondary vortex and outflow. The outflow distributes on the flow field uniformly; therefore, the maximum velocity is mainly influenced by primary vortex and secondary vortex.

Due to the more complicated flow field of the downburst in experiments compared with these in vortex model, i.e. the variable shapes of primary and secondary vortices, the setting of the vortex model especially after 0.2 s needs to be improved. As for the transient wind load, the peak pressures along the building height are essential. The estimated pressure time series at height 21.5 mm and 30 mm (Figure 3-3) illustrate that this vortex model can estimate the peak pressures at where the maximum velocity happens accurately, though the improvements for more accurate pressure time series at other elevations are needed.

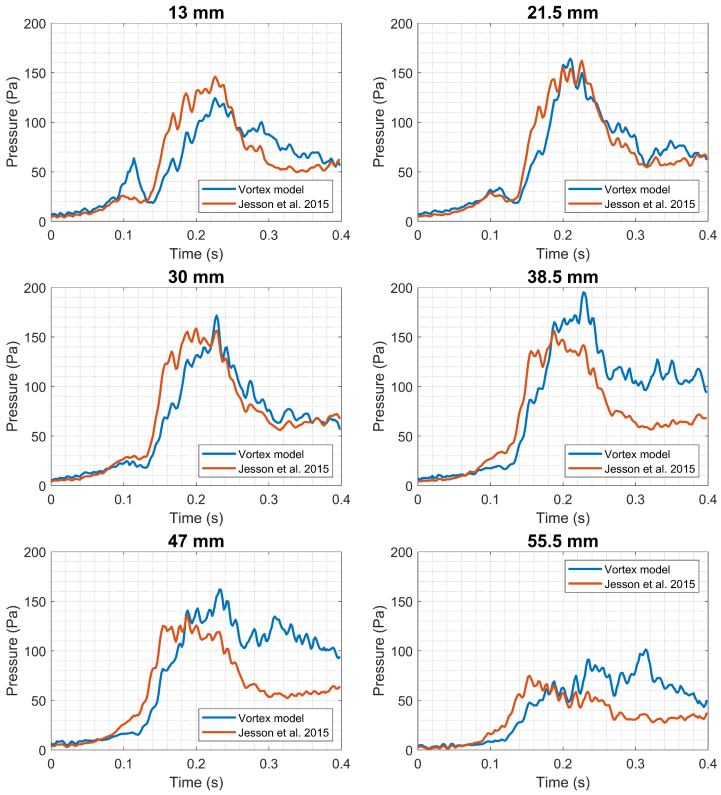


Figure 3-3. Pressure comparison between the results from the vortex model and UoB-TWS. Blue line represents the vortex model data; Orange line represents the UoB-TWS data.

3.2 Model full-scale downbursts using vortex model

In Section 3.2, the vortex model is adopted to simulate the process (starting from when the primary vortex first touches the ground to approximately twice the time of peak velocity) of six

full-scale downburst cases described in Section 1.2.2 and summarised in Table 1-3 (see Section 1.3.1), and the velocity profiles modelled from the vortex model were compared with these six full-scale downburst cases. Furthermore, the outputs of these six cases were compared with the microburst characteristics from Hjelmfelt (1988) to validate the accuracy of the modelled horizontal velocities along the radial distance. The thickness of the boundary layer is assumed to be half height of the maximum velocity since the effect of the mirror vortices can be neglected.

3.2.1 CASE 1

Initially, in order to validate whether this vortex model can model a full-scale event, a comparison is made between the average parameter values obtained from the 26 JAWS microburst field trails (summarised in Section 1.2.2) and a model simulation. The input data used for this comparison is shown in Table 3-1 with the corresponding output shown in Figure 3-4. The setting of the relative positions of the vortices in the vortex model is an essential factor for the vertical distribution of radial velocity, as the maximum velocity is generated by the high-speed region where the velocity maxima of the primary vortex and secondary vortex coincide. The average height for the maximum radial velocity is 80 m (see Section 1.2.2). Thus, based on the modelling procedure mentioned in Section 2.1, the input data for primary and secondary vortices has been selected (Table 3-1). The initial minimum diameter of the secondary vortex was assumed to be twice the minor radii (60 m) and increased with time to around 80 m over a 5-minute period and these parameters are chosen based on the characteristics of the 26 JAWS events mentioned in Section 1.2.2. The associated rate of change for minor radii was taken as 0.067 ms^{-1} (Table 3-1). The initial horizontal position for the primary vortex is the average radius of the downdraft flow plus the radius of primary vortex, i.e. the primary vortex is assumed to start with its rear edge at the edge of the downdraft. The mean radius of the

downdraft flow is around 900 m, as shown in Section 1.2.2. The negative value for the rate of change of circulation for the secondary vortex is due to the opposite direction to the primary vortex.

The modelled vertical distribution of horizontal velocity upper bound (maximum value for each vertical position) profile in green line (Figure 3-4 (a)) is close to the mean velocity profile from Hjelmfelt (1988) in solid black line, though there is an apparent difference (up to 0.15 difference of u/u_{max}) between the normalised vertical distribution of horizontal velocity profile at the time when the maximum velocity occurs as shown in the red line and the mean velocity profile from Hjelmfelt (1988) in solid black line. When the ratio of z/z_{vmax} above 1, the velocities from vortex model are lower than these from full-scale JAWS, while this situation is opposite when the ratio of z/z_{vmax} below 1, which results from the unpredictable variable sizes of vortices and relative positions of primary vortex and secondary vortex. In this vortex model, the dimensional variations and the relative positions of the primary vortex and secondary vortex are in a pre-designed pattern, i.e. the secondary vortex is always tangential to the ground; the primary vortex always tangents to the secondary vortex.

The radial velocity starting from the centre of the downburst is demonstrated in Figure 3-4 (b). The black lines (including solid, dashed and dashed-dot lines) are the radial velocity profiles from the 26 JAWS events (Hjelmfelt, 1988). The radial velocity of these lines starts from near zero and increases approximately linearly to maximum velocity and then decreases after reaching maximum velocity. However, the radial velocity profile from the vortex model (red line) does not start from zero. The main reason for this is due to the outflow arranged on the whole domain in the vortex model (see Section 1.3.4) and the velocity of outflow increases with time, which means that the radial velocity at the centre of the downburst contains the high radial

velocity from the flow field of outflow at the time of maximum velocity. This condition also happens at the radial distance after the maximum radial velocity. With the increase of the radial distance after the maximum radial velocity, the radial velocity should decrease to zero. Therefore, the variation of the outflow velocity along the radial position should be added into the vortex model.

Table 3-1. Summary of the input data of vortex modelling.

	Case 1 26 JAWS events	Case 2 20030619	Case 3 20080521	Case 4 20080619	Case 5 20080813	Case 6 20100308
Parameters for primary vortex						
major radii (m)	350	245	880	480	690	690
minor radii (m)	350	134	880	480	730	690
Rate of change for major radii (m/s)	-0.02	-1.10	-0.20	-0.5	-0.050	-0.40
Rate of change for minor radii (m/s)	-0.133	-0.009	-0.040	-0.096	-0.017	-0.10
Initial Circulation (m/s×m)	22682	13258	88068	48860	43214	77018
Rate of change of circulation (m/s×m/s)	-37.8	-110	-78	-166.12	-79.97	-308
Initial horizontal position (m)	1250	1145	1780	1380	1590	1590
Parameters for secondary vortex						
major radii (m)	80	14.5	150	150	90	80
minor radii (m)	30	2	70	70	56	30
Rate of change for major radii (m/s)	-0.010	-0.010	-0.050	-0.2	-0.005	-0.03
Rate of change for minor radii (m/s)	0.067	0.009	0.020	0.048	0.009	0.05
Initial Circulation (m/s×m)	0	0	0	0	0	0.00
Rate of change of circulation (m/s×m/s)	-15.27	-1.62	-12.00	-35.76	-10.79	-22.67
Initial horizontal position (m)	1330	1160	1930	1530	1680	1670

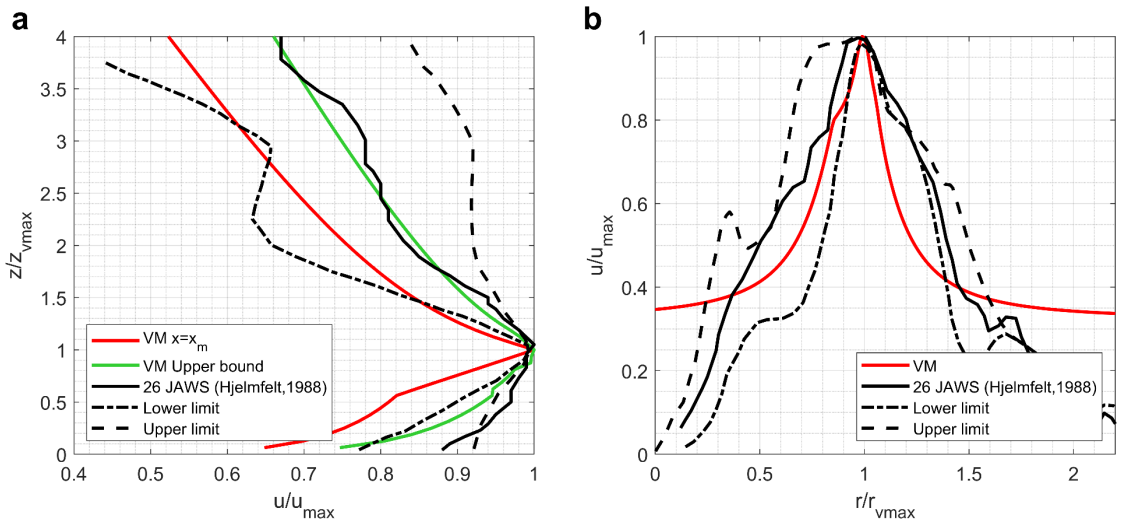


Figure 3-4. Velocity profiles comparison: (a) Profile of normalised maximum horizontal velocity with height. Velocity is normalised to the maximum velocity (u_{max}). Height scaled to the height of maximum velocity (z_{vmax}); (b) Profiles of normalised radial velocity along azimuth of maximum velocity and scaled radius from microburst centre at $t=t_m$. Velocity is normalised to the maximum velocity (u_{max}). Radius is scaled to the radius of the maximum velocity (r_{vmax}). "VM" represents the vortex model. x_m represents the radial position when the maximum velocity occurs. t_m is the time when the maximum velocity occurs. Upper bound represents the maximum velocity at each vertical position. Lower limit and upper limit come from the 26 JAWS events.

3.2.2 CASE 2

The full-scale downburst data for case two was recorded on June 19, 2003, at approximately 3:55 PM Central Daylight Time (CDT) from a 50 m tower with RM Young Gill 27005T u-v-w anemometers at five levels (Table 3-2) and the resolution of this anemometers is 0.01 ms^{-1}, detailed by Lombardo et al. (2018). The recorded 3 s filtered peak velocities are 24.41 ms^{-1} and 23.46 ms^{-1} at 4 m and 10 m respectively (Table 3-2, 0.01 ms^{-1} resolution for anemometers). The maximum velocities at each height are presented as upper bound velocities. In the vortex model, the vertical distribution of horizontal velocity at the time of the maximum velocity is the same as the data at the horizontal position of the maximum velocity, which is defined as the velocity profiles at $x = x_m$. The input data of the vortex model is shown in Table

3-1 based on the modelling procedure (Section 2.1). The selected duration for this downburst event is 100 s, as this period illustrates the characteristics of the downburst discussed in Section 1.2. The initial velocity of the downburst simulation was taken as 10.9 ms^{-1} (average value w.r.t. velocity from 50 s to 86 s), and the final outflow velocity for the simulation was assumed to be 14.3 ms^{-1} (average value w.r.t. velocity from 129 s to 150 s).

Table 3-2. Full-scale event data for Case 2.

	Full-scale downburst event data
Vertical position of measured points (m)	2.4, 4, 10, 21, 50
The upper bound velocities of measured points (m/s)	22.83, 24.41, 23.46, 22.63, 20.55
The velocity at $x = x_m$ of measured points (m/s)	22.30, 24.41, 23.13, 21.76, 19.42
The time period of downburst (s)	100
Initial velocity of downburst (m/s)	10.9 (50 s to 86 s)
The outflow velocity (m/s)	14.3 (129 s to 150 s)

The major radii, minor radii, rate of change for major radii, rate of change for minor radii and rate of change of circulation were obtained through a random combination based on step three which aimed to obtain the best fit of the vertical distribution of horizontal velocity profiles for case two (Table 3-1). The initial horizontal position for the primary vortex is 1145 m, the mean radius of the downdraft from the 26 JAWS events, 900 m, plus the major radius of the primary vortex, 245 m.

The comparison of the vertical distribution of horizontal velocity profiles at 102 s, the time of maximum velocity is shown in Figure 3-5 (a). The correlation coefficients (defined in Eq. (3.2)) of the vertical distribution of horizontal velocity profile $x = x_m$ and the vertical upper bound velocity profile between the vortex model and the full-scale downburst data are 0.997 and 0.996 respectively, which demonstrate a good agreement on the variations relative to the mean values of the vertical distribution of horizontal velocity profiles.

$$Corr(A(t), B(t)) = \frac{1}{N-1}\sum_{i=1}^{N}\left(\frac{A_i-\mu_A}{\sigma_A}\right)\left(\frac{B_i-\mu_B}{\sigma_B}\right) \quad (3.2)$$

where A(t) and B (t) are two different time histories. μ_A and σ_A are the mean value and standard deviation of time series A. μ_B and σ_B are the mean value and standard deviation of time series B. N is equal to the total time period dividing the sampling frequency.

The peak velocity from the full-scale measurement is 24.41 ms^{-1} (0.01 ms^{-1} resolution of the adopted anemometer), and the peak velocity from vortex model is 24.47 ms^{-1}. The blue line is the gust upper bound profile of horizontal winds at each height from full-scale measurement and the green line is the gust upper bound profile from the vortex model. The velocity profile from the vortex model at a higher elevation is slightly greater than the full-scale measurement, and the errors at 50 m height are 1.99% (<0.4 ms^{-1}). Due to the uncertainties associated with full-scale measurements, i.e. the relative position between anemometers and downburst centre, this small error demonstrated a well-matched result. The sizes of primary vortex cause the reason for this. In this vortex model, the height below 2 m follows the power law and the calculated α is 0.24.

The modelled position of maximum velocity occurs at x =1400 m and z = 4 m, and the modelled velocity time series at this position is shown in red (Figure 3-5 (b)). The velocity from the vortex model is higher (up to 9 ms^{-1}) than the velocity time series from the full-scale data. The larger values before the peak velocity are due to the initial sizes of the primary vortex and secondary vortex. If the sizes of the initial primary vortex and secondary vortex increase, the velocity time series before 102 s (where the peak velocity occurs at 1400 m, 4 m) can be decreased. However, the sizes of primary and secondary vortices are limited by the vertical distribution of horizontal velocity profiles. Considering the differences between the vertical distribution of velocity for the ABL and downbursts, the vertical distribution at the time of peak

velocity is arguably the more critical factor for the downburst events and hence is the primary target of the modelling in this research.

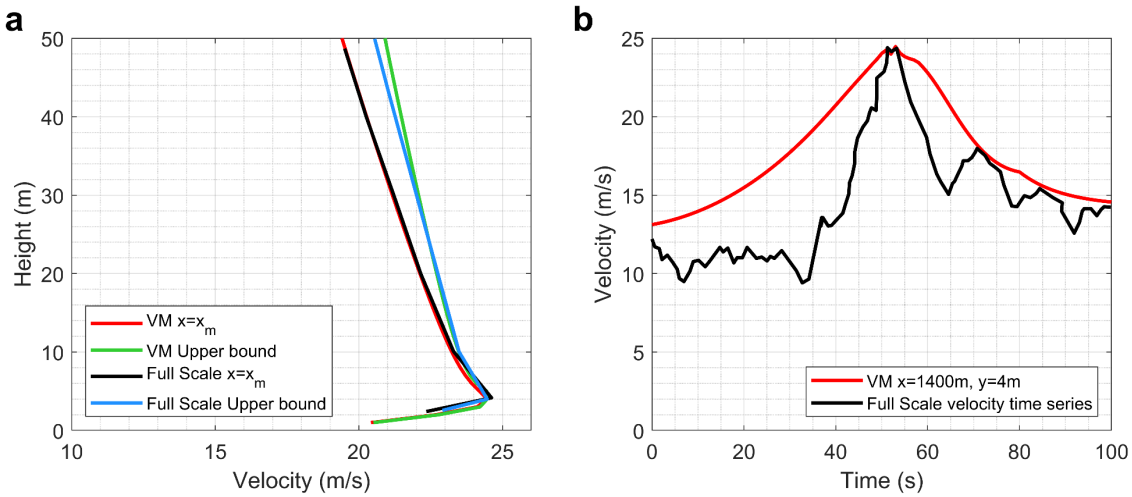


Figure 3-5. Velocity profiles comparison for case two: (a) Vertical distribution of horizontal velocity profiles of horizontal winds; (b) Velocity time series for the position of maximum velocity. "VM" represents the vortex model. x_m represents the radial position at the time of maximum velocity.

The chosen duration of velocity time series for this case is 100 s, which is the most relevant to the downburst event, and the comparisons of the vertical distribution of horizontal velocity profiles at different times between the vortex model and the full-scale records are shown in Figure 3-6. The vertical distributions of horizontal velocity profiles of vortex model at 40 s and 62 s are larger than these from full-scale downburst records, and the errors may be due to the sizes of primary and secondary vortices as discussed before. Therefore, the vortex model can only accurately estimate the vertical distribution of horizontal velocity profiles at the time when the maximum velocity occurs, and further improvements are needed.

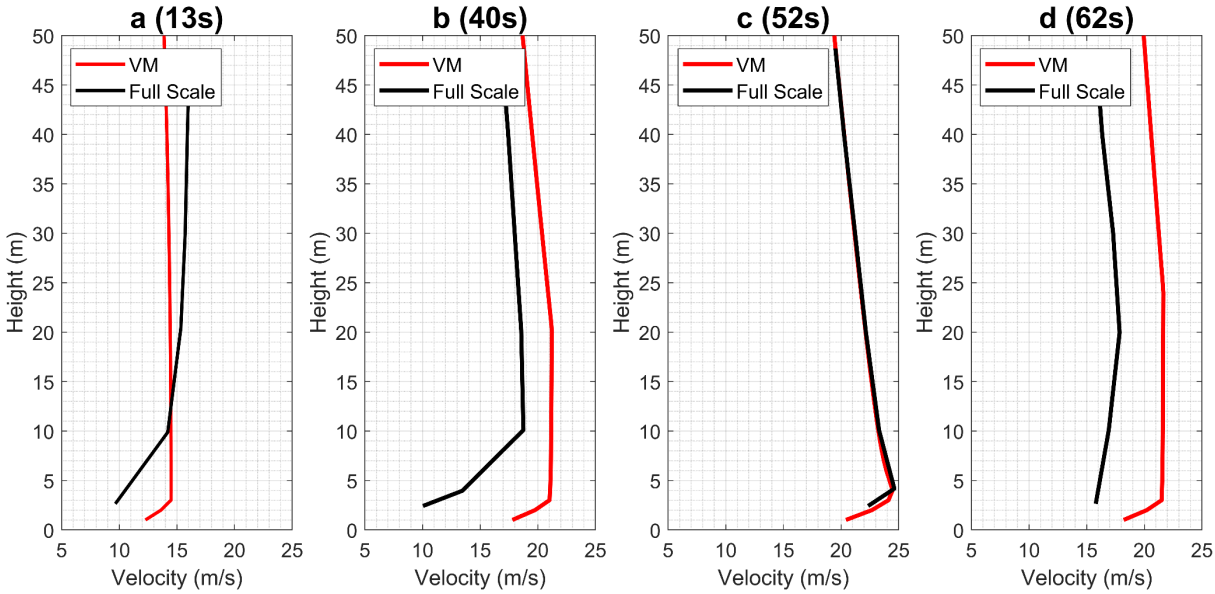


Figure 3-6. Comparison of the vertical distribution of horizontal velocity profiles at different times between the vortex model and full-scale data: (a) Prior to ramp-up; (b) During ramp-up; (c) At the time of maximum velocity; (d) During ramp-down. "VM" represents the vortex model.

3.2.3 CASE 3

The full-scale downburst event for case three was recorded at seven elevations on May 21, 2008 at the WERFL field site by Lombardo et al. (2014). The maximum velocities and the velocities at the time of maximum velocity at each elevation are listed in Table 3-3. The chosen time period is 850 s, as this variation of the velocity best satisfies the characteristics of downburst. The initial velocity of the downburst is 14.48 ms^{-1}, which is the mean value w.r.t. the velocity of the period from the 80 s to 345 s, before the sudden increase of the velocity. The outflow velocity is 13.13 ms^{-1}, which is the average value w.r.t. velocity of the period from 645 s to 930 s, after half of the downburst passes the tower. The input data (see Table 3-1) of modelling for case three is based on step three and step four (see Section 2.1).

Table 3-3. Full-scale event data for Case 3.

	Full-scale downburst event data
Vertical position of measured points (m)	1, 2, 4, 10, 116, 158, 200
The upper bound velocities of measured points (m/s)	18.33, 24.95, 29.34, 30.18, 29.82, 30.67, 30.45
The velocity at $x = x_m$ of measured points (m/s)	10.54, 14.83, 18.54, 23.39, 29.71, 30.67, 27.59
The time period of downburst (s)	850
Initial velocity of downburst (m/s)	14.48 (80 s to 345 s)
The outflow velocity (m/s)	13.13 (645 s to 930 s)

The vertical distributions of horizontal velocity profiles between the modelled vertical profile and measured full-scale downburst have been compared (Figure 3-7 (a)) and the correlation coefficients (see Table 3-4) are 0.71 and 0.95 for upper bound and vertical distribution of horizontal velocity profiles at $x = x_m$ relative to the mean values of the vertical distribution of horizontal velocity profiles respectively. In this vortex model simulation, the height below 79m follows the power law with an exponent of α =0.13. The comparison of the modelled velocity time series at the position of maximum velocity and the velocity time series from recorded full-scale data demonstrates a quite similar tendency based on observation (Figure 3-7 (b)). The correlation coefficient for the velocity time series between vortex model and full-scale downburst records is 0.786 for 75 s duration (37 s before the time of maximum velocity and 37 s after the time of maximum velocity) which is most related to the peak velocity. The modelled position of maximum velocity is situated at x=3640 m, y=158 m relative to the centre point of the downdraft on the ground surface.

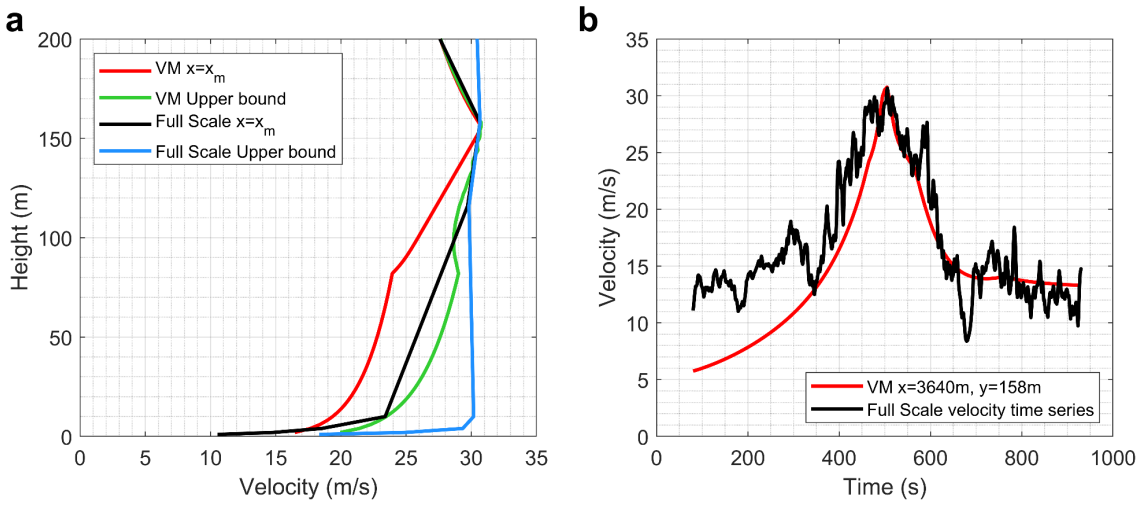


Figure 3-7. Velocity profiles comparison for case three: (a) Vertical distribution of horizontal velocity profiles of horizontal winds; (b) Velocity time series for the position of maximum velocity. "VM" represents the vortex model. x_m represents the radial position when the maximum velocity occurs.

Table 3-4. Summary of the correlation coefficients for the comparison for five sets of data.

	Case 1	Case 2	Case 3	Case 4	Case 5	Case 6
Upper bound velocity profile	\	0.996	0.711	0.963	0.942	0.687
x x_m Velocity profile	0.254	0.997	0.950	0.844	0.986	0.948
Velocity time-series	\	0.469 (8s)	0.786 (75s)	0.940 (25s)	0.249 (32s)	0.878 (26s)

3.2.4 CASE 4

The recorded full-scale downburst event for case four happened on June 19, 2008 at the WERFL field site by Lombardo et al. (2014), and the detailed information are presented in Table 3-5. The chosen period of this downburst time history is 250 s, and the velocity starts from approximately 18 ms^{-1} before the sharp rise of velocity. The adopted initial velocity of the downburst for modelling is 18.84 ms^{-1} (mean velocity of duration from 35 s to 183 s) and the outflow velocity for modelling is 19.70 ms^{-1} (mean velocity of duration from 236 s to 285 s). According to the step three and step four described in Section 2.1, the detailed input data of modelling for case four is listed in Table 3-1.

According to the observed comparison for the vertical distribution of horizontal velocity profiles (Figure 3-8 (a)), further amendments for the variable shapes of the vortices are needed. In this vortex model simulation, the height below 79 m follows the power law and the calculated α is 0.13. Even though the elevation of the application of the power law reaches up to 79 m, there is a noticeable increase of velocity with the decreasing of height from 110 m to 80 m, which demonstrates that half of the height of maximum velocity may not be suitable for every downburst case. The comparison of the velocity time series at the position of maximum velocity is shown in Figure 3-8 (b). The correlation coefficient for the velocity time series relative to the mean velocities of the time series between vortex model and full-scale downburst records is 0.94 for 25 s period (12 s before the time of maximum velocity and 12 s after the time of maximum velocity) which is most related to the peak velocity, that illustrates a good agreement. The results of the modelling also present that the position of maximum velocity is situated at x=2640 m, y= 158 m relative to the central point of the downdraft on the ground surface.

Table 3-5. Full-scale event data for Case 4.

	Full-scale downburst event data
Vertical position of measured points (m)	1, 2, 4, 10, 116, 158, 200
The upper bound velocities of measured points (m/s)	15.43, 19.05, 24.17, 27.01, 28.25, 28.32, 27.82
The velocity at $x = x_m$ of measured points (m/s)	7.45, 9.01, 11.62, 14.97, 27.91, 28.32, 25.63
The time period of downburst (s)	250
Initial velocity of downburst (m/s)	18.84 (35 s to 183 s)
The outflow velocity (m/s)	19.70 (236 s to 285 s)

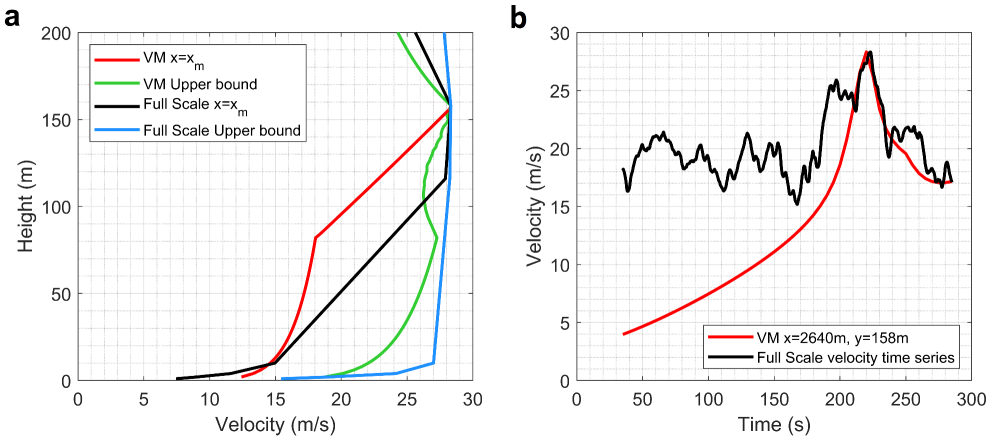


Figure 3-8. Velocity profiles comparison for case four: (a) Vertical distribution of horizontal velocity profiles of horizontal winds; (b) Velocity time series for the position of maximum velocity. "VM" represents the vortex model. x_m represents the radial position when the maximum velocity occurs.

3.2.5 CASE 5

The full-scale downburst event for case five was recorded at seven elevations on August 13, 2008 at the WERFL field site by Lombardo et al. (2014). The maximum velocities and the velocities when the maximum velocity occurs at each elevation are listed in Table 3-6. The maximum velocity is 26.29 ms^{-1} (0.01 ms^{-1} resolution of the adopted anemometer), and the chosen time period is 816 s which contains constant high velocity duration. The initial velocity of the downburst for modelling is 9.69 ms^{-1}, and the outflow velocity for modelling is 18.30 ms^{-1}. The detailed input data of modelling for case five are based on step three and step four demonstrated in Section 2.1, as shown in Table 3-1.

Table 3-6. Full-scale event data for Case 5.

	Full-scale downburst event data
Vertical position of measured points (m)	1, 2, 4, 10, 116, 158, 200
The upper bound velocities of measured points (m/s)	19.84, 23.3, 24.52, 25.16, 26.29, 26.04, 25.91
The velocity at $x = x_m$ of measured points (m/s)	12.34, 13.36, 14.09, 18.87, 26.29, 25.24, 24.56
The time period of downburst (s)	816
Initial velocity of downburst (m/s)	9.69 (151 s to 204 s)
The outflow velocity (m/s)	18.30 (552 s to 884 s)

The vertical distributions of horizontal velocity profiles from the vortex model (see red and green lines) are quite close to the vertical distribution of horizontal velocity profiles at $x = x_m$ (black line) from the full-scale downburst records (see Figure 3-9 (a)). In this vortex model simulation, the height below 58 m follows the power law and the calculated α is 0.13. The estimated position of maximum velocity in the Cartesian coordinate system from vortex model is x=5050 m, y=116 m and the zero horizontal axis starts from the centre of downdraft on the ground surface. There is a constant high velocity period from full-scale records lasting around 250 s (Figure 3-9 (b)) and the reason for this may be due to the microburst line event demonstrated by a few similar characteristics mentioned by Hjelmfelt (1988), i.e. the microburst line is characterised as two or more microbursts occur at the same time and form a line, and the maximum velocity of microburst line event is greater than individual microburst event with an average peak velocity at 26 ms^{-1} which is similar to the maximum velocity of 26.29 ms^{-1} for this full-scale downburst event; the diameter of the primary vortex for the microburst line is around 1400 m corresponding 1380 m in vortex model. Nevertheless, the distance between the maximum velocities is 3400 m for microburst line while the value of this in vortex model is 10100 m, and the measured average lifetime for the microburst line is 57 minutes though for this case the duration is only 14 minutes (816 s). Commonly, the current vortex model is only suitable for the typical single downburst event, and further enhancements of this vortex model can be made for microburst line event.

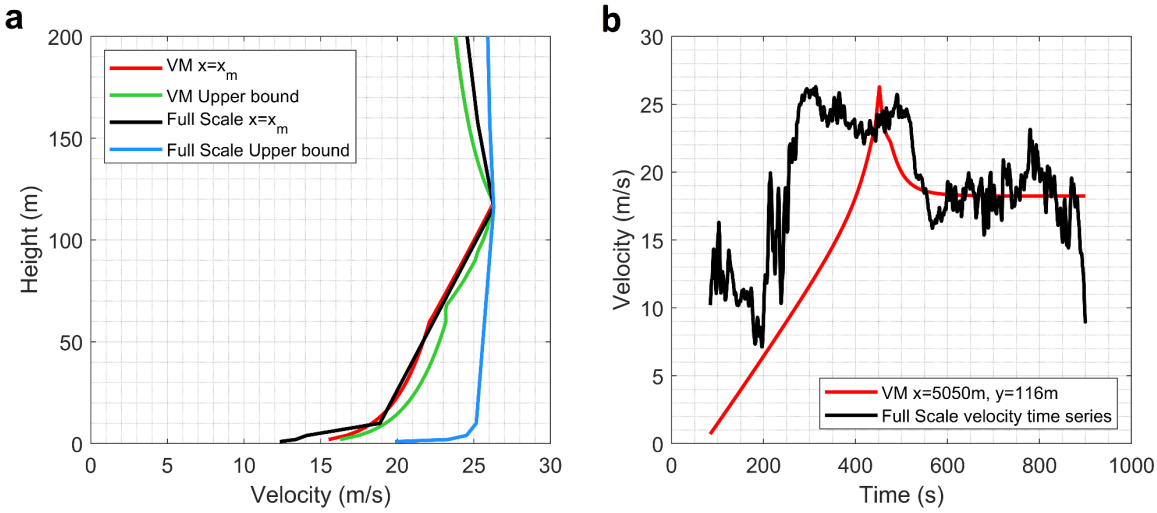


Figure 3-9. Velocity profiles comparison for case five: (a) Vertical distribution of horizontal velocity profiles of horizontal winds; (b) Velocity time series for the position of maximum velocity. "VM" represents the vortex model. x_m represents the radial position when the maximum velocity occurs.

3.2.6 CASE 6

The recorded full-scale downburst event of case six happened on March 08, 2010, at the WERFL field site by Lombardo et al. (2014) and the vertical distribution of maximum velocities and the velocities at the time of the maximum velocity at each elevation are listed in Table 3-7. The selected time period of modelling is 300 s, which is acceptable for the characteristics of the velocity time series of downburst. The initial velocity for this case is 18.70 ms^{-1} (mean value w.r.t. the velocity from 16 s to 116 s of the time series) and the outflow velocity is 23.8 ms^{-1} (mean value w.r.t. the velocity from 216 s to 316 s of the time series), which are used for modelling. The detailed input data of modelling for case six based on step three and step four discussed in Section 2.1 is presented in Table 3-1.

Table 3-7. Full-scale event data for Case 6.

	Full-scale downburst event data
Vertical position of measured points (m)	4, 10, 17, 47, 75, 116, 158, 200
The velocities upper bound of measured points (m/s)	22.15, 24.66, 27.88, 31.54, 34.40, 33.54, 30.83, 31.06
The velocity at $x = x_m$ of measured points (m/s)	18.24, 22.29, 25.40, 30.43, 34.40, 31.23, 28.57, 27.88
The time period of downburst (s)	300
Initial velocity of downburst (m/s)	18.70 (16 s to 116 s)
The outflow velocity (m/s)	23.80 (216 s to 316 s)

The modelled vertical distributions of horizontal velocity profiles demonstrate similar tendencies as the measured full-scale downburst velocity profiles based on the observation (see Figure 3-10). In this vortex model simulation, the height below 37.5 m follows the power law and the calculated α is 0.14. The comparison of the velocity time series at the position of maximum velocity (Figure 3-10 (b)) also expresses a quite close trend from observations. The correlation coefficient for the velocity time series between vortex model and full-scale downburst records is 0.878 for 26 s period (13 s before the time of maximum velocity and 13 s after the time of maximum velocity) which is most relative to the peak velocity period. The modelled position of maximum velocity relative to the central point of the downdraft on the ground surface is located at x=2780 m, y=75 m.

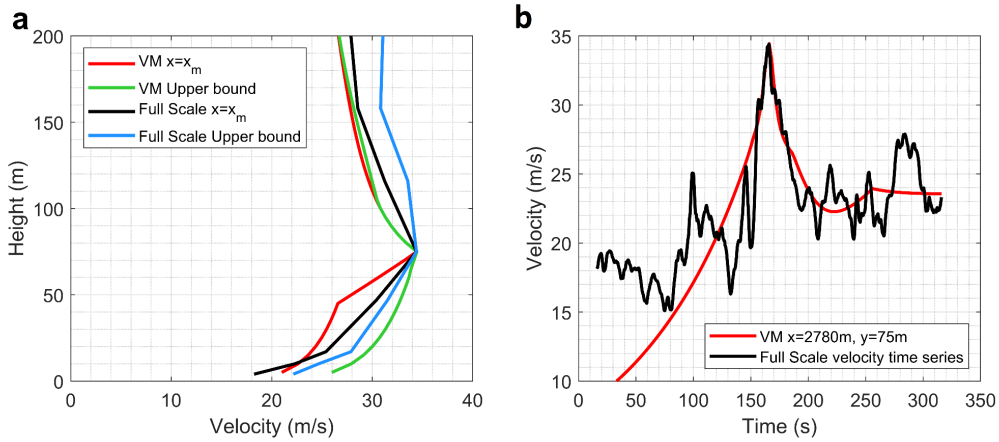


Figure 3-10. Velocity profiles comparison for case six: (a) Vertical distribution of horizontal velocity profiles of horizontal winds; (b) Velocity time series for the position of maximum velocity. "VM" represents the vortex model. x_m represents the radial position when the maximum velocity occurs.

3.2.7 Discussion

The initial velocity time-series obtained from the simulated results (shown in red line in Figure 3-7 (b), 3-8 (b), 3-9 (b) and 3-10 (b)) all start from relatively low values. The reason for this is associated with the position of the vortices, i.e. at the initial stage, the primary vortex in vortex model starts from the edge of the downdraft, and the influence of this on the position of maximum velocity (up to 5050 m) is relatively small. However, the high initial velocity time-series from vortex model for case 2 (Figure 3-5 (b)) is due to the short distance (1400 m) between the edge of downdraft and the position of maximum velocity; therefore, the influence of the combination of the flow fields on the position of maximum velocity at the initial stage is high. The high initial velocity of the primary vortex in the vortex model is due to the primary vortex produced aloft caused by the shear layer between the downdraft flow and surrounding static flow.

The normalised radial velocity profiles are shown in Figure 3-11, which displays that the modelled data cannot correctly represent the overall tendency of the velocity profile along the radial distance from the centre of the downdraft. The reason for this is due to the outflow in this model arranged for the whole domain and the velocity of outflow increases with time. At the time point of maximum velocity, the outflow almost reaches its maximum velocity for the whole domain. The vortex model does not consider the outflow variance with the radial distance. However, the radial velocities near the position of peak velocities (at around r/r_{max}= 1) exhibit a similar trend as the 26 JAWS full-scale downburst data, which exemplifies that the vortex model can accurately estimate the radial velocity profile near the position of peak values. Summarised correlation coefficients for the comparison for six sets of data are shown in Table 3-4. The correlation coefficients of the upper bound velocity profiles and the $x = x_m$ velocity

profiles relative to the mean values of the velocity profiles for case two to six display a good match between the vortex model and full-scale downburst data.

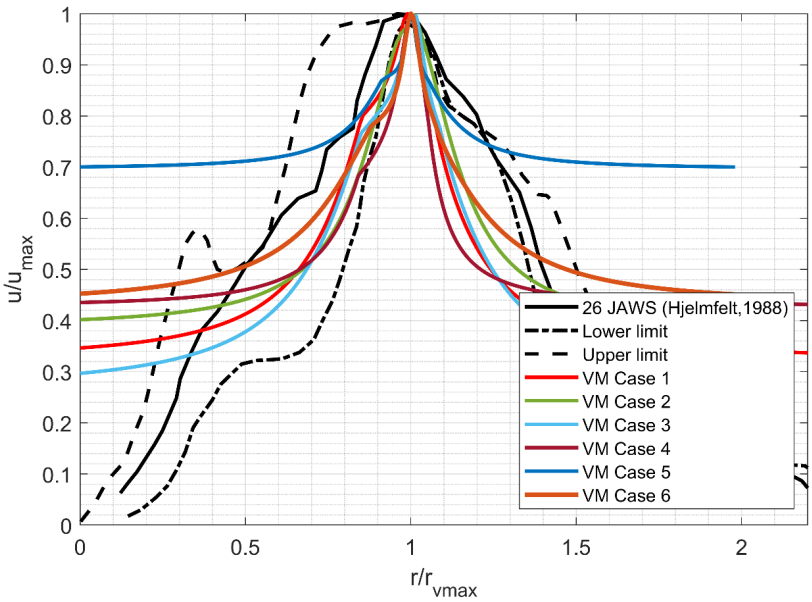


Figure 3-11. Profiles of normalised radial velocity along azimuth of maximum velocity and scaled radius from microburst centre at $t=t_m$. t_m is the time when the maximum velocity occurs. Velocity is normalised to the maximum velocity (u_{max}). Radius is scaled to the radius of the maximum velocity (r_{vmax}).

Summarised estimated data from the vortex model are compared with the 26 JAWS events microburst characteristics (Table 3-8). All the maximum velocities are within the range of the 26 JAWS events limits, and only the height of maximum velocity for case 1 and case 6 is in the range of microburst characteristics. The heights of maximum velocity for case 3, case 4 and case 5 are higher than the upper limit of microburst characteristics which may lead to the scales of the microburst larger than the limit of microburst characteristics. The diameter of the downdraft for these simulations is 1.8 km which may cause a small difference for the diameters between maximum velocity and leading edges of the microburst, and the scale of the downdraft diameter of microburst characteristics changes from 1.2 km to 3.1 km. The distance between maximum velocities for case 5 is quite high (up to 10.1 km) since when the circulation of the

secondary vortex reaches the maximum value, the velocity has not reached peak velocity. The leading edge of the microburst for case 5 is 27.63 km, triple of the upper limit of microburst characteristics and the reason for this is due to the long decay period.

Table 3-8. Comparison with microburst characteristics.

	Lower limit	Microburst characteristics (average)	Upper limit	Case 1 26 JAWS events	Case 2 0619, 2003	Case 3 0521, 2008	Case 4 0619, 2008	Case 5 0813, 2008	Case 6 0308, 2010
Maximum velocity (m/s)	12	24	42	23.98	24.47	30.75	28.33	26.28	34.44
Height of maximum velocity(m)	50	80	100	80	4	158	158	116	75
Distance between maximum velocity (km)	2	3.1	7	3.9	2.8	7.28	5.28	10.1	5.56
Depth of maximum (km)	0.3	0.7	1.2	0.7	0.268	1.76	0.96	1.46	1.38
Leading edges of the microburst (km)	2.7	5.4	9	5	4.28	18	7.56	27.63	12.89
Initial velocity (m/s)	4	9	16	9	10.9	14.48	18.84	9.69	18.7
Decay velocity (m/s)	6	12	27	12	14.3	13.13	19.70	18.30	23.8
Average total period (minute)	4:47	13:13	27:37	5:00	1:40	14:10	4:10	13:36	5:00
Time for reaching maximum	1:16	5:00	12:46	2:35	0:50	7:05	3:08	3:50	2:30
Time for decay	2:00	8:13	16:23	2:25	0:50	7:05	1:02	9:46	2:30

3.3 Summary

The vertical distribution of horizontal velocity profiles and the time series for the position of the maximum velocity can be estimated from the vortex model correctly for a single microburst event. The correlation coefficients of the velocity time series can reach up to 0.94 for four of six cases. Furthermore, the radial velocities along the radial distance can be estimated by the vortex model to some extent for the radial distance range near the radial position of maximum velocity. According to the comparisons of the velocity profiles, the vortex model can be

improved in further work. i.e. Comparisons of the normalised velocity w.r.t. scaled radius from the vortex model are different from the microburst characteristics. The radial velocity profile near the peak velocity is narrower than the velocity profile from full-scale data, and the velocity profile near the centre of the downdraft and far away from the downdraft should be lower. The further work for this point is that the variation of the outflow velocity profile along the radial of the centre of downdraft can be added. An approximately linear relationship of the radial velocity with the variation of the radial distance as suggested in Holmes and Oliver (2000) and other shape functions for the radial velocity profile along the radial distance mentioned in Abd-Elaal et al. (2013), which can be considered as a reference.

Chapter 4 Results and discussion of downburst wind loading on generic buildings

This chapter applies the combination of QS theory and concepts from the PTS method to estimate the downburst wind loading on generic building shapes, which includes three parts, i.e. the results from WT experiments (built up in Section 2.2) for obtaining the database of pressure coefficients from a range of azimuthal angles, elevation angles and turbulence intensities as discussed in Section 4.1, a preliminary validation of this technique combining the velocity and pressure time series from UoB-TWS as analysed in Section 4.2, and key findings as summarised in Section 4.3.

4.1 UoB-WT experiments for the database of pressure coefficients

The results from wind tunnel experiments undertaken in this research to evaluate the aerodynamic properties of downburst wind loads on buildings are detailed in this section based on the setup and methodology of the WT experiments detailed in Section 2.2. As such, this section contains five sections: normalised peak pressure coefficients from design codes and ABL data recorded by Richards and Hoxey (2012a), individual point analysis and area analysis of the pressure coefficient database (listed in Appendix A of this thesis) for two generic building models obtained from the experiments separately. A standard, linear wind tunnel of the University of Birmingham had been adopted to obtain the pressure coefficient database. These

experiments used building models supported on an angled stand, along with a passive turbulence generator, to obtain the required pressure coefficient data. The design of the passive turbulence generator is described in Section 2.2.4. In order to compare the pressure coefficient database with the previous research work, the peak pressure coefficients from design codes and ABL recorded data have been normalised as discussed in Section 4.1.1. TS downbursts are one type of non-stationary wind events over a relatively short period of time, and therefore the individual point analysis in Section 4.1.2 for cube building model and Section 4.1.3 for portal framed building is crucial to understand the pressure fluctuations on the roof of the building models. The area analysis of the pressure coefficient database in Section 4.1.4 for cube building model and Section 4.1.5 for portal framed building model can better evaluate the coherent structures generated by the downburst events on the roof of the buildings. Additionally, Section 4.1.2 concentrates on the analysis of pressure coefficients obtained from the wind tunnel experiments for different points on the roof of the cube building model. Both mean pressure coefficients and peak pressure coefficients are analysed.

4.1.1 Normalised peak pressure coefficient

The normalised peak pressure coefficients from design codes and previous study for ABL are analysed in this section. The building roofs have been divided into eight parts (Figure 4-1). A1, A2 and A3 correspond to roof edge regions and A6 corresponds to a central roof region as defined in Eurocode (2010). A4 and A5 are the roof edge regions defined in ASCE7 (2013). A7 and A8 have been selected to show the characteristics of the region where flow reattachment is likely to occur.

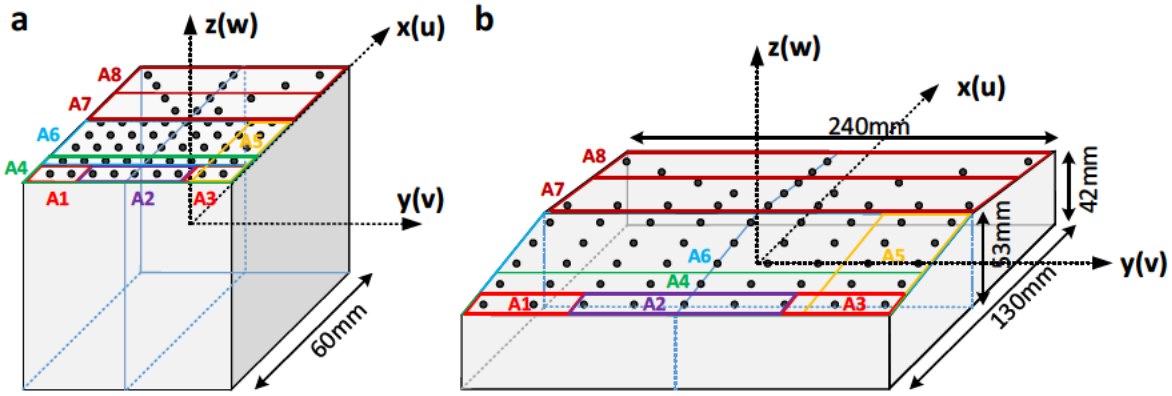


Figure 4-1. The dividing areas on the roof.

According to Eq. (2.2), the mean value of the longitudinal velocity time series measured from wind tunnel experiments has been adopted as the reference velocity for the pressure coefficients database. The differential pressure $(p - p_{ref})$ is measured by the DPMS directly. Considering the fluctuating pressures induced by the wind velocity with different turbulence intensities, both mean and peak pressures (defined in Eq. (4.1)) are adopted for the analysis of database. However, considering the non-stationary time series of TS downburst events, the database for the peak pressure coefficients based on the peak pressures will be adopted for the application of the methodology outlined in Section 1.4.4. The peak pressure for the database is defined in Eq. (4.1) and the peak pressure coefficient with mean azimuthal angle, mean elevation angle and specific turbulence intensity is defined in Eq. (4.2).

$$\hat{p} = \langle \hat{p}_{sub}(\theta, \beta) \rangle_{mean} \tag{4.1}$$

where $\hat{p}_{sub}$ represents the peak pressure in each subinterval and $<>_{mean}$ denotes the mean value of all subintervals. Data was sampled for a 40 s time period for each experimental run, which has been found to be stationary on the basis that the mean and standard deviation of the pressure have both converged after this time (Figure 4-2), and the sample time is divided into

ten subintervals as each subinterval has a representative peak value based on the pressure time series.

$$\hat{C}_p(\bar{\theta}, \overline{\beta}, I) = \frac{\hat{p}}{0.5\rho U^2} \tag{4.2}$$

$\overline{U}$ is the mean velocity and is summarised in Table 2-1. The mean pressure coefficient is defined in Eq. (4.3).

$$\bar{C}_p(\bar{\theta}, \overline{\beta}, I) = \frac{p}{0.5\rho U^2} \tag{4.3}$$

where $\bar{p}$ is the average value from the pressure history directly which henceforth is defined as mean pressure. $\overline{U}$ is the mean velocity and is summarised in Table 2-1.

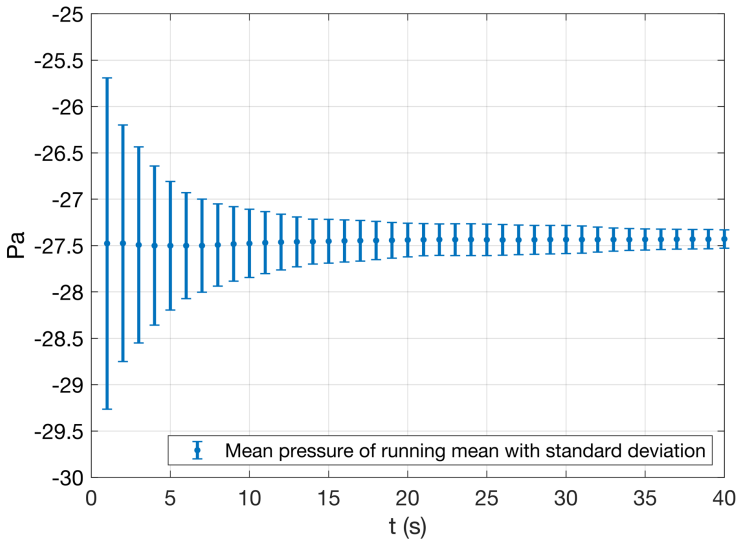


Figure 4-2. Mean and standard deviation of pressure for subsets of measurements spanning the range (A.M.S., 2018) at 45° azimuth, 0° elevation angle, TI=19.4% (TI5).

In order to compare the wind tunnel database with ABL data from Eurocode (2010), the normalised dynamic pressures are needed. In the wind tunnel database, the mean dynamic pressures are adopted based on the mean reference velocities. However, the pressure (Eurocode)

or pressure coefficient (ASCE) from the design codes (Eurocode and ASCE) are based on the peak dynamic pressures.

The peak dynamic pressure provided by Eurocode (2010) is equal to the exposure factor (see Figure C-1 in Appendix C from this thesis) multiplying the mean dynamic pressure. The mean dynamic pressure is based on the mean velocity at 10 m height for 10 minutes. As for the terrain category II (see Table D-1 of this thesis), the roughness length is 0.05 m, and the calculated turbulence intensity is 19% ($1/\mathrm{In}(z/z_0)$). The ratio of the peak dynamic pressure to mean dynamic pressure is 2.35 in terrain category II (see Figure D-1 of this thesis). The recommended air density is 1.25 kg/m^3.

In ASCE7 (2013), the peak dynamic pressure is based on 3-second gust speed at 10 m (33ft) above the ground in Exposure C (flat open country, grasslands, and all water surfaces in hurricane-prone regions) (see Table B-1, Appendix B of this thesis). The mean hourly wind speed at 10 m height in exposure C is equal to 0.65×3-second gust speed (detailed in ASCE7 (2013) 6.5.8, 0.65 is the mean hourly wind speed factor). Therefore, the calculated ratio of the peak dynamic pressure to mean dynamic pressure is 2.37. The design pressure is measured in exposure B at 9.1 m (30 ft) height above the ground. The adjustment factor for pressures with variable building heights and exposure categories for the corresponding surface roughness C at 10 m height is 1.43 (see Table B-2, Appendix B of this thesis). The summarised peak pressure coefficients from the standards are shown in Table 4-1. The turbulence intensity for exposure C at 10 m height is 20% ($0.2 \times (33/\bar{z})^{1/6}$ ($\bar{z}$ is in feet), 0.2 is the turbulence intensity factor depending on the exposure category; $\bar{z}$ represents the measured height in this case). The applied air density is 1.204 kg/m^3.

The peak pressure coefficients summarised in Table 4-1 are defined in Eq. (4.4) and Eq. (4.5) from Eurocode 1-4 and in Eq. (4.6) and Eq. (4.7) from ASCE7 (2013) based on mean dynamic pressure and peak dynamic pressure respectively.

$$\hat{C}_p = c_e(z) \times C_{pe} \tag{4.4}$$

where C_{pe} is the external pressure coefficient from Eurocode 1-4. $c_e(z)$ is the exposure factor with variable heights (see Figure C-1 of Appendix C in this thesis).

$$\hat{C}_p = C_{pe} \tag{4.5}$$

$$\hat{C}_p = \frac{p_{10m}}{0.5\rho {u_{hourly,10m}}^2} \tag{4.6}$$

$$\hat{C}_p = \frac{p_{10m}}{0.5\rho {u_{3s,gust,10m}}^2} \tag{4.7}$$

where $u_{3s,gust,10m}$ is the 3-second gust speed at 10-meter height. $\bar{u}_{hourly,10m}$ is the mean velocity in one hour at 10-meter height. The wind speed is assumed to come from any horizontal direction.

Table 4-1. Corresponded peak pressure coefficients calculated from design codes.

	Eurocode1-4			ASCE standard (<18.3 m (60 ft))		
	Areas	Based on Mean dynamic pressure	Based on peak dynamic pressure	Areas	Based on mean dynamic pressure	Based on peak dynamic pressure
Cube building Roof	A1, A3	-4.3	-1.8	A4	-2.8	-1.2
	A2	-2.9	-1.2	A5	-2.8	-1.2
	A6	-1.7	-0.7	A7, A8	-2.1	-0.9
	A7, A8	+-0.5	+-0.2			
Portal building roof (11.3°)	A1, A3	-3.6, +0.5	-1.5, +0.2	A4	-2.8	-1.2
	A2	-3.1, +0.5	-1.3, +0.2	A5	-2.8	-1.2
	A6	-1.7, +0.5	-0.7, +0.2	A7, A8	-2.1	-0.9
	A7	-2.2, +0.3	-0.9, +0.1			
	A8	-1.5, +0	-0.6, +0			

Richards and Hoxey (2012a) recommended the factor 3 as the ratio of the peak dynamic pressure to mean dynamic pressure since the average value for the ratio of the peak dynamic pressure to mean dynamic pressure from the recorded data is 3. However, this factor contains the considerations of the varying azimuthal angles and different measured positions (front surface and roof) on the cube building which lead to larger factor, 3, compared with the factors from standard code, 2.35 or 2.37. The peak instantaneous pressure and peak instantaneous peak velocity are the single most extreme value observed during the 12-minute period (Richards and Hoxey, 2012a). The turbulence intensity at roof height is 19% to 20% in the case of Richards and Hoxey (2012a). The mean pressure coefficients and peak pressure coefficients (based on mean and peak dynamic pressure) measured by Richards and Hoxey (2012a) near the roof edge on the streamwise central line of the roof are summarised in Table 4-2.

Table 4-2. Pressure coefficients with varying azimuthal angles for tap V7 (Richards and Hoxey, 2012a).

Azimuth (°)	90	75	60	45	30	15	0
C_p	-0.65	-0.84	-1.38	-1.55	-1.23	-1.01	-1.02
$\hat{C}_{p,peak\ dynamic\ pressure}$	-1.09	-1.36	-1.82	-1.9	-1.49	-1.2	-1.17
$\hat{C}_{p,mean\ dynamic\ pressure}$	-3.27	-4.08	-5.46	-5.7	-4.47	-3.6	-3.51

4.1.2 Individual point on cube building model

Results are presented from points P51, P71, P91 (roof edges), P73 (central region of the roof), P55 and P95 (roof centre line; P95 lies on edges as well) (see Figure 4-3). The separation region near the edges on the roof can produce large suction pressure which might lead to damage to the roof, and points P51, P71, P91 and P95 illustrate the dominant features in separation regions on the roof. P73 and P55 illustrate the main features on the centre of the roof, allowing comparison with the points near the edges.

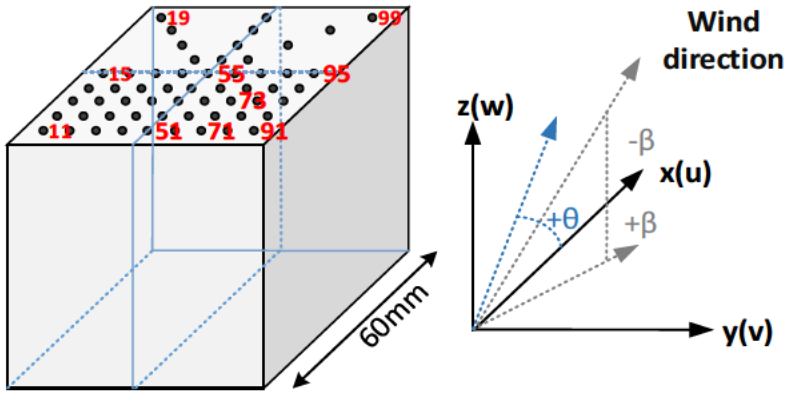


Figure 4-3. The points on the roof for cube building model (axis origin is in the centre of the building but shifted for clarity).

The effect of varying turbulence intensity on the mean pressure coefficient for each elevation angle with 0° azimuthal angle is not obvious (Figure 4-4). For the negative elevation angles of magnitude greater than 15° (e.g. -30°, elevation angles are defined in Figure 2-2), the mean pressure coefficients are near zero. As the elevation angle increases from -30° to around 15°, the mean pressure coefficients decrease to the minimum values due to the flow separation on the roof. With the increasing elevation angles varying from around 0° to 60°, the mean pressure coefficients increase from -1.5 to around 1 resulting from the wind flow changing from flow separation to the wind impinging on the roof. The minimum mean pressure coefficients on P91, P71 and P51 are around -1.8, -1.5, -1.4 respectively which are quite similar with the design pressure coefficients in Eurocode (2010), -1.8, -1.2, -1.2 respectively.

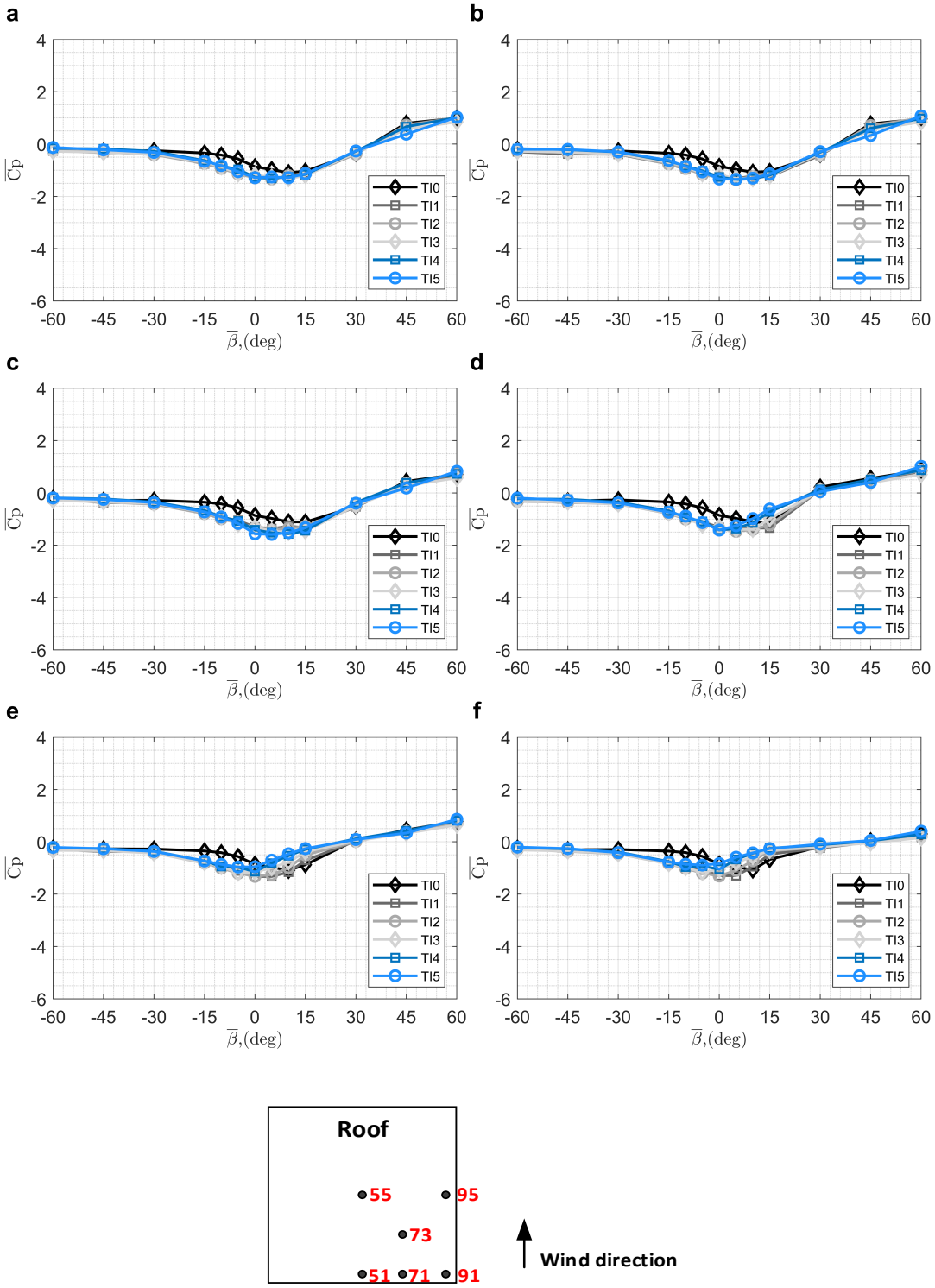


Figure 4-4. Mean pressure coefficients with six different turbulence intensities (TI) for cube building at locations: (a) P51, (b) P71, (c) P91, (d) P73, (e) P55, (f) P95, with variable elevation angles when the azimuthal angle is zero degrees (TI0=1.7%; TI1=3.9%; TI2=6.6%; TI3=10.9%; TI4=14.8%; TI5=19.4%).

The corresponding variation of peak pressure coefficients with turbulence intensity when the azimuthal angles are at 0° are shown in Figure 4-5. A distinct pattern of increasing magnitude of peak pressure coefficients with increasing turbulence intensity changing from 1.7% (TI0) to 19.4% (TI5) is evident, which is consistent with the results from the ABL wind tunnel experiments carried out by Fernández-Cabán and Masters (2018). For the separation regions on the roof, with the increasing of turbulence intensity (7.9% to 21.1%) at eave height, the magnitude of peak pressure coefficients increases (-3 to -6) near the edge of the roof (Fernández-Cabán and Masters, 2018). The minimum pressure coefficients occur at P91 when the elevation angle is around 0° to 15° with zero-degree azimuthal angle. For all positions, there is an apparent increase in the magnitude of the pressure coefficients as the elevation angles change from -30° to 15°. At the edges of the roof (P51, P71 and P91), the magnitude of the negative C_p reduces as the elevation angle increases from approximately 15° until at elevation angles greater than about 40°, and the pressure coefficients switch from negative pressures to positive pressures. A similar phenomenon is seen for the central region (P73, P55 and P95) when the elevation angle is over 0°, though the increase of pressure coefficients starts for lower elevation angles. The maximum peak suction pressure coefficients on P91, P71 and P51 are around -4, -3.2, -3.2 respectively which are quite close to the normalised peak pressure coefficients in Eurocode (2010), -4.3, -2.9, -2.9 respectively (Table 4-1) as the turbulence intensity is 19.4% (TI5) in wind tunnel (WT) database and 18.9% in Eurocode for terrain category II. However, the magnitudes of peak pressure coefficients for these points are larger than the peak pressure coefficient in ASCE, -2.8, with turbulence intensity (20%) for exposure C at 10 m height.

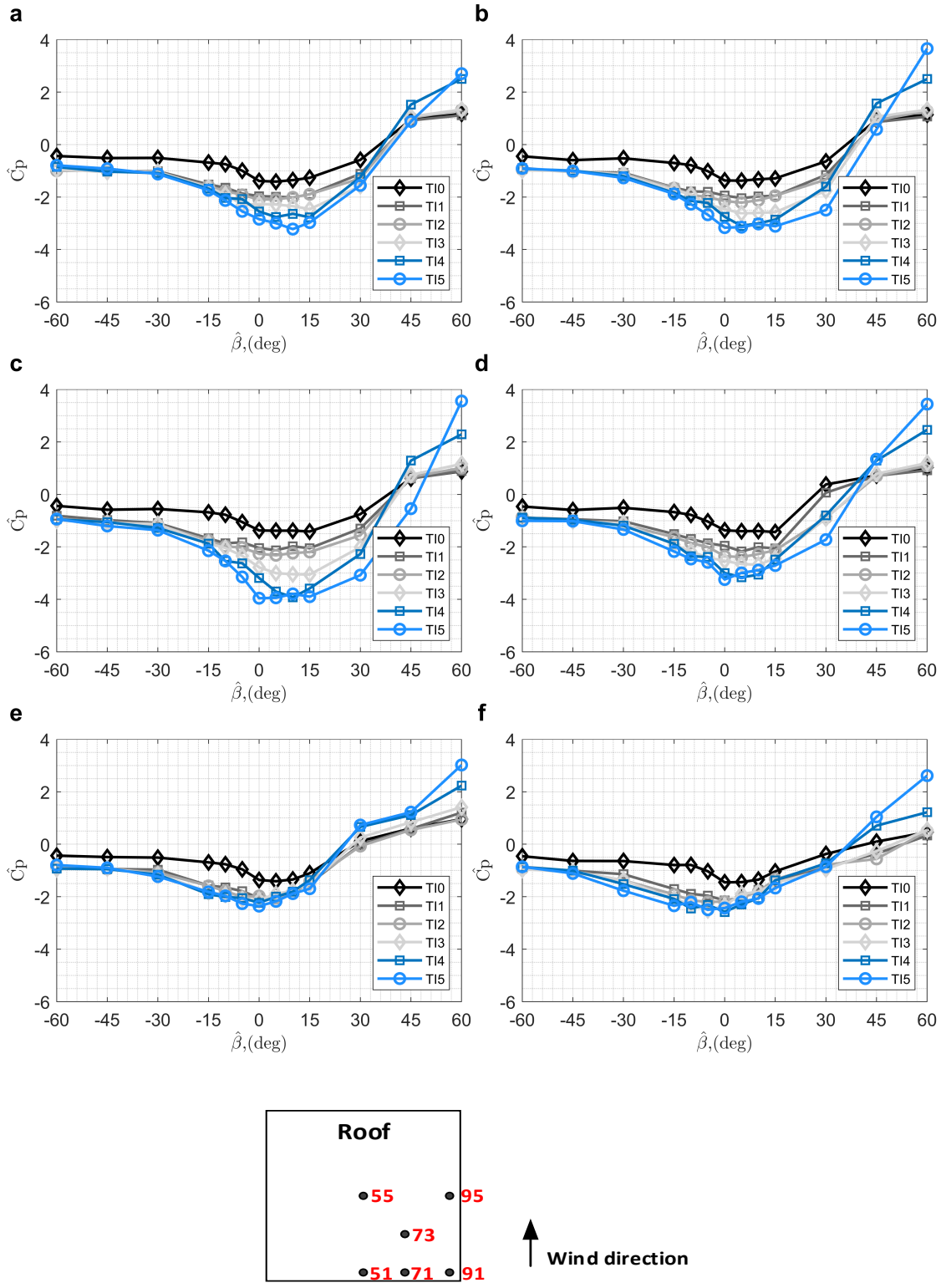


Figure 4-5. Peak pressure coefficients with six different turbulence intensities for cube building at locations: (a) P51, (b) P71, (c) P91, (d) P73, (e) P55, (f) P95, with variable elevation angles when the azimuthal angle is zero degrees (TI0=1.7%; TI1=3.9%; TI2=6.6%; TI3=10.9%; TI4=14.8%; TI5=19.4%).

4.1.3 Individual point on portal framed building model

The point positions on the portal building model are shown in Figure 4-6. With the increasing levels of turbulence intensities, Figure 4-7 shows an increasing magnitude of the fluctuating peak pressure coefficients. With the increase of elevation angles (>30°), the pressures change from negative to positive. The peak negative pressure coefficients for P51, P71 and P91 (Figure 4-6) are -4, -4, -4.4 respectively and the corresponding peak pressure coefficients for these positions from ABL in Eurocode (2010) are -3.1, -3.1, -3.6 respectively and the relative higher values (<23% of difference value) from WT experiments may partially due to the higher TI (19.8% (TI5) from WT database and 18.9% from Eurocode). Additionally, the elevation angles within the range of -15° to 15° are also obviously affected by the increase of turbulence intensities for all positions. The pressure coefficients for P51 are constant when the elevation angles vary from -60° to approximately 10° at TI0 (Figure 4-7 (a)). However, the magnitude of pressure coefficients starts to increase when the elevation angle exceeds approximately -15° at TI5, which demonstrates that higher turbulence intensity can lead to greater magnitude of peak C_p starting from lower elevation angles.

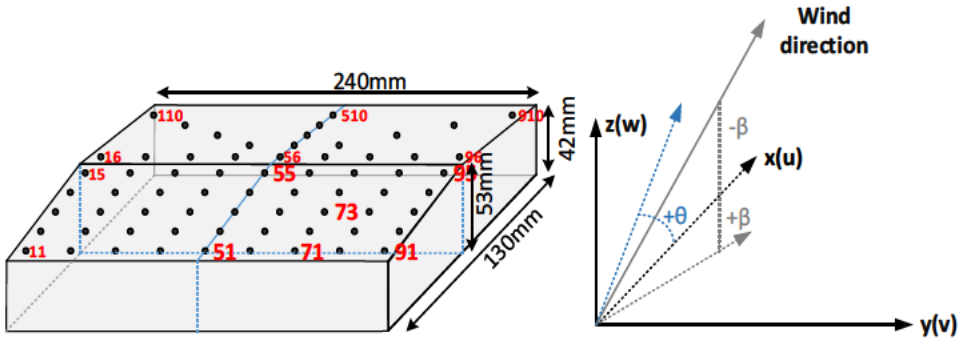


Figure 4-6. The points on the roof for the portal building model and axis definition (axis origin is in the centre of the building but shifted for clarity).

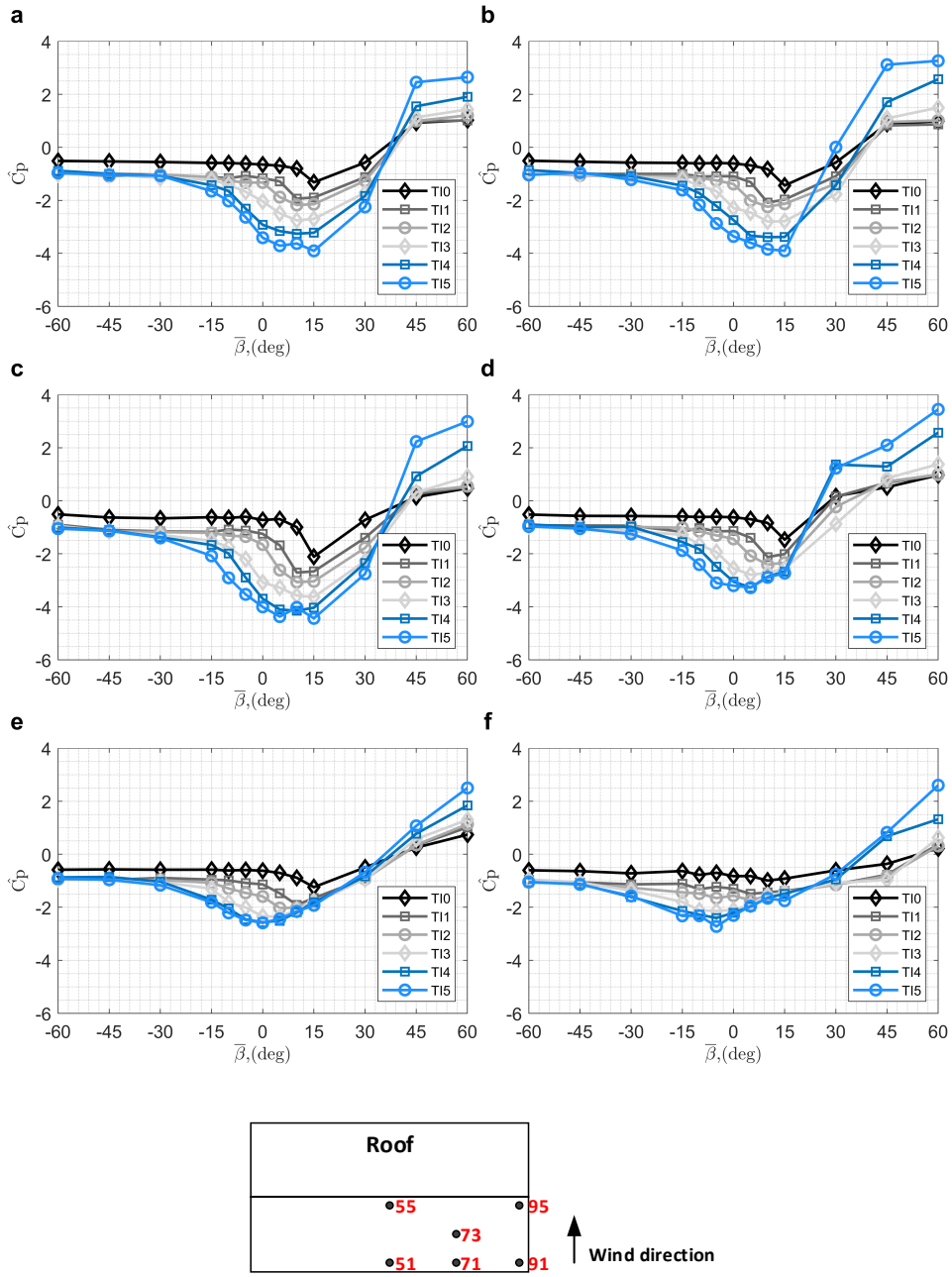


Figure 4-7. Peak pressure coefficients with six different turbulence intensities for portal building at locations: (a) P51, (b) P71, (c) P91, (d) P73, (e) P55, (f) P95, with variable elevation angles when the azimuthal angle is zero degrees (TI0=1.6%; TI1=3.8%; TI2=6.4%; TI3=11.3%; TI4=15.3%; TI5=19.8%).

4.1.4 Separate areas on cube building model

This section focuses on the analysis of area-mean pressure coefficients obtained from the wind tunnel experiments for different areas calculated using all of the pressure tappings on each area

of the roof of the cube and portal buildings, e.g. the pressure on A1 in Figure 4-8 is equal to $(p_{11} \times A_{11} + p_{21} \times A_{21})/A_1$. p_{11} and p_{12} are the pressures on tapping 11 and tapping 21 respectively; A_{11} and A_{21} are the areas represented by tapping 11 and tapping 21 respectively). The defined areas are illustrated in Figure 4-8 for cube building and Figure 4-10 for portal framed building (same as Figure 4-1).

The magnitude of C_p shows an apparent increase with increasing turbulence intensity for A1, A2, A3, A4, A5 and A6 though the influence of the turbulence intensity is small on the reattachment regions (A7 and A8) (Figure 4-9). The maximum magnitude of peak pressure coefficients happens when the elevation angles are between 0° and 15° for separation regions (A1, A2, A3, A4, A5 and A6), which is the same as the results of the points analysis on the roof (Figure 4-5). The maximum negative pressure coefficients occur at the corner edges on the roof (A1 and A3) due to the vortices near the edges (Figure 4-9 (a) and Figure 4-9 (c)). The maximum magnitude of peak pressure coefficients on A1, A2, A3 and A6 are -4.2, -3.2, -3.9 and -3 respectively with the turbulence intensity at 19.4% (TI) which are approximately similar to the peak pressure coefficients in Eurocode (2010), -4.3, -2.9, -4.3 and -1.7 respectively with the turbulence intensity at 18.9%, excluding 43% difference for A6 nevertheless more conservative values from WT database. The maximum negative pressure coefficients on A4 and A5 are -3.5 and -3.2 respectively, and the corresponding normalised peak pressure coefficients on A4 and A5 from ASCE7 (2013) are -2.8 and -2.8 (<20% difference) with turbulence intensity at 20% for exposure C, which illustrates that the peak pressure coefficients from WT database are more conservative for the design.

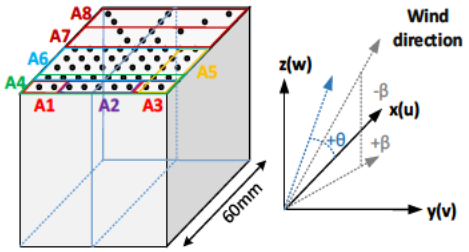


Figure 4-8. The layout of the areas on the roof for cube building model (axes shifted for clarity; origin is in the centre of the building).

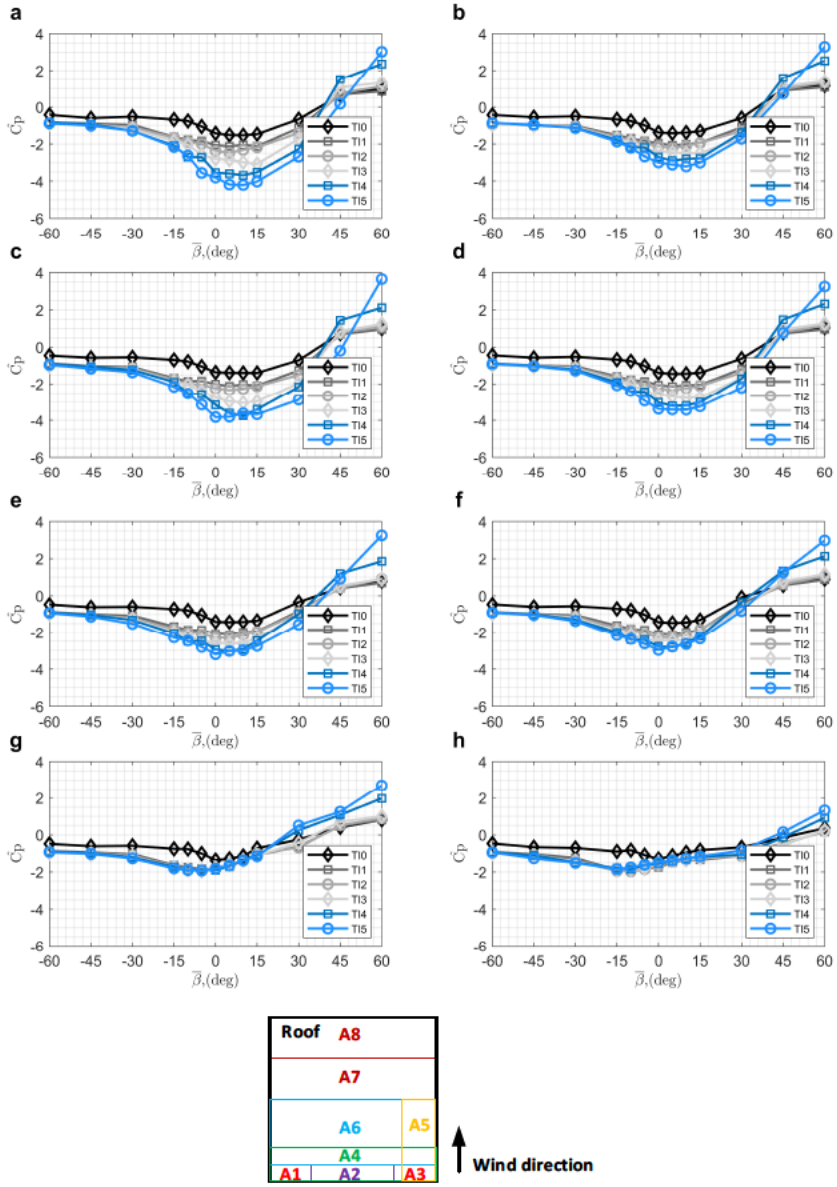


Figure 4-9. Peak pressure coefficients for cube building with six different turbulence intensities at locations: (a) A1, (b) A2, (c) A3, (d) A4, (e) A5, (f) A6, (g) A7, (h) A8, with variable elevation angles when the azimuthal angle is zero degrees (TI0=1.7%; TI1=3.9%; TI2=6.6%; TI3=10.9%; TI4=14.8%; TI5=19.4%).

4.1.5 Separate areas on portal framed building model

The same method of dividing the roof areas is presented in Figure 4-10. With increasing turbulence intensity, a clear trend of increasing magnitude of peak pressure coefficients is evident for 0 ° azimuthal angles (Figure 4-11). The maximum negative peak pressure coefficients at the front edges (A1, A2 and A3) on the roof happen when the elevation angle is between 0° and 15° (Figure 4-11 (a), (b) and (c)). As the elevation angle increases beyond 30° the pressures change from negative to positive. When the elevation angle is over 45°, the horizontal flow is divided into two directions at the edge line between the roof and front surface, and the effect of flow separation becomes weak. The maximum negative pressure coefficients for A1, A2, A3 and A6 are -5, -3.8, -4.1, -3.1 respectively with turbulence intensity at 19.8% (TI5) and the corresponding peak pressure coefficients for these positions from ABL Eurocode (2010) are -3.6, -3.1, -3.6 and -1.7 respectively with turbulence intensity at 18.9% for terrain category II, where the difference in value can reach up to 45% for A6, though the data from WT database demonstrates a more reliable tendency for design. The maximum negative pressure coefficients from the WT database for A4 and A5 are -3.9 and -3.1 respectively, and normalised peak pressure coefficients from ASCE7 (2013) for these positions are -2.8 and -2.8 with turbulence intensity at 20% for exposure C which are slightly smaller (<28% difference) than WT database values, though the WT database data is certified to be more conservative for the design once more. Furthermore, the elevation angles within the range of -15° to 15° are more apparently affected by the increase of turbulence intensity. The pressure coefficients for A1 remain constant as the elevation angles vary from -60° to approximately 10° at TI0 (Figure 4-11 (a)) while the magnitude of the pressure coefficients starts to increase when the elevation angle is greater than approximately -15° at 19.8% (TI5), matching the points analysis in Section

4.1.3. Therefore, large magnitude of C_p values is caused by the combination of elevation angle and turbulence intensity.

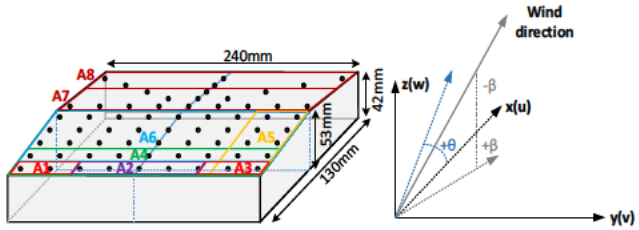


Figure 4-10. The layout of the areas on the roof for portal building model (axes shifted for clarity; origin is in the centre of the building).

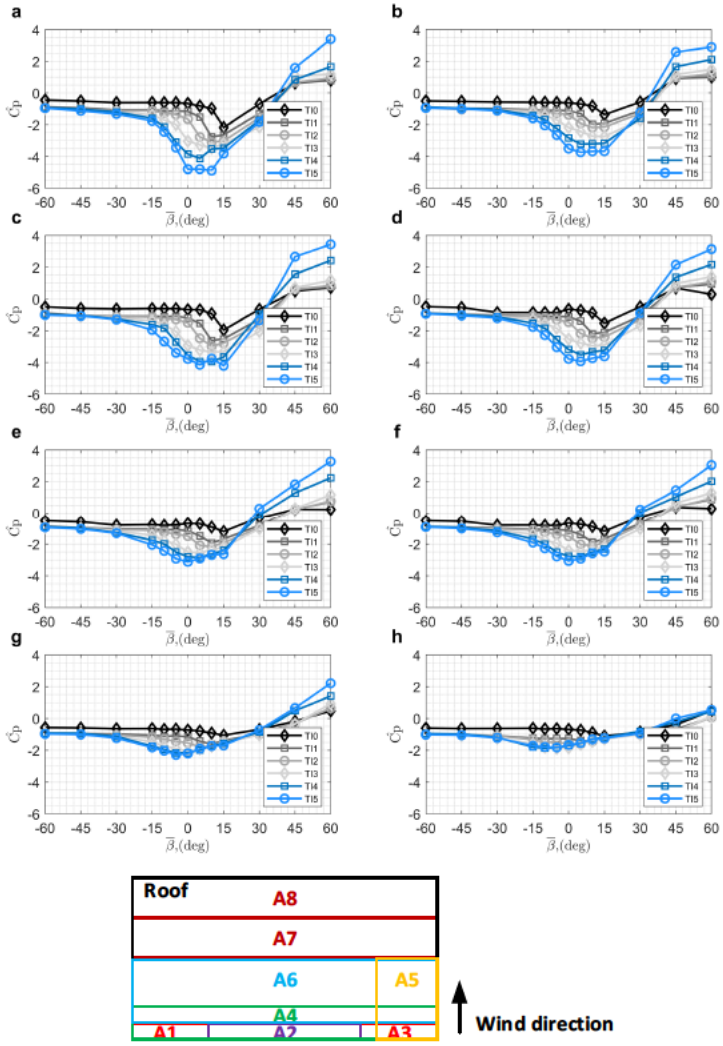


Figure 4-11. Peak pressure coefficients for portal building with six different turbulence intensities at locations: (a) A1, (b) A2, (c) A3, (d) A4, (e) A5, (f) A6, (g) A7, (h) A8, with variable elevation angles when the azimuthal angle is zero degrees (TI0=1.6%; TI1=3.8%; TI2=6.4%; TI3=11.3%; TI4=15.3%; TI5=19.8%).

4.2 Preliminary validation

This section is divided into five parts, the data analysis for non-stationary time series, the individual point validation and the area validation. Section 4.2.1 is concerned with the application of wavelet analysis in order to obtain the turbulence intensity time series from the TWS velocity time-series and employs the 5×H integral length scale limit as recommended by Wu and Kopp (2018). Section 4.2.2 and 4.2.3 are related to the analysis of the cube and portal frame buildings separately using the method proposed by Jesson et al. (2019) and outlined in Section 1.4.4, i.e. a combination of quasi-steady (QS) theory and partial turbulence simulation (PTS) concepts are combined to estimate the wind loading on the aforementioned structures arising from a microburst. Six representative points on the roof of the building models have been chosen to compare the predicted pressure time series with the TWS data. Finally, Section 4.2.4 and 4.2.5 examine the applicability of the area loading method for azimuthal angles of 0° and 45° for the cube building model and for an azimuthal angle of 0° for the portal frame building model separately. The predicted pressure time series on eight corresponding partition areas with the design codes is compared with the TWS data and analysed in Section 4.2.4 and 4.2.5.

4.2.1 Data analysis for non-stationary time series

In order to compare the pressure coefficients and pressures between the estimated time series from wind tunnel database and UoB-TWS, the pressure coefficient time series from the UoB-TWS were calculated from the experimental pressure and velocity time series and the predicted C_p time-series were constructed from the database following the process detailed in the flowchart (Figure 4-12). Ideally, the calculation of the experimental pressure coefficient

requires simultaneous measurements of velocity and pressure. However, due to experimental limitations, Jesson et al. (2015b) measured each of these separately, using different runs of the UoB-TWS. The pressure coefficient is calculated here by assuming that the pressure on the front face of the building is highly correlated with the horizontal velocity and synchronising the time-series when the velocity first reaches half of the maximum velocity and the pressure first reaches half of the maximum magnitude of pressure. This method can also reduce the errors of the non-synchronization between pressure time series and velocity time series induced by the adjacent crests for peak values of the velocity time series (see Figure 4-13). Two adjacent peak velocities occur at around 0.08 s and 0.12 s respectively, as shown in Figure 4-14, and it is not evident which should be synchronised with the peak pressure. The occurrence of these two adjacent peak velocities may be due to small-scale turbulence during the large-scale peak. Therefore, this synchronisation method, matching the time at which half of the peak value occurs, is adopted. The high-speed region is contained within a 0.4 s period, and this extract of the time-series was used for the comparison (see Figure 4-14), meanwhile an appropriate duration for the analysis of the full-scale non-stationary downburst event was 240 s suggested by many researchers (Lombardo et al., 2014) discussed in Section 1.2.2, which corresponds to a model-scale of 0.4 s.

According to the geometry, the azimuth and elevation angle time series is given by:

$$\theta(t) = tan^{-1}\left(\frac{v(t)}{u(t)}\right) \tag{4.8}$$

$$\beta(t) = tan^{-1}\left(\frac{w(t)}{\sqrt{u^2(t)+v^2(t)}}\right) \tag{4.9}$$

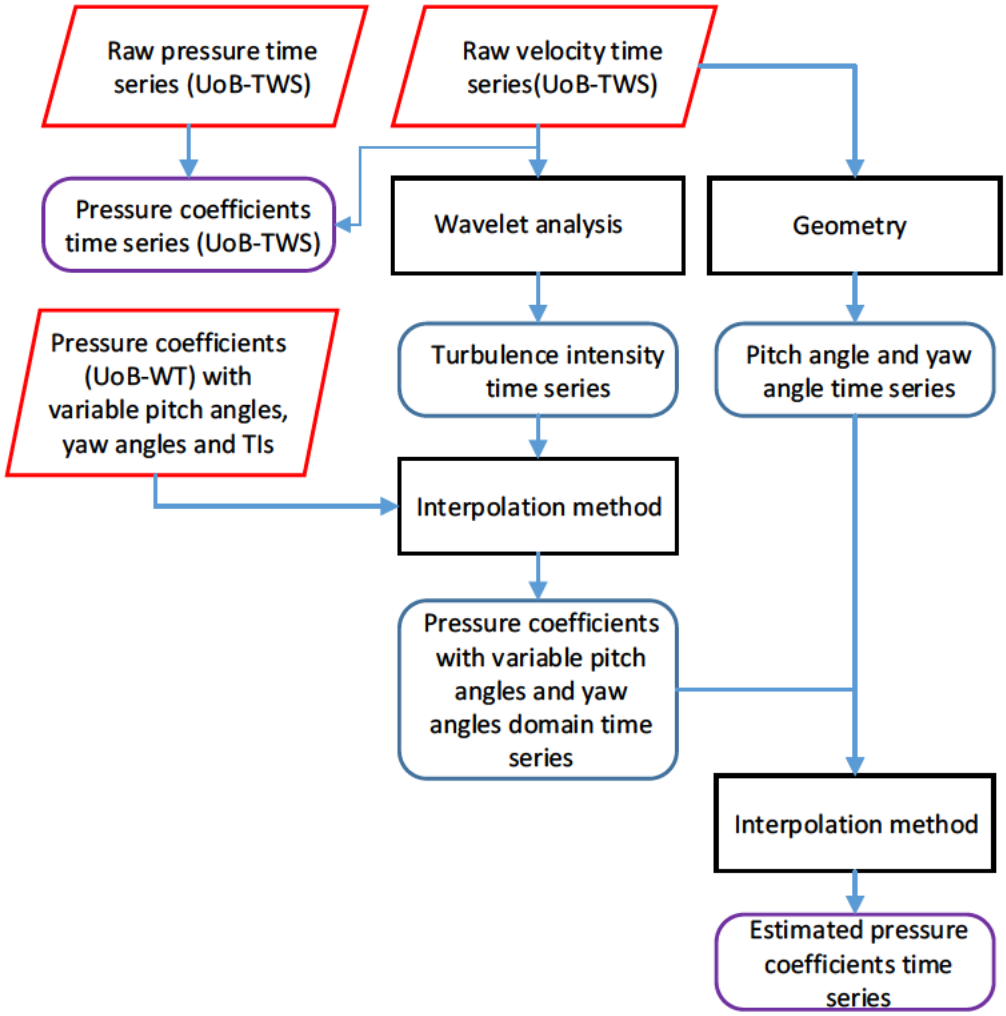


Figure 4-12. Construction of the predicted pressure coefficient time-series. Red rhombic boxes contain the inputs. Purple rectangular boxes with rounded corners contain the outputs. Black rectangular boxes and blue rectangular boxes with rounded corners are the calculation processes.

As discussed in Section 1.2.5, the wavelet decomposition and wavelet reconstruction were adopted to calculate the turbulence intensity time series of UoB-TWS, as the downburst wind is non-stationary and so traditional definitions are not valid. The velocity time series at height 60 mm (96 m full-scale equivalent) which is the roof height of the cube building model is adopted as the reference velocity in Eq. (1.48). The wavelet scales are limited by the cut-off integral length scale, 5×H where H is the height of the building. The wavelet reconstruction (inverse CWT) algorithm (Erickson, 2016; Solari et al., 2015) is applied to acquire specific ranges of the frequency components. The turbulence intensity time series through wavelet

analysis method based on the velocity time series at 60 mm height is shown in Figure 4-13. A 50-point moving average was applied to the turbulence intensity (TI) time-series, corresponding to 3 s duration (Section 1.3.2) at full-scale. The raw turbulence intensity time-series changes from 0.074% to 7.25% during the 0.4 s peak velocity period (starting from half of the peak velocity). The mean raw TI time series of the peak velocity period at 60 mm height is 1.67%. As discussed in Section 1.4.4, the range of the turbulence intensity for the full-scale downburst velocity time series based on the wavelet analysis method is around 1% to 5% for heights between 4 m and 158 m. The mean turbulence intensity (1.67%) is within the range of 1% to 5%, which demonstrates that the TI based on the wavelet analysis is a reasonable approximation of that of a full-scale event.

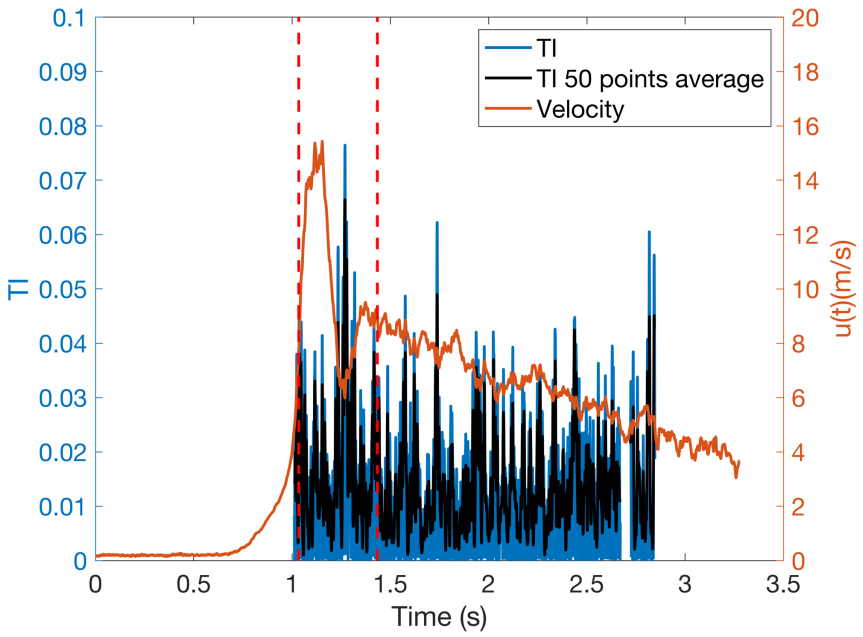


Figure 4-13. Wavelet decomposition of velocity time series at height 60 mm. Blue line is the TI time series. Orange line is the horizontal velocity time series. Black line is 50 points moving average TI time series. For clarity, TI is only shown when $u > u_{mean}$. Red dashed lines represent the 0.4s range used for comparison with full-scale data.

The detailed velocity time series and turbulence intensity time series for the 0.4 s period from 1.034 s to 1.434 s in the original time-series are shown in Figure 4-14. For clarity, the time axis

has been shifted to start at zero, and this range of 0 s to 0.4 s is used the following comparison. The database of the peak pressure coefficients is used to construct the predicted C_p time-series for the comparison, as the influence of turbulence intensity is obvious on peak pressure coefficients and peak values are more important for the non-stationary downburst events.

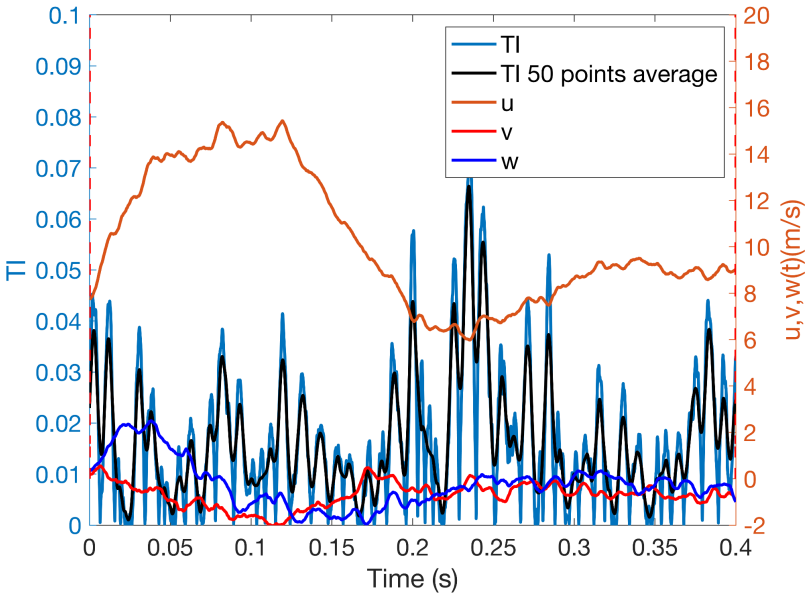


Figure 4-14. Wavelet decomposition of velocity time series at height 60mm. Blue line is the TI time series. Orange line is the horizontal velocity time series. Black line is 50 points moving average TI time series. For clarity, TI is only shown when u > u_{mean}.

When the time series of the azimuthal angles, elevation angles and turbulence intensity time series have been acquired from the analysis of the velocity time series of UoB-TWS, the estimated instantaneous pressure coefficient is defined as,

$$C_{p_{inst}}(t) = C_p(\theta(t), \beta(t), TI(t)) \tag{4.10}$$

C_p is calculated from the pressure coefficients database through interpolation method based on the azimuth, elevation angles and turbulence intensity time series calculated from the velocity time series of the UoB-TWS.

4.2.2 Cube building model - Individual point

The analysis of the velocity time series from UoB-TWS for different points is detailed in Figure 4-15. The azimuth time series and elevation angle time series (Figure 4-15 (c)) are calculated based on the velocity time series (Figure 4-15 (b)) using Eq. (4.8) and Eq. (4.9). The pressure coefficient time series (Figure 4-15 (d)) is calculated from the pressure time series and the velocity time series using Eq. (1.48). The maximum magnitude of the pressure occurs during the first 0.1 s which is the most important part for comparison, and the elevation angles during this period can reach up to 11.5°.

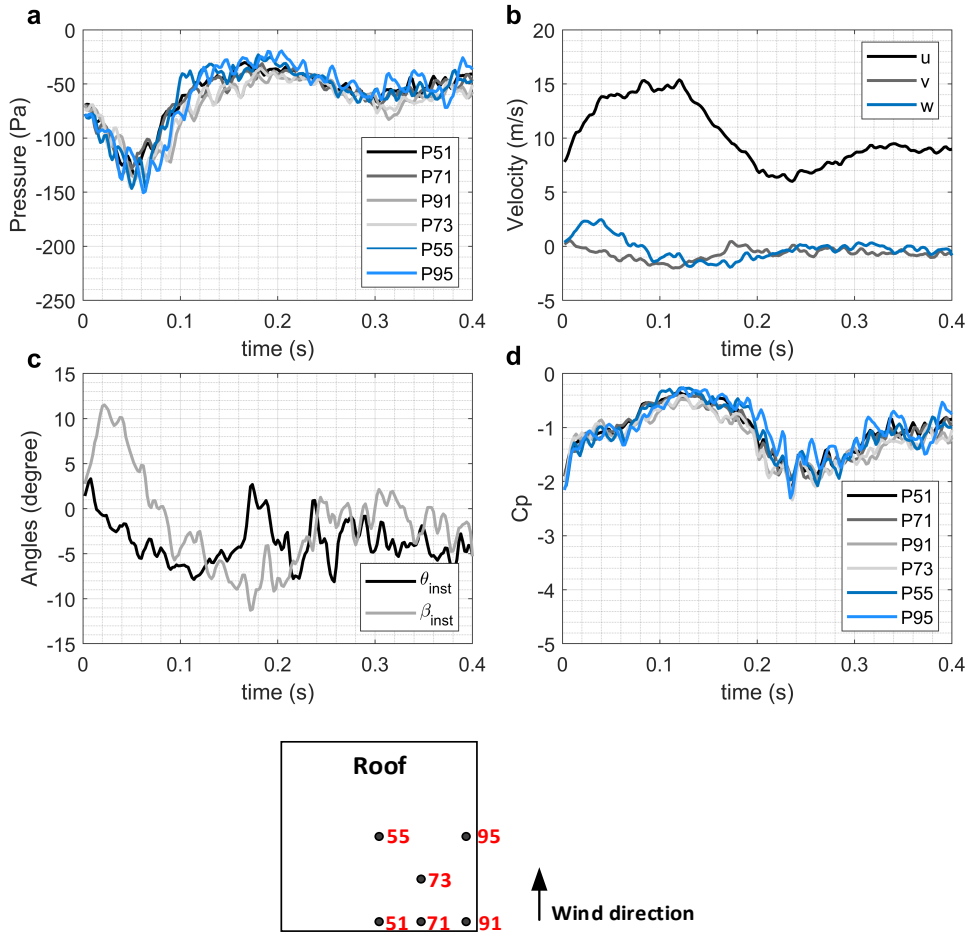


Figure 4-15. Basic information of downburst simulation for P51, P71, P91, P73, P55 and P95 on the roof of the cube building: (a) Pressures on different positions; (b) Velocity time series in three directions; (c) Variation of the angles; (d) C_p time series.

As discussed in Section 4.2.1, the estimated pressure coefficient time-series has been formed by extracting the appropriate value from the UoB-WT database, based on the elevation angles, azimuthal angles and TI calculated from the velocity time-series of the transient simulations. The time-series of the pressure coefficients constructed from the UoB-WT database is qualitatively as measured in the UoB-TWS, though somewhat flattened (see Figure 4-16). The relative errors of the predicted C_p to the maximum magnitude of C_p from UoB-TWS for these points are less than 40%. The corresponding pressure comparisons for different points are shown in Figure 4-17. The estimated pressure time series during the first 0.03 s period illustrates a good consistency (<20% difference value) compared with UoB-TWS based on observation, while the estimated suction pressure from the database is higher (< 70% difference value) than the suction pressure from TWS during the period of 0.03 s to 0.1 s.

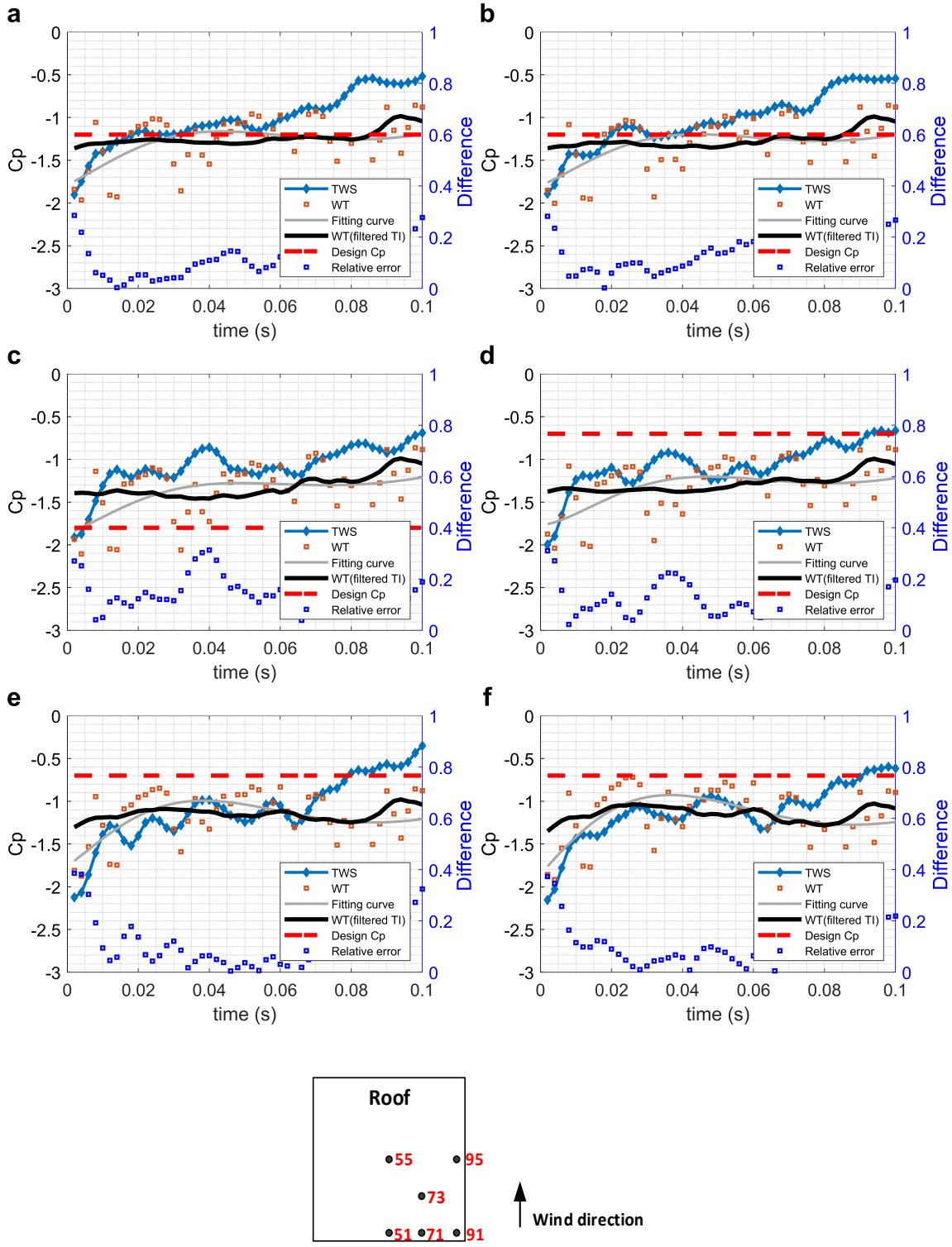


Figure 4-16. Comparison of peak pressure coefficient for cube building: (a) P51; (b) P71; (c) P91; (d) P73; (e) P55; (f) P95. WT represents the estimated values. Fitting curves are based on the orange squares. Filtered TI represents database C_p values extracted using the 50 points moving averaged TI. Relative error is the ratio of the values to the maximum magnitude of C_p measured in the TWS. The design C_p comes from Eurocode 1-4.

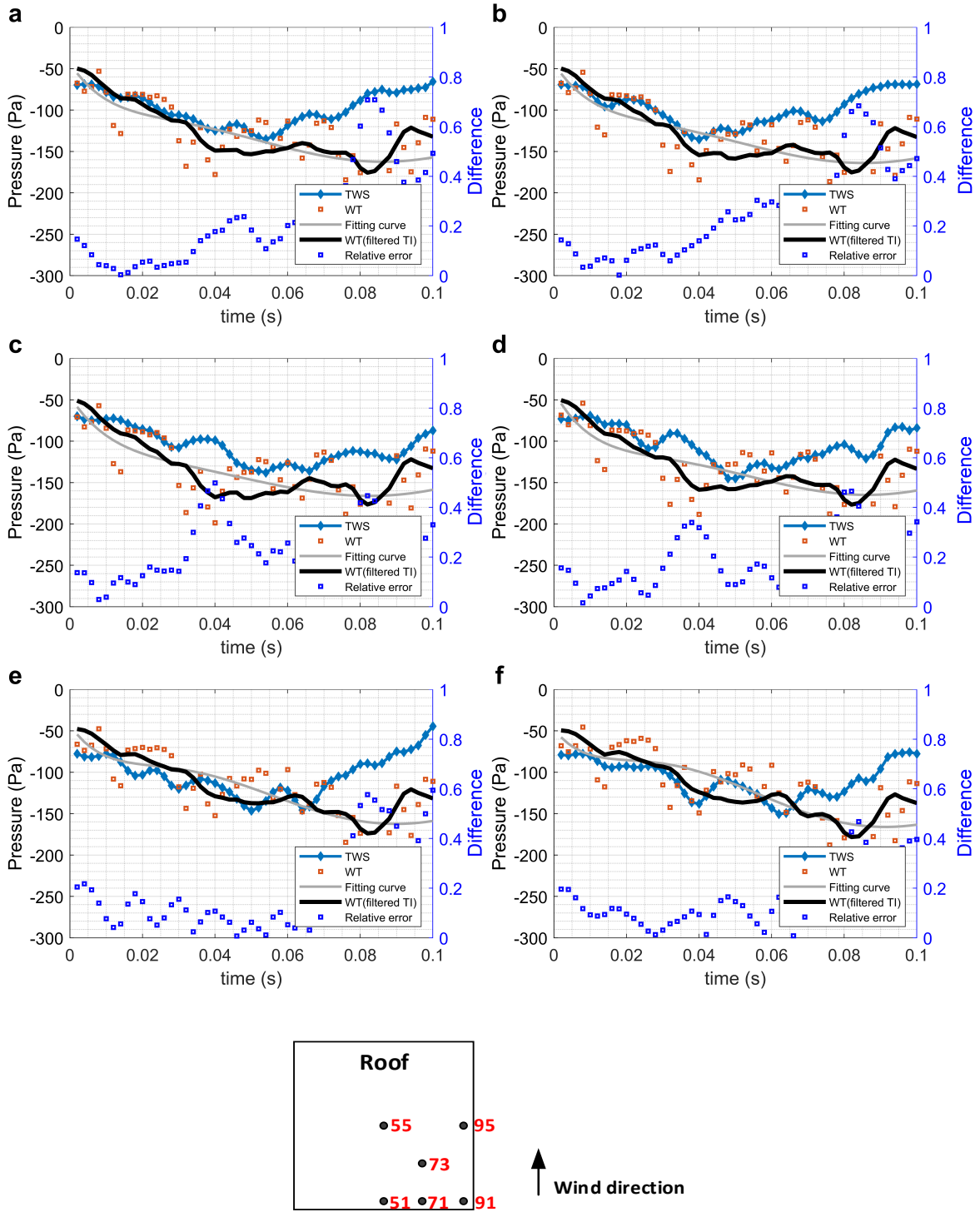


Figure 4-17. Comparison of pressures for cube building: (a) P51; (b) P71; (c) P91; (d) P73; (e) P55; (f) P95. Relative error is the ratio of the values to the maximum magnitude of pressure measured in the TWS.

The RMS errors defined in Eq. (4.11) of the pressure coefficients and pressures for these points for 0.1 time period are summarised in Table 4-3.

$$RMS_{error} = \sqrt{\frac{1}{T}\sum_0^t (C_{p_{TWS}}(t) - C_{p_{database}}(t))^2} \quad (4.11)$$

where $C_{p_{TWS}}$ is the pressure coefficient from UoB-TWS. $C_{p_{database}}$ is the estimated pressure coefficient from WT database. T is the time period.

The RMS errors of the pressure coefficients for these points range from 0.3 to 0.36 and the RMS errors of the pressures change from 31 Pa to 42 Pa (<28% of the peak suction pressure for these six points, -150 Pa), which demonstrates an encouraging comparison result between the estimated time series (C_p and Pressure) and the time series from TWS.

Table 4-3. Summary of RMS errors of Cp and pressures for cube building.

Points analysis			P51	P71	P91	P73	P55	P95		
Cube	$\theta = 0°$	C_p	0.33	0.35	0.32	0.30	0.36	0.30		
		Pressure (Pa)	41	42	35	33	39	31		
Portal	$\theta = 0°$	C_p	0.42	0.53	0.61	0.38	0.35	0.42		
		Pressure (Pa)	28	34	34	22	31	38		
Areas analysis			A1	A2	A3	A4	A5	A6	A7	A8
Cube	$\theta = 0°$	C_p	0.37	0.33	0.32	0.31	0.29	0.31	0.44	0.43
		Pressure (Pa)	33	40	36	34	32	34	48	48
	$\theta = 45°$	Pressure (Pa)	15	37	67	25	31	17	31	22
Portal	$\theta = 0°$	C_p	0.48	0.52	0.54	0.48	0.45	0.36	0.35	0.41
		Pressure (Pa)	30	33	30	28	28	20	41	48

4.2.3 Portal framed building model - Individual point

The maximum negative pressure for P51 occurs at around 0.028 s and the overall variations of the pressures on the roof illustrate that the first peak induced by the primary vortex and secondary vortex occurs at around 0.02 s to 0.04 s (see Figure 4-18 (a)), which is earlier than the peak pressure period (around 0.05 s) of cube building model. This indicates that the roof with pitch shortens the time and distance of flow separation. In this case, the first 0.1 s, when the peak pressure for different points of portal building occurs, has been chosen for the

comparisons, which is in keeping with the time period of peak pressures for cube building model. The calculated pressure coefficient time series for P51, P71, P91, P73, P55 and P95 on the roof of the portal building model are shown in Figure 4-18 (b).

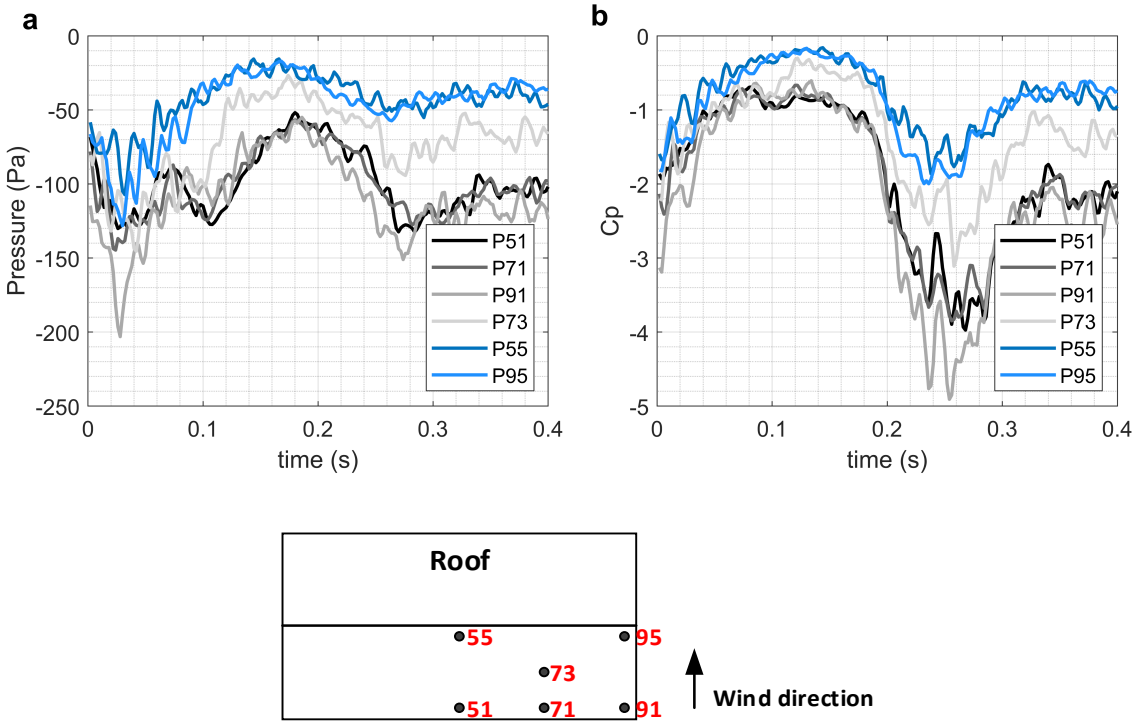


Figure 4-18. Basic information of downburst simulation for P51, P71, P91, P73, P55 and P95 on the roof of the portal building: (a) Pressures on different positions; (b) C_p time series.

A large negative pressure coefficient of UoB-TWS during the period of 0 s to 0.04 s occurs (see Figure 4-19) compared with the estimated values. The higher relative errors of pressure coefficient occur at the beginning of the time series caused by a quite small velocity time series from TWS. After 0.04 s, the relative errors of the pressure coefficient are smaller than 20% for P51, P71, P91 and P73 (Figure 4-19), which demonstrates a better result compared with these for cube building model, whose relative errors of pressure coefficient can reach up to 36% - the reason for this is due to the higher pressure coefficients of WT database for cube building model compared with these for portal building model since the flow separation on the cube building roof can generate higher velocity gradient and higher turbulence compared with these on portal

building roof. Furthermore, the portal building with around 10° pitch roof is equivalent of adding positive elevation angle of the wind direction, which results in the corresponding overall elevation angle for cube building model reaching up to 20°. As shown in Figure 4-5, the magnitudes of peak pressure coefficients tend to decrease when the elevation angle is over 15°. The maximum relative errors for P55 and P95 reach up to 30%, which illustrates that the accuracy of the predictions near the edges is higher than the estimated values in central areas. The RMS errors of the pressure comparisons (Figure 4-20) change from 28 Pa to 38 Pa for P51, P71, P91, P73, P55 and P95 detailed in Table 4-3. The suction pressures during the period of 0.04 s to 0.1 s from estimated data are lower than the UoB-TWS for P51, P71 and P73 while the overall tendencies from the estimated pressure time series are similar as the pressure time series from TWS.

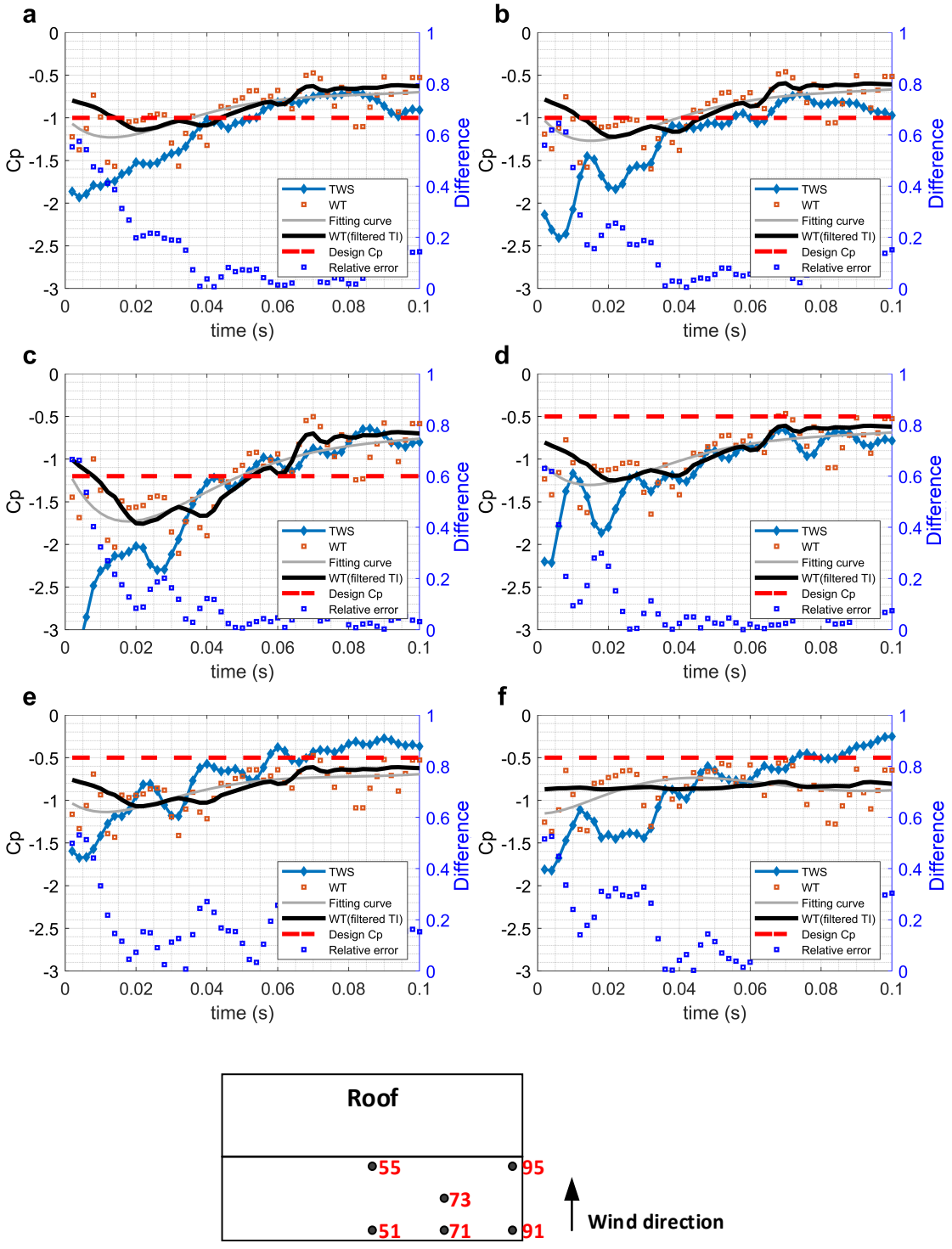


Figure 4-19. Comparison of pressure coefficient for portal building: (a) P51; (b) P71; (c) P91; (d) P73; (e) P55; (f) P95. WT represents the estimated values. Fitting curves are based on the orange squares. Filtered TI represents database C_p values extracted using the 50 points moving averaged TI. Relative error is the ratio of the values to the maximum magnitude of C_p measured in the TWS. The design C_p comes from Eurocode 1-4.

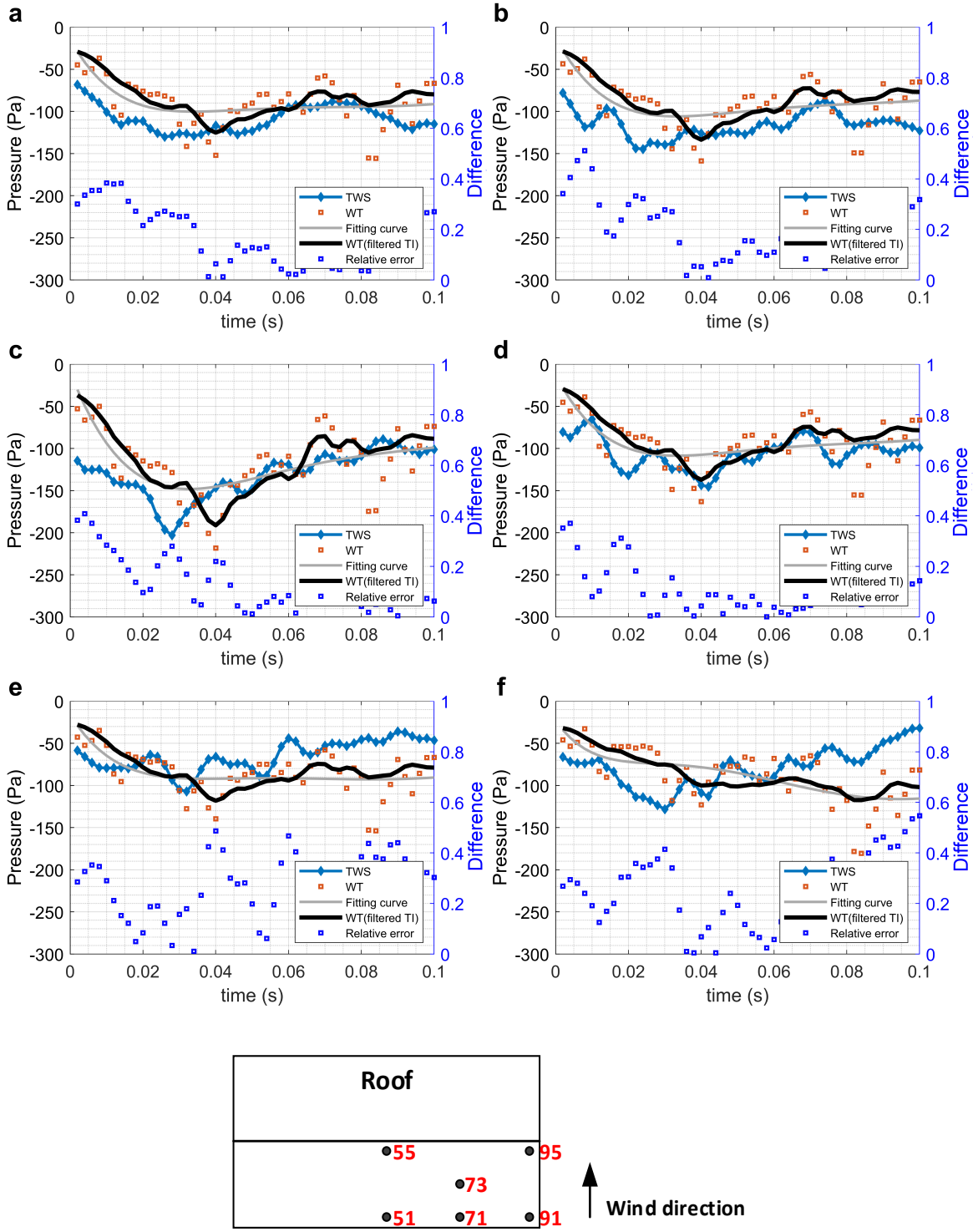


Figure 4-20. Comparison of pressure for portal building: (a) P51; (b) P71; (c) P91; (d) P73; (e) P55; (f) P95. Relative error is the ratio of the values to the maximum magnitude of pressure measured in the TWS.

4.2.4 Cube building model - Areas

The original data from UoB-TWS for different areas on the cube building roof is shown in Figure 4-21. The area-averaged pressure time series of eight parts on the roof (Figure 4-21 (a)) demonstrates that the peak pressure period is focused on the first 0.1 s, meanwhile, the elevation angle during this period can reach up to 11.5° and the azimuthal angle varies from -7° to 3°, and the corresponding pressure coefficient time series of different regions on the roof (Figure 4-21 (d)) are calculated then. Additionally, Wu and Kopp (2018) demonstrated that larger elevation angles resulted in larger suction pressure coefficients on the roof, with approximately 13% variation of pressure coefficients when the elevation angles ranged from 2.5° to 45° and the azimuthal angles varied within 0° to 7°.

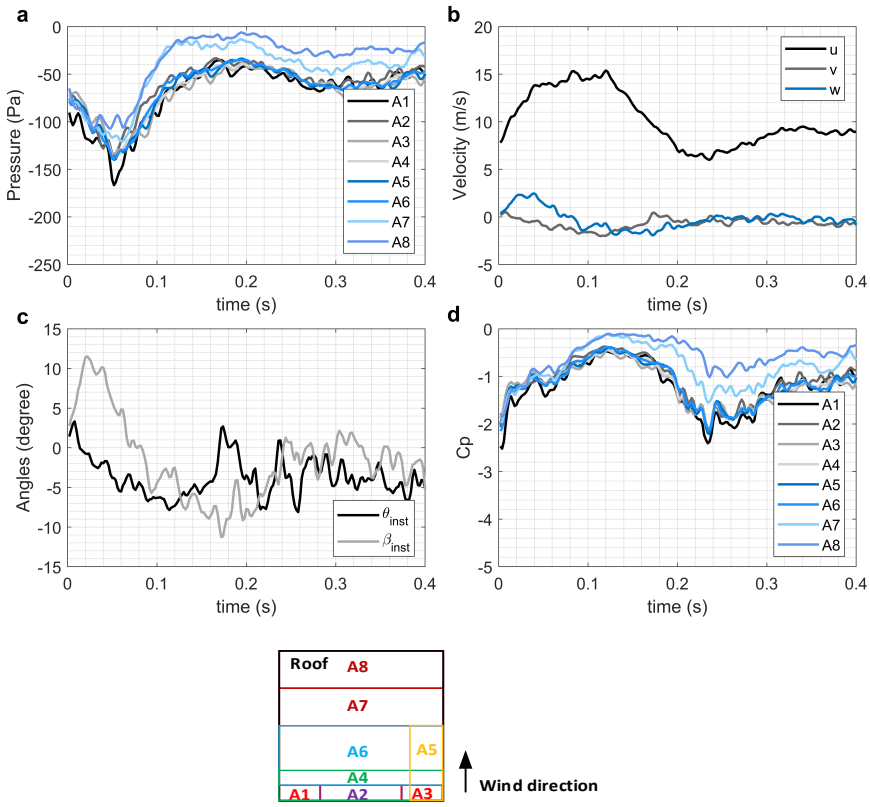


Figure 4-21. Basic information about UoB-TWS for A1, A2, A3, A4, A5, A6, A7 and A8 on the roof of the cube building: (a) Pressures on different positions; (b) Velocity time series in three directions; (c) Variation of the angles; (d) C_p time series.

The estimated pressure coefficients (Figure 4-22) are lower magnitude than the pressure coefficients from UoB-TWS for the first 0.01 s at different areas while the difference of the pressures is around 20 Pa (see Figure 4-23) due to the small velocity during this period. The tendencies of the WT estimated pressure coefficients and pressures demonstrate a good consistency compared with the corresponding time series from UoB-TWS for the separation regions (A1 to A6), see Figure 4-22 and Figure 4-23. The relative errors of C_p for separation regions during the period of 0.01 s to 0.1 s are less than 30% and the RMS errors between the predicted C_p time series and TWS C_p time series for areas A1 to A6 are 0.37, 0.33, 0.32, 0.31, 0.29 and 0.31 respectively, while the RMS errors for A7 and A8 are relatively high, 0.44 and 0.43 (see Table 4-3). Compared with the design pressure coefficients from design codes (Table 4-1), only the pressure coefficient time series at the corner areas is within the design values, which illustrates that more accurate design C_p should be improved for downburst events. The peak negative pressures on the roof in ABL flow measured at 6 m height (TI=19.3%) by Hoxey et al. (2002) are approximately -172 Pa (if a gust factor of 3.5 is assumed) for edge regions (A1, A2 and A3) and -147 Pa for central region (A6) which are smaller magnitudes of pressure than the estimated peak pressures from WT database (Figure 4-23). The maximum suction pressures on edge regions (A1, A2 and A3) and central region (A6) are approximately -180 Pa from estimated pressure time series. The RMS errors between the estimated pressure time series and pressure time series of UoB-TWS change from 32 Pa to 40 Pa for separation regions (A1, A2, A3, A4, A5 and A6) (see Table 4-4), which is less than 24% of peak pressure (167 Pa) of UoB-TWS. The maximum difference of the peak pressures is 27 Pa on A3 which indicates that the peak pressures can be predicted within the error of 16%. Therefore, the WT database can be regarded as an encouraging method for pressure prediction.

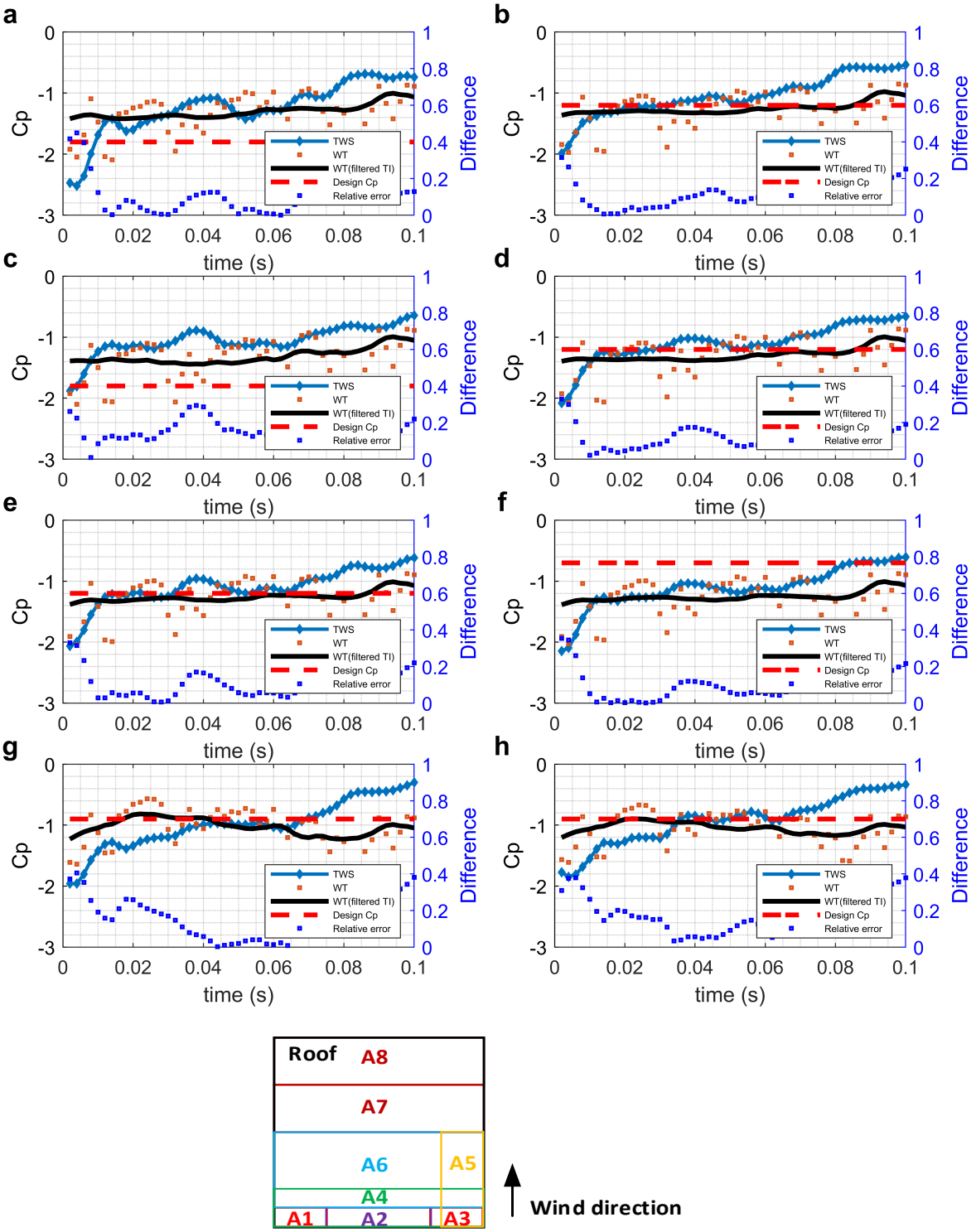


Figure 4-22. Comparison of C_p for cube building: (a) A1; (b) A2; (c) A3; (d) A4; (e) A5; (f) A6; (g) A7; (h) A8. WT represents the estimated values. Filtered TI represents database C_p values extracted using the 50 points moving averaged TI. Relative error is the ratio of the values to the maximum magnitude of C_p measured in the TWS. The design C_p comes from Eurocode 1-4.

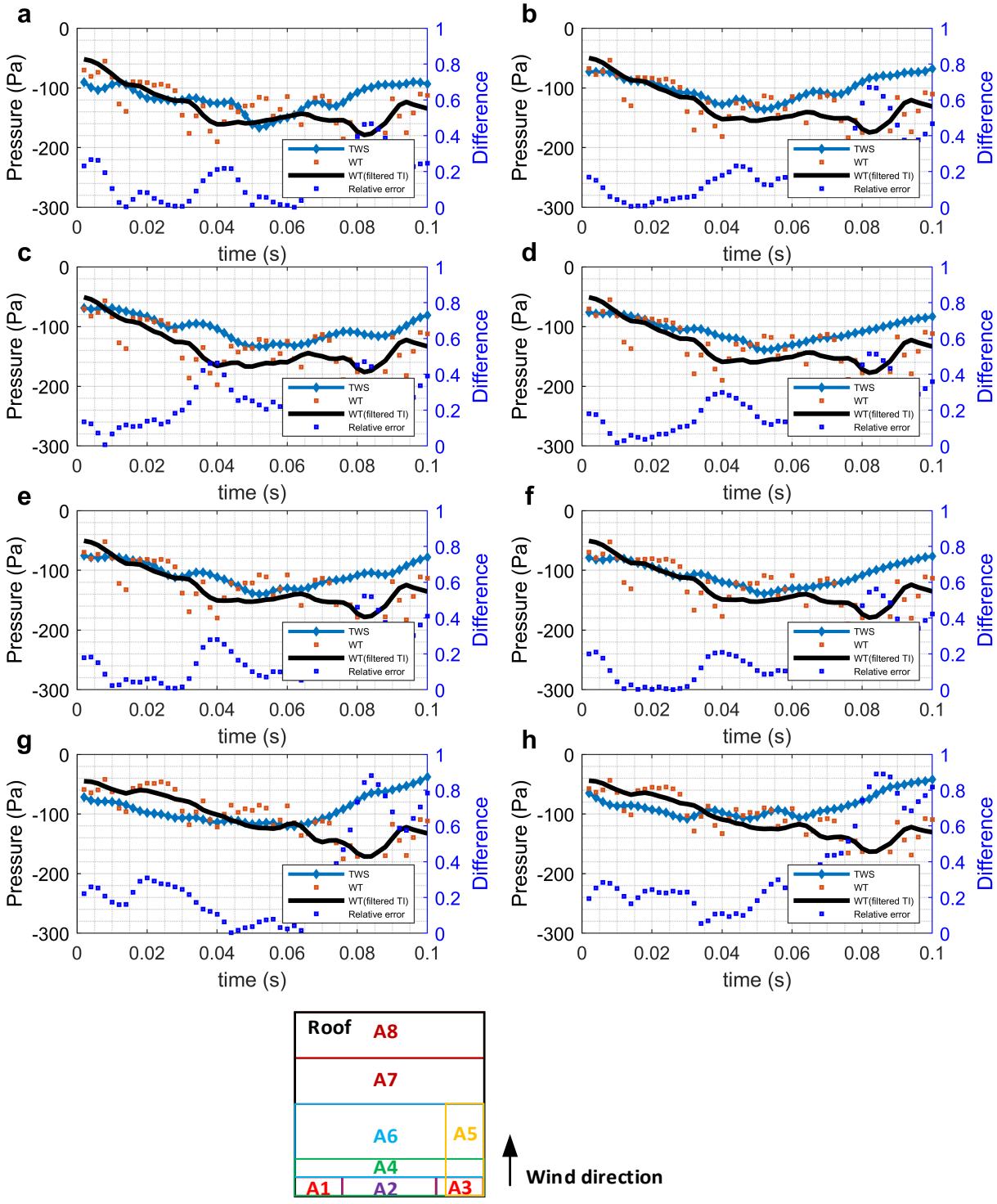


Figure 4-23. Comparison of pressure for cube building: (a) A1; (b) A2; (c) A3; (d) A4; (e) A5; (f) A6; (g) A7; (h) A8. Relative error is the ratio of the values to the maximum magnitude of pressure measured in the TWS.

Table 4-4. Comparison of the peak pressures on the roof for cube building.

	Areas	A1	A2	A3	A4	A5	A6	A7	A8
Peak Pressure (Pa)	UoB-TWS	-167	-136	-134	-139	-140	-139	-121	-108
	WT estimated	-157	-153	-161	-158	-151	-151	-116	-83

The pressure coefficient database can also predict the pressure time series when the azimuthal angle is 45° (Figure 4-24). Except for A3 with a 67 Pa RMS error, the predicted pressure time series demonstrate a quite similar tendency as the pressure time series from TWS even for reattachment regions. At the corner region, A3, the high predicted negative pressures at around 0.04 s are due to the large pressure coefficients from the WT database as the conical vortices take place, meanwhile, the turbulence intensity at 0.04 s reaches up to 2.5%. The RMS errors of pressure time series for A1, A2, A4, A5, A6, A7 and A8 vary from 15 Pa to 37 Pa, therefore, the accuracy of the predicted pressure time series when the azimuthal angle is 45 degrees demonstrates well-matched results compared with the time series from TWS, except A3. The peak pressure on the roof in ABL flow, using the C_p values measured by Hoxey et al. (2002), is approximately -184 Pa (if a gust factor of 3.5 is assumed) for corner regions (A3) which is lower magnitude than the estimated peak pressure, -210 Pa, from WT database (Figure 4-24).

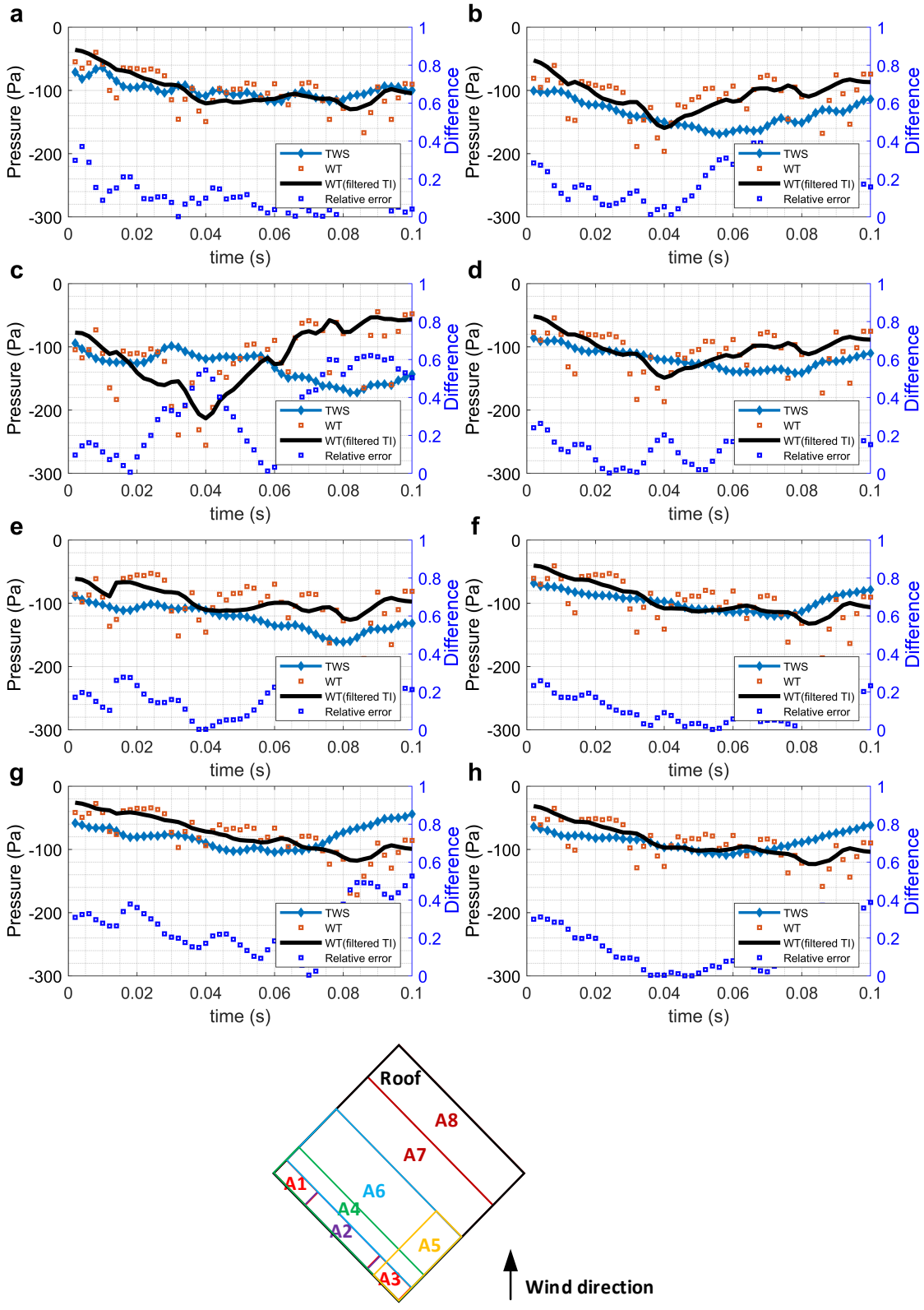


Figure 4-24. Comparison of pressure for cube building: (a) A1; (b) A2; (c) A3; (d) A4; (e) A5; (f) A6; (g) A7; (h) A8. Relative error is the ratio of the values to the maximum magnitude of pressure measured in the TWS.

4.2.5 Portal framed building model- Areas

The original pressure time series and the calculated pressure coefficients from TWS of portal building for different areas are shown in Figure 4-25. The peak suction pressures on the roof occur at around 0.03 s (Figure 4-25 (a)) while the peak velocity occurs at around 0.08 s (Figure 4-21 (b)).

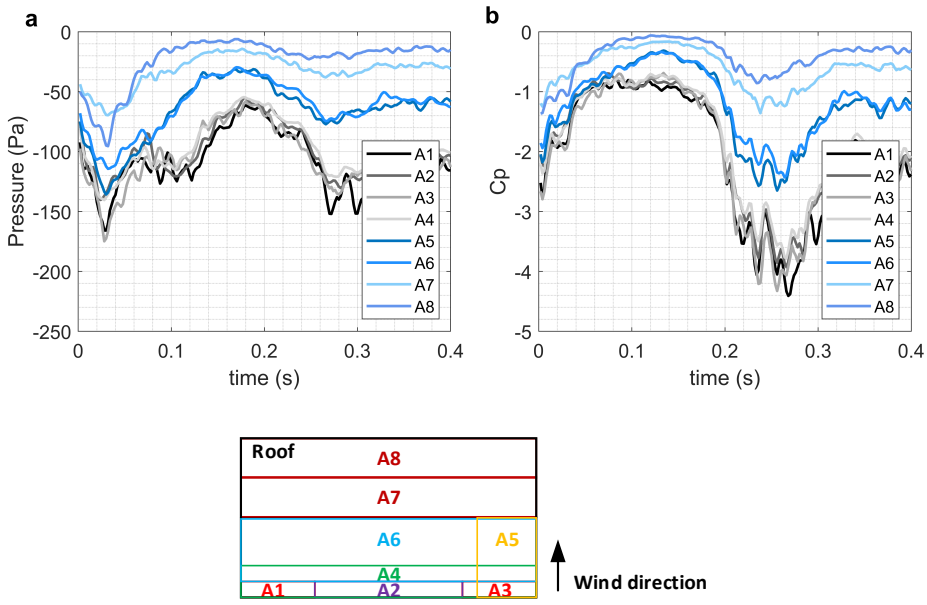


Figure 4-25. Basic information about UoB-TWS for A1, A2, A3, A4, A5, A6, A7 and A8 on the roof of the portal building: (a) Pressures on different positions; (b) C_p time series.

The predicted pressure coefficients and pressures on the separation regions (A1, A2, A3, A4, A5 and A6) for portal building also demonstrate a quite similar tendency and magnitude as the corresponding data from TWS (Figure 4-26 and Figure 4-27). The similar tendency between the predicted values (pressure coefficients and pressures) and TWS values are also suitable for A7 and A8 to some extent, but high relative errors can be observed obviously after 0.04 s (see Figure 4-26 (g) and (h); Figure 4-27 (g) and (h)). The RMS errors of pressure time series for A7 and A8 can reach up to 41 Pa and 48 Pa (Table 4-3), which are higher than the RMS errors in separation regions, changing from 20 Pa to 33 Pa (less than 19% of peak pressure from TWS

for portal building, 176 Pa). Moreover, the relative errors for A1 to A6 after 0.03 s are less than 20%. According to the statistical analysis, although the RMS errors of pressure coefficient for A1 to A6 have reached up to 0.54, the predicted pressure time series for A1 and A6 can demonstrate a good match with the pressure time series from TWS.

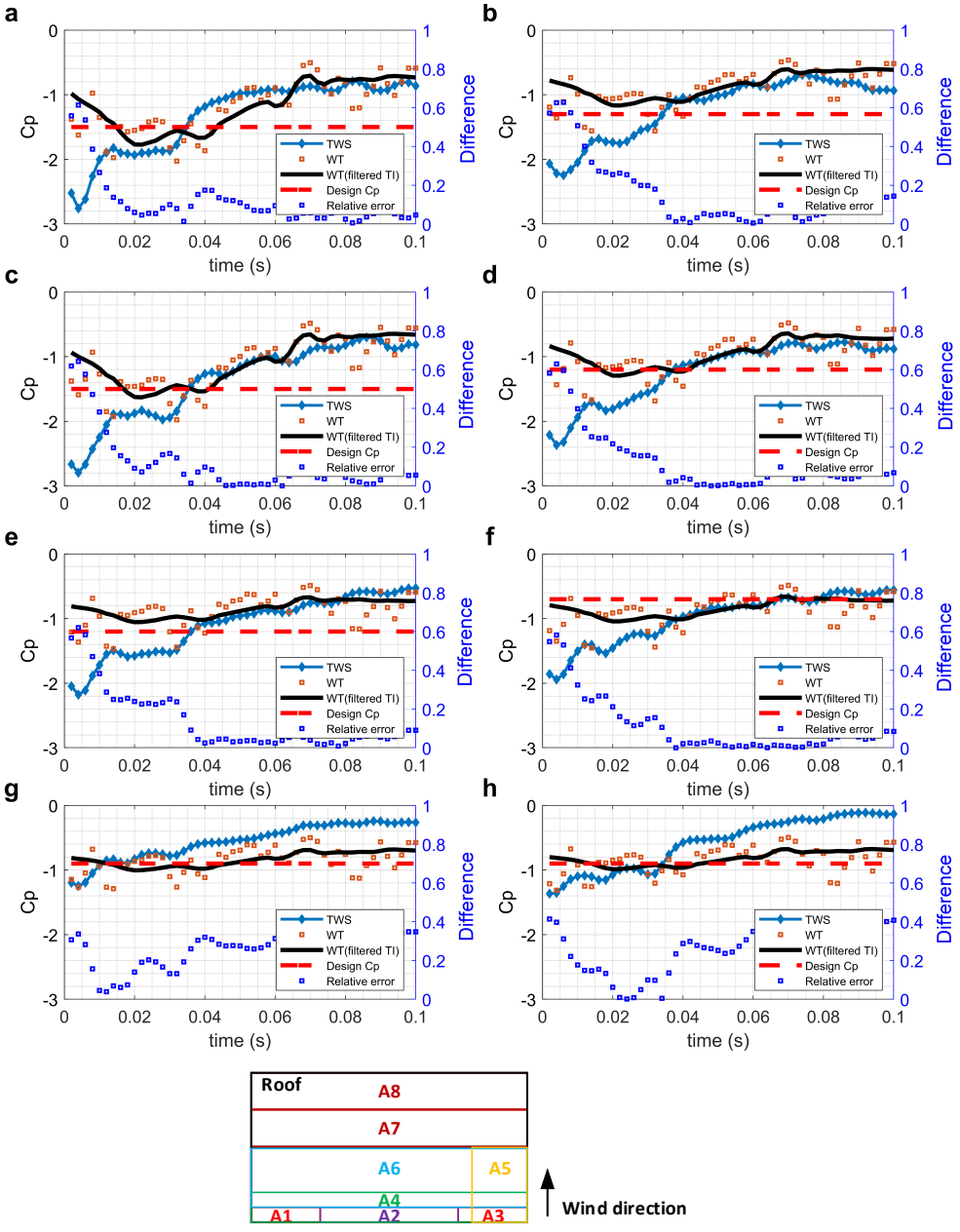


Figure 4-26. Comparison of C_p for portal building: (a) A1; (b) A2; (c) A3; (d) A4; (e) A5; (f) A6; (g) A7; (h) A8. WT represents the estimated values. Filtered TI represents database C_p values extracted using the 50 points moving averaged TI. Relative error is the ratio of the values to the maximum magnitude of C_p measured in the TWS. The design C_p comes from Eurocode.

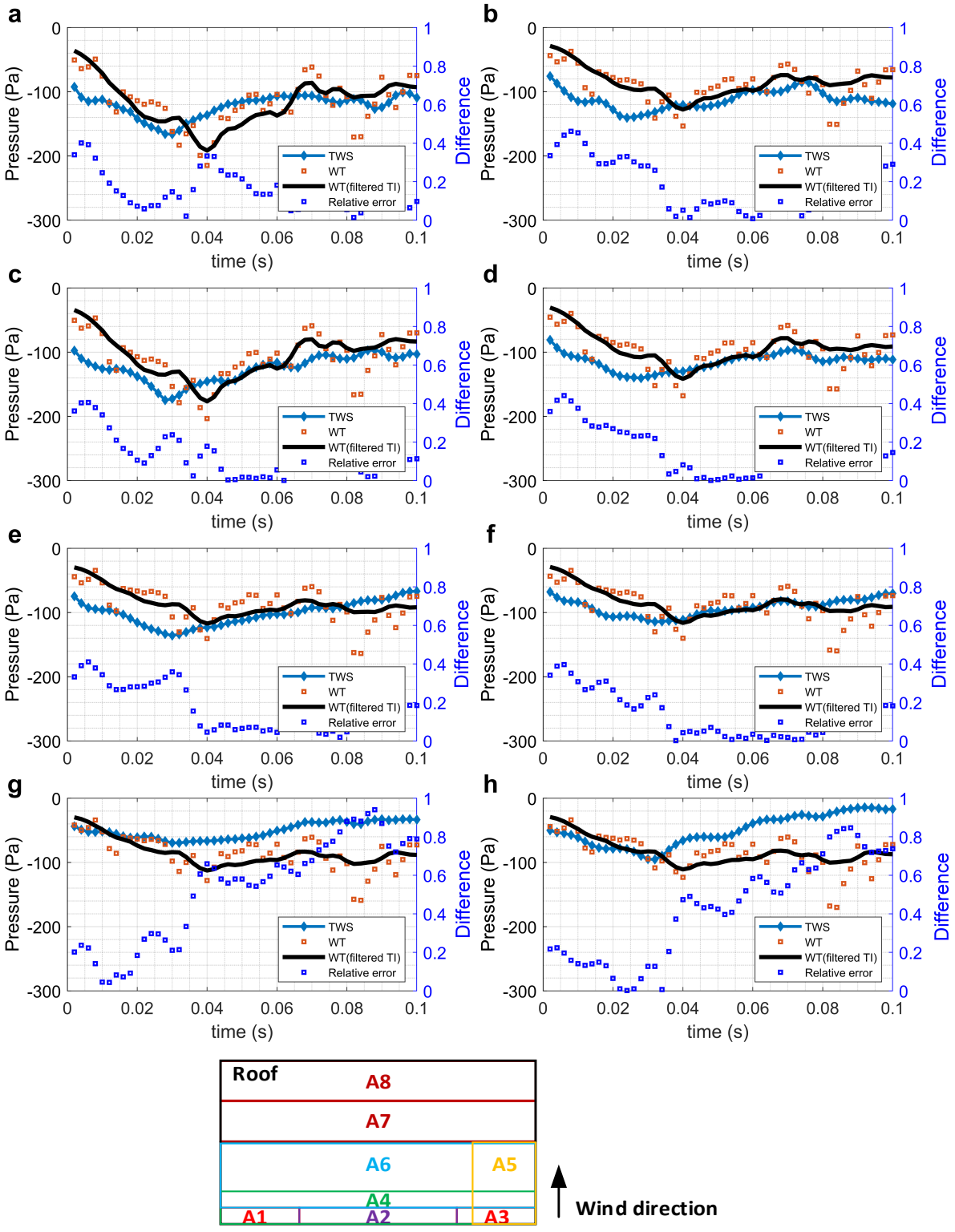


Figure 4-27. Comparison of pressures for portal building: (a) A1; (b) A2; (c) A3; (d) A4; (e) A5; (f) A6; (g) A7; (h) A8. Relative error is the ratio of the values to the maximum magnitude of pressure measured in the TWS.

4.3 Summary

The mean pressure coefficient database and peak pressure coefficient database for different points on the roof have been discussed in Section 4.1.2. The increasing magnitude of the peak pressure coefficients with increasing turbulence intensity (from around 2% to 20%) is evident. According to the comparison with the ABL data from Eurocode (2010), good consistency and reliability of the WT database are evident, while the pressure coefficients from WT database are larger than the corresponding normalised values from ASCE. In the separation region, the maximum magnitude of pressure coefficients occurs when the elevation angle is between 0° and 15° with zero azimuthal angles. However, for a 45° azimuthal angle, the maximum magnitude of peak C_p occurs when the elevation angle is between -15° and 0°. Furthermore, the turbulence intensities affect the elevation angles at which the maximum magnitude of pressure coefficient occurs, with higher turbulence intensities having maximum magnitudes at lower elevation angles.

The peak pressure coefficient database for different areas on the roof has been discussed in Section 4.1.4 and 4.1.5. The increasing magnitude of the peak pressure coefficients with increasing turbulence intensity (2% to 20%) is evident for the separation regions, which is the same trend as seen for the point analysis. However, the influence of the turbulence intensities on the reattachment regions is negligibly small. Compared with the ABL normalised peak pressure coefficient values given by Eurocode (2010) and ASCE7 (2013), the peak pressure coefficients from the database are closer to the values from the Eurocode at the roof edge A1, A2 and A3 and are larger than the values from the Eurocode and ASCE away from the roof edge at A6, A4 and A5 when the turbulence intensity is approximately 20%, meanwhile more reliable design values from database at A4, A5 and A6 are evident as well, which also

demonstrates a similar result in point analysis. The maximum magnitude of pressure coefficients occurs (for separation region) when the elevation angle is between 0° and 15° at 0° azimuthal angle. However, the maximum magnitude of pressure coefficients occurs (for separation region) when the elevation angle is between -15° and 0° at 45° azimuthal angle (same as point analysis). The analysis of the magnitude of peak pressure coefficients at varying azimuthal angles when the elevation angle is zero degrees testifies that elevation angle is an important influence factor for peak pressure coefficients on the corner of the roof of portal building. Furthermore, increasing turbulence intensity affects the elevation angles at which the maximum magnitude of pressure coefficients occurs. Higher turbulence intensities result in lower elevation angles for the maximum magnitude of pressure coefficients (same as point analysis). Therefore, several factors containing position on the roof, turbulence intensity, elevation angle and azimuthal angle can influence the magnitude of peak pressure coefficients, which verifies that the aerodynamic properties on the buildings depend on these parameters as discussed in Section 1.4.4.

According to the pressure time series of TWS for cube building and portal framed building, the development of the flow separation on the roof of the portal framed building is suppressed, demonstrated by the earlier occurrence of peak pressure. However, the high turbulence near the corner of the portal building roof is obvious since the magnitude of peak pressure on the portal building roof is higher than the magnitude of peak pressure on the cube building roof. For the portal building roof, the elevation angle varying from 0° to 15° can contribute to the increasing of pressure coefficients, which is illustrated in Figure 4-11 in Chapter 4.

Combining the pressure coefficients calculated from the database with the dynamic pressures calculated from UoB-TWS has been shown to provide an accurate prediction of the actual

pressure field on the roof to some extent. The variation of the estimated pressure time series is close to the trends of the pressure time series of TWS for separation areas on the roof even though the estimated pressure time series is flattened. However, this method needs more consideration for the reattachment area on the roof, illustrated on both cube building model and portal building model, as the RMS errors of the pressure on these regions are larger than 40 Pa (maximum pressure is 167 Pa for cube building roof and 176 Pa for portal building roof from area analysis). The RMS errors of pressure coefficients for the separation regions of the portal building are higher than those of the cube building, though the RMS errors of pressures for the separation regions of portal building are smaller compared with these for cube building, which is due to the time period with large relative error for pressure coefficient corresponding to low velocities (see Figure 4-26 for portal building, duration of 0 s - 0.02 s).

Furthermore, the area analysis illustrates a good consistency with the point analysis, while the pressure RMS error of area analysis is smaller than that from point analysis, e.g. the RMS errors of pressure coefficient and pressure for P51 of cube building are 0.33 and 41 Pa, which are similar as these for A2 of cube building, 0.33 and 40 Pa; the RMS errors of pressure coefficient and pressure for P91 of portal building are 0.61 and 34 Pa and the corresponding values for A3 of portal building are 0.54 and 30 Pa which proves that the area analysis is better than the point analysis since very localised effects essentially have a small length scale and when they are averaged over a relatively large distance, then these effects become small. However, for some specific cases, the RMS errors of pressure coefficient and pressure for P51 of portal building are 0.42 and 28 Pa which are lower than these for A2 on portal building roof, 0.52 and 33 Pa - the reason for this may be caused by the non-coherent structures on A2 which lead to the obvious localised effects. Moreover, the pressure RMS errors at A7 of portal building (41 Pa) are lower than this of cube building (48 Pa), which is caused by the influence of flow separation

when the flow passes over the peak of the building. When the azimuthal angle is 45°, the RMS errors of pressures decrease from 67 Pa, 37 Pa to 15 Pa for cube building roof areas A3, A2 to A1 respectively, demonstrating that the areas with a relatively large length scale can have better results since this area can be considered to be within the coherent structures. Therefore, the areas analysis in the flow separation regions with the coherent structures can obtain better comparison results.

The higher magnitude of estimated suction pressures on the roof for downburst wind flow compared with ABL flow demonstrates that the downburst wind flow can produce more severe damage on the roof. Further validations with a larger range of variations of the elevation angles and azimuthal angles are needed.

Chapter 5 Results and discussion of TWDS

Previously, Chapter 4 studies the aerodynamic properties of the TS downburst wind load on building roofs. This chapter revisits the random vibration theory for evaluating the dynamic response of buildings under the influence of TS downbursts (Song et al., 2021a). Section 2.3 formulates the TWDS and scrutinises its controlling parameters that the structures can be considered as sets of oscillators that filter the input acceleration induced by the outflow wind, to then conform the output acceleration of the structures interacted with the TS downbursts. This proposed method uses the PSD of the reduced turbulent fluctuations as well as spatial correlation laws to describe the turbulent nature of TS downbursts. A parametric analysis was completed in Section 5.1, aiming to establish the variability of outflow velocity, structural dimensions, mass, and natural frequency; and their influence on the design spectra, in addition to variations induced by different damping ratios and terrain categories. Section 5.2 introduces the CAARC standard tall building which is utilised for validations in this chapter. Section 5.3 revalidated the WDS technique on a benchmark tall building. Section 5.4 illustrates the application of the novel TWDS algorithm on a benchmark tall building to estimate its dynamic performance and the results are compared with the equivalent numerical integration methods and FEM method with the modelling of a benchmark tall building in SAP2000 (Ondrej, 2013). Section 5.5 summarises the main conclusions and identifies further research avenues.

5.1 Scrutinising of controlling parameters of TWDS

The input variables of the TWDS are investigated based on the building dimensions with a width of 20 m, an aspect ratio of 10, and the ratio between chord and width of 1. The damping ratio of this building is 0.025, and the assumed height for the peak velocity of downburst outflow is 50 m. The reference velocity at a 10-metre height above the ground is set at 25 m/s. Then, the overall design spectra of the output acceleration with varying $\bar{U}_{max,10}$ is shown in Figure 5-1 (c) with varying natural period, T. According to the properties of the structures, it is reasonable to assume the investigating range of the natural frequency is from 0.1 Hz to 10 Hz and the corresponding range of the natural period varies from 10 s to 0.1 s. The design spectra for resonant components illustrate an obvious rising tendency with the reference velocity, particularly for the low fundamental frequency range. When the natural frequency of the structure matches 0.2 Hz, the overall design spectrum of the output acceleration at 50 m/s is about 5 times higher than its counterpart at 25 m/s. When the natural frequency reduces to 0.1, the ratio of the overall design spectra at 50 m/s and 25 m/s is around 5.4. The induced high ratio of the design spectra between different velocities is mainly caused by the resonant response. The resonant design spectra are the dominant reflections on the influence of the mechanical admittance when the frequency is close to the natural frequency. Figure 5-1 (b) also shows that the background design spectra do not vary much with the natural frequency since they represent the quasi-static response caused by the gust turbulent fluctuations below the natural frequency. This also demonstrates consistency with Kareem and Tamura (2013) that the output acceleration response mainly occurs at the resonant frequency.

The dimensions of the structure are also non-negligible, as shown in Figure 5-1 (d) for the aspect ratio, H/W, and Figure 5-1 (e) for the ratio of L/W. The descending dimensions of the

structures relative to the structural width can lead to higher design spectra for both ratios of H/W and L/W since higher structures have a longer natural period with less acceleration, while lower structures have higher natural frequencies with high accelerations. Moreover, the lower damping of the higher buildings also contributes to the higher design spectra. At the same time, with the increase in structural height, the cross-spectral acceleration was expected to decrease following the coherence function. For the natural frequency of 0.2 Hz, the ratio of the design spectra when $H/W = 1$ and $H/W = 10$ is around 4.2. The ratio of these decreases to 4 for the natural frequency of 0.1 Hz. Similarly, the ratio of the design spectra when $L/W = 0.4$ and $L/W = 2$ is around 5.1 and 5 for the $n_1 = 0.2$ Hz and $n_1 = 0.1$ Hz respectively. This tendency demonstrates that when the natural periods of the structures increase from 5 s to 10 s, the effects of the input parameters are mitigated.

As shown in Figure 5-1 (f), with the rising damping ratio, the design spectra decrease obviously, particularly in the low natural frequency range where the design spectra decline more rapidly. A slight influence of the height on the peak value of the slowly varying mean velocity can be observed in Figure 5-1 (g). When the height of this parameter rises from 50 m to 100 m, the design spectra rise from 0.054 m/s^2 to 0.094 m/s^2 when the natural frequency of the structures is 0.1 Hz. The influence of the terrain types on the design spectra is shown in Figure 5-1 (h). The impact of the terrain exposure categories is mainly reflected in the turbulence intensities and integral length scale in the procedure of the design spectra. The rougher ground surface can increase the fluctuating turbulence in the low-frequency range, which can lead to larger design spectra of the output acceleration, see Figure 5-1 (h).

Therefore, the reference velocities of the downburst outflow and the dimensions of the structures are the main parameters for the TWDS of the output acceleration. The damping ratio

is more sensitive to the lower natural frequencies of the structures. Furthermore, variations in the damping ratio are more obvious in the lower frequency range.

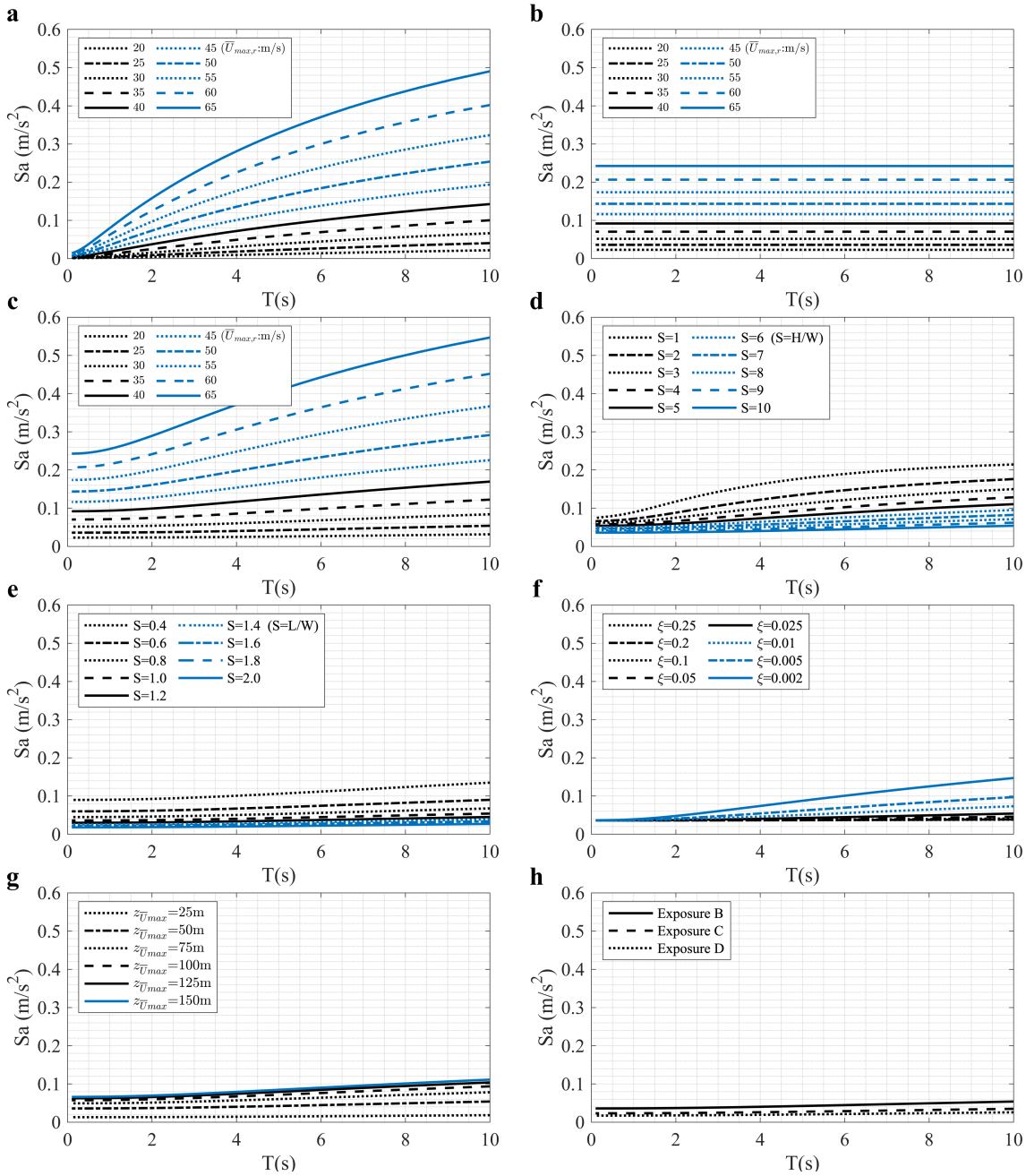


Figure 5-1. Design spectra of output acceleration with variable parameters based on basic properties (Default values: $\bar{U}_{max,10}$=25 m/s, W=20 m, H/W=10, L/W =1, ξ =0.025, $z_{\bar{U}max}$=50 m and Terrain exposure B): (a) Resonant component; (b) Background component; (c) $\bar{U}_{max,10}$; (d) H/W; (e) L/W; (f) ξ; (g) $z_{\bar{U}max}$; (h) Terrain exposure.

5.2 Description of CAARC benchmark tall building

The CAARC standard tall building (Holmes et al., 1990), which was experimentally analysed by six different laboratory research centres for the international comparative wind tunnel model studies, including the measurement of surface pressures and dynamic responses (Melbourne, 1980), and has been regarded as a standard prototype of a tall building for studying the dynamic analysis as well as a representative to study the impact of downbursts on tall buildings (Chen and Letchford, 2004a; Chen and Letchford, 2004b). Although this database from the wind tunnel experiments is currently limited to the ABL winds, more researchers are attempting to use this CAARC model for the experimental study under the influence of simulated TS downbursts (Haines, 2015). Due to the current limitations of the aerodynamic and mechanical properties of the high-rise building under the influence of the TS downburst (as discussed in Section 1.3), this simple 3-D CAARC standard tall building is adequate to be chosen for the preliminary validation of TWDS in this chapter since the mechanical properties of this CAARC tall building are provided and it is easy to do the comparison with the results from the influence of the ABL winds.

This building has a 46 m transverse width × 30 m longitudinal width × 183 m vertical height, as shown in Figure 5-2 (a). The natural frequency of the building is 0.2 Hz in the x and y directions. The fraction of the critical damping equals 0.01 and the mass per unit volume of the building is 160 kg·m^{-3}.

The CAARC building was assumed to be a uniform cantilever structure with a MDOF system, which is represented by a series of equivalent SDOF oscillators with cross-sectional dimensions of 30 m × 46 m. This building is equally divided into 19 elements with 19 nodes in the vertical directions of the domain, i.e. $z_i = (i-1) \times 9.89 + 5$ m, $i = 1, 2, \ldots, 19$, starting from 5 m to

183 m with around 9.89 m increments. Considering the partial correlations of the winds on buildings, the transverse-width of the building is equally divided into 5 bays with enclosed in 6 nodes, i.e. $y_j = (j-1) \times 9.2$ m, $j = 1, 2, \ldots, 6$. The chord of the building is equally divided into 3 bays confined by 4 nodes, i.e. $x_j = (l-1) \times 10$ m, $l = 1, 2, \ldots, 4$.

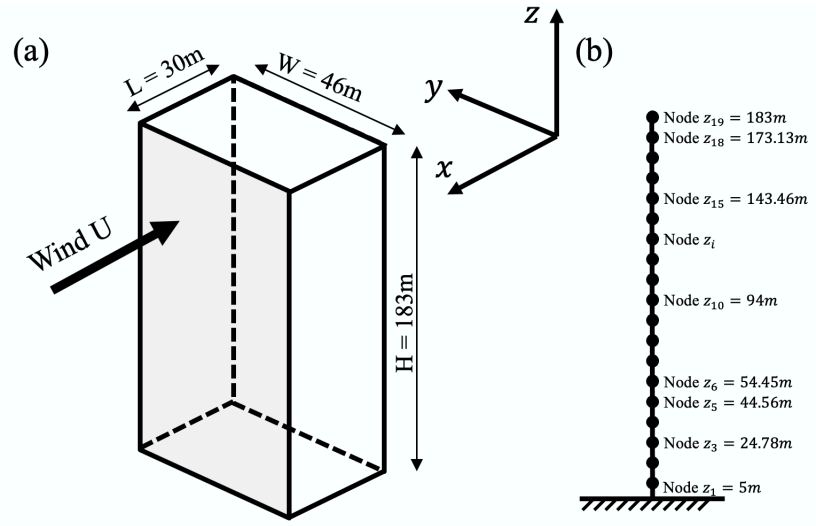


Figure 5-2. The CAARC benchmark building: (a) The dimensions; (b) The simplified modelling.

5.3 Validation of WDS for synoptic wind[c]

The application of the WDS subjected to stationary winds to the building model described in Section 5.2 is introduced in this section. The velocity with varying height can be expressed as Eq. (5.1). The turbulence intensity at the top of the building is around 10.57% and a linear relationship of the turbulence intensity with varying heights is assumed, where the turbulence intensity at a height of 0.5×H is around 13.34%. The static and dynamic displacements estimated at the top of the building are illustrated in Table 5-1. It is assumed that the drag

[c] This section is required to validate the algorithm when using synoptic winds - noting that there is no such robust experimental evidence of the dynamic response of buildings like then one reported by Melbourne (1980).

coefficients in x and y directions are 1.21 and 1.03 respectively, where the mean values measured at 2/3×H are adopted. The comparisons of the reduced displacements between the design spectra method and experiments from Melbourne (1980) at the top of the building with varying reduced velocity (see Eq. (5.2)) are illustrated in Figure 5-3, where β represents the angle of the deviation of the wind direction to x-axis in x-y plane. The static displacements in x-direction calculated from the design spectra are slightly lower than those from the fit curve obtained from experiments, while a good agreement for the static displacements can be observed in y-direction. The maximum divergence of 0.073 m occurs when $\overline{U}_{10}$=25 m/s in x-direction and 0.005 m in y-direction at the same reference velocity. The dynamic displacements in both directions from the design spectra are slightly higher than those from experiments. The maximum divergence is 0.021 m in the x-direction when the $\overline{U}_{10}$=15 m/s and is 0.041 m in the y-direction when $\overline{U}_{10}$=25 m/s, respectively.

$$\overline{U}(z) = \overline{U}_H \times (z/H)^{\epsilon} \tag{5.1}$$

$$\frac{d_x}{L} = 3.7 \times 10^{-4}\left(\frac{U_H}{n_0 W}\right)^2 \; ; \; \frac{\sigma_x}{L} = 3 \times 10^{-5}\left(\frac{U_H}{n_0 W}\right)^3 \; ; \; \frac{d_y}{W} = 1.2 \times 10^{-4}\left(\frac{U_H}{n_0 W}\right)^2 \; ; \; \frac{\sigma_y}{W} = 9.5 \times 10^{-6}\left(\frac{U_H}{n_0 W}\right)^3 \tag{5.2}$$

Table 5-1. Static and dynamic displacements (m) at the top of the building.

Wind direction	U_{10} (m/s)	U_H (m/s)	$\frac{U_H}{n_0 W}$	Static response		Dynamic response	
				WDS	Exp.	WDS	Exp.
x	5	11.28	1.234	0.014	0.017	0.007	0.002
	10	22.56	2.468	0.057	0.069	0.027	0.014
	15	33.85	3.701	0.128	0.155	0.067	0.046
	20	45.13	4.935	0.228	0.275	0.129	0.110
	25	56.41	6.169	0.356	0.429	0.218	0.215
y	5	11.28	1.234	0.008	0.008	0.004	0.001
	10	22.56	2.468	0.033	0.033	0.018	0.007
	15	33.85	3.701	0.073	0.075	0.043	0.022
	20	45.13	4.935	0.130	0.134	0.084	0.052
	25	56.41	6.169	0.204	0.209	0.143	0.102

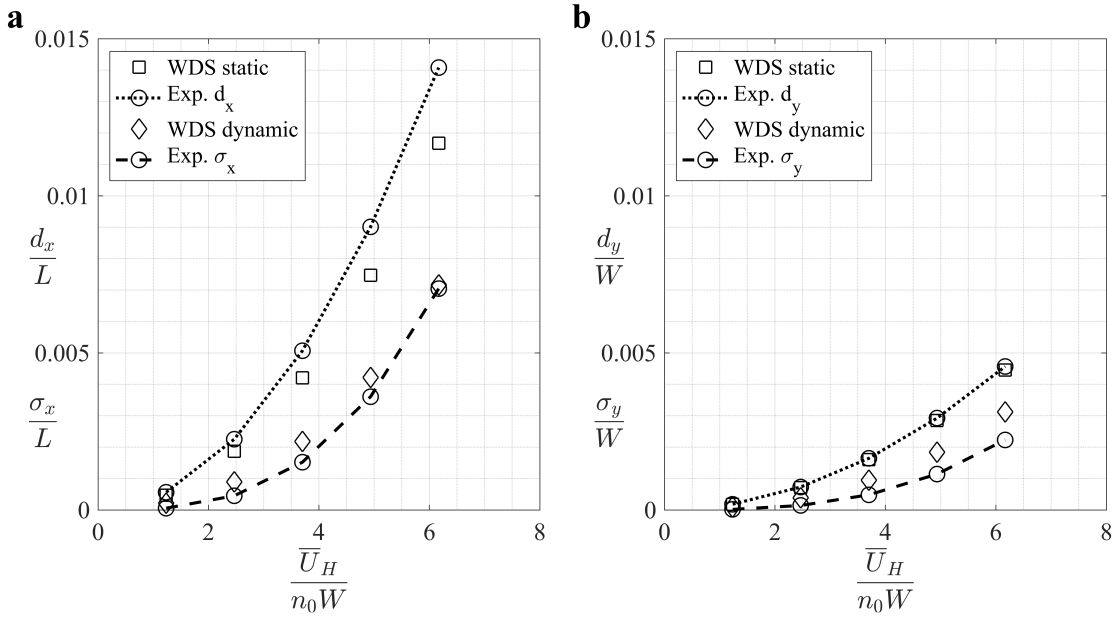


Figure 5-3. Comparison of the displacements at the top of the CAARC building model: (a) β=0°; (b) β=90°.

5.4 Validation of TWDS for TS downburst wind

The previous section shows that the original algorithm for synoptic wind by Martinez-Vazquez (2020) has been correctly implemented. In this section, the method to calculate the structural dynamic response of the 3-D CAARC benchmark building under the impact of the TS downburst is described.

5.4.1 Application of TWDS

Since a MDOF system of this benchmark building is assumed, the dynamic response of equivalent SDOF oscillators can be calculated according to the modal analysis (see Section 2.3.3). In running a modal spectral analysis where the proposed design spectra fit, the dynamic displacement response, σ_d (rms of dynamic displacement), can be obtained by using Eq. (2.25a). It should be noted that the maximum value (36.5 m/s) of the slowly varying mean wind

velocity at 13 m height with 50-year return period (Solari et al., 2015; Solari et al., 2013) is adopted as the reference height and velocity in the TWDS as well as wind field simulation (see Section 5.4.2).

The static and dynamic displacements at different heights obtained from the TWDS are shown in Table 5-2. In Eq. (2.18), the correlation function in both vertical and transverse directions of the windward surface of the building is considered. The results from the design spectra combined with the partially correlated function only in the vertical direction are also demonstrated in Table 5-2, where the oscillation amplitude of the displacement at the top of the building, i.e. 0.351 m, is larger than 0.328 m since the correlation in the transverse direction is considered as full correlation. The comparison of these two situations is demonstrated in Figure 5-4, where d_x and d_y represent the lateral displacement amplitude in x and y direction separately. Higher correlation can cause a higher displacement amplitude of the oscillation.

The WDS for ABL wind with varying heights are also compared as shown in Table 5-2 and Figure 5-4 where the turbulence intensity for stationary wind has been assumed to be the same as TS downburst and the maximum velocity for these two wind events is the same ($\overline{U}(z,t) = \overline{U}_{max}(z/H)^{\epsilon}, \epsilon = 0.28$, $\overline{U}_{max}$=41.14 m/s). The displacement at the top of the building obtained from the WDS for boundary layer wind is slightly lower than those triggered by downburst outflow, and the divergence is 0.030 m. Previous investigations of full-scale measurements demonstrated that the turbulence intensity for downburst events is generally lower than that for boundary layer wind (Solari et al., 2015).

Table 5-2. The static and dynamic lateral displacements.

Height (m)	U_h (m/s)	Static $\Delta f_1/k_1$	Design Spectra for TS downburst				WDS for ABL	Num. Int. Newmark	Num. Int. I.O.E.
			Davenport's coherence (vertical and horizontal)		Partial correlated (vertical only)		Davenport's coherence (vertical and horizontal)	Partial correlated (vertical only)	
			Dynamic	Total	Dynamic	Total	Total	Total	Total
					x-direction				
183.0	32.06	0.200	0.128	0.328	0.151	0.351	0.298	0.435	0.434
173.1	33.04	0.184	0.121	0.305	0.143	0.327	0.267	0.405	0.400
163.2	34.00	0.168	0.114	0.282	0.135	0.302	0.237	0.371	0.372
153.3	34.95	0.152	0.107	0.259	0.127	0.278	0.211	0.351	0.355
143.4	35.86	0.136	0.100	0.236	0.118	0.254	0.186	0.315	0.322
133.6	36.74	0.120	0.093	0.213	0.110	0.230	0.163	0.282	0.289
123.7	37.59	0.105	0.086	0.191	0.102	0.207	0.142	0.242	0.248
113.8	38.38	0.090	0.079	0.169	0.094	0.184	0.123	0.200	0.205
103.9	39.10	0.076	0.073	0.148	0.086	0.162	0.105	0.183	0.179
94.0	39.75	0.063	0.066	0.128	0.078	0.140	0.089	0.156	0.153
84.1	40.31	0.050	0.059	0.109	0.069	0.120	0.075	0.130	0.127
74.2	40.75	0.039	0.052	0.091	0.061	0.100	0.062	0.114	0.112
64.3	41.04	0.029	0.045	0.074	0.053	0.082	0.050	0.089	0.089
54.4	41.14	0.021	0.038	0.059	0.045	0.066	0.040	0.068	0.072
44.6	40.98	0.014	0.031	0.045	0.037	0.050	0.031	0.039	0.041
34.7	40.45	0.008	0.024	0.032	0.029	0.036	0.023	0.020	0.022
24.8	39.34	0.004	0.017	0.021	0.020	0.024	0.015	0.012	0.013
14.9	37.14	0.001	0.010	0.012	0.012	0.014	0.009	0.006	0.006
5.0	31.81	0.000	0.004	0.004	0.004	0.004	0.003	0.001	0.001
					y-direction				
183.0	32.06	0.112	0.084	0.196	0.094	0.206	0.175	0.244	0.243
173.1	33.04	0.103	0.079	0.182	0.089	0.192	0.157	0.227	0.224
163.2	34.00	0.094	0.075	0.168	0.084	0.178	0.140	0.207	0.208
153.3	34.95	0.085	0.070	0.155	0.079	0.163	0.125	0.196	0.199
143.4	35.86	0.076	0.066	0.141	0.074	0.149	0.110	0.177	0.180
133.6	36.74	0.067	0.061	0.128	0.069	0.136	0.097	0.158	0.162
123.7	37.59	0.059	0.057	0.115	0.063	0.122	0.085	0.136	0.139
113.8	38.38	0.050	0.052	0.102	0.058	0.109	0.074	0.112	0.115
103.9	39.10	0.043	0.047	0.090	0.053	0.096	0.064	0.102	0.100
94.0	39.75	0.035	0.043	0.078	0.048	0.083	0.054	0.087	0.086
84.1	40.31	0.028	0.038	0.067	0.043	0.071	0.046	0.073	0.071
74.2	40.75	0.022	0.034	0.056	0.038	0.060	0.038	0.064	0.063
64.3	41.04	0.016	0.029	0.046	0.033	0.049	0.031	0.050	0.050
54.4	41.14	0.012	0.025	0.036	0.028	0.040	0.025	0.038	0.040
44.6	40.98	0.008	0.020	0.028	0.023	0.030	0.019	0.022	0.023
34.7	40.45	0.004	0.016	0.020	0.018	0.022	0.014	0.011	0.012
24.8	39.34	0.002	0.011	0.013	0.013	0.015	0.010	0.007	0.007
14.9	37.14	0.001	0.007	0.008	0.008	0.008	0.006	0.003	0.003
5.0	31.81	0.000	0.002	0.002	0.003	0.003	0.002	0.000	0.000

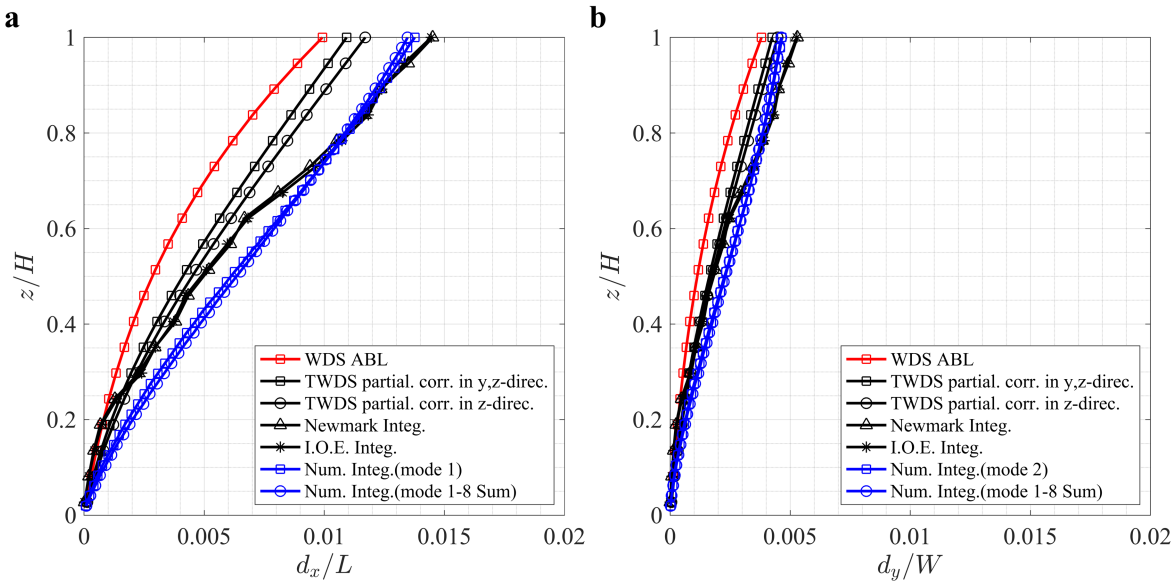


Figure 5-4. Reduced lateral displacements with varying heights: (a) In x-direction; (b) In y-direction.

5.4.2 Simulation of downburst wind field

This section illustrates the process for the simulation of downburst wind data series. These data series were applied to the model as well as for the two validation stages of the developed TWDS subjected to TS downburst wind, reported in Section 5.4.3 and Section 5.4.4.

The generation of random fluctuating velocity time series is built up in four steps based on the spectral representation (Priestley, 1965). Those steps are: (1) Obtain the EPSD matrix proposed by Chen and Letchford (2004a); (2) Do the Cholesky decomposition of the cross-spectral density matrix; (3) Follow a random stationary Gaussian stochastic process (Deodatis, 1996); and (4) Generate data series with fast Fourier transformations.

In parallel to the TWDS technique, this approach used 19 recording stations to match the vertical position of the benchmark building described in Figure 5-2 (b). The cut-off circular frequency is assumed to be 4 rad/s, and the number of circular frequency steps, N, is equal to

2048. It is reasonable to assume the sampling frequency of the simulated fluctuation is equal to 2.56 Hz.

The PSD function (see Eq. (1.29c)) of the longitudinal fluctuating velocity with unit standard deviation at different heights is computed in Figure 5-5 (a) and the corresponding coherence function (see Eq. (2.18)) between different heights is shown in Figure 5-5 (b). The higher nodes have more turbulence in the lower frequency range, which contains large eddies produced by wind gusts, while PSD in the lower nodes distributes more energy in the higher frequency range, which contains more small eddies. Furthermore, it is obvious that the closer the two points are, the higher the coherence function.

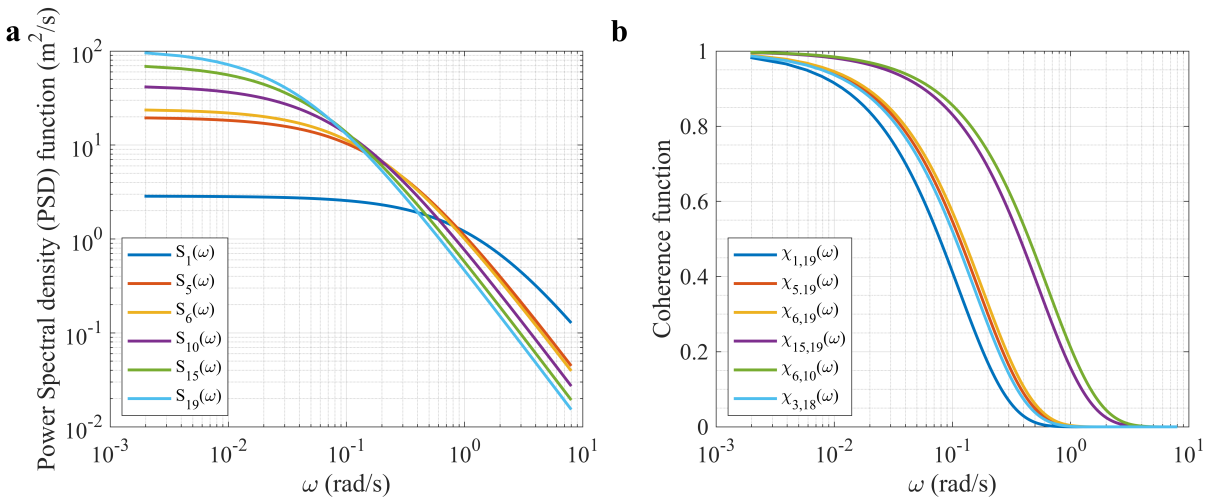


Figure 5-5. (a) PSD function at different levels; (b) Coherence function between any two vertical points.

The simulated rapidly varying fluctuating velocity time history, labelled as $\tilde{u}'$, is demonstrated in Figure 5-6 purple line. The amplitude modulation factor ($\bar{I}_u(z)$) of a linear relationship with varying height obtained from experiments is adopted to obtain the fluctuating velocity time history, u' (i.e. $u'(z,t) = a(z,t)\kappa(z,t)$, $a(z,t) = \bar{I}_u(z)\bar{U}(z,t)$, where $\kappa(z,t)$ represents a stationary Gaussian stochastic process and $a(z,t)$ is the amplitude modulation function). Combining with Eq. (1.24) - Eq. (1.28) of the vertical shape function of horizontal wind and

the time function of the velocity time series of the downburst, the overall velocity time series is illustrated in the blue line of Figure 5-6. The 3-second peak velocity time history is adopted for the further validation of TWDS.

The comparison of the target PSD, $S_{i,i}(\omega)$, of the sample function $\kappa(z_i,t)$ and the corresponding PSD estimated from the simulation of $\kappa(z_i,t)$ is shown in Figure 5-7. The PSD of $\kappa(z_i,t)$ is expressed as $\varphi(z,\omega)=\frac{18\left(\frac{z}{U_{max(z)}}\right)}{\left[1+27\left(\frac{\omega z}{2\pi U_{max(z)}}\right)\right]^{5/3}}$ with $\int_{-\infty}^{+\infty}\varphi(z,\omega)d\omega=1$. The target cross-correlation function $R_{i,j}$ of $\kappa(z_i,t)$ and $\kappa(z_j,t)$ and the corresponding cross-correlation function computed from the simulated $\kappa(z_i,t)$ and $\kappa(z_j,t)$ are shown in Figure 5-8, which demonstrates consistency between the simulated results and the target expectations.

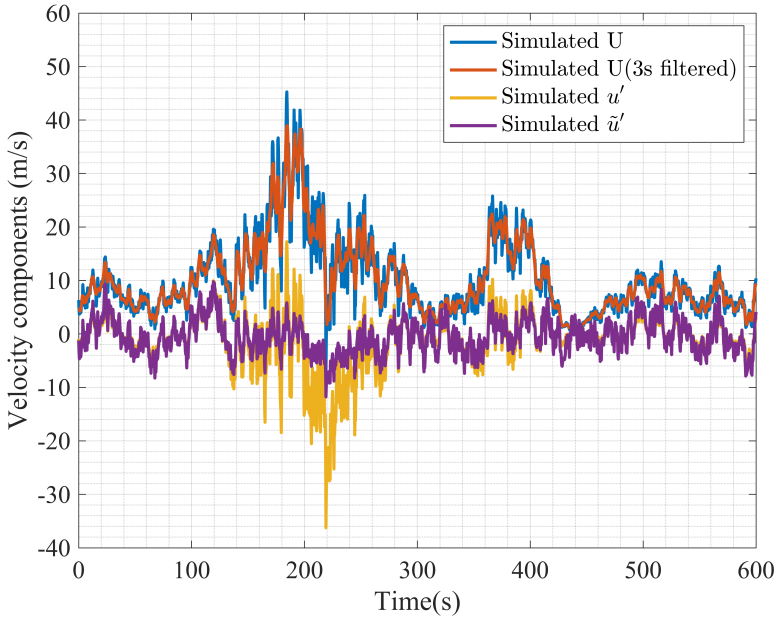


Figure 5-6. Simulated velocity time series of horizontal wind at top of the building.

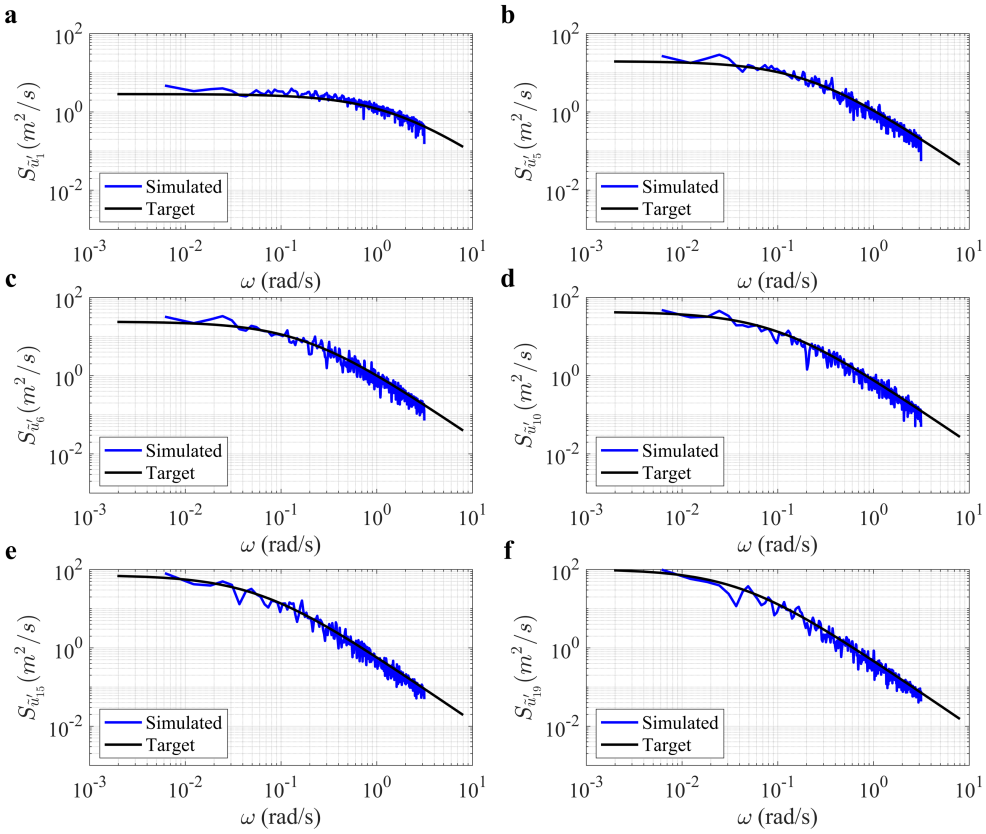


Figure 5-7. Comparison of the PSD function between the simulated time history and the target.

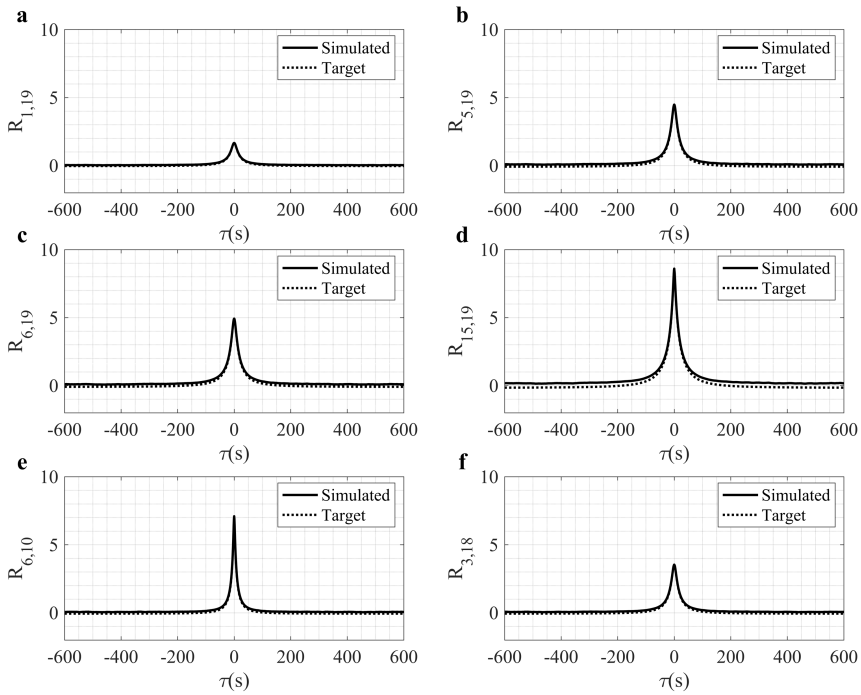


Figure 5-8. Comparison of the cross-correlation function between the simulated time history and the target.

5.4.3 Validation Stage 1: Based on Numerical Integration

The peak displacements calculated from the simulated wind field using time series analysis methods, i.e. the Newmark method and interpolation of excitation method (IOE) (detailed in Chopra (2011)), are illustrated in Table 5-2. In this case, the simulated wind time histories are applied for numerical integration. Different from Eq. (2.26b), the first modal force is calculated by Eq. (5.3).

$$\bar{f}_1(z_i,t) = c_D \times 0.5\rho W(L)\overline{U}^2(z_i,t)\sum_1^i\left[\int_{z_i}^{z_{i+1}}\alpha^2(z)\phi_1(z)dz\right] \tag{5.3}$$

In the wind field simulation, the synthetic velocity time history only considers the coherence function in the vertical direction, which results in higher displacements than those from TWDS, where the coherence functions in the horizontal and vertical directions are considered. When the same turbulent coherence condition is considered, the displacements obtained from the numerical integration are slightly higher than those from the TWDS, and the ratios between these are around 1.24 for the Newmark method and 1.23 for the IOE method.

5.4.4 Validation Stage 2: Based on FEM Modelling

The CAARC standard building has been modelled as a high-rise steel structure in SAP2000 V21 (Ondrej, 2013). The span in the transverse direction is 5.75 m × 8 and the span in the longitudinal direction is 5 m × 6 (see Figure 5-9 (a)). The building height integrates 3.6 m (ground floor) and 3.9 m × 46 (number of storeys) (see Figure 5-9 (b) and (c)). The inverted V-shaped braces are mounted in the intermediate two frames on each floor along the longitudinal direction. The gravity force of each floor is 8439 kN (7790 kN for the first floor),

which has been applied as concentrated loads on all the joints of every storey uniformly. The sectional design is detailed in Table 5-3.

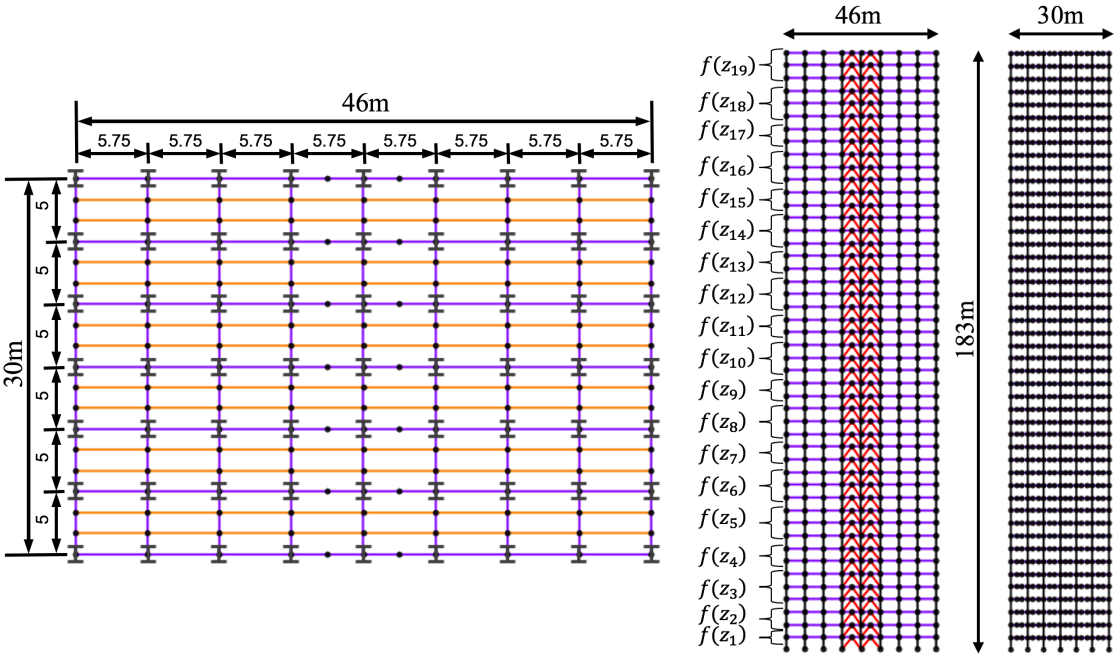


Figure 5-9. The layout of each storey for CAARC benchmark building: (a) Building plan; (b) Elevation section in x-direction; (c) Elevation section in y-direction.

Table 5-3. Design and modal properties.

Storey	Columns	Primary beams	Secondary beams	Brace in x-direction
1-20	HE1000M	HE800A	HE650A	HE320A
21-40	HE900B	HE800A	HE650A	HE320A
41-47	HE800B	HE800A	HE650A	HE320A
Material grades	S355	S275	S275	S235

The modal frequencies of the first ten modes of this building are illustrated in Table 5-4. The simulated transient force time history ($f(z) = c_d 0.5\rho U(z,t)^2 W(L) H_{storey}$, c_d =1.2 in x-direction and c_d =1.03 in y-direction (calculated from Melbourne (1980)), ρ = 1.225 kg/m^3) has been applied to each floor as the concentrated force acting at all the joints of each floor. The roughness length is assumed to be 0.5. The lateral deformations induced by the downburst outflow in two directions are illustrated in Figure 5-4 and detailed in Table 5-5. The lateral displacement at the top of the building caused by the partially correlated wind load is consistent

with the counterpart resulting from the TWDS, and the induced peak displacements at the top of the building calculated from the TWDS, i.e. 0.351 m is 17.7% lower than the value of 0.413m obtained from the FEM analysis in the x-direction, and the peak displacement of 0.206 m obtained from the TWDS is 3.9% lower than the counterpart, i.e. 0.214 m, taken from the FEM analysis in the y-direction.

Table 5-4. Natural period, frequency, modal mass participate factor for the first ten modes.

Mode	1	2	3	4	5	6	7	8	9	10
Period	4.98	4.95	3.76	1.46	1.43	1.22	0.74	0.73	0.68	0.50
Frequency	0.20	0.20	0.27	0.68	0.70	0.82	1.35	1.37	1.47	2.00
Modal participating mass ratio (Sum UX)	0.70	0.70	0.70	0.70	0.88	0.88	0.88	0.92	0.92	0.94
Modal participating mass ratio (Sum UY)	0.00	0.71	0.71	0.86	0.86	0.86	0.91	0.91	0.91	0.91

In this research, it has been assumed that the fundamental mode is dominant. The comparison of the displacement response from the modal integration for only the first mode and the first eight modes in x-direction, and for only the second mode and first eight modes in y-direction illustrates the rationality of this assumption. The displacement responses at the top of the building for these two conditions are demonstrated in Table 5-5 and only a small difference can be observed since a linear superposition method is considered. In x-direction, the lateral deformation at the top of the building can reach up to 0.413 m when the first mode of vibration is considered, while a minor decline can be found, i.e. 0.404 m, when the first eight modes are linearly added. In y-direction, this value changes from 0.214 m to 0.213 m, which is ignorable. The results from the theoretical numerical integrations, i.e. the Newmark integration and I.O.E integration are obviously higher than the results from the TWDS and modal integration of the modelling when the height is approximately higher than 145 m (see Figure 5-4), while it needs to notice that the simulated downburst outflow is typical for each run. Therefore, the lateral displacements induced by the TS outflow wind load can be represented by only the

consideration of the first mode in x-direction and the second mode in y-direction though the modal participating mass ratio for the first two modes can only reach up to 70%. A slight difference in the response merging the rest of the modes (summarised modal participating mass ratio up to 90%) can be reasonably ignored.

Table 5-5. Lateral displacements on each storey from modal integration by linear add (Unit, Meter).

Storeys	Height	Wind load	x-direction		y-direction	
			Lateral Dis. Mode 1	Lateral Dis. Mode 1-8	Lateral Dis. Mode 2	Lateral Dis. Mode 1-8
47	183.0	$f(z_{19})$	0.413	0.404	0.214	0.213
46	179.1		0.404	0.397	0.211	0.209
45	175.2		0.396	0.389	0.207	0.206
44	171.3	$f(z_{18})$	0.388	0.381	0.203	0.202
43	167.4		0.379	0.373	0.200	0.199
42	163.5		0.370	0.364	0.196	0.195
41	159.6	$f(z_{17})$	0.361	0.356	0.192	0.191
40	155.7		0.351	0.347	0.188	0.187
39	151.8	$f(z_{16})$	0.342	0.338	0.184	0.183
38	147.9		0.332	0.329	0.179	0.179
37	144.0		0.322	0.320	0.175	0.174
36	140.1	$f(z_{15})$	0.313	0.311	0.170	0.170
35	136.2		0.303	0.302	0.166	0.165
34	132.3	$f(z_{14})$	0.293	0.293	0.161	0.160
33	128.4		0.282	0.283	0.156	0.156
32	124.5		0.272	0.274	0.151	0.151
31	120.6	$f(z_{13})$	0.262	0.264	0.146	0.146
30	116.7		0.251	0.254	0.140	0.141
29	112.8	$f(z_{12})$	0.241	0.245	0.135	0.135
28	108.9		0.230	0.235	0.129	0.130
27	105.0		0.220	0.225	0.124	0.125
26	101.1	$f(z_{11})$	0.209	0.215	0.118	0.119
25	97.2		0.199	0.205	0.113	0.114
24	93.3	$f(z_{10})$	0.188	0.195	0.107	0.108
23	89.4		0.178	0.185	0.101	0.103
22	85.5		0.168	0.175	0.096	0.097
21	81.6	$f(z_9)$	0.157	0.165	0.090	0.092
20	77.7		0.147	0.156	0.084	0.086
19	73.8	$f(z_8)$	0.138	0.146	0.079	0.081
18	69.9		0.128	0.137	0.073	0.075
17	66.0		0.119	0.127	0.068	0.070
16	62.1	$f(z_7)$	0.110	0.118	0.062	0.064
15	58.2		0.101	0.109	0.057	0.059
14	54.3	$f(z_6)$	0.092	0.100	0.052	0.054
13	50.4		0.083	0.091	0.046	0.048
12	46.5		0.075	0.082	0.041	0.043
11	42.6	$f(z_5)$	0.067	0.074	0.036	0.038
10	38.7		0.059	0.065	0.032	0.033
9	34.8		0.051	0.057	0.027	0.029
8	30.9	$f(z_4)$	0.044	0.049	0.023	0.024
7	27.0		0.037	0.041	0.019	0.020
6	23.1	$f(z_3)$	0.030	0.034	0.015	0.016
5	19.2		0.023	0.027	0.011	0.012
4	15.3		0.017	0.020	0.008	0.009
3	11.4	$f(z_2)$	0.012	0.014	0.005	0.006
2	7.5		0.007	0.008	0.003	0.003
1	3.6	$f(z_1)$	0.002	0.003	0.001	0.001

5.5 Summary

This chapter further develops a relatively new design spectra technique, in this case, applied to the TS downburst. It is also an attempt to extend the performance-based design philosophy applied in earthquake engineering applications to study wind effects on structures. It builds on previous research that dealt with the TWDS for regular prismatic buildings subjected to stationary winds. The framework of the TWDS technique develops in the time-frequency domain and it takes the PSD of the reduced turbulent fluctuations as its basis. Following classical spectral techniques, spatial correlations of the turbulent fluctuations are used to describe the wind structure in time and space. The robust links between the wind actions and structural response hence derive from the application of coherence and the transfer function, which affect background and resonant components, the latter being the one that triggers higher values of TWDS, evidently linked to the natural vibration of structures. It is also true that higher correlations of wind gusts can induce higher amplitudes of vibrations.

The main findings of this research are illustrated in the following points.

- The investigation into the input parameters of the design spectra illustrates that the design spectra of the output accelerations significantly rise with the increasing velocities of the downburst outflow when the natural frequency descends from 10 Hz to 0.1 Hz. The higher values of the design spectra occur when the aspect ratio and the building's width to chord ratio are lower. Furthermore, variations in the damping ratio are more obvious in the lower frequency range. The changeable heights for the maximum slowly varying mean velocity of the downburst outflow also reflected a slight effect on the design spectra, and the maximum design spectrum is only 0.111 m/s^2 when the height

of this maximum value is 150 m. Finally, a slight influence of the terrain exposures can also be non-negligible.

- The comparison between the results of the TWDS in the time-frequency domain and the equivalent numerical simulation in the time domain, as well as the finite element analysis for the benchmark tall building demonstrate the applicability of the spectral technique. The peak displacement amplitudes calculated from the numerical analysis method and FEM analysis under the simulated outflow wind field are respectively around 24% and 18% higher than those from the TWDS technique in the x-direction, and these differences separately decrease to 18% and 4% in the y-direction. This recently developed TWDS technique provides an alternative to determine the dynamic response induced by the TS downburst; its equivalence with earthquake spectral techniques makes it easy to implement in commercial packages for structural analysis.
- The displacement response for high-rise buildings obtained from TWDS subjected to downburst outflows works under the hypothesis that the turbulence intensity profile for these two wind regimes is the same, which is consistent with previous research. Notably, the outflow induced peak displacement is slightly higher than that triggered by boundary layer wind. However, generally, the turbulence intensity statistically analysed from the recorded full-scale downbursts is slightly lower than those from boundary layer wind according to the previous full-scale downburst records.

The preliminary validations of the TWDS technique are encouraging. This could enable quick yet reliable estimation of the dynamic response of the structures under the impact of the TS downburst, for example, via modal spectral analyses.

The hypothesis of constant turbulence intensity makes the research interesting to investigate the effects of the evolution of the PSD. It is also worth comparing the TWDS technique with other proposed methods employed in the time-frequency domain. The exploration of the pressure coefficients on tall buildings for transient wind loading will also improve the accuracy of this technique.

Chapter 6 Results and discussion of Generalisation of TWDS

This chapter introduces an alternative method to estimate the dynamic response of structures subjected to downburst outflow wind, as proposed by Song et al. (2021b). The proposed spectral generalisation is derived from three-dimensional non-linear regression models of normalised design spectra combined with an existing three-dimensional non-linear polynomial regression model. Section 6.2.1 and Section 6.2.2 present the basic algorithm and preliminary validation of this generalised method. The regression approach identifies the controlling parameters of a surface generated by an ensemble of design spectra to concentrate these on one polynomial equation for practical use. The simulated spectra can be adopted to run standard modal analysis (see Section 2.3.3), as it enables the use of commercial software to determine the displacement amplitude of the structures. Section 6.2.3 illustrates the effectiveness of the simulated non-linear regression model that has been validated by comparing the results obtained through the use of real and simulated spectra for the analysis of the CAARC benchmark building.

6.1 Investigation of input parameters

According to the original formulation used to generate TWDS (see Section 2.3), the multi-dimensional nature of TWDS of the output acceleration can be represented by Eq. (6.1). The input parameters include the maximum slowly varying mean velocity at reference height

($\bar{U}_{max,r}$), the width of the building (W), the chord length (L), the height of the building (H), the height for the maximum slowly varying mean velocity ($z_{U_{max}}$), damping ratio (ξ), structural mass (m_v), drag coefficient (C_D), terrain type, and modal shape factor (ψ).

$$S_a = f(\bar{U}_{max,r}, W, L, H, z_{U_{max}}, \xi, m_v, C_D, terrain, \psi) \quad (6.1)$$

The consequences of the identified input parameters on the TWDS are demonstrated in Figure 6-1. In this formulation, the reference maximum slowly varying mean velocity is a dominant input, as its magnitude covers a large range. For instance, when $\bar{U}_{max,r}$ equals 50 m/s and 70 m/s, respectively, the output structural acceleration S_a varies from 0.292 m/s^2 to 0.652 m/s^2 for a building with a natural frequency of 0.1 s. The effect of the building width can be demonstrated when observing that S_a slightly descends from 0.066 m/s^2 to 0.045 m/s^2 when W increases from 10 m to 50 m, a 32% decrease, for the same fundamental frequency of 0.1 s. Figure 6-1 (c) and Figure 6-1 (d) display the effect of the varying height (from 20 m to 200 m) and chord width (from 8 m to 40 m) on the output acceleration. It is also worth noting that, in the absence of evidence to the contrary, the cross-correlation of input parameters is negligible.

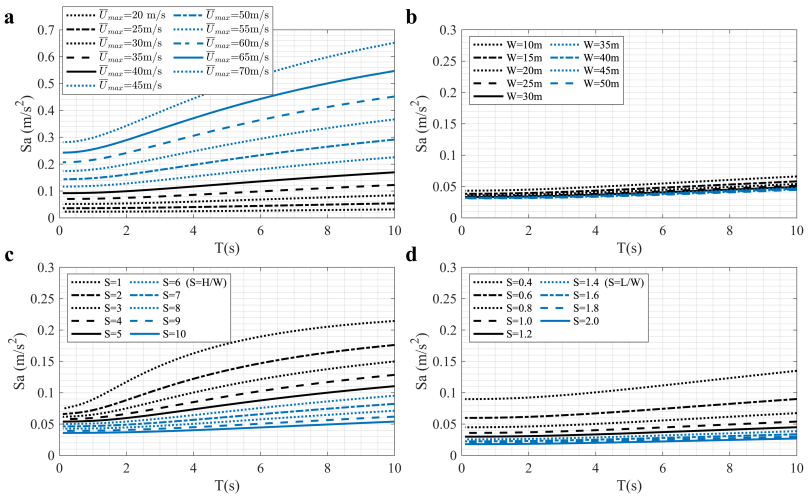


Figure 6-1. TWDS of output acceleration with varying input parameters (Default values: $\bar{U}$max,10=25 m/s, W=20 m, H=200 m, L=20 m, ξ=0.025, $z_{\bar{U}_{max}}$=50 m, Terrain exposure B, m_v=384 kg/m3, c_d=1 and ψ=1.5) (Song et al., 2021b).

6.2 Three-dimensional non-linear regression model

6.2.1 Introduction

Following an examination of several regression techniques, the multi-order polynomial models are chosen. Then, a typical fitting approach is used to optimise scaling factors. Following this optimisation process, the design spectra are simulated through Eq. (6.2). This equation reflects the prominence of the varying $\overline{U}_{max,r}$ and natural frequency while taking into account the effect of all other controlling variables through sub-regression models (scale factors), f_s.

$$\widehat{S_a} = f\left(T, \overline{U}_{max,r}\right) \cdot f_s(T, W) \cdot f_s(T, L/W) \cdot f_s(T, H/W) \cdot f_s(T, \xi) \cdot f_s(T, z_{U_{max}}/H) \cdot f_s(T, terrain) \cdot f_s(T, \psi) \cdot f_s(T, m_v) \cdot f_s(T, c_d) \quad (6.2)$$

Note in this equation the change to non-dimensional variables such as chord to width (L/W), height to width (H/W) and $z_{U_{max}}/H$ ratio which modifies Eq. (6.1) as in Eq. (6.3).

$$S_a = f(\overline{U}_{max,r}, W, L/W, H/W, z_{U_{max}}/H, \xi, m_v, c_D, terrain, \psi) \quad (6.3)$$

Furthermore, the non-linear relationship of the TWDS, T and $\overline{U}_{max,r}$ define a three-dimensional surface as presented in Figure 6-2, abstracted in the three-order polynomial regression model given by Eq. (6.4).

$$\widehat{S_{a,u}} = b_1 + b_2\overline{U}_{max,r} + b_3T + b_4\overline{U}^2_{max,r} + b_5T^2 + b_6T\overline{U}_{max,r} + b_7\overline{U}^3_{max,r} + b_8\overline{U}^2_{max,r}T + b_9\overline{U}_{max,r}T^2 + b_{10}T^3 \quad (6.4)$$

In this equation, $T = T + \Delta T_0$ and $\overline{U}_{max,r} = \overline{U}_{max,r} + \Delta\overline{U}_{max,r,0}$. The unknown parameters b_j were adjusted to minimise the discrepancy between the TWDS and the non-linear regression

model (NLRM). This difference was calculated using $\underset{b_{j,p}}{min}\sum_{i=1}^{n}(\frac{\widehat{S_{a,i}}-S_{a,i}}{S_{a,i}})^2$, where n denotes the number of data points, i denotes an index for the current TWDS values, j represents the index of the unknown sequence of scaling factors, and p denotes the random input parameters (in this instance, $\overline{U}_{max}$). As a result, the mean square error of the proposed model is $\frac{1}{n}\sum_{i=1}^{n}(\widehat{S_{a,i}}-S_{a,i})^2$.

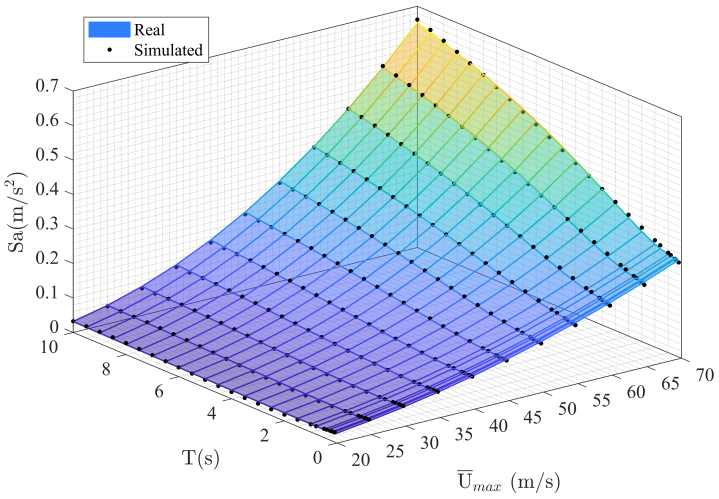


Figure 6-2. Comparison between the real and simulated values of TWDS with varying T and $\overline{U}_{max}$ (Song et al., 2021b).

As a result, changes in spectral ordinates with respect to other controlling parameters can be determined using independent polynomial regression modelling, which brings in the relationship $S_{a,P}/S_{a,P_d}$ - where P_d is a randomly selected controlling parameter. Eq. (6.5) provides such a mathematical definition.

$$\widehat{S_{a,P}}/\widehat{S_{a,P_d}} = b_{1,P} + b_{2,P}P + b_{3,P}T + b_{4,P}P^2 + b_{5,P}T^2 + b_{6,P}TP + b_{7,P}P^3 + b_{8,P}P^2T + b_{9,P}PT^2 + b_{10,P}T^3 \quad (6.5)$$

With this in hand, the TWDS can be finally obtained with Eq. (6.6).

$$\widehat{S_a} = \widehat{S_{a,U_{max}}} \times \left(\widehat{S_{a,W}}/\widehat{S_{a,W_d}}\right) \times \left(\widehat{S_{a,L/W}}/\widehat{S_{a,(L/W)_d}}\right) \times \left(\widehat{S_{a,H/W}}/\widehat{S_{a,(H/W)_d}}\right) \times \left(\widehat{S_{a,\xi}}/\widehat{S_{a,\xi_d}}\right) \times \left(\widehat{S_{a,z_{U_{max}}}}/\widehat{S_{a,(z_{U_{max}})_d}}\right) \times \left(\widehat{S_{a,\psi}}/\widehat{S_{a,\psi_d}}\right) \times \left(\widehat{S_{a,m_v}}/\widehat{S_{a,(m_v)_d}}\right) \times \left(\widehat{S_{a,c_d}}/\widehat{S_{a,(c_d)_d}}\right) \times \left(\widehat{S_{a,terrain}}/\widehat{S_{a,(terrain)_d}}\right) \quad (6.6)$$

In this context, the variation of the main polynomial regression model with respect to any controlling parameter is inferred. Eq. (6.7) is illustrated by using the width of the building.

$$\widehat{S_{a,W}}\Big/\widehat{S_{a,W_d}} = b_{1,W} + b_{2,W}W + b_{3,W}T + b_{4,W}W^2 + b_{5,W}T^2 + b_{6,W}TW + b_{7,W}W^3 + b_{8,W}W^2T + b_{9,W}WT^2 + b_{10,W}T^3 \quad (6.7)$$

The optimised scaling factors used to fit the three-dimensional NLRM of the TWDS and normalised TWDS are presented in Table 6-1. The root mean square error (RMSE) between the simulated and real TWDS with variable velocity is 0.0036 in this scenario (see - Figure 6-2).

Table 6-1. Scaling factors for three-dimensional NLRM of the TWDS and normalised TWDS.

	TWDS $\widehat{S_{a,\bar{U}_{max}}}$	Normalised TWDS ($\widehat{S_{a,P}}/\widehat{S_{a,P_d}}$)								
Inputs, P	$\bar{U}_{max}$ (m/s)	$W(m)$	L/W	H/W	ξ	$z_{\bar{U}_{max}}$ $/H$	Terrain	ψ	m_v (kg/m^3)	c_d
Initials	25	20	1	10	0.025	50	B	1.5	384	1
$b_{1,P}$	-0.0044	8.6196	6.8902	2.4571	1.0110	-0.4401	1.6860	0.7397	6.4135	0.0000
$b_{2,p}$	0.0013	-1.1379	-18.3407	-1.7015	-0.8597	7.6957	-0.1931	0.3502	-0.0383	1.0000
$b_{3,P}$	-0.0084	0.4278	0.0016	0.5236	0.0240	-0.0278	0.0001	0.0145	0.0004	-0.0000
$b_{4,P}$	0.0000	0.0691	24.3069	0.6987	9.9217	-9.1043	-0.1227	-0.1594	0.0001	-0.0000
$b_{5,P}$	0.0027	0.0257	-0.0005	0.0333	-0.0046	0.0031	-0.0000	-0.0000	-0.0000	0.0000
$b_{6,p}$	-0.0003	-0.0578	-0.0021	-0.3223	-0.4193	0.1001	-0.0000	-0.0157	-0.0000	0.0000
$b_{7,p}$	0.0000	0.0000	-17.0451	-0.1304	-26.8763	3.7998	0.0239	0.0279	-0.0000	0.0000
$b_{8,p}$	0.0000	0.0025	0.0010	0.0578	1.1876	-0.0246	0.0000	0.0035	0.0000	-0.0000
$b_{9,P}$	0.0000	0.0001	0.0004	0.0201	-0.0037	-0.0032	0.0000	0.0002	0.0000	-0.0000
$b_{10,P}$	-0.0001	-0.0058	0.0001	-0.0160	0.0003	-0.0002	0.0000	-0.0000	0.0000	-0.0000
RMSE	0.0036	0.0141	0.0042	0.0265	0.0303	0.0134	0.0000	0.0005	0.0078	0.0000

6.2.2 Validation of non-linear regression model

The comparisons of the normalised design spectra between the real and simulated values are shown in Figure 6-3 and Figure 6-4. The root mean square errors (RMSE) of these comparisons are summarised in Table 6-1.

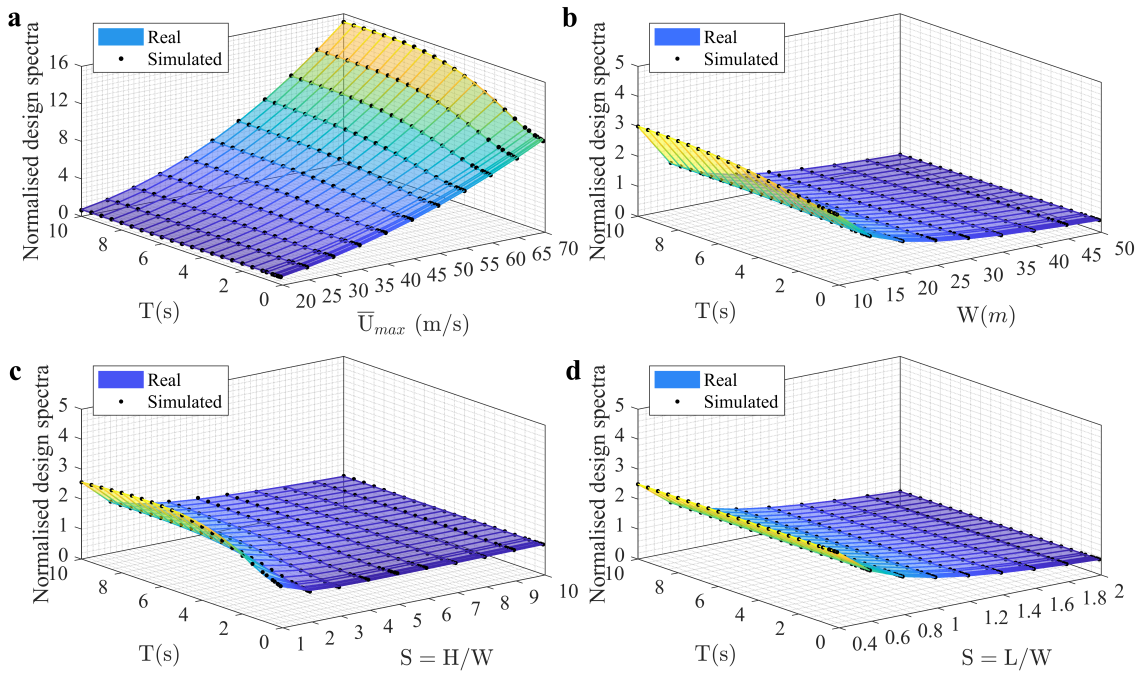


Figure 6-3. Comparison between the normalised TWDS and normalised non-linear regression model for varying input parameters: (a) $\overline{U}_{max}$; (b) Structural width exposed to wind action; (c) H/W; (d) L/W.

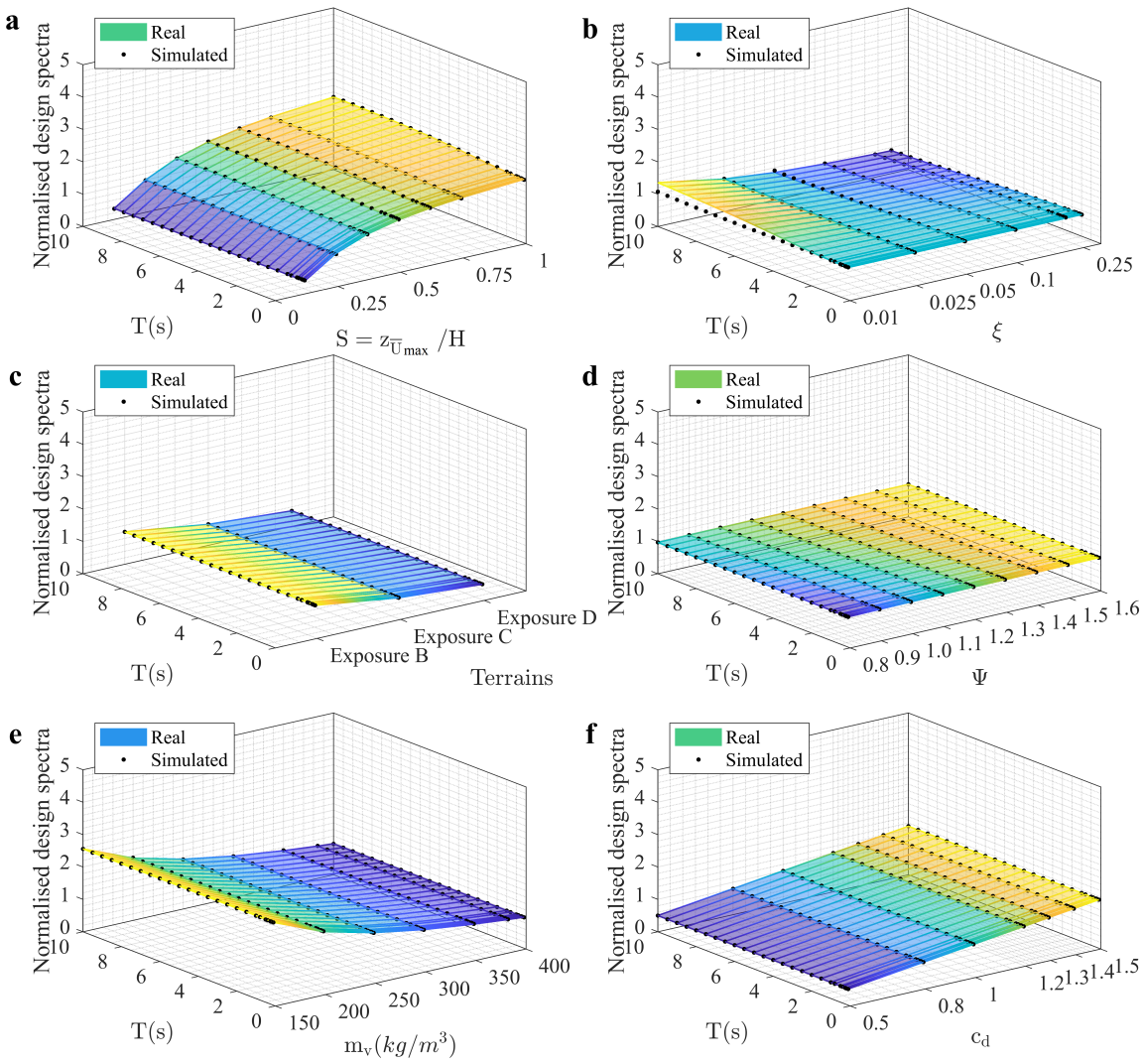


Figure 6-4. Comparison between the scaled TWDS and scaled non-linear regression model for varying input parameters: (a) $z_{\bar{U}_{max}}$; (b) Damping ratio; (c) Terrain categories; (d) ψ; (e) m_v; (f) c_d.

The comparisons of the real and simulated TWDS based on the proposed NLRM are shown in Figure 6-5 and Figure 6-6. The RMSE between the real and simulated TWDS are shown in Table 6-2 to Table 6-4.

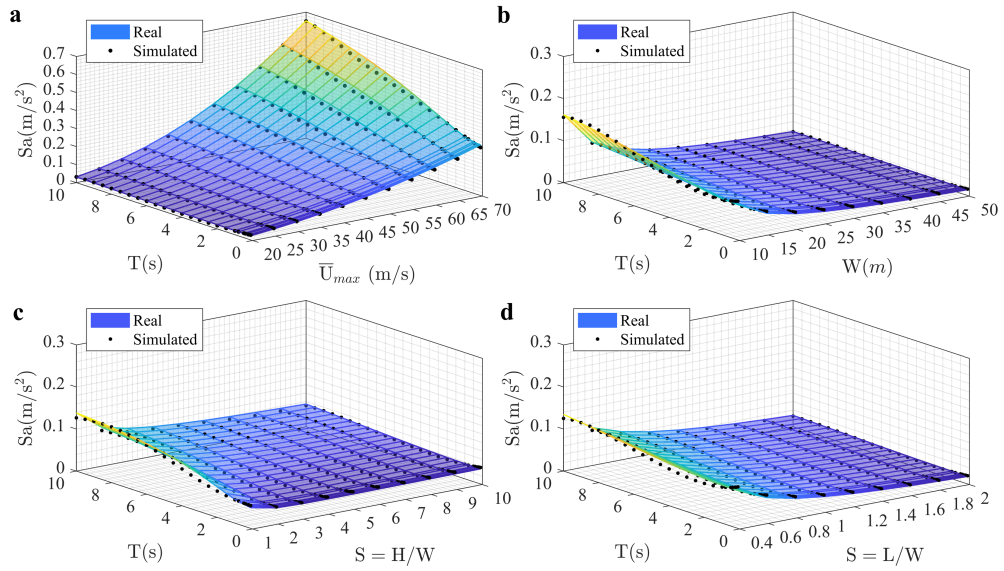


Figure 6-5. Comparison between the real and simulated TWDS considering local variations of input parameters: (a) $\bar{U}_{max}$; (b) W; (c) H/W; (d) L/W (Song et al., 2021b).

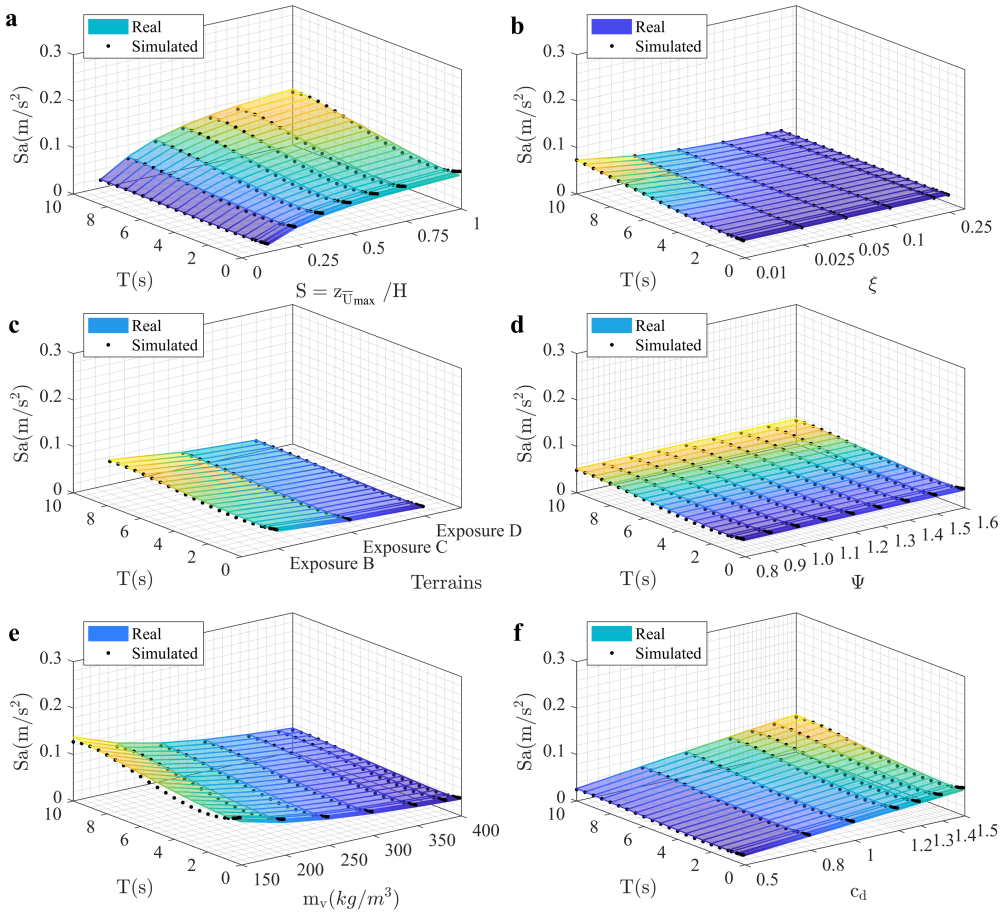


Figure 6-6. Comparison between the real and simulated TWDS for varying input parameters: (a) $z_{\bar{U}_{max}}$; (b) Damping ratio; (c) Terrain categories; (d) ψ; (e) m_v; (f) c_d.

The largest estimated error (14.36%) for these values occurs at a velocity of 20 m/s. Note that the error parameter remains below 7.6% when the velocity is equal to or greater than 25 m/s. The maximum error ratios of the simulated TWDS with varying W, H/W and L/W equal 8.29%, 8.18% and 8.02%, respectively.

Table 6-2. RMSE for varying parameters - Part 1 (Song et al., 2021b).

$U_{max,r}$ (m/s)	$\sqrt{e^2}$	S_a	$\sqrt{e^2}/S_a$	W (m)	$\sqrt{e^2}$	S_a	$\sqrt{e^2}/S_a$	H/W	$\sqrt{e^2}$	S_a	$\sqrt{e^2}/S_a$
20	0.0037	0.0258	0.1436	10	0.0077	0.1144	0.0671	1	0.0078	0.0950	0.0818
25	0.0032	0.0421	0.0760	15	0.0040	0.0622	0.0638	2	0.0032	0.0615	0.0516
30	0.0032	0.0632	0.0509	20	0.0032	0.0421	0.0760	3	0.0042	0.0526	0.0806
35	0.0037	0.0896	0.0418	25	0.0023	0.0318	0.0721	4	0.0037	0.0485	0.0754
40	0.0048	0.1216	0.0393	30	0.0018	0.0255	0.0718	5	0.0033	0.0461	0.0717
45	0.0063	0.1594	0.0394	35	0.0015	0.0214	0.0712	6	0.0033	0.0446	0.0730
50	0.0082	0.2034	0.0405	40	0.0014	0.0185	0.0743	7	0.0035	0.0436	0.0793
55	0.0107	0.2537	0.0421	45	0.0011	0.0163	0.0656	8	0.0034	0.0429	0.0784
60	0.0137	0.3106	0.0440	50	0.0012	0.0146	0.0829	9	0.0028	0.0424	0.0672
65	0.0172	0.3743	0.0460					10	0.0032	0.0421	0.0760
70	0.0215	0.4449	0.0483								

S_a is the mean value of the real TWDS of the output acceleration with varying T (natural period).

With altering the damping ratio, the largest inaccuracy (19.74%) occurs when this parameter is set to 0.01. The RMSE floats at 8% when the damping ratio is increased. The predicted errors are smaller than 8.43% when the modal shape factor (φ), the structural mass per unit volume (m_v), the terrain and the ratio of the $z_{U_{max}}/H$ are varied.

Table 6-3. RMSE for varying parameters - Part 2 (Song et al., 2021b).

L/W	$\sqrt{e^2}$	S_a	$\sqrt{e^2}/S_a$	ξ	$\sqrt{e^2}$	S_a	$\sqrt{e^2}/S_a$	φ	$\sqrt{e^2}$	S_a	$\sqrt{e^2}/S_a$
0.4	0.0081	0.1052	0.0768	0.01	0.0097	0.0493	0.1974	0.8	0.0030	0.0400	0.0751
0.6	0.0053	0.0701	0.0752	0.025	0.0032	0.0421	0.0760	0.9	0.0030	0.0405	0.0752
0.8	0.0042	0.0526	0.0794	0.05	0.0030	0.0392	0.0767	1.0	0.0031	0.0408	0.0753
1.0	0.0032	0.0421	0.0760	0.1	0.0031	0.0376	0.0823	1.1	0.0031	0.0412	0.0754
1.2	0.0026	0.0351	0.0740	0.2	0.0031	0.0368	0.0840	1.2	0.0031	0.0414	0.0755
1.4	0.0023	0.0301	0.0775	0.25	0.0030	0.0366	0.0821	1.3	0.0032	0.0417	0.0757
1.6	0.0021	0.0263	0.0802					1.4	0.0032	0.0419	0.0758
1.8	0.0017	0.0234	0.0735					1.5	0.0032	0.0421	0.0760
2.0	0.0016	0.0210	0.0775					1.6	0.0032	0.0423	0.0760

Table 6-4. RMSE for varying parameters - Part 3 (Song et al., 2021b).

m_v (kgm^{-3})	$\sqrt{e^2}$	S_a	$\sqrt{e^2}/S_a$	$Terr.$	$\sqrt{e^2}$	S_a	$\sqrt{e^2}/S_a$	$z_{U_{max}}/H$	e^2	S_a	$\sqrt{e^2}/S_a$
150	0.0085	0.1077	0.0789	B	0.0032	0.0421	0.076	0.125	0.0012	0.0147	0.0843
200	0.0061	0.0808	0.0752	C	0.0021	0.0272	0.076	0.250	0.0032	0.0421	0.0760
250	0.0052	0.0646	0.0811	D	0.0015	0.0201	0.076	0.375	0.0042	0.0596	0.0703
300	0.0043	0.0539	0.0805					0.5	0.0048	0.0704	0.0678
350	0.0034	0.0462	0.0747					0.625	0.0053	0.0776	0.0686
384	0.0032	0.0421	0.0760					0.75	0.0060	0.0827	0.0722
400	0.0033	0.0404	0.0815					1	0.0060	0.0894	0.0674

Finally, Figure 6-7 depicts the discrepancies discovered in six distinct circumstances. The RMSE for these six situations is 0.0032, 0.0244, 0.0113, 0.0118, 0.0349, and 0.0174, respectively, with a maximum error of less than 3.5%.

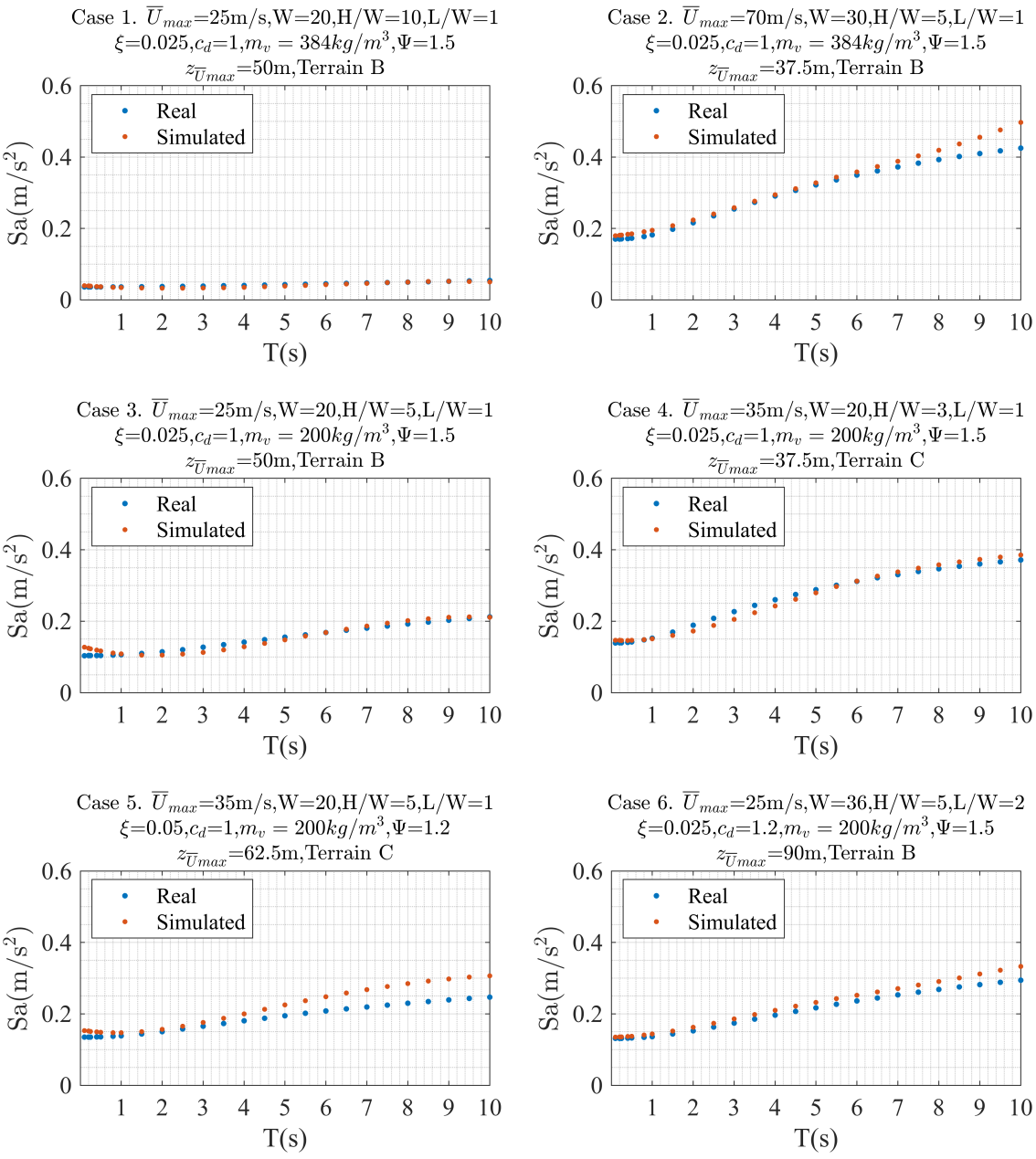


Figure 6-7. Comparison of real and simulated design spectra for scenarios (Song et al., 2021b).

6.2.3 Application on CAARC benchmark tall building

The benchmark building described in Section 5.2 has been used in a conventional modal analysis using the simulated TWDS. The sum of the static displacement and the *rms* of the dynamic displacement yields the peak displacement response. The real and simulated dynamic displacements at the structural roof level are shown in Table 6-5. The research investigated two

scenarios: (a) horizontal and vertical wind fluctuations, and (b) wind gusts that were only moderately associated in the vertical direction. This leads to a peak displacement of 0.328 m and 0.351 m at the top of the building for scenarios (a) and (b), respectively. When synthetic design spectra are used, the corresponding displacements are 0.328 m and 0.341 m, respectively. This results in differences of 0% and 9.7% for these two scenarios, being the most accurate simulation, whose actual spectra have taken into consideration of the horizontal and vertical gust correlation. These results are demonstrated in Figure 6-8, where d_x and d_y denote the lateral displacement amplitudes at various heights in the x and y directions, respectively.

Table 6-5. Lateral displacements at the structural roof level.

Direction	$\overline{U}_H$ (ms^{-1})	Static $\Delta = f_1/k_1$	Davenport's coherence (vertical and horizontal)				Partial correlated (vertical only)			
			Real Dyna.	Simu. Dyna.	Real Total	Simu. Total	Real Dyna.	Simu. Dyna.	Real Total	Simu. Total
x	32.06	0.200	0.128	0.128	0.328	0.328	0.151	0.141	0.351	0.341
y	32.06	0.112	0.084	0.067	0.196	0.179	0.094	0.072	0.206	0.184

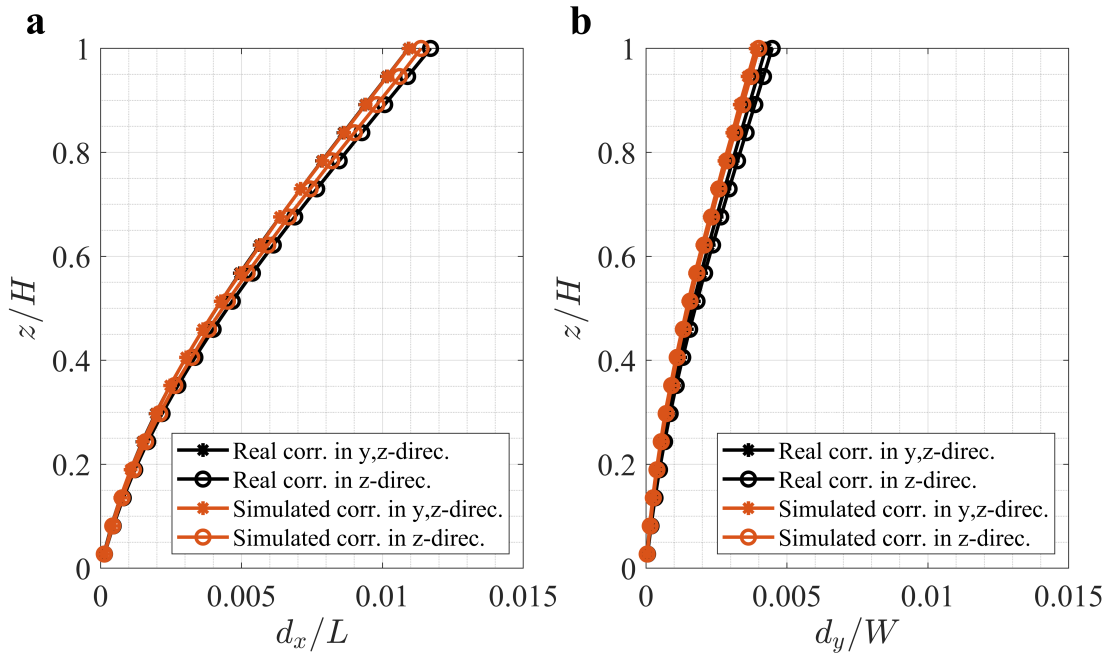


Figure 6-8. Comparisons for the lateral displacements with varying heights: (a) In x-direction; (b) In y-direction.

6.3 Summary

This chapter demonstrates how a non-linear regression model can be used to generalise the created TWDS (detailed in Chapter 5) using random input variables. This regression technique condenses the governing input parameters into a single polynomial equation, significantly simplifying the process of deriving design spectra, which was previously done on a one-by-one basis, i.e. taking into consideration mechanical and aerodynamic features of structures. The regression model's accuracy was evaluated using a variety of situations in which the controlling parameters varied randomly. This estimated RMSE of actual and simulated spectra is less than 3.5%. After that, real and synthetic design spectra were utilised to conduct a conventional model analysis to verify the effectiveness of this approach. The dynamic analysis was conducted on a benchmark structure with regular geometry and homogeneous mass distribution, which revealed variances in peak dynamic displacements of less than 10%. This shows that the synthetic TWDS can be a viable option for designers looking for a rapid way to compute the dynamic response of buildings.

Chapter 7 Results and discussion of ductility demands for damaged tall steel structures under downburst wind loading

Since the dynamic response of structures under the influence of the TS downburst can be effectively estimated by the TWDS technique, it is necessary to further understand the structural performance, i.e. the ductility demand and collapse mechanisms of buildings under the influence of the TS downburst. Hence, the novel computational procedure presented in Section 2.4 is adopted in this section for investigating the downburst-induced ductility demands of damaged tall steel structure. The computational procedure proposed in Section 2.4 combines the step-by-step nonlinear adaptive pushover analysis with the dynamic time history analysis within a restart analysis framework to obtain the base shear-roof displacement relationship for different damage levels. Accordingly, the global plastic deformation mechanism that leads to collapse can be identified.

This chapter aims to primarily validate this novel algorithm on a tall steel building and the results are discussed. Section 7.1 introduces the design of a 20-storey tall steel building. Section 7.2 demonstrates the initial model analysis, including steps 1-3 of the multi-hazard analysis framework (see Section 2.4.2). Section 7.3 illustrates the simulation of eleven downburst wind

fields which were applied to the designed building as secondary hazards, and the results are discussed in Section 7.4.

7.1 Introduction of tall steel building

In this investigation, a 20-storey building frame designed according to the Uniform Building Code (1994) is created in ABAQUS using beam elements, as shown in Figure 7-1. The height of the building is 78.68 m including the basement. The ground and the first floor have a 4.57 m height, while all other floors have each a 3.66 m incremented height. The plan view dimensions of the building are 36.6 m × 24.4 m with a 6.1 m bay width in either direction. The terrain type for wind design is exposure B with a basic wind speed of 31 m/s, and earthquake-resisting design is for Zone 4 and soil type S2. The seismic base shear coefficient is 0.03 while the drift limitation is 0.025. Gravity loads acting on floors equal 6.23 kPa and 3.59 kPa acting on the roof, which complements with a cladding load of 1.44 kPa.

The pushover and wind load are applied in the weak direction of the building, as shown in Figure 7-1. Considering the symmetry of this building, one exterior moment resisting frame (MRF) and one interior equivalent gravity frame (GF) are considered to represent half of the building and to simulate the second-order effects. The columns in the interior equivalent GF are defined by the generalised sectional properties. The sectional area and the moment of inertia in major and minor directions for the columns have been appropriately scaled to represent 2½ gravity frames, i.e. 2.5 times the original values. Concentrated masses have been assigned to the building joints.

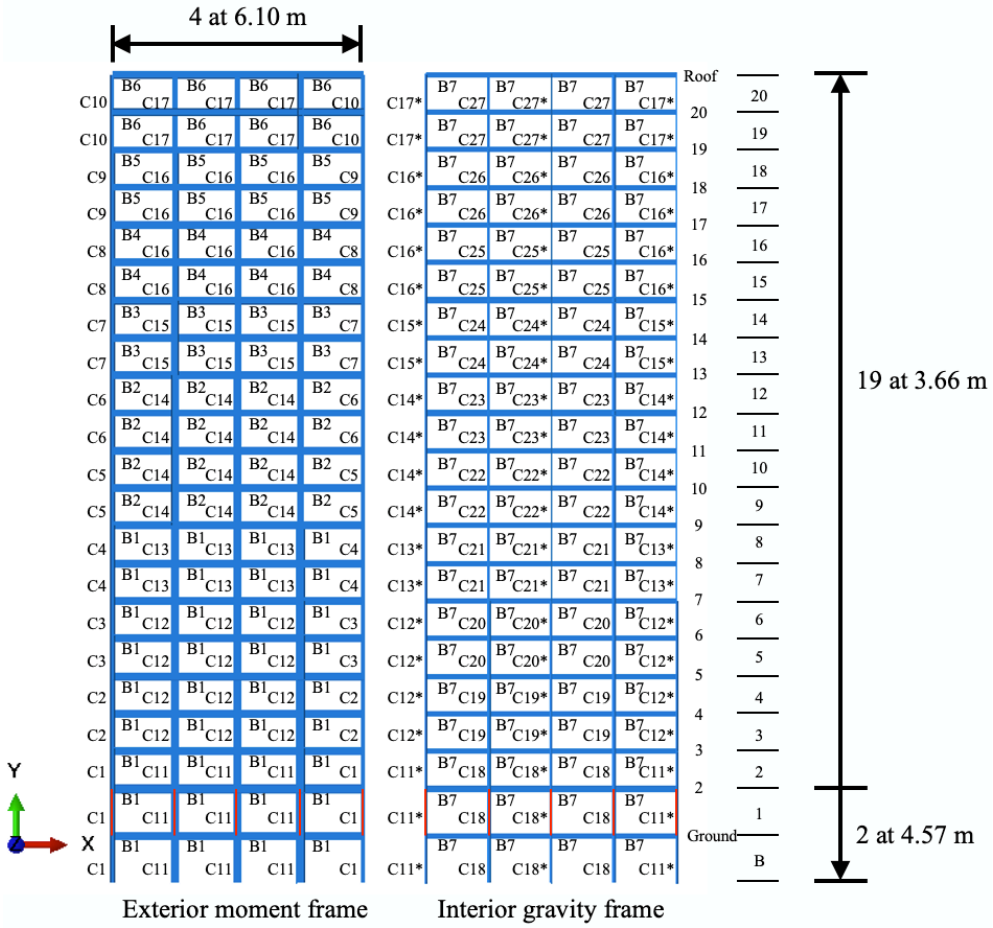


Figure 7-1. Basic information of frames for the 20-storey steel building, * represents weak axis orientation (Hall, 2017).

Table 7-1. The dimensions for the column and beam elements of 20-storey frame building in Figure 7-1 (Hall, 2017).

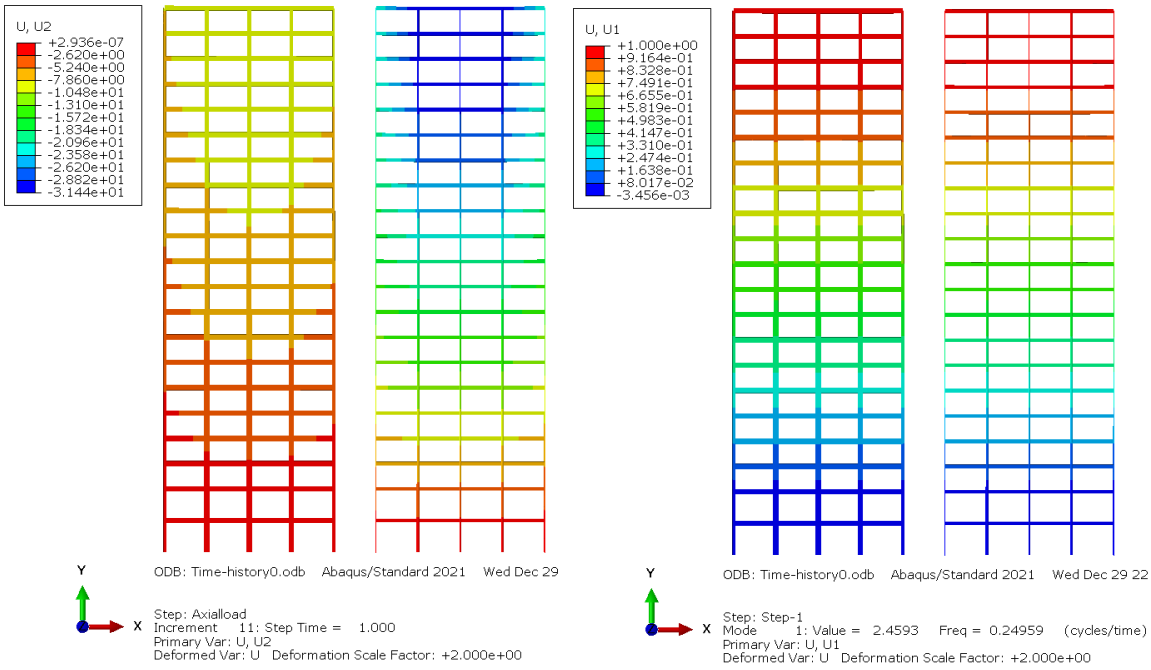
Label	Element	Label	Element	Label	Element
C1	W14X370	C13	W30X173	C25	W14X74
C2	W14X342	C14	W27X178	C26	W14X61
C3	W14X311	C15	W24X162	C27	W14X53
C4	W14X283	C16	W24X146	B1	W30X124
C5	W14X257	C17	W21X122	B2	W30X116
C6	W14X211	C18	W14X176	B3	W30X108
C7	W14X176	C19	W14X159	B4	W30X99
C8	W14X159	C20	W14X145	B5	W27X94
C9	W14X132	C21	W14X120	B6	W27X84
C10	W14X109	C22	W14X109	B7	W21X50
C11	W30X211	C23	W14X99		
C12	W30X191	C24	W14X90		

These two adjacent frames are connected at the level of each storey through pinned Link type of MPC (i.e. multi-point constraints) to approximately represent diaphragmatic rigidity. Steel is modelled as a bilinear elastic isotropic material with modulus of elasticity E=210 GPa, density ρ=7850 kg/m^3 and Poisson ratio ν=0.3. The half weight of this building is 54.46 MN. The yield strength of the steel is 248 MPa and the ultimate strength is 400 MPa.

The bottom of the basement columns of the building frame has been fully constrained, and the ground floor has been laterally restrained. The beam connections in the exterior moment frame are fully fixed, and the beam connections in the interior GF are fully pinned connections. The sectional designs for the columns and beams of the building model are given in Table 7-1.

7.2 Model analysis

This procedure starts from the analysis of the axial load and frequency analysis as shown in Figure 7-2. The fundamental natural period of the building is 4.01 seconds, which is higher than the value of 3.63 seconds of Hall (2017) since the beam ends of the GF in the present study have been simulated as perfect pins. In Hall (2017)'s model, the strength and stiffness of beams of the GF were reduced by 90% to simulate pinned connections, which explains the lower natural period.



(a) (b)

Figure 7-2. Displacement distribution: (a) Gravity load; (b) Frequency analysis.

Figure 7-3 (a) compares the pushover curves as obtained from the present ABAQUS model with results based on three case studies examined by Hall (2017). Hall (2017) examined three different simulation techniques for the steel building: (a) the Case A where strength and stiffness of the GF were ignored in the modelling while hardening and softening behaviour of the beam ends was accounted through plastic hinge models; (b) the Case B where both of the above factors were ignored in the modelling; and (c) the Case C where both of the above factors were considered in the modelling. In the present ABAQUS model, the strength and stiffness of the GF are taken into account in the analysis while plasticity is considered through inelastic beam-column modelling that ignores degradation effects.

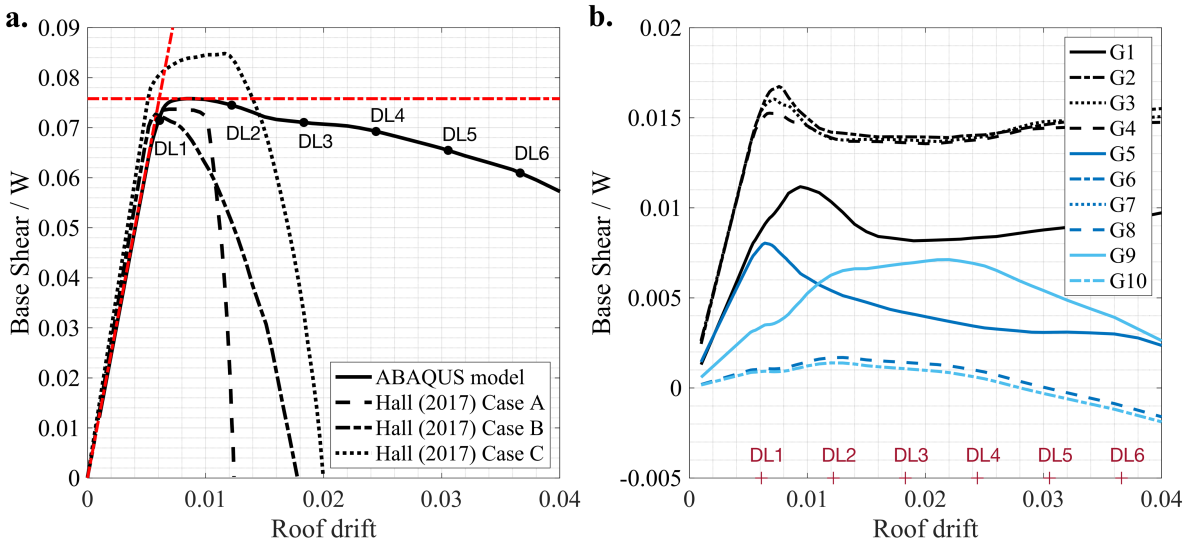


Figure 7-3. Pushover curves (base shear force at the ground level is normalised by the frame weight; roof drift represents the roof displacement divided by the overall height of the building): (a) entire frame model; (b) each column.

In Figure 7-3 (a), the yielding point on the pushover curve can be defined by the corresponding horizontal coordinates of the intersection of the red lines (Castiglioni et al., 2017), i.e. the total base shear to roof drift at the elastic range and the peak value of the total base shear at the maximum capacity of the structure. Then, the target ductility can be calculated for different ductility levels using Eq. (7.1),

$$\mu_1 = \frac{d_{target}}{d_{yielding}} \tag{7.1}$$

In this equation, d_{target} is the target roof drift (roof displacement divided by the total height of the building), $d_{yielding}$ is the yielding drift, and μ_1 represents the roof displacement ductility level, denoted as DLn, n=1, 2,…, 6, i.e. $\mu_1 = 1$ is denoted as DL1. Accordingly, d_{target} is 0.0061, 0.0122, 0.0182, 0.0244, 0.0305 and 0.0366 for DL1, DL2, DL3, DL4, DL5 and DL6 primary damage state which corresponds to a roof displacement ductility of 1, 2, 3, 4, 5 and 6 respectively, where the yielding drift d_y = 0.0061. The base shear force - roof drift relationship

of each column is shown in Figure 7-3, where C1-C10 represent the column 1 to 10 from the left side of the building model.

Figure 7-3 (b) illustrates the shear force - roof drift relationship for each column at the ground level. G1 - G10 denote the number of columns located from the left side of the 2-D frame (red lines in Figure 7-1). Strength decreases rapidly in columns G6, G8, and G10 after reaching DL4. These three columns were originally designed at weak axis orientation.

7.3 Simulation of downburst wind field

The hybrid theoretical procedure for developing an artificial wind velocity field proposed in Section 5.4.2 is adopted in this chapter. According to this approach, 20 non-stationary wind velocity time histories are simulated, which are used to match the vertical position of the modelled building and are regarded as concentrated loads applied to each storey of the building. Three characteristics of the simulated downburst wind field are considered, including the height of the maximum slowly varying mean velocity, the vertical profiles of turbulence intensity, and the maximum velocity.

Firstly, the 3-second gust wind velocity time histories at each storey height for profile 1-3 (i.e. $z_{U_{max}}$= 30 m, 50 m, and 70 m above the ground, are demonstrated in Figure 7-4 (a)- Figure 7-6 (a). The maximum velocities, U_{max}, are 59 m/s, 63 m/s, and 68 m/s for $z_{U_{max}}$=30 m, 50 m, and 70 m, respectively. This defines three different velocity profiles along the building height, thus affecting the lateral input load distribution and energy absorption capacity of the building. The terrain category is exposure B. The downburst wind loads are then calculated by $f = C_d \times 0.5\rho U(t)^2 A$ (see Figure 7-4 (b)- Figure 7-6 (b)) for each storey, imposed as concentrated

loads on each storey of the building frame, where C_d is assumed to be equal to 1.2 (Melbourne, 1980), ρ is equal to 1.225 kg/m^3 and A is the storey area exposed to wind.

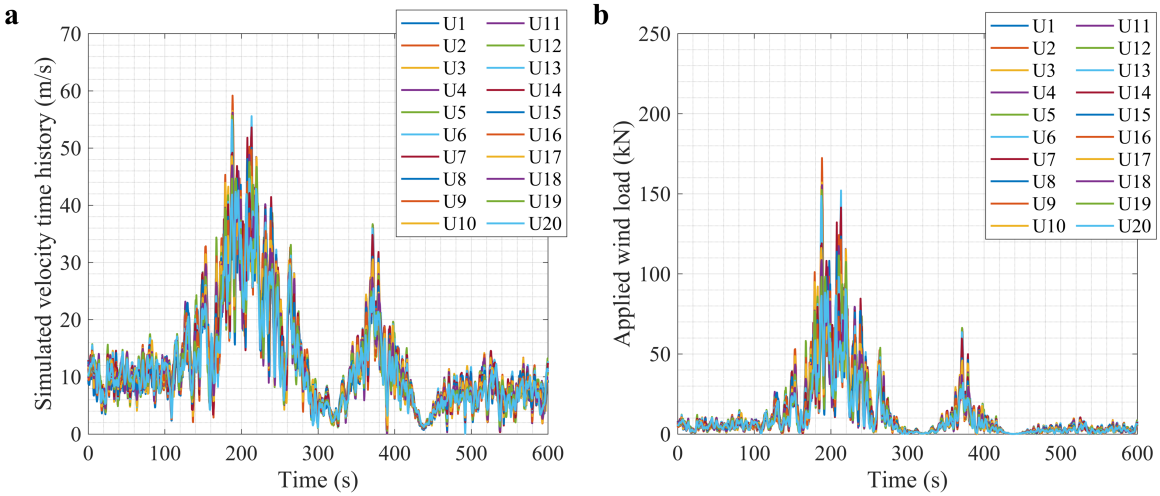


Figure 7-4. Time history of the simulated transient winds when $z_{\bar{U}_{max}}$ = 30 m: (a) Simulated velocity time history; (b) Downburst wind loading on each storey.

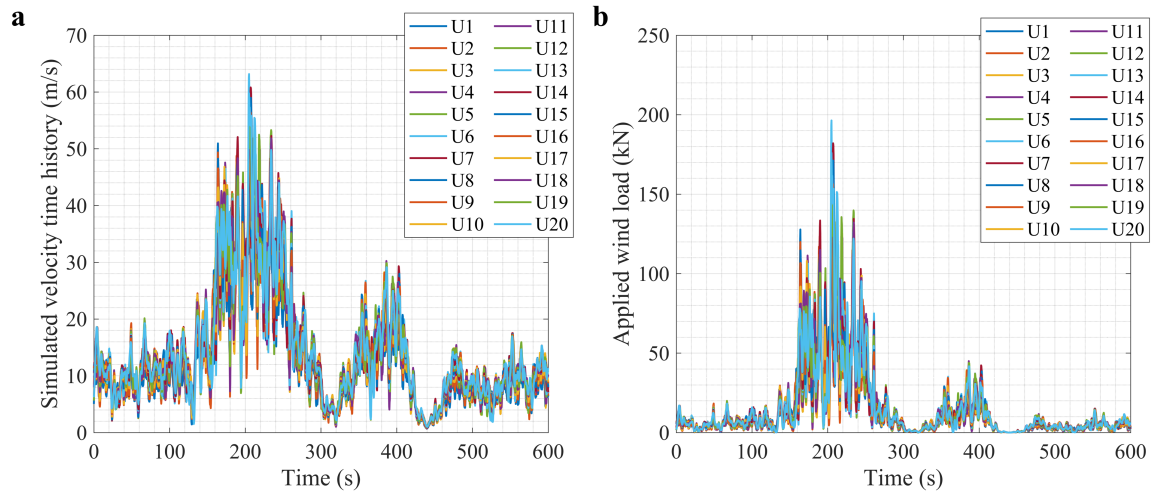


Figure 7-5. Time history of the simulated transient winds when $z_{\bar{U}_{max}}$ = 50 m: (a) Simulated velocity time history; (b) Downburst wind loading on each storey.

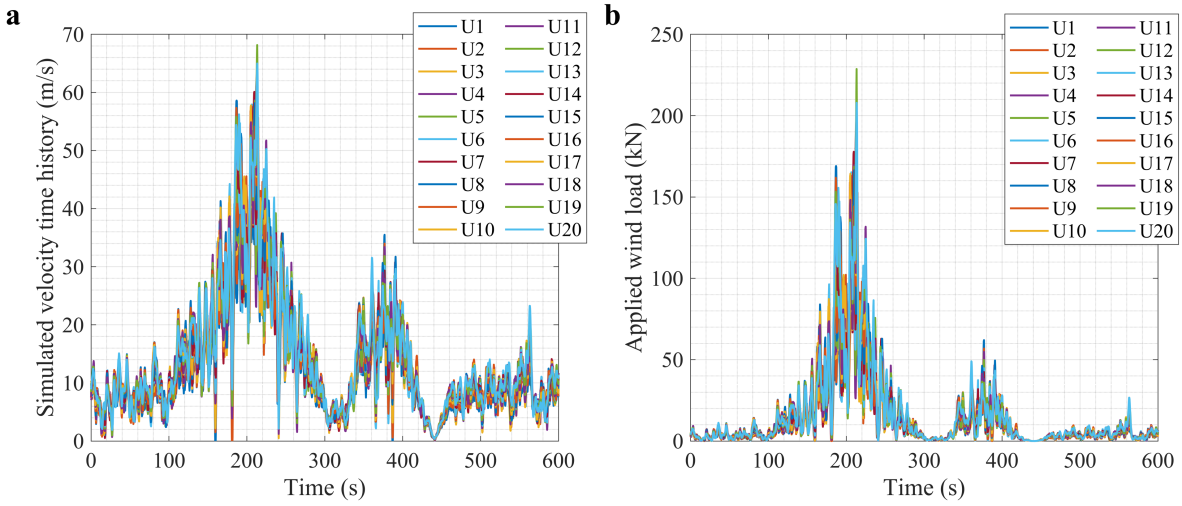


Figure 7-6. Time history of the simulated transient winds when $z_{\bar{U}_{max}}$=70 m: (a) Simulated velocity time history; (b) Downburst wind loading on each storey.

The 3-second peak velocity time histories at the height of maximum slowly varying mean velocity, $\bar{U}_{max}$, and the vertical profiles of the peak horizontal wind for these three scenarios are compared in Figure 7-7 (a) and (b), respectively, where the dashed lines in Figure 7-7 (b) are the trendlines for each scenario.

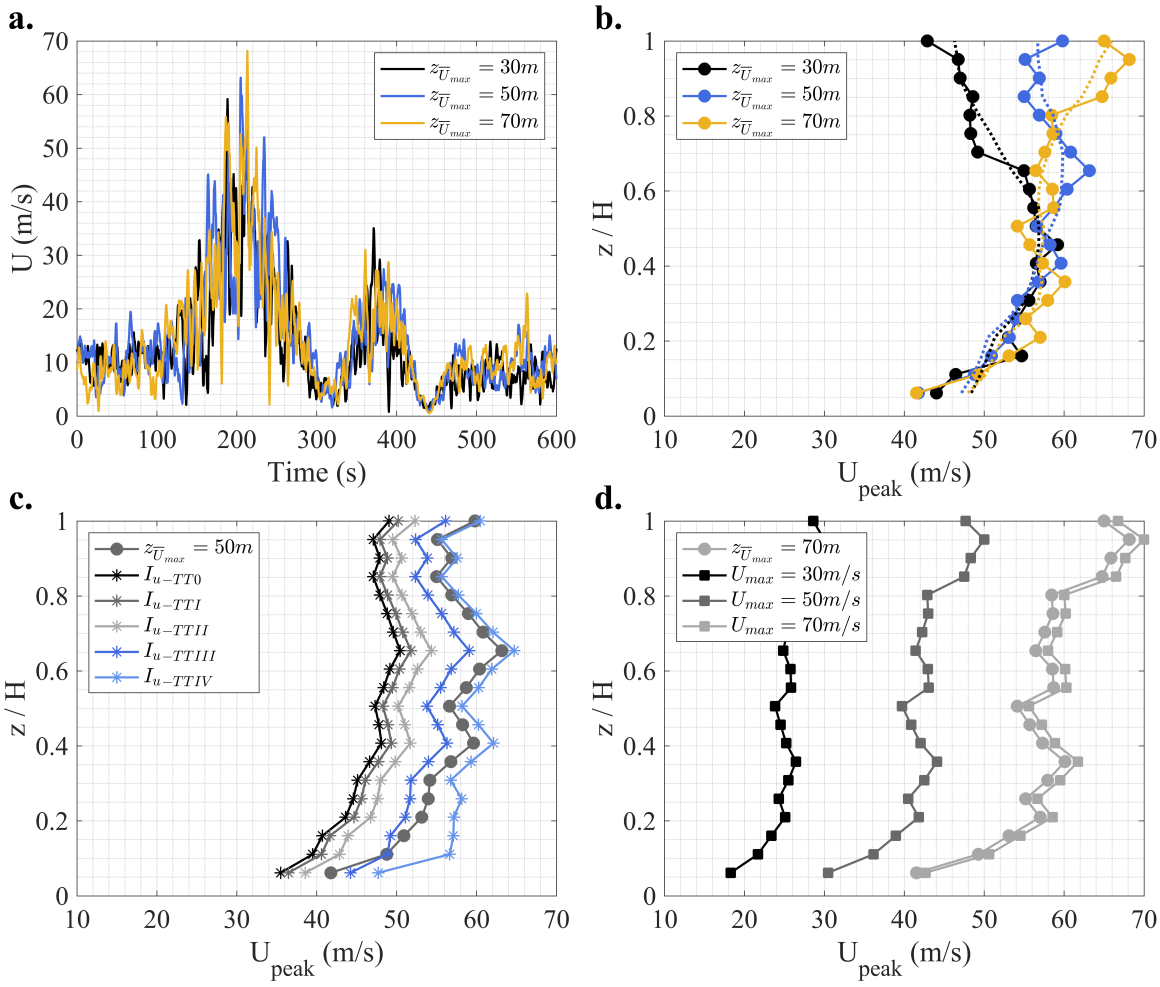


Figure 7-7. Horizontal and vertical profiles of downburst velocity: (a) Horizontal velocity time history at the height of maximum velocity; (b) Peak velocity at each storey with varying $z_{\overline{U}_{max}}$; (c) Peak velocity at each storey with varying vertical profiles of I_u; (d) Peak velocity at each storey with varying U_{max}.

Secondly, the velocity profiles with varying vertical profiles of the turbulence intensity from different terrain types (i.e. 0, I, II, III, IV from Eurocode (2010)) are obtained when $z_{U_{max}}$= 50 m. It is assumed that the simulated downburst wind field has the same turbulence intensity profile as the synoptic wind. Based on this assumption, the comparison of the peak velocities along with the building height is shown in Figure 7-7 (c). With the increase in terrain roughness, the turbulence intensities are obviously increasing, which causes the higher peak velocities along with the height. In this case, the slowly varying mean velocities and the simulated rapidly

varying turbulent fluctuations are consistent with the wind field in Figure 7-7 (a), $z_{U_{max}}$= 50 m. The turbulence intensity profiles above the ground under different terrain types lead to variable slowly varying standard deviations of the simulated velocity time history. In these five profiles, the maximum velocities are 50 m/s, 52 m/s, 54 m/s, 59 m/s, and 65 m/s, which correspond to the turbulence intensities of TT0, TTI, TTII, TTIII, and TTIV, respectively.

Thirdly, the downburst wind field in Figure 7-7 (a), i.e. $z_{U_{max}}$= 70 m, has been normalised by the maximum velocity to 30 m/s, 50 m/s, and 70 m/s, respectively, and the vertical profiles of the peak velocities are shown in Figure 7-7 (d). The limitation here is that the pressure coefficient used for calculating the wind load is independent of the height above the ground due to the insufficient recorded data for this parameter caused by downbursts on buildings.

7.4 Results and discussion

7.4.1 TS downburst wind load only

This section presents analysis results under the synthetic wind profiles alone. These results are used as reference data for comparison with that obtained from the multi-hazard analysis in the later section. Thus, the eleven synthetic downburst wind profiles are applied on the undamaged building and the base shear - roof drift relationship for each synthetic load is shown in Figure 7-8. It can be observed from this figure that the deformations of the building are within the elastic range under downburst wind profiles 1, 3, 4, 5, 9, and 10 and all corresponding ductility demands are less than one, i.e. 0.91, 0.95, 0.81, 0.88, 0.19, and 0.51, respectively (see Table 7-2). A plastic response can be seen in Figure 7-8 under wind profiles 2, 7, and 8, where the corresponding ductility demands are equal to 1.57, 1.33, and 1.9, with a peak non-linear displacement of 0.75 m, 0.64 m, and 0.91 m (see Figure 7-9 (b)), respectively. The obvious

larger maximum velocity can be seen for these three wind profiles, i.e. 63 m/s, 59 m/s, and 65 m/s respectively, and particularly $z_{U_{max}}$= 50 m for all three wind profiles. The damages for these obvious increases can be found in Figure 7-9 (a) where apparent large peak storey drift ratios (SDR) are observed from the 1st to 9th storey, and the large increase of the peak displacement occurs at this storey range, as shown in Figure 7-9 (b).

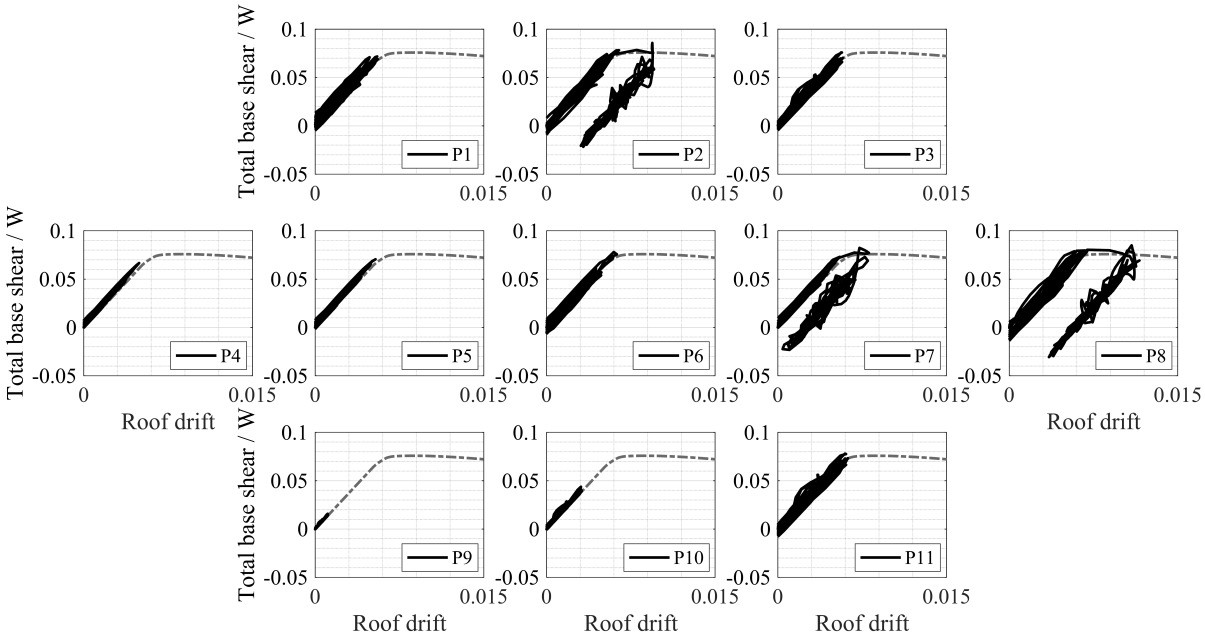


Figure 7-8. Pushover curves of the building frame under different downburst profiles (Grey dash line represents the pushover curves as shown in Figure 7-3).

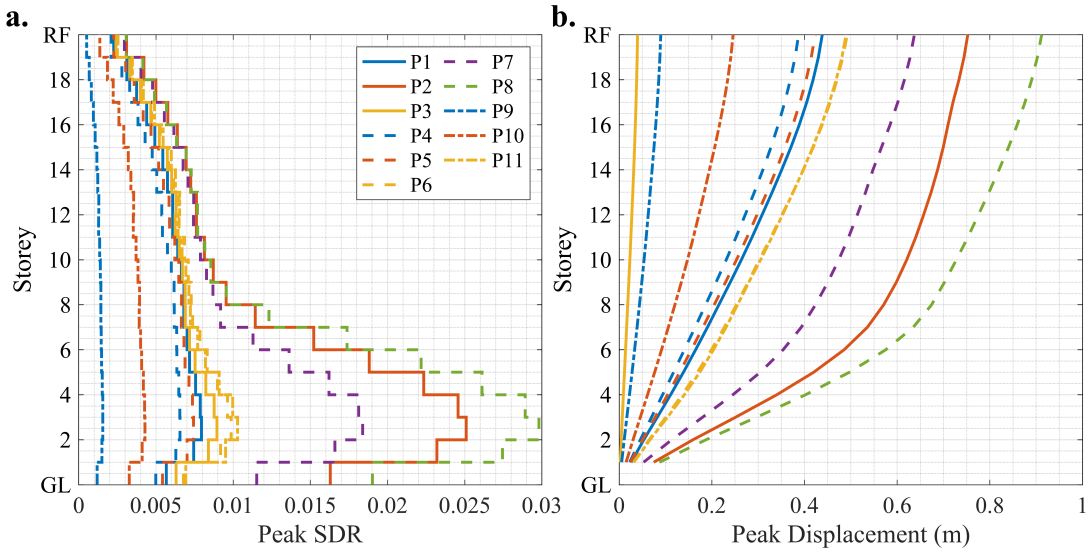
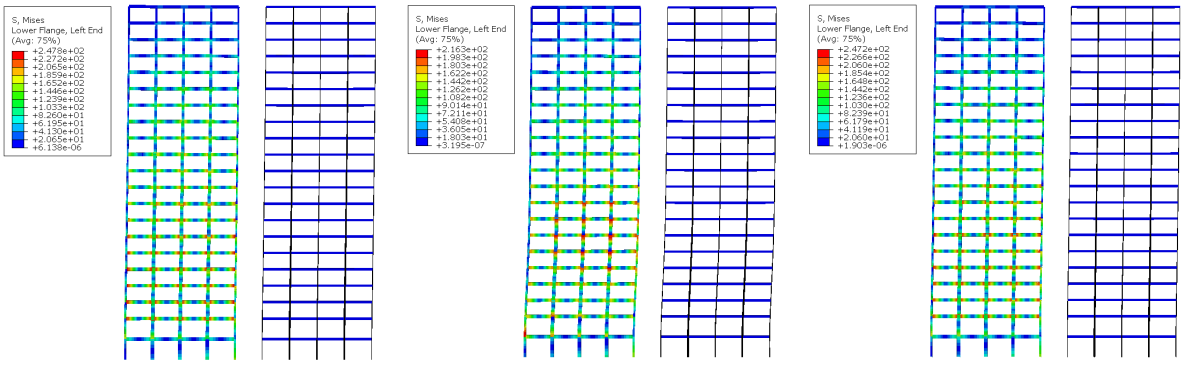


Figure 7-9. (a) Peak SDR and (b) Peak displacement of the building frame for each storey under the downburst wind fields.

The global stress distributions under the downburst wind profile 1 with $z_{U_{max}}$= 30 m and profile 3 with $z_{U_{max}}$= 70 m when the maximum displacement ductility occurs are shown in Figure 7-10 (a) and Figure 7-10 (c), which indicate that high stresses are concentrated across the first ten storeys of the building. The global stress distribution for profile 2 with $z_{U_{max}}$= 50 m at the maximum displacement ductility is shown in Figure 7-10 (b), where high-stress locations are observed across the 4th to 8th storeys and at the base of column G1, which demonstrates that the height of $\overline{U}_{max}$ can change the high-stress regions of the building frame, which is consistent with the discussions above.



(a) $z_{U_{max}}$ =30 m (b) $z_{U_{max}}$ =50 m (c) $z_{U_{max}}$ =70 m

Figure 7-10. Global stress distribution at the time of maximum displacement under the downburst wind profile 1, 2, and 3.

7.4.2 Primary and secondary multi-hazard analysis

7.4.2.1 Varying height of $\overline{U}_{max}$

The base shear - roof drift relationship of the multi-hazard analysis is illustrated in Figure 7-11. By performing a pushover analysis, the frame reaches the following ductility levels, hence damage states: DL1, DL2, DL3, DL4, DL5 and DL6. For each damage state, a restart dynamic analysis is performed by subjecting the deformed frame to the three simulated downburst wind profiles with varying height of $\overline{U}_{max}$ (i.e., 30m, 50m, 70m). The secondary ductility demands of the sequential analysis as obtained for each damage state are summarised in Table 7-2. In

general, it can be seen from this table that as the primary target ductility level increases, the secondary ductility demands tend to increase (see red dash line in Figure 7-11).

Under the sequential analysis of the downburst wind profile 1, secondary ductility demands remained at the same level with those of the primary event indicating that the structure behaved almost elastically (Figure 7-11 (a1) - (e1)). There might be some accumulation of fatigue damage, but this has not increased the roof displacement. A significant increase of secondary ductility demands which indicate global collapse is observed after reaching DL6 during the primary event (Figure 7-11 (f1)). High-stress locations are observed between 1st and 10th storey for the primary damage state DL1 and DL2 (see Figure 7-12 (a1) - (b1)) and between 1st and 9th storey for the primary damage state DL3 and DL4 (see Figure 7-12 (c1) - (d1)). For the primary damage state DL5 and DL6, similar high-stress locations are observed between 2nd and 6th storey (see Figure 7-12 (e1) -(f1)).

Under the sequential analysis of the downburst wind profile 2, the structure responds inelastically and higher plastic deformations are observed than those during the wind profile 1. The maximum ductility is found to be 1.62 (0.78 m) and 3.05 (1.46 m) when the downburst event follows the primary damage state DL1 and DL2, respectively, which is a 62% and 52% increase of the initial ductility demand, respectively. High stresses are observed between the 4th and 8th storeys for primary damage state DL1 and 1st and 9th storeys of the building for primary damage state DL2 (see Figure 7-12 (a2) and (b2)). The ductility demands increase significantly when the downburst event follows the primary damage state DL3, DL4, DL5 and DL6 resulting in four- and three-times higher ductility demands than those of the primary event, i.e. 11.52, 12.07, 11.37, and 11.67 respectively (see Figure 7-11 (c2) - (f2)). Excessive yielding areas have been formed, and steel beams have reached their maximum tensile strength. Under these

ductility levels, a collapse mechanism has been formed that involves the 2nd and 6th storey of the building, as shown in Figure 7-12 (c2) - (f2).

Under the sequential analysis of the downburst wind profile 3, the ductility demands increase to 1.01, 2.17, 3.34, and 4.60 when the downburst event follows the primary damage state DL1, DL2, DL3, and DL4 which are 1%, 8.5%, 11.3%, and 15% increase, respectively. The high-stress locations for profile 3 are similar to those for profile 1, but the building exhibited an overall collapse mechanism earlier. As shown in Figure 7-11 (e3), global collapse is observed after reaching the primary damage state DL5.

The results of these three analysis profiles demonstrate that although the maximum velocity of the downburst occurs in profile 3, the downburst wind profile 2 imposes higher ductility demands leading the structure to global collapse. These results indicate that the height at which the maximum wind velocity occurs alongside with the shape of the vertical wind profile are two important parameters for consideration as they control the input energy and excessive plastic deformations of the structure.

Table 7-2. Summarised ductility demand [d] (maximum roof drift[e]) for eleven downburst wind profiles (Profile 1-3 for varying $z_{\bar{U}_{max}}$; Profile 4-8 for varying I_u; Profile 9-11 for varying U_{max}).

Wind profile	$Z_{U_{max}}$ (m)	I_u	U_{ma} (m/s)	Wind load	DL1	DL2	DL3	DL4	DL5	DL6
	Step-by-step static pushover				1.00 (0.0061)	2.00 (0.0122)	3.00 (0.0182)	4.00 (0.0244)	5.00 (0.0305)	6.00 (0.0366)
P1	30	B	59	0.91 (0.0056)	1.00 (0.0061)	2.00 (0.0122)	2.98 (0.0182)	3.98 (0.0243)	5.08 (0.0310)	11.74 (0.0716)
P2	50		63	1.57 (0.0096)	1.62 (0.0099)	3.05 (0.0187)	11.52 (0.0703)	12.07 (0.0736)	11.37 (0.0694)	11.67 (0.0712)
P3	70		68	0.95 (0.0058)	1.01 (0.0062)	2.17 (0.0132)	3.34 (0.0204)	4.60 (0.0281)	12.61 (0.0769)	11.71 (0.0714)
P4	50	TT0	50	0.81 (0.0049)	1.00 (0.0061)	2.00 (0.0122)	3.07 (0.0187)	4.23 (0.0258)	5.36 (0.0327)	7.18 (0.0438)
P5		TTI	52	0.88 (0.0054)	1.00 (0.0061)	2.02 (0.0123)	3.14 (0.0192)	4.30 (0.0262)	11.84 (0.0722)	11.96 (0.0730)
P6		TTII	54	1.03 (0.0063)	1.08 (0.0066)	2.16 (0.0132)	3.30 (0.0201)	4.47 (0.0273)	12.45 (0.0759)	11.60 (0.0708)
P7		TTIII	59	1.33 (0.0081)	1.38 (0.0084)	2.47 (0.0151)	3.73 (0.0228)	12.58 (0.0767)	12.28 (0.0749)	11.26 (0.0687)
P8		TTIV	65	1.9 (0.0116)	1.93 (0.0118)	3.67 (0.0224)	13.03 (0.0795)	11.60 (0.0708)	11.12 (0.0678)	12.56 (0.0766)
P9	70	B	30	0.19 (0.0011)	1.00 (0.0061)	2.00 (0.0122)	2.98 (0.0182)	4.00 (0.0244)	5.00 (0.0305)	6.00 (0.0366)
P10			50	0.51 (0.0031)	1.00 (0.0061)	2.00 (0.0122)	2.98 (0.0182)	4.00 (0.0244)	5.10 (0.0311)	6.23 (0.0380)
P11			70	1.02 (0.0062)	1.06 (0.0065)	2.23 (0.0136)	3.42 (0.0209)	5.34 (0.0326)	13.11 (0.0800)	11.74 (0.0716)

[d] Ductility demand denotes the maximum non-linear roof displacement divided by the yielding roof displacement of the overall structure.

[e] Maximum roof drift denotes the maximum roof displacement divided by the total height of the building.

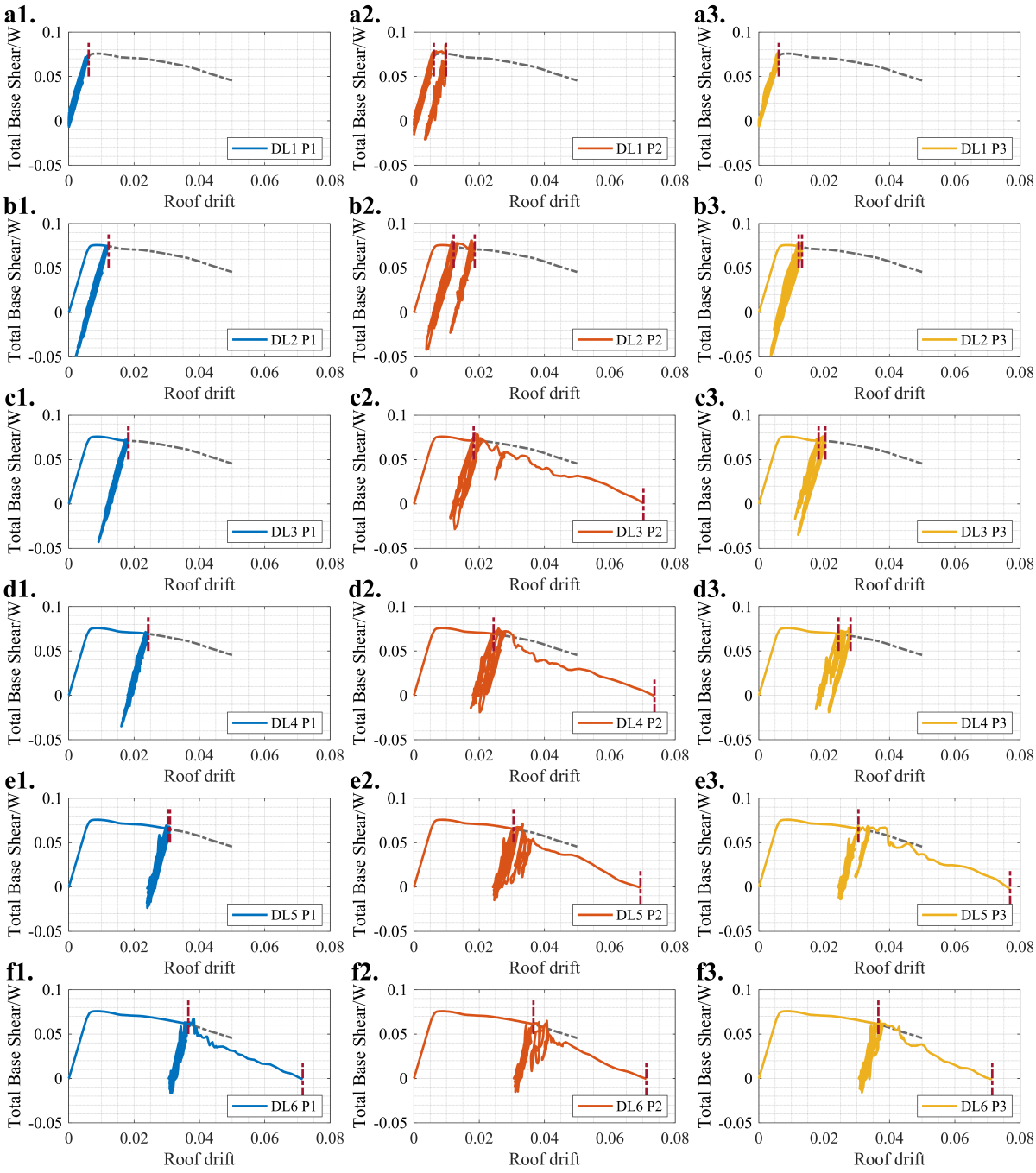
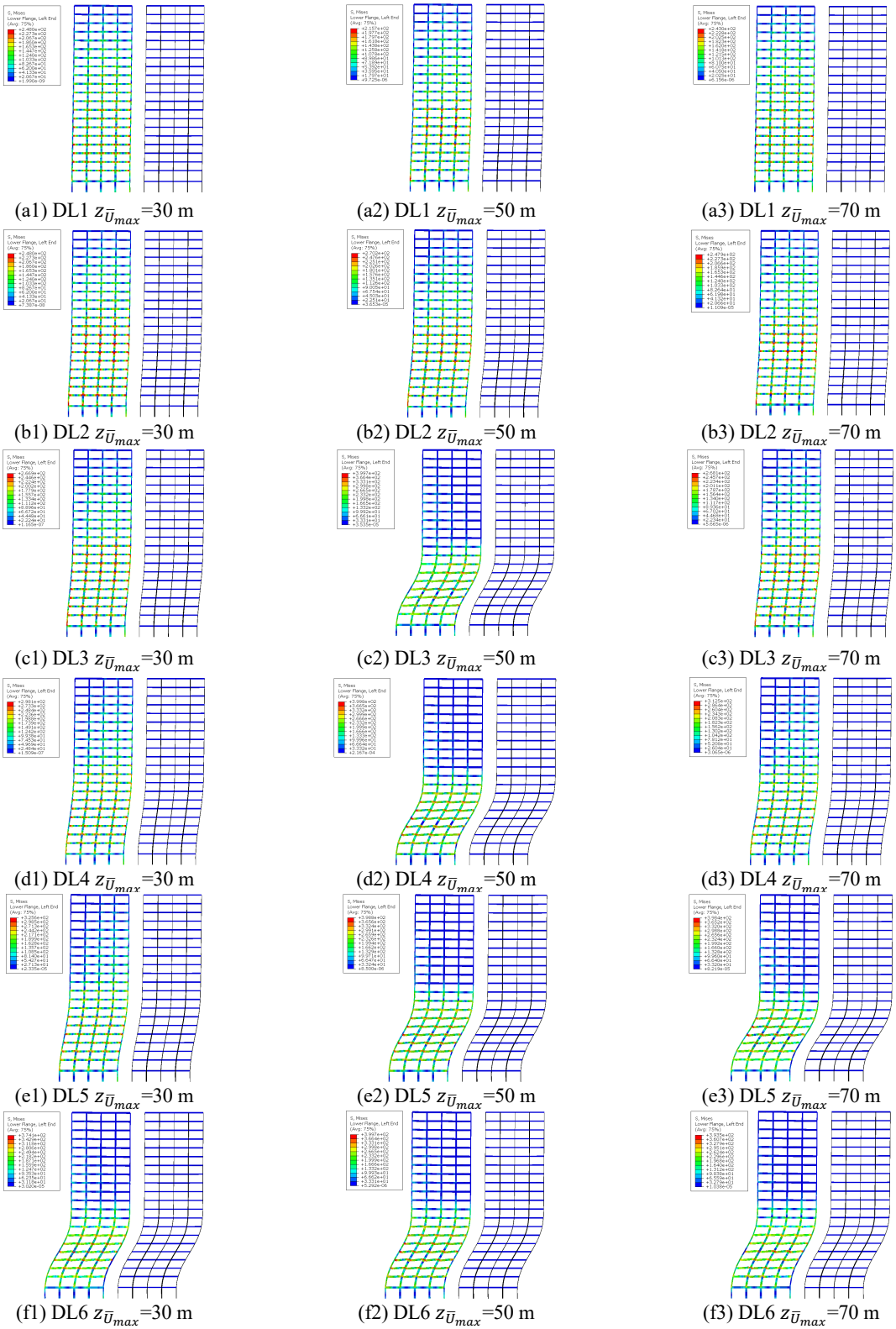


Figure 7-11. Pushover curves of the damaged building under secondary downburst wind hazard with varying $z_{\bar{U}_{max}}$: (a) DL1-Downburst wind; (b) DL2-Downburst; (c) DL3-Downburst; (d) DL4-Downburst; (e) DL5-Downburst; (f) DL6-Downburst (Grey dash line represents the pushover curves as shown in Figure 7-3; Red dash line represents the maximum displacement after the primary and secondary hazards separately).



(a1) DL1 $z_{\bar{U}_{max}}$=30 m (a2) DL1 $z_{\bar{U}_{max}}$=50 m (a3) DL1 $z_{\bar{U}_{max}}$=70 m

(b1) DL2 $z_{\bar{U}_{max}}$=30 m (b2) DL2 $z_{\bar{U}_{max}}$=50 m (b3) DL2 $z_{\bar{U}_{max}}$=70 m

(c1) DL3 $z_{\bar{U}_{max}}$=30 m (c2) DL3 $z_{\bar{U}_{max}}$=50 m (c3) DL3 $z_{\bar{U}_{max}}$=70 m

(d1) DL4 $z_{\bar{U}_{max}}$=30 m (d2) DL4 $z_{\bar{U}_{max}}$=50 m (d3) DL4 $z_{\bar{U}_{max}}$=70 m

(e1) DL5 $z_{\bar{U}_{max}}$=30 m (e2) DL5 $z_{\bar{U}_{max}}$=50 m (e3) DL5 $z_{\bar{U}_{max}}$=70 m

(f1) DL6 $z_{\bar{U}_{max}}$=30 m (f2) DL6 $z_{\bar{U}_{max}}$=50 m (f3) DL6 $z_{\bar{U}_{max}}$=70 m

Figure 7-12. Global Stress distribution at maximum displacement for profiles 1, 2, and 3, (a) DL1-Downburst; (b) DL2-Downburst; (c) DL3-Downburst; (d) DL4-Downburst; (e) DL5-Downburst; (f) DL6-Downburst.

7.4.2.2 Varying vertical profiles of I_u

This section discusses the ductility demands induced by downburst winds with varying vertical profiles of turbulence intensities derived from changing terrain types 0, I, II, III, and IV, which cause the maximum velocities to change from 50 m/s to 65 m/s, and the height of $\overline{U}_{max}$ for these downburst wind events is 50 m.

As shown in the first column of Figure 7-13 under the wind profile 4 with terrain type 0 (TT0), the ductility demands induced by the sequential downburst wind loads tend to increase with the increase in primary target ductility levels of the damaged building. The occurrence of the downburst has almost no effect on the first three damage scenarios, namely primary damage state DL1, DL2, and DL3, but does notably impact on the primary damage state DL4, DL5, and DL6, as secondary ductility demands induced by the sequential secondary hazard become 4.23 (DL4), 5.36 (DL5), and 7.18 (DL6) - see Table 7-2. The observed stress concentrations spread across larger areas for primary damage state DL1- DL3 than for primary damage state DL4 - DL6. For the latter, stresses attenuate across top storeys and increase at the base of the structure (i.e. from between 1st and 9th storeys to between 2nd and 6th storeys).

The results for terrain type 1 (TT1) in wind profile 5 follow similar patterns to those reported for TT0 in wind profile 4. The secondary hazard event imposes ductility demands below a 1.08 magnification threshold for primary damage state DL1 - DL4, compared with those from the primary hazard event. In contrast, the accumulated secondary ductility demands of 11.84 and 11.96 nearly duplicate the primary ductility demands for primary damage state DL5 and DL6, respectively, since the building frame has collapsed - see Figure 7-13. The global stress distribution patterns follow the same patterns as those observed for scenario TT0.

The patterns for the increase of ductility demand discussed above replicate for TTII, TTIII, and TTIV under wind profiles 6-8, although with more notable accumulation of fatigue damages with increased roof displacement. With the increase of the turbulence intensities under the same primary damage state, the accumulated secondary ductility demands are obviously increased, and the collapse of the building can happen even when the ductility levels of the primary damage state are lower. For instance, the ductility demands increase from 2.00 (0.96 m) to 3.67 (1.76 m) during the wind profiles of 4 to 8 (see Table 7-2) for the primary damage state DL2. The collapse of the building under wind profile 6 (TTII) happens at the primary damage state DL5, and the collapses of the building frame under wind profiles 7 (TTIII) and 8 (TTIV) occur at the primary damage state DL4 and DL3. The stress distributions observed for TTII, TTIII, and TTIV under wind profiles 6-8 show no qualitative difference with respect to those observed for TT0 and TTI under wind profile 4-5, albeit obvious differences in stress levels.

Therefore, when the slowly varying mean velocities and the simulated rapidly varying turbulent fluctuations are the same, downburst wind fields under varying turbulence intensities from different terrain types can influence the ductility demands of the damaged steel structures since higher velocity occurs with the increase in slowly varying standard deviation of the simulated velocity time histories.

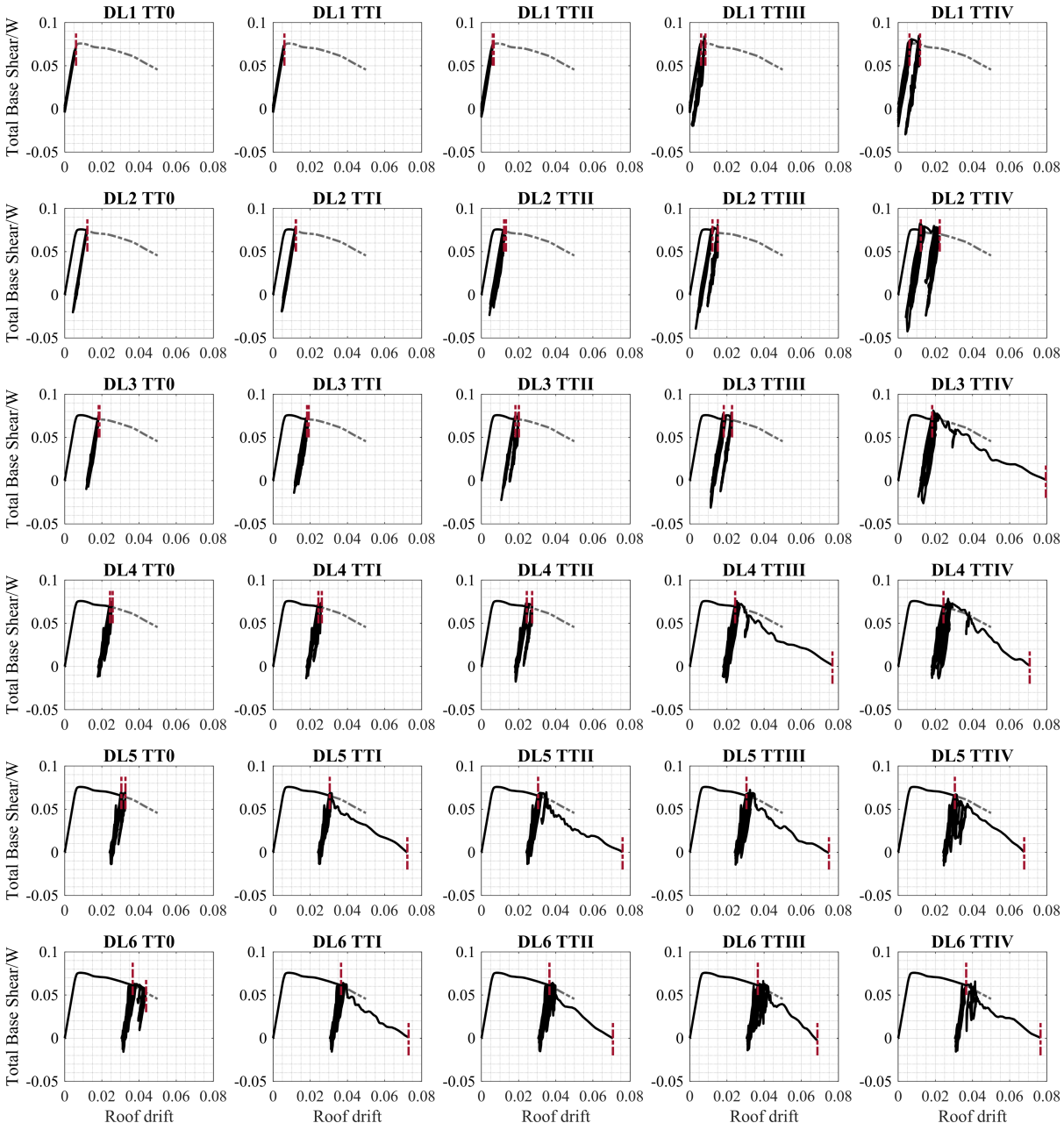
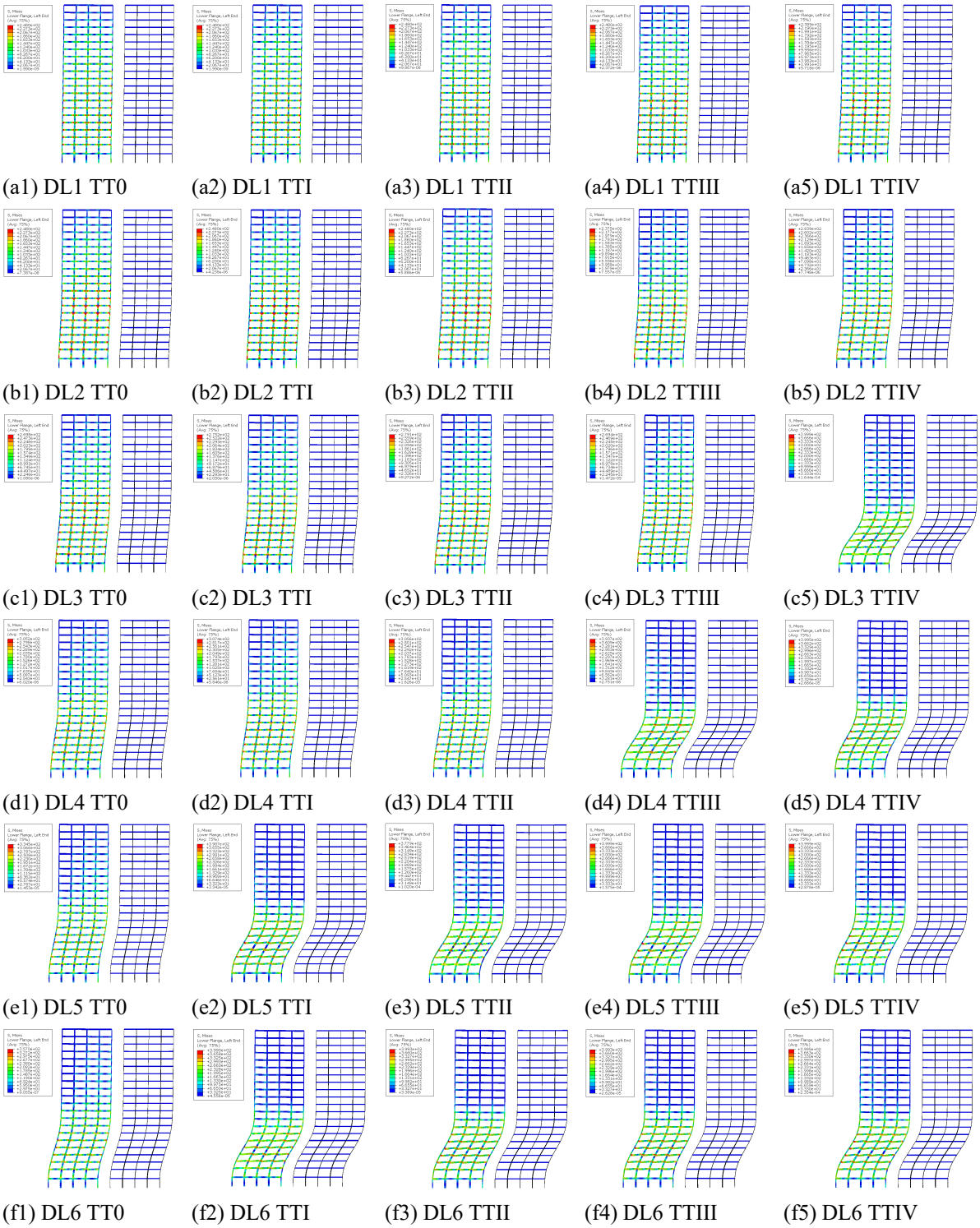


Figure 7-13. Pushover curves of the damaged building under secondary downburst wind hazard with varying vertical profiles of I_u from variable terrain types (0, I, II, III, IV), (Grey dash line represents the pushover curves as shown in Figure 7-3; Red dash line represents the maximum displacement after the primary and secondary hazards separately).



(a1) DL1 TT0 (a2) DL1 TTI (a3) DL1 TTII (a4) DL1 TTIII (a5) DL1 TTIV

(b1) DL2 TT0 (b2) DL2 TTI (b3) DL2 TTII (b4) DL2 TTIII (b5) DL2 TTIV

(c1) DL3 TT0 (c2) DL3 TTI (c3) DL3 TTII (c4) DL3 TTIII (c5) DL3 TTIV

(d1) DL4 TT0 (d2) DL4 TTI (d3) DL4 TTII (d4) DL4 TTIII (d5) DL4 TTIV

(e1) DL5 TT0 (e2) DL5 TTI (e3) DL5 TTII (e4) DL5 TTIII (e5) DL5 TTIV

(f1) DL6 TT0 (f2) DL6 TTI (f3) DL6 TTII (f4) DL6 TTIII (f5) DL6 TTIV

Figure 7-14. Global Stress distribution at maximum displacement for profile 4, 5, 6, 7, and 8: (a) DL1-Downburst; (b) DL2-Downburst; (c) DL3-Downburst; (d) DL4-Downburst; (e) DL5-Downburst; (f) DL6-Downburst.

7.4.2.3 Varying U_{max}

The multi-hazard analysis with stronger secondary thunderstorm downburst events, i.e. higher maximum velocity, acting on the building frame illustrates a more obvious increase in ductility demand or a higher probability of building collapse. In order to gain a better understanding of the extent to which TS downburst events can influence damaged structures caused by primary hazard events, this section investigates the impact of downburst wind loads with varying maximum velocities. In this analysis, the height of $\overline{U}_{max}$ is 70 m and I_u comes from exposure B of terrain category in ASCE7 (2013) while the selected maximum velocity levels are 30 m/s, 50 m/s, and 70 m/s.

The results show that accumulated secondary ductility demands of the building frame for all the primary damage state DL1-DL6 remain within the 1.04 magnification threshold when the maximum velocity reaches 30 m/s and 50 m/s (see Table 7-2) and no global collapse happens - see Figure 7-15 (a1) - (f1). That threshold is exceeded for all primary ductility DL1-DL6 when the maximum velocity reaches 70 m/s. Notably, the accumulated secondary ductility demand of 13.11 recorded for DL5 is over two times of the ductility demands induced during the primary hazard event. Finally, the analyses in Figure 7-15 show the same collapsing mechanism observed during the previous parametric scenarios - see Figure 7-11 and Figure 7-13. The high-stress regions are located between the 2nd and 6th storeys of the building before the collapse, which is the same collapsing mechanism as the counterpart under the influence of previous downburst velocity profiles. The detailed values of the ductility demands are illustrated in Table 7-2.

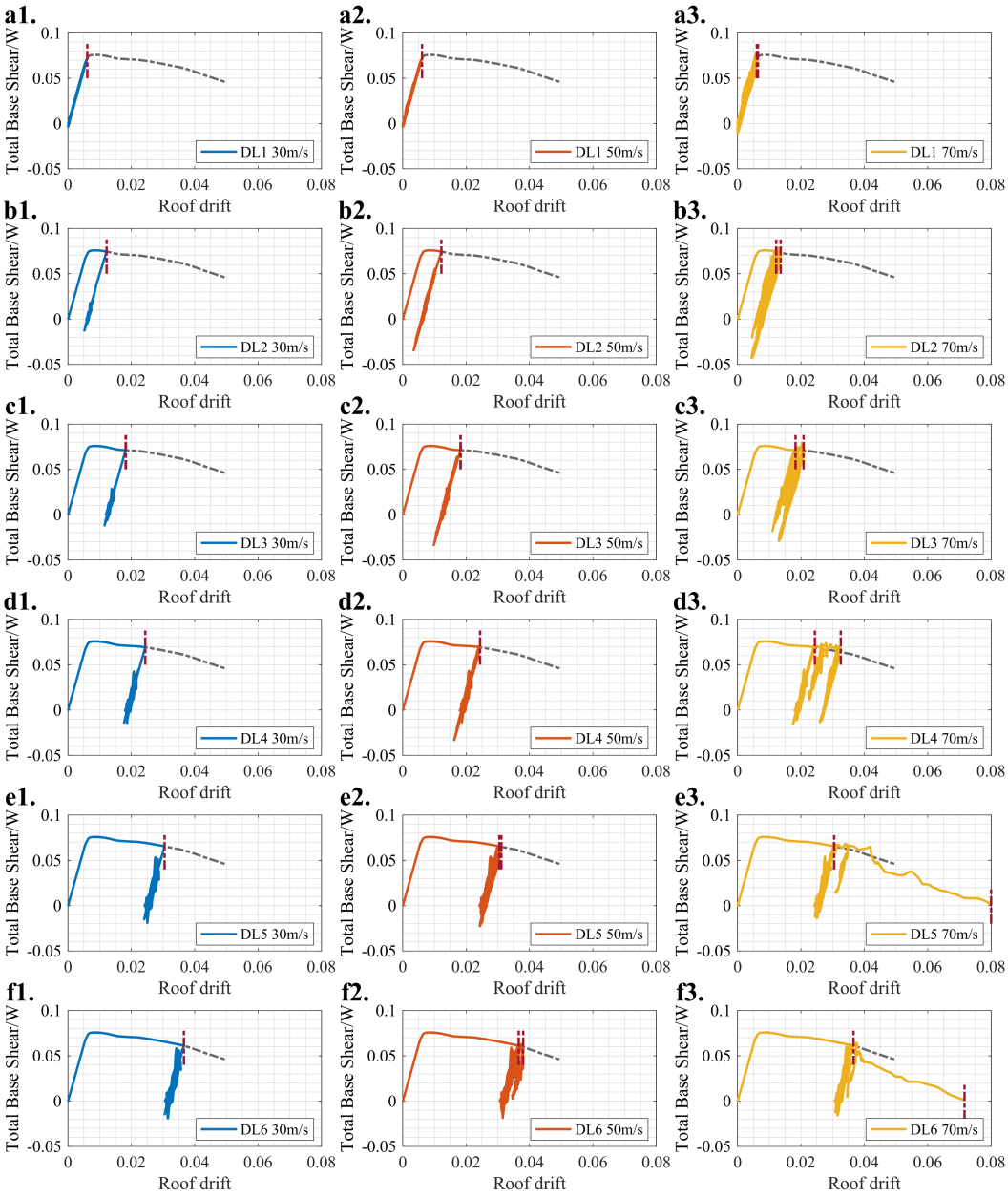


Figure 7-15. Pushover curves of the damaged building under secondary downburst wind hazard with varying U_{max} (Grey dash line represents the pushover curves as shown in Figure 7-3; Red dash line represents the maximum displacement after the primary and secondary hazards separately).

7.4.2.4 Peak SDR and Peak displacement

The comparisons of the peak SDR and peak displacement at each storey of the building frame are demonstrated in Figure 7-16 and Figure 7-17, respectively. Under the primary hazard event alone, the maximum values of peak SDR along the building height happen at the 4th storey with the increase of primary damage state DL1 to DL6, see black line of H1 in Figure 7-16 (a) - (f),

where the values of peak SDR are 0.009, 0.029, 0.05, 0.07, 0.092, and 0.114, respectively. When the primary hazard event drives the building frame into the primary damage state DL1, the occurrence of the followed secondary downburst winds with profile 2, 7, and 8 can cause an obvious increase of maximum SDR, and their values increase from 0.009 to 0.026, 0.02, and 0.031, respectively, i.e. 2-3 times of increase in maximum SDR before and after the secondary downburst wind hazard. No obvious effects are observed under the other downburst wind profiles as shown in Figure 7-16 (a). When the primary damage state increases to DL2, these three wind profiles (2, 7, and 8) can cause more serious damage, and the maximum SDR can reach up to 0.053, 0.044, and 0.067, respectively. A maximum 38% increase (wind profile 11) can be obtained from the rest of the downburst wind profiles for primary damage state DL2 – see Figure 7-16 (b).

When the primary damage state of the building frame reaches DL3 (Figure 7-16 (c)), wind profiles 2 and 8 can drive the structure to high inelastic level and possible collapse, and the maximum SDR reaches 0.272 and 0.321. A 42% maximum increase of the peak SDR can be found under the other downburst wind profiles, see purple dash line in Figure 7-16 (c). As the primary damage stage increases from DL3 to DL4, DL5, and DL6, 3, 7, and 8 of the 11 downburst wind profiles can lead to global collapses respectively, as shown in Figure 7-16 (d), (e), and (f). The maximum SDR of the damaged building frame for the rest of the combinations with the other downburst wind profiles can reach 0.103, 0.105, and 0.149 with an increase in 49%, 16%, and 31% compared with the values under the primary hazard event alone when the primary damage state is DL4, DL5, and DL6, respectively - see Figure 7-16 (d), (e), and (f).

The secondary hazard event can apparently aggravate the damage level of the storey drift and the obvious protruding part, i.e. 1st to 8th storeys, are the scenarios that have already collapsed.

The massive increase of the peak displacement started from the 1st storey and ended to the 8th storey (see Figure 7-17), and there is only a slight growth in peak deformation for the rest of the storeys, which is consistent with the observation of the global stress distribution. Therefore, the collapse of the building is due to the large peak storey drift of the weak regions of this building frame.

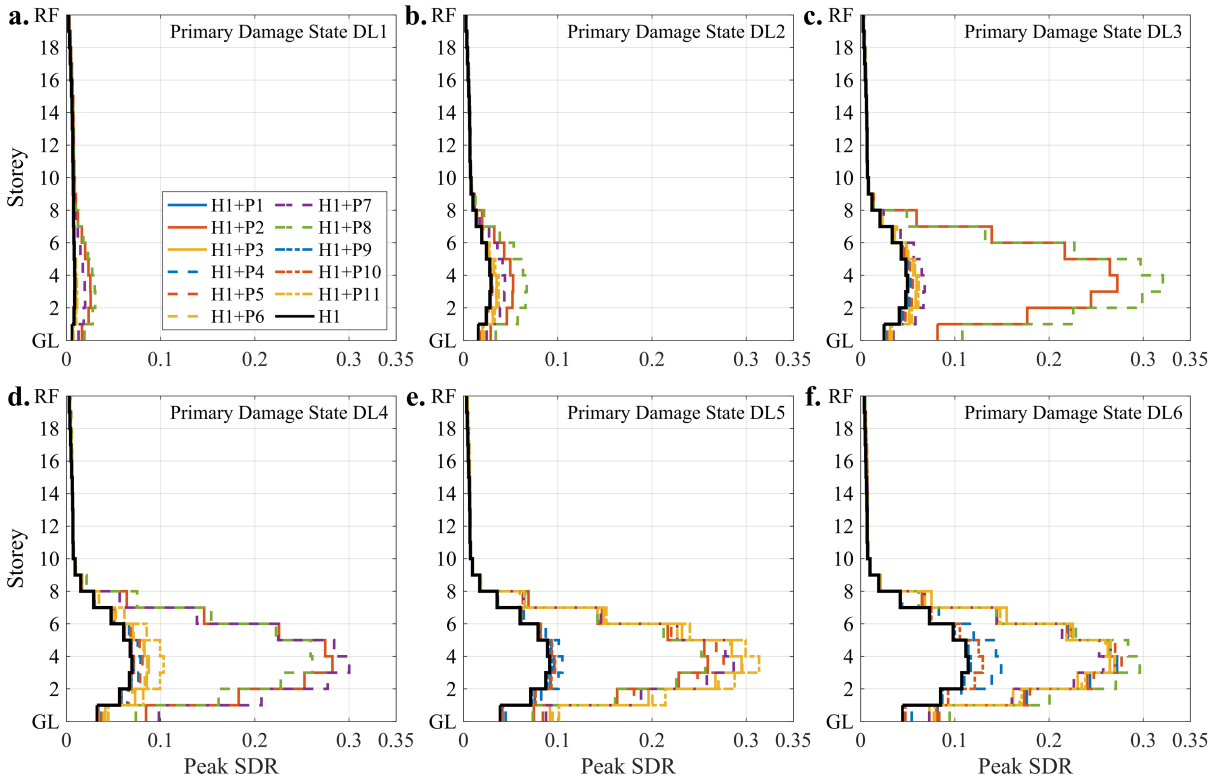


Figure 7-16. Peak SDR for each storey: (a) DL1-Downburst; (b) DL2-Downburst; (c) DL3-Downburst; (d) DL4-Downburst; (e) DL5-Downburst; (f) DL6-Downburst (H1 denotes the primary hazard alone).

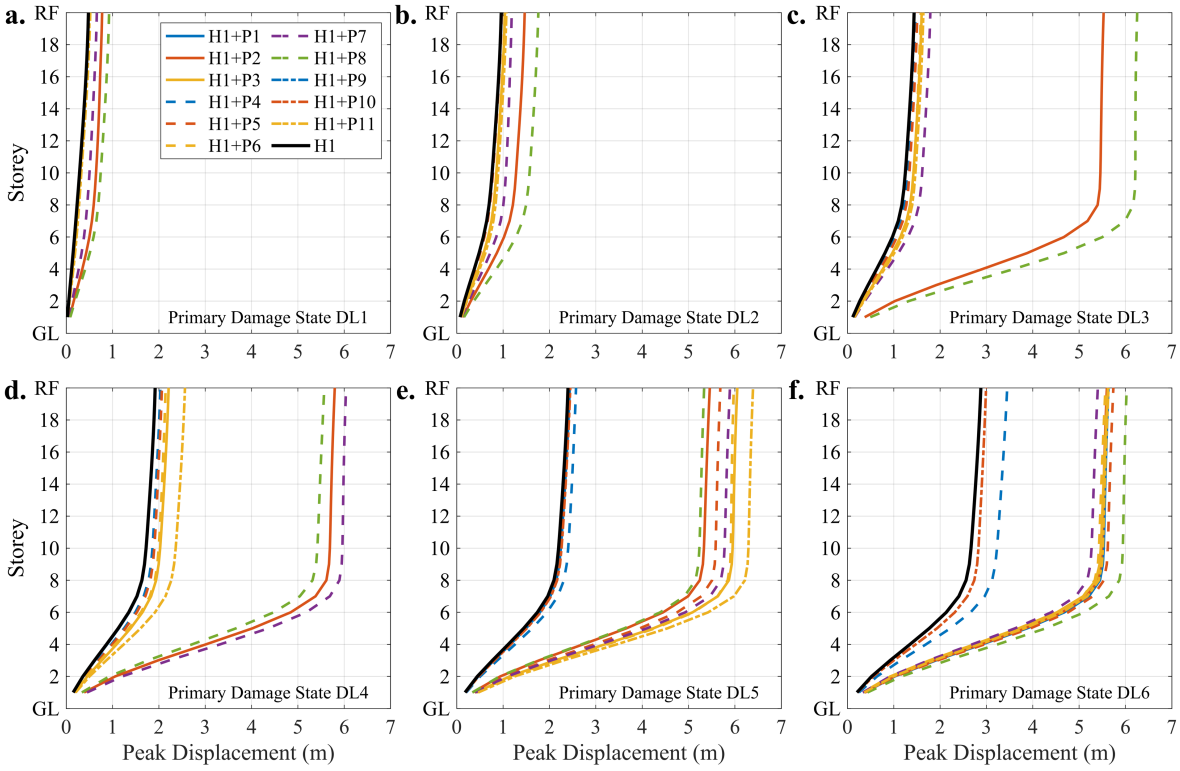


Figure 7-17. Peak displacement for each storey: (a) DL1-Downburst; (b) DL2-Downburst; (c) DL3-Downburst; (d) DL4-Downburst; (e) DL5-Downburst; (f) DL6-Downburst (H1 denotes the primary hazard alone).

7.5 Summary

In this chapter, a novel algorithm has been proposed for the nonlinear analysis of buildings under sequential hazard loads. The merit of this procedure is that the primary hazard analysis can stop at any pre-defined ductility level (i.e. single-hazard design) and the secondary hazard event can be applied as a sequential event. This allows for a direct quantification of the additional ductility demands due to the secondary hazard event. Furthermore, this method can be applied for the consideration of high modes of vibration based on the combination rules. This method is validated on a 20-storey steel building designed based on the 1994 Uniform Building Code in which primary damage has been initially induced through a ductility-controlled pushover analysis. Eleven downburst synthetic records were applied as secondary

hazard events having different vertical wind profiles and maximum wind velocity, as well as velocity profiles with varying turbulence intensities. The main conclusions of this study are as follows:

- The input energy from the sequential downburst event may drive the structure from elasticity to plasticity, or reinforce the plastic deformation, thus exceeding the single-hazard ductility demands. The level of damage exhibited by the structure during the secondary hazard event increases with the ductility demands of the primary event. For the scenarios without fully collapsing, the ductility demands induced by the secondary hazard event can result in an increase of up to 93% (H1+P8, from 1 to 1.93). Severe downburst events can directly lead to the collapse of structures, and the ductility demands before the collapse are 2 to 4 times of those resulting from the primary hazard events.
- The multi-hazard analysis results demonstrate the importance of the height at which the maximum wind velocity occurs and that of the shape of the vertical wind profile. Both parameters control the input wind energy and determine the number of storeys in a structure that are involved in the global plastic collapse mechanism.
- Under the sequential analysis of downburst wind profile 2, where the height of the maximum slowly varying mean velocity is 50 m, ductility demands increase significantly when the downburst event follows the primary damage state DL3 (i.e. ductility level is 3) to DL6 (i.e. ductility level is 6), resulting in four- and three-times higher ductility demands than that of the primary event, i.e. 11.52, 12.07, 11.37, and 11.67 respectively. Under these ductility levels, a collapse mechanism is formed that involves the 2^{nd} and 6^{th} storeys of the building.

- The weak regions at storey range of 1st to 8th of the building frame and the observed collapse mechanism of large peak SDR and obvious peak displacement change can be determined through the proposed computational procedure. Compared with the results from the wind profile 2, the same collapse mechanism can be observed under other sequential downburst wind profiles (3, 5, 6, 7, 8, and 11) when the ductility level induced by the primary hazard event reaches primary damage state DL5 and DL6.
- The collapses happen when the downburst wind loads are applied after the primary damage state DL3, DL4, DL5, and DL6 for downburst wind profiles with terrain types IV, III, II, I, and 0 respectively. Even though the building has not been fully collapsed, the occurrence of the secondary hazard can lead to an increase of 84%, 24%, 12%, 8%, and 7% of the ductility demands compared with those produced by primary hazards.

Therefore, the proposed computational procedure can accurately identify the weak regions, capacity margins, and collapse mechanisms of the structures under multi-hazards and can effectively quantify the increased ductility demands due to the sequential hazard events.

Chapter 8 Conclusions and Further work

8.1 Introduction

The aim of this research is to investigate the impact of TS downburst type events on buildings and to evaluate if the structural dynamic response induced by such wind loading can be represented using thunderstorm downburst wind design spectra (TWDS). Four objectives related to this aim mentioned in Section 1.7 have been met, as shown below.

8.1.1 Objective 1

An analytical model named the "vortex model" has been introduced and developed in order to simulate the process of the full-scale downburst events recorded by JAWS and WERFL. It has been shown that the noteworthy features of the downburst events examined can be acquired from the vortex model easily, i.e. the vertical distributions of longitudinal wind velocity; the velocity time series at the time of maximum velocity; the radial velocity along with the radial distance; the distance between the centre of the downdraft and the position of maximum velocity; the scale of the downburst; the time for the ramp-up period, and decay period. All of the aforementioned features were compared with the measured data and the model's ability to reproduce such phenomena was clearly demonstrated.

8.1.2 Objective 2

This objective is based on the theory that the wind load on the structures can be attained by the combination of the velocity field of TS downburst (including lateral and vertical components and turbulence intensity) and a database of pressure coefficients obtained from wind tunnel measurements with variable azimuthal angles, elevation angles and turbulence intensities. An ABL wind tunnel experiment was set up aiming to establish a pressure coefficient database for two generic building models: a cube building and a portal framed building. The buildings were positioned on a rotational support ensuring that surface pressures corresponding to different flow directions were obtained. Different turbulence intensities in the approaching flow were introduced via a passive turbulence generator (grid) arranged at a set of upstream positions. Finally, the estimated pressures were calculated by combining the estimated pressure coefficients obtained from the wind tunnel (WT) database with dynamic pressures from physical simulations of a downburst flow field in the University of Birmingham transient wind simulation (UoB-TWS); these pressures were compared with the measured pressures from the TWS.

8.1.3 Objective 3

This objective illustrates an innovative TS downburst wind design spectral technique to evaluate the deformation of the SDOF and MDOF system buildings according to the random vibration theory, which integrates the spatio-temporal description of turbulence induced by TS downbursts. This built framework investigates the weight of the parameters, including outflow velocity, structural dimensions, mass, damping ratio, terrain type, and height for the maximum slowly varying mean velocity. Then, the proposed thunderstorm downburst wind design spectra

(TWDS) technique is applied to estimate the dynamic performance of a benchmark building and compare it with the results from the numerical integrations. Furthermore, this benchmark building has been built in the SAP2000 and the deformation of this building under the effects of the simulated non-stationary wind field has been obtained and compared with the counterpart calculated using the TWDS technique. Finally, an equivalent generalised technique is put forward, based on sets of non-linear regression models (NLRM).

8.1.4 Objective 4

This objective has proposed a computational method for evaluating the ductility demands imposed by two sequential hazards (i.e. earthquakes or storms, and post-disaster-thunderstorm downbursts) on steel structures. The effect of the primarily hazard is simulated through a nonlinear pushover analysis of the building which drives the structure at a target inelastic deformation (i.e., pre-defined ductility). The secondary hazard, which is a transient non-stationary wind load induced by the TS downburst event, is then applied after the structure has reached a pre-defined ductility level. Then, the new displacement ductility demand of the originally damaged structures can be quantified, and the global plastic deformation mechanism that causes the collapse can be identified. This novel procedure has been applied to a tall steel building structure, and eleven artificial downburst records have been used for analysis.

8.2 Notable Findings

8.2.1 Objective 1

The velocity time series obtained from the “vortex model” at different heights was compared with the velocity time series of UoB-TWS, and good agreement was demonstrated since the

variation tendencies of velocity time series between the simulated results from the vortex model and the data from TWS are similar, and the maximum RMS error of velocity time series between these is 13.9% of the maximum velocity. Additionally, based on the research contained in this thesis, it can be stated that the vortex model can effectively simulate the vertical distribution of the horizontal velocity profile at the time of maximum velocity and the relevant velocity time series (at the position of the maximum velocity) for full-scale downburst events - the correlation coefficients of the velocities at different heights between the vortex model-simulated data and full-scale downburst measured data were over 0.94 for four out of the six cases. Furthermore, the radial velocities along the radial distance can be estimated by the vortex model for the radial distance range near the radial position of maximum velocity. Therefore, this vortex model has been considered as an appropriate method for the simulation of the velocity time series for the TS downburst.

Comparisons between the velocity time series from the vortex model and the corresponding values from the full-scale downburst measurements of JAWS and WERFL illustrate that some further development of the vortex model is required. For example, the outflow velocity profile and radial direction from the centre of downdraft could be included to capture reasonable radial velocity profiles at the time of maximum velocity.

8.2.2 Objective 2

The passive turbulence generator can produce uniform flow profiles (velocities and turbulence intensities) over heights spanning between 0.26 m and 0.64 m successfully. The designed bars near the edges of the grid are important for obtaining the uniform flow near the tunnel walls (e.g., ground surface), and half-width of the bars is recommended for the design of the edge bars.

The increasing magnitude of the peak pressure coefficients from the WT database with the increasing turbulence intensity (2% to 20%) is evident for the separation regions. However, the influence of the turbulence intensities of the approaching flow on the reattachment regions is small compared with that on separation regions, since the separation regions have high-velocity gradients and high turbulence. Compared with the ABL normalised peak pressure coefficient values from Eurocode (2010) and ASCE7 (2013), the peak pressure coefficients from the wind tunnel database demonstrate a good consistency with the values from Eurocode and are larger than the values from ASCE when the turbulence intensity is around 20%. In the separation region, the maximum pressure coefficients at different turbulence intensities occur when the elevation angle varies between 0° and 15° at 0° azimuthal angle, while when the azimuthal angle is 45°, the maximum pressure coefficients at different turbulence intensities happen between -15° and 0° of elevation angle. Furthermore, the increasing turbulence intensities can affect the elevation angles of the maximum pressure coefficient at different turbulence intensities. Higher turbulence intensity in the approaching flow can lead to the maximum pressure coefficient occurring at lower elevation angle. Therefore, different positions on the roof, turbulence intensities, variable elevation angles, and variable azimuthal angles can influence the peak pressure coefficients, which verifies that the aerodynamic properties on the buildings depend on these parameters.

A preliminary validation of the technique adopted, i.e. combining the dynamic pressures based on Quasi-Steady theory and the pressure coefficient database from UoB-WT experiments, can predict the pressures on the generic buildings effectively - differences in RMS errors of pressure time series between the predicted and measured are less than 50 Pa which is less than one-third of the maximum pressure of TWS (167 Pa for cube building; 176 Pa for portal framed building from area analysis). However, this method is not suitable for the reattachment regions on the

roof. A comparison between point analysis data and an area analysis has been undertaken, which showed that the simulations perform better if an area of the roof is considered rather than a point.

8.2.3 Objective 3

This objective continues developing a relatively new design spectra technique, now applied to TS downburst. The investigation builds on previous research that implemented wind design spectra to determine synoptic wind-structure interactions. The established framework follows classical spectral techniques enhanced with methods to capture the spatial correlation of wind gusts, hence ensuring the correct description of the non-synoptic wind regime in time and space. The robust links between the wind actions and structural response required harmonising the relevant coherence and transfer functions, which in effect enables separating background and resonant wind dynamic effects.

The main findings of this objective are illustrated in the following points.

- It was assumed for this investigation that the turbulence intensity for synoptic and non-synoptic wind regimes was compatible, which has been common practise so far. Notwithstanding, it is acknowledged that there is an ongoing debate amongst scientists regarding the potential distinction that should be made when evaluating the turbulence profile.
- In working out TWDS, higher output accelerations on SDOF systems are observed with increasing downburst outflow velocities, particularly in the low-frequency spectral range. To an extent, this was an expected outcome given the energy imparted by low-frequency wind gusts.

- Design spectral ordinates (pseudo-acceleration) increase with the aspect ratio. This implies that low-rise buildings would undergo higher levels of response acceleration than taller buildings.
- The variations in the damping ratio, although of lower impact, become more evident in the lower frequency range. Furthermore, the changeable heights for the maximum slowly varying mean velocity of the downburst outflow also reflected a slight effect on the design spectra, and the maximum design spectrum is only 0.111 m/s^2 when the height of this maximum value is 150 m.
- The observed slight influence of the terrain exposures can also be non-negligible for non-synoptic wind scenarios.
- The comparison between the results of the TWDS in the frequency-domain and the equivalent numerical simulation in the time-domain as well as the finite element analysis for the benchmark tall building demonstrate the applicability of the spectral technique.
- The peak displacement amplitudes obtained through simplified and refined modelling showed differences ranging between 9.2% and 25.9%, where the latter is the side of the building with a larger area exposed, hence the input force induced displacements exhibited larger differences. This seems related to the cross-correlation decay, which is not accurately estimated through simplified modelling based on rigid bars.

Notwithstanding, the evidence generated highlights the design spectral technique as an alternative to determine the dynamic response of buildings exposed to TS downburst. Its affinity with earthquake spectral techniques makes it easy to implement in commercial packages for structural analysis. The results obtained so far, however, suggest that this method can be

identified as a quick yet reliable vehicle to determine the dynamic response of the structures subjected to TS downburst via classical modal spectral techniques.

8.2.4 Objective 4

A novel technique for the nonlinear analysis of buildings under consecutive hazard loads, i.e. seismic load and strong TS downbursts, has been developed. This procedure can terminate at any pre-defined ductility level generated by the primary hazard, and the secondary hazard event can be applied as a sequential event. This enables a direct quantification of the additional ductility demands caused by the secondary hazard occurrence.

This method has been applied to a 20-storey steel building, which consists of one exterior moment resisting frame and one interior equivalent gravity frame in accordance with the 1994 Uniform Building Code. Eleven downburst synthetic records were applied as secondary hazard events, having different vertical wind profiles and maximum wind velocity, as well as having velocity profiles with varying terrain types. Accordingly, the input energy caused by the consecutive transient non-stationary wind loads can result in visible plastic deformation of the structure exceeding the ductility demands imposed by the primary hazard. With the increase of the ductility demands for the primary hazard event, a more serious damage degree of the structure due to the secondary hazard event can be observed.

Furthermore, the results from this multi-hazard sequential analysis demonstrated the importance of the height where the maximum wind velocity occurs, which is related to the collapse mechanism of the structure. Both parameters control the input wind energy and determine the storey in a structure that are prone to excessive plastic deformations. Firstly, ductility demands increased significantly when the downburst event followed the DL3 to DL6

initial damage state resulting in four- and three-times higher ductility demands than those of the primary event, i.e. 11.52, 12.07, 11.37 and 11.67 respectively, when the sequential analysis of downburst profile 2 is applied. A collapse mechanism was formed that involved the 2nd and 6th storeys of the building under these ductility levels. The same collapse mechanism can be observed for the other velocity profiles that cause the dramatic increase in ductility demands. Secondly, the terrain types of the building can obviously influence the simulated transient non-stationary wind field based on the assumption that the effects of the roughness length on TS downburst wind hazard are the same as the synoptic wind. The changing of the terrain types, i.e. from TT0 to TTIV, can cause an increase in the slowly varying standard deviation when the reduced turbulent fluctuations are the same and can enhance the simulated wind loads. Finally, the obvious increase in ductility demands of the building between the primary and secondary natural hazards or the collapse of the damaged building after the influence of the secondary downburst outflow winds depends on how strong the sequential transient wind load is, while this phenomenon can be enhanced if the height of the peak velocity is consistent with the height of the weak regions of buildings.

Therefore, the analysis results have demonstrated that the proposed analysis method can successfully identify the capacity margins and collapse mechanisms of the structures under multi-hazards and can effectively quantify the increased ductility demands due to the sequential hazard event.

8.3 Recommendations for further work

Firstly, in this research, only six full-scale downburst events are modelled by the vortex model, of which two can typically be regarded as special downburst cases. Extra full-scale downburst

modelling of this vortex model is necessary. Analytical models and physical simulations of the microburst to date only concentrate on the single microburst, and the information about the flow field for the constant high velocity time period (e.g., microburst line) is quite limited.

Secondly, the initial validation results of this innovative method using wind tunnel experiments to estimate the downburst wind load time series on the roof are encouraging. However, the velocity time series from the full-scale downburst measurements with larger elevation angles should be validated further. Additionally, the current method is limited to the wind load on the roof, and a further improved wind tunnel experiment can be built for the wind load on the front surface of the buildings.

Thirdly, further validation of the spectral technique is required, for example, through cross comparison with other existing methods. The final limitation of this research is that the pressure coefficient used for calculating the wind load and the TWDS is independent of the height above the ground due to the insufficient recorded data for this parameter caused by downburst outflows on buildings. Real-time recorded TS downburst events are needed for further investigation.

Reference

A.M.S. (2018). "Gust". Glossary. American Meteorological Society. http://glossary.ametsoc.org/wiki/Gust.

ABAQUS. (2020). User Documentation. In.

ABCNEWS. (2017). Hurricane Katia mudslide leaves two dead in Mexico after earthquake clean-up begins. Available at www.abc.net.au/news/2017-09-10/deadly-quake-hurricane-katia-a-one-two-punch-for-mexico/8889064 [Accessed on 20.09.17].

Abd-Elaal, E.-S., Mills, J. E.and Ma, X. (2013). An analytical model for simulating steady state flows of downburst. *Journal of wind engineering and industrial aerodynamics, 115*, 53-64. doi:http://dx.doi.org/10.1016/j.jweia.2013.01.005

Abd-Elaal, E.-S., Mills, J. E.and Ma, X. (2014). Empirical models for predicting unsteady-state downburst wind speeds. *Journal of wind engineering and industrial aerodynamics, 129*, 49-63. doi:https://doi.org/10.1016/j.jweia.2014.03.011

Abd-Elaal, E.-S., Mills, J. E.and Ma, X. (2018). Numerical simulation of downburst wind flow over real topography. *Journal of wind engineering and industrial aerodynamics, 172*, 85-95.

Aboshosha, H., Bitsuamlak, G.and El Damatty, A. (2015). Turbulence characterization of downbursts using LES. *Journal of wind engineering and industrial aerodynamics, 136*, 44-61. doi:http://dx.doi.org/10.1016/j.jweia.2014.10.020

Acheson, D. J. (1991). Elementary fluid dynamics. In: ASA.

Allen, J. (1977). Short term spectral analysis, synthesis, and modification by discrete Fourier transform. *IEEE Transactions on Acoustics, Speech, and Signal Processing, 25*(3), 235-238.

Aly, A. M.and Abburu, S. (2015). On the design of high-rise buildings for multihazard: fundamental differences between wind and earthquake demand. *Shock and Vibration, 2015*. doi:https://doi.org/10.1155/2015/148681

Asano, K., Iida, Y.and Uematsu, Y. (2019). Laboratory study of wind loads on a low-rise building in a downburst using a moving pulsed jet simulator and their comparison with other types of simulators. *Journal of wind engineering and industrial aerodynamics, 184*, 313-320.

ASCE7. (2013). *Minimum Design Loads for Buildings and Other Structures (ASCE/SEI 7-10)*.

Baines, W.and Peterson, E. (1951). An investigation of flow through screens. *Trans. Am. Soc. Mech. Engrs., 73*.

Batchelor, G. K. (1953). The Theory of Homogeneous Turbulence. Cambridge University Press, London.

Bearman, P.and Morel, T. (1983). Effect of free stream turbulence on the flow around bluff bodies. *Progress in aerospace sciences, 20*(2-3), 97-123.

Brooks, H. E. (2013). Severe thunderstorms and climate change. *Atmospheric Research, 123*, 129-138. doi:https://doi.org/10.1016/j.atmosres.2012.04.002

Burlando, M., Romanić, D., Solari, G., Hangan, H.and Zhang, S. (2017). Field data analysis and weather scenario of a downburst event in Livorno, Italy, on 1 October 2012. *Monthly Weather Review, 145*(9), 3507-3527.

Butler, K., Cao, S., Tamura, Y., Kareem, A.and Ozono, S. (2010). Characteristics of surface pressures on prisms immersed in a transient gust front flow field. *J. Wind Eng. Ind. Aerodyn, 98*, 299-316.

Butler, K.and Kareem, A. (2007). *Physical and numerical modeling of downburst generated gust fronts*. Paper presented at the Proceedings of the 12th International Conference on Wind Engineering, Cairns, Australia.

Castiglioni, C., Alavi, A., Brambilla, G.and Kanyilmaz, A. (2017). *A Procedure for the Assessment of the Behaviour Factor for Steel MRF Systems Based on Pushover Analysis".* Paper presented at the COMPDYN 2017.

Castro, I.and Robins, A. (1977). The flow around a surface-mounted cube in uniform and turbulent streams. *Journal of Fluid Mechanics, 79*(2), 307-335.

Chay, M.and Albermani, F. (2005). Dynamic response of a SDOF system subjected to simulated downburst wind.

Chay, M., Albermani, F.and Wilson, R. (2006). Numerical and analytical simulation of downburst wind loads. *Engineering Structures, 28*(2), 240-254.

Chay, M.and Letchford, C. (2002). Pressure distributions on a cube in a simulated thunderstorm downburst—Part A: stationary downburst observations. *Journal of wind engineering and industrial aerodynamics, 90*(7), 711-732.

Chen, L.and Letchford, C. (2004a). A deterministic–stochastic hybrid model of downbursts and its impact on a cantilevered structure. *Engineering Structures, 26*(5), 619-629. doi:http://dx.doi.org/10.1016/j.engstruct.2003.12.009

Chen, L.and Letchford, C. (2004b). Parametric study on the along-wind response of the CAARC building to downbursts in the time domain. *Journal of wind engineering and industrial aerodynamics, 92*(9), 703-724. doi:http://dx.doi.org/10.1016/j.jweia.2004.03.001

Chen, L.and Letchford, C. (2006). Multi-scale correlation analyses of two lateral profiles of full-scale downburst wind speeds. *Journal of wind engineering and industrial aerodynamics, 94*(9), 675-696. doi:http://dx.doi.org/10.1016/j.jweia.2006.01.021

Chen, L.and Letchford, C. (2007). Numerical simulation of extreme winds from thunderstorm downbursts. *Journal of wind engineering and industrial aerodynamics, 95*(9-11), 977-990. doi:http://dx.doi.org/10.1016/j.jweia.2007.01.021

Chen, X. (2008). Analysis of alongwind tall building response to transient nonstationary winds. *Journal of Structural Engineering, 134*(5), 782-791. doi:http://dx.doi.org/10.1061/(ASCE)0733-9445(2008)134:5(782)

Choi, E. C. (2004). Field measurement and experimental study of wind speed profile during thunderstorms. *Journal of wind engineering and industrial aerodynamics, 92*(3-4), 275-290. doi:http://dx.doi.org/10.1016/j.jweia.2003.12.001

Choi, E. C.and Hidayat, F. A. (2002a). Dynamic response of structures to thunderstorm winds. *Progress in Structural Engineering and Materials, 4*(4), 408-416. doi:http://dx.doi.org/10.1002/pse.132

Choi, E. C.and Hidayat, F. A. (2002b). Gust factors for thunderstorm and non-thunderstorm winds. *Journal of wind engineering and industrial aerodynamics, 90*(12-15), 1683-1696.

Chopra, A. K. (2011). *Dynamics of structures : theory and applications to earthquake engineering* (4th ed. ed.): Upper Saddle River, N.J. : Prentice Hall ; London : Pearson Education [distributor], 2011.

Chopra, A. K.and Goel, R. K. (2002). A modal pushover analysis procedure for estimating seismic demands for buildings. *Earthquake engineering & structural dynamics, 31*(3), 561-582. doi:https://doi.org/10.1002/eqe.144

Code, U. B. (1994). International conference of building officials (ICBO). *Whittier, CA*.

Cook, N. J. (1986). Designers guide to wind loading of building structures. Part 1.

Cooper, D., Jackson, D., Launder, B. E., Liao, G. J. I. J. o. H.and Transfer, M. (1993). Impinging jet studies for turbulence model assessment—I. Flow-field experiments. *36*(10), 2675-2684.

Davenport, A. (1977). The prediction of the response of structures to gusty wind. *Safety of structures under dynamic loading, 1*, 257-284.

De Gaetano, P., Repetto, M. P., Repetto, T.and Solari, G. (2014). Separation and classification of extreme wind events from anemometric records. *Journal of wind engineering and industrial aerodynamics, 126*, 132-143.

Deodatis, G. (1996). Simulation of ergodic multivariate stochastic processes. *Journal of Engineering Mechanics, 122*(8), 778-787. doi:http://dx.doi.org/10.1061/(ASCE)0733-9399(1996)122:8(778)

Durañona, V., Sterling, M.and Baker, C. J. (2007). An analysis of extreme non-synoptic winds. *Journal of wind engineering and industrial aerodynamics, 95*(9-11), 1007-1027. doi:http://dx.doi.org/10.1016/j.jweia.2007.01.014

Duthinh, D.and Potra, F. (2011). Probabilistic and Optimization Considerations in Multihazard Engineering. In *Vulnerability, Uncertainty, and Risk: Analysis, Modeling, and Management* (pp. 501-509).

Duthinh, D.and Simiu, E. (2010). Safety of structures in strong winds and earthquakes: multihazard considerations. *Journal of Structural Engineering, 136*(3), 330-333. doi:https://doi.org/10.1061/(ASCE)ST.1943-541X.0000108

Dyrbye, C.and Hansen, S. O. (1997). *Wind loads on structures*.

Elias, S., Rupakhety, R.and Olafsson, S. (2019). Analysis of a benchmark building installed with tuned mass dampers under wind and earthquake loads. *Shock and Vibration, 2019*. doi:https://doi.org/10.1155/2019/7091819

Erickson, J. (2016). Continuous Wavelet Transform and Inverse - File Exchange - MATLAB Central [WWW Document]. Retrieved from https://uk.mathworks.com/matlabcentral/fileexchange/20821

ESDU. (1993). Computer program for wind speeds and turbulence properties: flat or hilly sites in terrain with roughness changes, version 2.1. Engineering Sciences Data Unit (ESDU). In.

Eurocode. (2010). 1: Actions on structures–Part 1.4: General actions–wind actions. *Brussels: The European Standard EN*.

Farge, M. (1992). Wavelet transforms and their applications to turbulence. *Annual review of fluid mechanics, 24*(1), 395-458.

Fernández-Cabán, P. L.and Masters, F. J. (2018). Effects of freestream turbulence on the pressure acting on a low-rise building roof in the separated flow region. *Frontiers in built environment, 4*, 17.

Fujita, T. T. (1976). Spearhead echo and downburst near the approach end of a John F. Kennedy Airport runway, New York City.

Fujita, T. T. (1985a). The downburst, report of Projects NIMROD and JAWS. *Chicago: University of Chicago*.

Fujita, T. T. (1985b). The downburst: microburst and macroburst. University of Chicago. *SMRP Research 210*, 112.

Fujita, T. T. (1990). Downbursts: meteorological features and wind field characteristics. *Journal of wind engineering and industrial aerodynamics, 36*, 75-86. doi:http://dx.doi.org/10.1016/0167-6105(90)90294-M

Fujita, T. T.and Wakimoto, R. M. (1981). Five scales of airflow associated with a series of downbursts on 16 July 1980. *Monthly Weather Review, 109*(7), 1438-1456.

Gast, K.and Schroeder, J. (2003). *Supercell rear-flank downdraft as sampled in the 2002 thunderstorm outflow experiment.* Paper presented at the Proc., 11th Int. Conf. on Wind Engineering (11ICWE).

Golden, J. (1961). Scale-model Techniques. *MS Thesis, New York Univ.*

Gunter, W. S.and Schroeder, J. L. (2015). High-resolution full-scale measurements of thunderstorm outflow winds. *Journal of wind engineering and industrial aerodynamics, 138*, 13-26.

Haines, M., Sterling, M.and Quinn, A. (2013). *Interference effects around two model high rise buildings in a simulated non-synoptic event.* Paper presented at the Proceedings of the European-African Conference on Wind Engineering.

Haines, M.and Taylor, I. (2018). Numerical investigation of the flow field around low rise buildings due to a downburst event using large eddy simulation. *Journal of wind engineering and industrial aerodynamics, 172*, 12-30.

Haines, M. R. (2015). *The simulation of non-synoptic effects and their implications for engineering structures.* University of Birmingham,

Hall, J. F. (2017). On the descending branch of the pushover curve for multistory buildings. *Earthquake engineering & structural dynamics, 47*(3), 772-783. doi:https://doi.org/10.1002/eqe.2990

Hangan, H., Refan, M., Jubayer, C., Romanic, D., Parvu, D., LoTufo, J.and Costache, A. (2017). Novel techniques in wind engineering. *Journal of wind engineering and industrial aerodynamics, 171*, 12-33.

Hangan, H., Romanic, D.and Jubayer, C. (2019). Three-dimensional, non-stationary and non-Gaussian (3D-NS-NG) wind fields and their implications to wind–structure interaction problems. *Journal of Fluids and Structures, 91*, 102583. doi:http://dx.doi.org/10.1016/j.jfluidstructs.2019.01.024

Hemond, H. F.and Fechner, E. J. (2014). *Chemical fate and transport in the environment*: Elsevier.

Hilber, H. M., Hughes, T. J.and Taylor, R. L. (1977). Improved numerical dissipation for time integration algorithms in structural dynamics. *Earthquake engineering & structural dynamics, 5*(3), 283-292.

Hinze, J. (1959). Turbulence: An introduction to its mechanism and theory. *McGraw-I-I111*.

Hjelmfelt, M. R. (1988). Structure and life cycle of microburst outflows observed in Colorado. *Journal of Applied Meteorology, 27*(8), 900-927. doi:http://dx.doi.org/10.1175/1520-0450(1988)027%3C0900:SALCOM%3E2.0.CO;2

Holmes, J., Forristall, G.and McConochie, J. (2005). *Dynamic response of structures to thunderstorm winds.* Paper presented at the Proc., 10th Americas Conf. on Wind Eng.(10ACWE).

Holmes, J., Hangan, H., Schroeder, J., Letchford, C.and Orwig, K. (2008). A forensic study of the Lubbock-Reese downdraft of 2002. *Wind and Structures, 11*(2), 137-152. doi:http://dx.doi.org/10.12989/was.2008.11.2.137

Holmes, J. D. (1999). Modeling of extreme thunderstorm winds for wind loading of structures and risk assessment. *Wind engineering into the 21st century*, 1409-1415.

Holmes, J. D. (2018). *Wind loading of structures*: CRC press.

Holmes, J. D.and Oliver, S. (2000). An empirical model of a downburst. *Engineering structures, 22*(9), 1167-1172.

Holmes, J. D., Walker, G. R.and Melbourne, W. H. (1990). *A commentary on the Australian standard for wind loads AS 1170 Part 2, 1989*: Australian Wind Engineering Society.

Housner, G. W., Martel, R.and Alford, J. (1953). Spectrum analysis of strong-motion earthquakes. *Bulletin of the Seismological Society of America, 43*(2), 97-119.

Hoxey, R., Richards, P.and Short, J. (2002). A 6 m cube in an atmospheric boundary layer flow-Part 1. Full-scale and wind-tunnel results. *Wind and Structures, 5*(2_3_4), 165-176.

Ivan, M. (1986). A ring-vortex downburst model for flight simulations. *Journal of Aircraft, 23*(3), 232-236.

Jenkinson, A. F. (1955). The frequency distribution of the annual maximum (or minimum) values of meteorological elements. *Quarterly Journal of the Royal Meteorological Society, 81*(348), 158-171.

Jesson, M., Lombardo, F. T., Sterling, M.and Baker, C. (2019). The physical simulation of a transient, downburst-like event–How complex does it need to be? *Journal of wind engineering and industrial aerodynamics, 189*, 135-150. doi:http://dx.doi.org/10.1016/j.jweia.2019.03.021

Jesson, M.and Sterling, M. (2018). A simple vortex model of a thunderstorm downburst–A parametric evaluation. *Journal of wind engineering and industrial aerodynamics, 174*, 1-9.

Jesson, M., Sterling, M., Letchford, C.and Baker, C. (2015a). Aerodynamic forces on the roofs of low-, mid-and high-rise buildings subject to transient winds. *Journal of wind engineering and industrial aerodynamics, 143*, 42-49.

Jesson, M., Sterling, M., Letchford, C.and Haines, M. (2015b). Aerodynamic forces on generic buildings subject to transient, downburst-type winds. *Journal of wind engineering and industrial aerodynamics, 137*, 58-68.

Junayed, C., Jubayer, C., Parvu, D., Romanic, D.and Hangan, H. (2019). Flow field dynamics of large-scale experimentally produced downburst flows. *Journal of wind engineering and industrial aerodynamics, 188*, 61-79.

Kaimal, J. C., Wyngaard, J., Izumi, Y.and Coté, O. (1972). Spectral characteristics of surface-layer turbulence. *Quarterly Journal of the Royal Meteorological Society, 98*(417), 563-589. doi:http://dx.doi.org/10.1002/qj.49709841707

Kareem, A., Hu, L., Guo, Y.and Kwon, D.-K. (2019). Generalized wind loading chain: Time-frequency modeling framework for nonstationary wind effects on structures. *Journal of Structural Engineering, 145*(10), 04019092. doi:http://dx.doi.org/10.1061/(ASCE)ST.1943-541X.0002376

Kareem, A.and Tamura, Y. (2013). *Advanced structural wind engineering*: Springer.

Kim, J.and Hangan, H. (2006). Numerical Simulation of Downbursts and Comparison with Full Scale Data. *JWE: 日本風工学研究会誌*(108), 801-804.

Kim, J.and Hangan, H. (2007). Numerical simulations of impinging jets with application to downbursts. *Journal of wind engineering and industrial aerodynamics, 95*(4), 279-298. doi:http://dx.doi.org/10.1016/j.jweia.2006.07.002

Kim, T., Han, S. W.and Cho, S. I. (2022). Effect of Wind Loads on Collapse Performance and Seismic Loss for Steel Ordinary Moment Frames. *Applied Sciences, 12*(4), 2011.

Kuethe, A., Chow, C., Vought, A.and Helicopters, B. M. (1986). Foundations of Aerodynamics: Bases of Aerodynamic Design—Fourth edition.

Kwag, S., Gupta, A., Baugh, J.and Kim, H.-S. (2021). Significance of multi-hazard risk in design of buildings under earthquake and wind loads. *Engineering Structures, 243*, 112623. doi:https://doi.org/10.1016/j.engstruct.2021.112623

Kwon, D.-K.and Kareem, A. (2009). Gust-front factor: New framework for wind load effects on structures. *Journal of Structural Engineering, 135*(6), 717-732. doi:http://dx.doi.org/10.1061/(ASCE)0733-9445(2009)135:6(717)

Kwon, D. K.and Kareem, A. (2019). Towards codification of thunderstorm/downburst using gust front factor: Model-based and data-driven perspectives. *Engineering Structures, 199*, 109608. doi:http://dx.doi.org/10.1016/j.engstruct.2019.109608

Laneville, A. (1973). *Effects of turbulence on wind induced vibrations of bluff cylinders.* University of British Columbia,

Le, T.-H.and Caracoglia, L. (2017). Computer-based model for the transient dynamics of a tall building during digitally simulated Andrews AFB thunderstorm. *Computers & Structures, 193*, 44-72. doi:http://dx.doi.org/10.1016/j.compstruc.2017.07.019

Lee, D. T.and Yamamoto, A. (1994). Wavelet analysis: theory and applications. *Hewlett Packard journal, 45*, 44-44.

Letchford, C.and Chay, M. (2002). Pressure distributions on a cube in a simulated thunderstorm downburst. Part B: moving downburst observations. *Journal of wind engineering and industrial aerodynamics, 90*(7), 733-753.

Letchford, C., Iverson, R.and McDonald, J. (1993). The application of the quasi-steady theory to full scale measurements on the Texas Tech Building. *Journal of wind engineering and industrial aerodynamics, 48*(1), 111-132.

Letchford, C.and Marwood, R. (1997). On the influence of v and w component turbulence on roof pressures beneath conical vortices. *Journal of wind engineering and industrial aerodynamics, 69*, 567-577.

Levitan, M. L.and Mehta, K. C. (1992). Texas Tech field experiments for wind loads part 1: building and pressure measuring system. *Journal of wind engineering and industrial aerodynamics, 43*(1-3), 1565-1576.

Li, C., Li, Q., Xiao, Y.and Ou, J. (2012). A revised empirical model and CFD simulations for 3D axisymmetric steady-state flows of downbursts and impinging jets. *Journal of wind engineering and industrial aerodynamics, 102*, 48-60. doi:http://dx.doi.org/10.1016/j.jweia.2011.12.004

Li, Y., Song, R.and Van De Lindt, J. W. (2014). Collapse fragility of steel structures subjected to earthquake mainshock-aftershock sequences. *Journal of Structural Engineering, 140*(12), 04014095.

Lin, W., Orf, L., Savory, E.and Novacco, C. (2007). Proposed large-scale modelling of the transient features of a downburst outflow. *Wind and Structures, 10*(4), 315-346.

Lin, W.and Savory, E. (2006). Large-scale quasi-steady modelling of a downburst outflow using a slot jet. *Wind and Structures, 9*(6), 419-440.

Lin, W. E. (2010). *Validation of a novel downdraff outflow simulator: A slot jet wind tunnel* (Vol. 72).

Lombardo, F. T. (2009). Analysis and Interpretation of Thunderstorm Wind Flow and its Effects on a Bluff Body.

Lombardo, F. T., Mason, M. S.and de Alba, A. Z. (2018). Investigation of a downburst loading event on a full-scale low-rise building. *Journal of wind engineering and industrial aerodynamics, 182*, 272-285. doi:https://doi.org/10.1016/j.jweia.2018.09.020

Lombardo, F. T., Smith, D. A., Schroeder, J. L.and Mehta, K. C. (2014). Thunderstorm characteristics of importance to wind engineering. *Journal of wind engineering and industrial aerodynamics, 125*, 121-132. doi:http://dx.doi.org/10.1016/j.jweia.2013.12.004

Loredo-Souza, A. M., Lima, E. G., Vallis, M. B., Rocha, M. M., Wittwer, A. R.and Oliveira, M. G. (2019). Downburst related damages in Brazilian buildings: Are they avoidable? *Journal of wind engineering and industrial aerodynamics, 185*, 33-40. doi:https://doi.org/10.1016/j.jweia.2018.11.022

Lundgren, T., Yao, J.and Mansour, N. (1992). Microburst modelling and scaling. *Journal of Fluid Mechanics, 239*, 461-488.

Machine, W. (2008). Stability of Air. *https://web.archive.org/web/20080209030952/http://www.ace.mmu.ac.uk/eae/Weather/Older/Stability_of_Air.html*.

Martin, J., Alipour, A.and Sarkar, P. (2019). Fragility surfaces for multi-hazard analysis of suspension bridges under earthquakes and microbursts. *Engineering Structures, 197*, 109169.

Martinez-Vazquez, P. (2016). Wind-induced vibrations of structures using design spectra. *International Journal of Advanced Structural Engineering, 8*(4), 379-389. doi:http://dx.doi.org/10.1007/s40091-016-0139-4

Martinez-Vazquez, P. (2017). Strength reduction factors for wind and earthquake effects. *Proceedings of the Institution of Civil Engineers-Structures and Buildings, 170*(10), 735-750. doi:https://doi.org/10.1680/jstbu.16.00086

Martinez-Vazquez, P. (2020). Wind design spectra for generalisation. *Wind and Structures, 30*(2), 155. doi:https://doi.org/10.12989/was.2020.30.2.155

Martinez-Vazquez, P., Gkantou, M.and Baniotopoulos, C. (2019). Strength and ductility demands on wind turbine towers due to earthquake and wind load. *Proceedings of the Institution of Civil Engineers-Structures and Buildings, 172*(8), 556-563. doi:https://doi.org/10.1680/jstbu.17.00154

Mason, M., James, D.and Letchford, C. (2009a). Wind pressure measurements on a cube subjected to pulsed impinging jet flow. *Wind and Structures, 12*(1), 77-88.

Mason, M., Letchford, C.and James, D. (2005). Pulsed wall jet simulation of a stationary thunderstorm downburst, Part A: Physical structure and flow field characterization. *Journal of wind engineering and industrial aerodynamics, 93*(7), 557-580.

Mason, M. S., Fletcher, D.and Wood, G. (2010). Numerical simulation of idealised three-dimensional downburst wind fields. *Engineering Structures, 32*(11), 3558-3570.

Mason, M. S., Wood, G. S.and Fletcher, D. F. (2009b). Numerical simulation of downburst winds. *Journal of wind engineering and industrial aerodynamics, 97*(11-12), 523-539.

MATLAB. (2021). https://www.mathworks.com/help/pdf_doc/matlab/rn.pdf.

McConville, A., Sterling, M.and Baker, C. (2009). The physical simulation of thunderstorm downbursts using an impinging jet. *Wind and Structures, 12*(2), 133.

McConville, A. C. (2008). "Physical simulation of thunderstorm downdrafts", PhD thesis, University of Birmingham, UK.

McDonald, J.and Mehta, K. C. (2006). A recommendation for an enhanced Fujita scale. *Wind Science and Engineering Center, Texas Tech Univ., Lubbock, TX* http://www.depts.ttu.edu/nwi/Pubs/FScale/EFScale.pdf.

Melbourne, W. (1980). Comparison of measurements on the CAARC standard tall building model in simulated model wind flows. *Journal of wind engineering and industrial aerodynamics, 6*(1-2), 73-88. doi:https://doi.org/10.1016/0167-6105(80)90023-9

Mooneghi, M. A., Irwin, P.and Chowdhury, A. G. (2016). Partial turbulence simulation method for predicting peak wind loads on small structures and building appurtenances. *Journal of wind engineering and industrial aerodynamics, 157*, 47-62.

Nakamura, Y., Ohya, Y.and Ozono, S. (1988). The effects of turbulence on bluff-body mean flow. *Journal of wind engineering and industrial aerodynamics, 28*(1-3), 251-259.

NEWS. (2021). Storm complicates earthquake response as it soaks Haiti. Available at https://www.nbcnews.com/news/world/storm-complicates-earthquake-response-it-soaks-haiti-n1276944 [Accessed on 17.08.2021].

Ondrej. (2013). CSi Knowledge Base - SAP2000 21V https://wiki.csiamerica.com/display/sap2000/Home.

Orwig, K. D.and Schroeder, J. L. (2007). Near-surface wind characteristics of extreme thunderstorm outflows. *Journal of wind engineering and industrial aerodynamics, 95*(7), 565-584. doi:http://dx.doi.org/10.1016/j.jweia.2006.12.002

Oseguera, R. M.and Bowles, R. L. (1988). A simple, analytic 3-dimensional downburst model based on boundary layer stagnation flow. NASA Tech. Memo. 100632.

Papazafeiropoulos, G., Muñiz-Calvente, M.and Martínez-Pañeda, E. (2017). Abaqus2Matlab: A suitable tool for finite element post-processing. *Advances in Engineering Software, 105*, 9-16. doi:https://doi.org/10.1016/j.advengsoft.2017.01.006

Peng, L., Huang, G., Chen, X.and Yang, Q. (2018). Evolutionary spectra-based time-varying coherence function and application in structural response analysis to downburst winds. *Journal of Structural Engineering, 144*(7), 04018078. doi:http://dx.doi.org/10.1061/(ASCE)ST.1943-541X.0002066

Piccardo, G.and Solari, G. (1998). Closed form prediction of 3-D wind-excited response of slender structures. *Journal of wind engineering and industrial aerodynamics, 74*, 697-708.

Priestley, M. B. (1965). Evolutionary spectra and non-stationary processes. *Journal of the Royal Statistical Society: Series B (Methodological), 27*(2), 204-229. doi:https://doi.org/10.1155/2015/945203.

Rädler, A. T., Groenemeijer, P. H., Faust, E., Sausen, R.and Púčik, T. (2019). Frequency of severe thunderstorms across Europe expected to increase in the 21st century due to rising instability.

npj Climate and Atmospheric Science, 2(1), 1-5. doi:https://doi.org/10.1038/s41612-019-0083-7

Rajaratnam, N. (1976). *Turbulent jets* (Vol. 5): Elsevier.

Repetto, M. P., Burlando, M., Solari, G., De Gaetano, P., Pizzo, M.and Tizzi, M. (2018). A web-based GIS platform for the safe management and risk assessment of complex structural and infrastructural systems exposed to wind. *Advances in Engineering Software, 117*, 29-45.

Richards, P.and Hoxey, R. (2012a). Pressures on a cubic building—Part 1: Full-scale results. *Journal of wind engineering and industrial aerodynamics, 102*, 72-86.

Richards, P.and Hoxey, R. (2012b). Pressures on a cubic building—Part 2: Quasi-steady and other processes. *Journal of wind engineering and industrial aerodynamics, 102*, 87-96.

Richards, P., Hoxey, R., Connell, B.and Lander, D. (2007). Wind-tunnel modelling of the Silsoe Cube. *Journal of wind engineering and industrial aerodynamics, 95*(9-11), 1384-1399.

Richards, P., Hoxey, R.and Wanigaratne, B. (1995). The effect of directional variations on the observed mean and rms pressure coefficients. *Journal of wind engineering and industrial aerodynamics, 54*, 359-367.

Richards, P. J.and Hoxey, R. P. (2004). Quasi-steady theory and point pressures on a cubic building. *Journal of wind engineering and industrial aerodynamics, 92*(14-15), 1173-1190.

Roach, P. (1987). The generation of nearly isotropic turbulence by means of grids. *International journal of heat and fluid flow, 8*(2), 82-92.

Roisin, B. C. (2019). ENVIRONMENTALFLUID MECHANICS http://www.dartmouth.edu/~cushman/courses/engs151/chapters.html. *Thayer School of EngineeringDartmouth CollegeHanover, New Hampshire 03755*.

Romanic, D. (2021). Mean Flow and Turbulence Characteristics of a Nocturnal Downburst Recorded on a 213-m Tall Meteorological Tower. *Journal of the Atmospheric Sciences, 78*(11), 3629-3650.

Romanic, D., Chowdhury, J., Chowdhury, J.and Hangan, H. (2020a). Investigation of the Transient Nature of Thunderstorm Winds from Europe, the United States, and Australia Using a New Method for Detection of Changepoints in Wind Speed Records. *Monthly Weather Review, 148*(9), 3747-3771.

Romanic, D., Nicolini, E., Hangan, H., Burlando, M.and Solari, G. (2020b). A novel approach to scaling experimentally produced downburst-like impinging jet outflows. *Journal of wind engineering and industrial aerodynamics, 196*, 104025.

Roncallo, L.and Solari, G. (2020). An evolutionary power spectral density model of thunderstorm outflows consistent with real-scale time-history records. *Journal of wind engineering and industrial aerodynamics, 203*, 104204. doi:https://doi.org/10.1016/j.jweia.2020.104204

Rossetto, T., De la Barra, C., Petrone, C., De la Llera, J. C., Vásquez, J.and Baiguera, M. (2019). Comparative assessment of nonlinear static and dynamic methods for analysing building response under sequential earthquake and tsunami. *Earthquake engineering & structural dynamics, 48*(8), 867-887.

Roy, T., Saito, T.and Matsagar, V. (2021). Multihazard framework for investigating high-rise base-isolated buildings under earthquakes and long-duration winds. *Earthquake engineering & structural dynamics, 50*(5), 1334-1357.

Sarkar, P. P., Haan, J., Fred L, Balaramudu, V.and Sengupta, A. (2006). *Laboratory simulation of tornado and microburst to assess wind loads on buildings.* Paper presented at the Structures Congress 2006: Structural Engineering and Public Safety.

Scruton, C. (1981). An Introduction to Wind Effects on Structures-Oxford University Press. In: Oxford, UK.

Selvam, R. P.and Holmes, J. (1992). Numerical simulation of thunderstorm downdrafts. *Journal of wind engineering and industrial aerodynamics, 44*(1-3), 2817-2825.

Sengupta, A.and Sarkar, P. P. (2008). Experimental measurement and numerical simulation of an impinging jet with application to thunderstorm microburst winds. *Journal of wind engineering and industrial aerodynamics, 96*(3), 345-365.

SensorTechnics. (2014). HCLA Series Miniature Amplified Low Pressure Sensors Datasheet. SensorTechnics.

Serras, D. N., Skalomenos, K. A.and Hatzigeorgiou, G. D. (2021). A displacement/damage controlled seismic design method for MRFs with concrete-filled steel tubular columns and composite beams. *Soil Dynamics and Earthquake Engineering, 143*, 106608. doi:https://doi.org/10.1016/j.soildyn.2021.106608

Sharma, R.and Richards, P. (1999). The influence of Reynolds stresses on roof pressure fluctuations. *Journal of wind engineering and industrial aerodynamics, 83*(1-3), 147-157.

Shinozuka, M.and Deodatis, G. (1991). Simulation of stochastic processes by spectral representation. doi:http://dx.doi.org/10.1115/1.3119501

Simiu, E.and Scanlan, R. H. (1986). Wind effects on structures: An introduction to wind engineering. Second edition. Wiley, New York.

Simiu, E.and Scanlan, R. H. (1996). Wind effects on structures: fundamentals and applications to design.

Skalomenos, K. A., Hatzigeorgiou, G. D.and Beskos, D. E. (2015). Application of the hybrid force/displacement (HFD) seismic design method to composite steel/concrete plane frames. *Journal of Constructional Steel Research, 115*, 179-190. doi:http://dx.doi.org/10.1016/j.jcsr.2015.08.007

Skalomenos, K. A., Kurata, M.and Nakashima, M. (2018a). On-line hybrid test method for evaluating the performance of structural details to failure. *Earthquake engineering & structural dynamics, 47*(3), 555-572.

Skalomenos, K. A., Nakashima, M.and Kurata, M. (2018b). Seismic capacity quantification of gusset-plate connections to fracture for ductility-based design. *Journal of Structural Engineering, 144*(10), 04018195.

Skalomenos, K. A.and Papazafeiropoulos, G. (2019). A computational method for performing nonlinear adaptive pushover analysis of structures through ABAQUS simulation. *Proceedings of 7th COMPDYN. Heraklion, Crete, Greece*.

Solari, G. (1989). Wind response spectrum. *Journal of Engineering Mechanics, 115*(9), 2057-2073. doi:http://dx.doi.org/10.1061/(ASCE)0733-9399(1989)115:9(2057)

Solari, G. (2016). Thunderstorm response spectrum technique: theory and applications. *Engineering Structures, 108*, 28-46. doi:http://dx.doi.org/10.1016/j.engstruct.2015.11.012

Solari, G. (2020). Thunderstorm downbursts and wind loading of structures: Progress and prospect. *Frontiers in built environment, 6*, 63. doi:https://doi.org/10.3389/fbuil.2020.00063

Solari, G., Burlando, M., De Gaetano, P.and Repetto, M. P. (2015). Characteristics of thunderstorms relevant to the wind loading of structures. *Wind and Structures, 20*(6), 763. doi:http://dx.doi.org/10.12989/was.2015.20.6.763

Solari, G., Burlando, M.and Repetto, M. P. (2020). Detection, simulation, modelling and loading of thunderstorm outflows to design wind-safer and cost-efficient structures. *Journal of wind engineering and industrial aerodynamics, 200*, 104142.

Solari, G., De Gaetano, P.and Repetto, M. P. (2013). *Wind loading and response of structures in mixed climates.* Paper presented at the Proceedings of the Eight Asia Pacific Conference on Wind Engineering.

Solari, G.and Piccardo, G. (2001). Probabilistic 3-D turbulence modeling for gust buffeting of structures. *Probabilistic engineering mechanics, 16*(1), 73-86. doi:http://dx.doi.org/10.1016/S0266-8920(00)00010-2

Solari, G., Rainisio, D.and De Gaetano, P. (2017). Hybrid simulation of thunderstorm outflows and wind-excited response of structures. *Meccanica, 52*(13), 3197-3220. doi:http://dx.doi.org/10.1007/s11012-017-0718-x

Solari, G., Repetto, M. P., Burlando, M., De Gaetano, P., Pizzo, M., Tizzi, M.and Parodi, M. (2012). The wind forecast for safety management of port areas. *Journal of wind engineering and industrial aerodynamics, 104*, 266-277.

Solari, G. D. G., P; Repetto, MP. (2015). Thunderstorm response spectrum: fundamentals and case study. *Journal of wind engineering and industrial aerodynamics, 143*, 62-77. doi:http://dx.doi.org/10.1016/j.jweia.2015.04.009

Song, J., Martinez-Vazquez, P.and Skalomenos, K. A. (2021a). A framework on the dynamic response of tall structures to non-stationary wind using design spectrum. *8th ECCOMAS Thematic Conference on Computational Methods in Structural Dynamics and Earthquake Engineering, Athens, Greece*. doi:https://2021.compdyn.org/proceedings/pdf/19699.pdf

Song, J., Martinez-Vazquez, P.and Skalomenos, K. A. (2021b). Generalisation for thunderstorm downburst wind design spectra. *The 2021 World Congress on Advances in Structural Engineering and Mechanics (ASEM21) GECE, Seoul, Korea, August 23-26, 2021*.

Stenabaugh, S. E., Iida, Y., Kopp, G. A.and Karava, P. (2015). Wind loads on photovoltaic arrays mounted parallel to sloped roofs on low-rise buildings. *Journal of wind engineering and industrial aerodynamics, 139*, 16-26.

Straka, J. M.and Anderson, J. R. (1993). Numerical simulations of microburst-producing storms: Some results from storms observed during COHMEX. *Journal of the Atmospheric Sciences, 50*(10), 1329-1348.

T.F.I. (2017). Turbulent Flow Instrumentation. Retrieved from https://www.turbulentflow.com.au/Downloads/Cat_CobraProbe.pdf

Taha, A. (2021). Vibration Control of a Tall Benchmark Building under Wind and Earthquake Excitation. *Practice Periodical on Structural Design and Construction, 26*(2), 04021005. doi:https://doi.org/10.1061/(ASCE)SC.1943-5576.0000569

Takeda, K.and Kato, M. (1992). Wind tunnel blockage effects on drag coefficient and wind-induced vibration. *Journal of wind engineering and industrial aerodynamics, 42*(1-3), 897-908.

Thilakarathna, S. N., Anwar, N., Norachan, P.and Naja, F. A. (2018). The effect of wind loads on the seismic performance of tall buildings. *Athens Journal of Technology & Engineering, 5*(3), 251-276. doi:https://doi.org/10.30958/ajte.5-3-3

Tieleman, H., Surry, D.and Mehta, K. (1996). Full/model-scale comparison of surface pressures on the Texas Tech experimental building. *Journal of wind engineering and industrial aerodynamics, 61*(1), 1-23.

Tieleman, H. W. (2003). Wind tunnel simulation of wind loading on low-rise structures: a review. *Journal of wind engineering and industrial aerodynamics, 91*(12-15), 1627-1649.

Tilloy, A., Malamud, B. D., Winter, H.and Joly-Laugel, A. (2019). A review of quantification methodologies for multi-hazard interrelationships. *Earth-Science Reviews, 196*, 102881. doi:https://doi.org/10.1016/j.earscirev.2019.102881

Torrence, C.and Compo, G. P. (1998). A practical guide to wavelet analysis. *Bulletin of the American Meteorological society, 79*(1), 61-78.

Vickery, B. (1965). On the flow behind a coarse grid and its use a model of atmospheric turbulence in studies related to wind loads on buildings. *NPL Aero Report 1143*.

Vickery, B. (1968). Load fluctuations in turbulent flow. *Journal of the Engineering Mechanics Division, 94*(1), 31-46.

Vicroy, D. D. (1992). Assessment of microburst models for downdraft estimation. *Journal of Aircraft, 29*(6), 1043-1048. doi:http://dx.doi.org/10.2514/3.46282

Vita, G., Hemida, H., Andrianne, T.and Baniotopoulos, C. C. (2018). Generating atmospheric turbulence using passive grids in an expansion test section of a wind tunnel. *Journal of wind engineering and industrial aerodynamics, 178*, 91-104.

von Kármán, T. (1948). Progress in the statistical theory of turbulence. *Proceedings of the National Academy of Sciences of the United States of America, 34*(11), 530. doi:http://dx.doi.org/10.1073/pnas.34.11.530

Wang, H. (2018). *Fluid Mechanics as I Understand It*: Guo fang gong ye chu ban she.

Wang, L. (2008). *Stochastic modeling and simulation of transient events*: University of Notre Dame.

Welsh, A. (2013). Low Turbulence Wind Tunnel Design and Wind Turbine Wake Characterization.

Wilson, J. W., Roberts, R. D., Kessinger, C.and McCarthy, J. (1984). Microburst wind structure and evaluation of Doppler radar for airport wind shear detection. *Journal of Climate and Applied Meteorology, 23*(6), 898-915.

Wilson, J. W.and Wakimoto, R. M. (2001). The discovery of the downburst: TT Fujita's contribution. *Bulletin of the American Meteorological society, 82*(1), 49-62.

Wood, G.and Kwok, K. (1998). *An empirically derived estimate for the mean velocity profile of a thunderstorm downburst.* Paper presented at the Proceedings of the 7th Australian Wind Engineering Society Workshop, Auckland.

Wood, G. S., Kwok, K. C., Motteram, N. A.and Fletcher, D. F. (2001). Physical and numerical modelling of thunderstorm downbursts. *Journal of wind engineering and industrial aerodynamics, 89*(6), 535-552. doi:http://dx.doi.org/10.1016/S0167-6105(00)00090-8

Wtopnews. (2012). Microburst does heavy damage to buildings in Spotsylvania County.Available at https://wtop.com/news/2012/07/microburst-does-heavy-damage-to-buildings-in-spotsylvania-county/ [Accessed on 07.09.2012].

Wu, C.-H. (2017). Estimation of Turbulence Effects on Wind-induced Suctions on the Roof of a Low-rise Building.

Wu, C.-H., Akon, A. F.and Kopp, G. A. (2017). Effects of turbulence on the mean pressure field in the separated-reattaching flow above a low-rise building. *Journal of wind engineering and industrial aerodynamics, 171*, 79-92.

Wu, C.-H.and Kopp, G. A. (2016). Estimation of wind-induced pressures on a low-rise building using quasi-steady theory. *Frontiers in built environment, 2*, 5.

Wu, C.-H.and Kopp, G. A. (2018). A quasi-steady model to account for the effects of upstream turbulence characteristics on pressure fluctuations on a low-rise building. *Journal of wind engineering and industrial aerodynamics, 179*, 338-357.

Wu, F. (2000). *Full-scale study of conical vortices and their effects near roof corners.* Texas Tech University,

Xhelaj, A., Burlando, M.and Solari, G. (2020). A general-purpose analytical model for reconstructing the thunderstorm outflows of travelling downbursts immersed in ABL flows. *Journal of wind engineering and industrial aerodynamics, 207*, 104373. doi:http://dx.doi.org/10.1016/j.jweia.2020.104373

Zawistowski, T.and Shah, P. (2010). An introduction to sampling theory. *Exemple de mostreig i sobremostreig*.

Zhang, S., Solari, G., De Gaetano, P., Burlando, M.and Repetto, M. P. (2018). A refined analysis of thunderstorm outflow characteristics relevant to the wind loading of structures. *Probabilistic engineering mechanics, 54*, 9-24. doi:http://dx.doi.org/10.1016/j.probengmech.2017.06.003

Zhang, Y., Hu, H.and Sarkar, P. P. (2014). Comparison of microburst-wind loads on low-rise structures of various geometric shapes. *Journal of wind engineering and industrial aerodynamics, 133*, 181-190.

Zhang, Y., Sarkar, P.and Hu, H. (2013). An experimental study of flow fields and wind loads on gable-roof building models in microburst-like wind. *Experiments in fluids, 54*(5), 1511.

Zhu, S.and Etkin, B. (1985). Model of the wind field in a downburst. *Journal of Aircraft, 22*(7), 595-601.

Appendix A Database of the pressure coefficients

According to the discussion in Chapter 4, the magnitude of the pressure coefficients varies obviously with the turbulence intensities when the elevation angles are within $\pm$15°. Therefore, the pressure coefficients under crucial elevation angles within the separation regions are shown in Appendix A.

Table A-1. Database for cube building at TI0. Number in the left-hand column is the tapping index.

Elevation	0							15							30							-15						
Azimuth	0	15	30	45	60	75	90	0	15	30	45	60	75	90	0	15	30	45	60	75	90	0	15	30	45	60	75	90
11	-1.40	-1.15	-0.96	-0.95	-0.88	-1.14	-1.31	-1.44	-1.11	-1.07	-0.94	-0.94	-1.05	-1.24	-0.69	-0.90	-1.16	-1.19	-0.94	-0.93	-1.22	-0.69	-0.70	-0.67	-0.77	-0.90	-0.94	-1.28
21	-1.46	-1.13	-0.96	-0.97	-1.01	-1.17	-1.44	-1.50	-1.17	-1.13	-1.06	-1.05	-1.00	-1.36	-0.63	-0.75	-0.88	-0.97	-0.81	-0.76	-1.30	-0.67	-0.71	-0.69	-0.79	-0.88	-1.05	-1.43
31	-1.42	-1.11	-0.96	-1.13	-1.19	-1.25	-1.53	-1.42	-1.29	-1.32	-1.22	-1.13	-0.99	-1.50	-0.60	-0.65	-0.77	-0.84	-0.72	-0.68	-1.40	-0.68	-0.67	-0.71	-0.79	-0.85	-1.09	-1.56
41	-1.38	-1.09	-0.95	-1.29	-1.40	-1.27	-1.59	-1.33	-1.40	-1.44	-1.38	-1.21	-1.03	-1.54	-0.57	-0.61	-0.74	-0.82	-0.70	-0.67	-1.40	-0.65	-0.64	-0.70	-0.79	-0.82	-1.08	-1.64
51	-1.39	-1.14	-0.97	-1.40	-1.64	-1.16	-1.56	-1.27	-1.46	-1.55	-1.55	-1.34	-0.97	-1.47	-0.58	-0.58	-0.70	-0.78	-0.73	-0.61	-1.36	-0.69	-0.65	-0.68	-0.82	-0.86	-1.06	-1.60
61	-1.34	-1.12	-0.95	-1.62	-1.82	-1.23	-1.48	-1.24	-1.61	-1.76	-1.82	-1.52	-1.05	-1.42	-0.61	-0.55	-0.71	-0.87	-0.77	-0.62	-1.32	-0.65	-0.64	-0.71	-0.79	-0.83	-1.02	-1.54
71	-1.37	-1.17	-0.98	-2.00	-1.89	-1.35	-1.46	-1.29	-1.91	-2.17	-2.21	-1.68	-1.37	-1.42	-0.64	-0.62	-0.79	-0.95	-0.74	-1.08	-1.32	-0.70	-0.66	-0.73	-0.77	-0.84	-1.04	-1.50
81	-1.37	-1.17	-0.99	-2.63	-1.44	-1.38	-1.44	-1.40	-2.16	-3.06	-1.93	-1.13	-1.68	-1.45	-0.69	-0.72	-0.75	-0.39	-0.44	-1.73	-1.32	-0.72	-0.69	-0.72	-0.80	-0.86	-1.06	-1.49
91	-1.38	-1.17	-0.95	-2.12	-1.04	-1.29	-1.45	-1.41	-2.40	-1.55	-0.78	-1.69	-1.68	-1.45	-0.75	-0.53	0.27	-0.05	-0.64	-1.91	-1.33	-0.68	-0.67	-0.69	-0.75	-0.82	-1.01	-1.48
12	-1.48	-1.19	-1.01	-0.94	-0.92	-0.97	-1.28	-1.54	-1.16	-1.08	-1.01	-1.12	-0.94	-1.22	-0.45	-0.92	-1.18	-1.23	-0.91	-0.93	-1.22	-0.70	-0.74	-0.73	-0.83	-0.98	-0.89	-1.25
22	-1.48	-1.17	-0.98	-1.01	-1.11	-0.88	-1.37	-1.63	-1.23	-1.19	-1.17	-1.29	-0.74	-1.32	-0.66	-0.78	-0.91	-1.06	-0.71	-0.68	-1.26	-0.69	-0.72	-0.73	-0.80	-0.90	-0.91	-1.38
32	-1.44	-1.16	-0.96	-1.16	-1.40	-0.96	-1.45	-1.44	-1.35	-1.36	-1.52	-0.92	-0.70	-1.44	-0.61	-0.67	-0.81	-0.74	-0.43	-0.59	-1.32	-0.66	-0.69	-0.71	-0.78	-0.85	-0.97	-1.47
42	-1.42	-1.17	-1.00	-1.34	-1.37	-1.05	-1.55	-1.38	-1.47	-1.56	-1.67	-0.59	-0.84	-1.48	-0.63	-0.64	-0.74	-0.46	-0.42	-0.57	-1.37	-0.68	-0.71	-0.74	-0.81	-0.86	-1.06	-1.54
52	-1.37	-1.13	-0.95	-1.51	-1.22	-1.17	-1.50	-1.32	-1.50	-1.79	-1.23	-0.53	-0.97	-1.43	-0.61	-0.60	-0.59	0.01	-0.39	-0.57	-1.34	-0.66	-0.65	-0.72	-0.78	-0.82	-1.02	-1.51
62	-1.37	-1.17	-1.00	-1.72	-1.21	-1.32	-1.48	-1.29	-1.73	-2.03	-0.63	-0.55	-1.17	-1.44	-0.65	-0.63	0.16	0.04	-0.37	-0.83	-1.32	-0.68	-0.67	-0.72	-0.80	-0.85	-1.04	-1.49
72	-1.39	-1.21	-1.01	-1.57	-1.17	-1.42	-1.45	-1.38	-1.98	-1.49	-0.50	-0.73	-1.56	-1.40	-0.66	-0.50	0.25	-0.02	-0.38	-1.39	-1.31	-0.70	-0.67	-0.73	-0.80	-0.86	-1.03	-1.47
82	-1.37	-1.19	-0.98	-1.32	-1.14	-1.38	-1.43	-1.41	-1.94	-0.51	-0.56	-1.27	-1.79	-1.40	-0.66	0.59	0.23	0.07	-0.36	-1.95	-1.28	-0.69	-0.65	-0.70	-0.74	-0.82	-1.00	-1.43
92	-1.39	-1.18	-1.03	-2.19	-1.08	-1.36	-1.46	-1.46	-1.28	-0.50	-0.56	-2.60	-1.76	-1.42	-0.69	0.34	0.26	0.17	-2.27	-1.99	-1.30	-0.71	-0.68	-0.70	-0.74	-0.84	-0.99	-1.44
13	-1.45	-1.21	-0.99	-0.92	-0.94	-0.93	-1.23	-1.49	-1.20	-1.13	-1.12	-0.63	-0.92	-1.21	0.01	-0.45	-0.75	-0.89	-0.79	-0.91	-1.17	-0.74	-0.69	-0.70	-0.79	-0.89	-0.88	-1.22
23	-1.46	-1.18	-0.97	-1.07	-0.90	-0.88	-1.28	-1.55	-1.25	-1.30	-1.13	-0.52	-0.71	-1.25	0.26	-0.28	-0.43	-0.55	-0.56	-0.67	-1.22	-0.69	-0.71	-0.70	-0.78	-0.81	-0.95	-1.29
33	-1.42	-1.13	-0.96	-1.23	-0.76	-1.01	-1.36	-1.51	-1.35	-1.46	-0.79	-0.54	-0.78	-1.35	0.33	0.19	-0.26	-0.40	-0.50	-0.58	-1.25	-0.68	-0.70	-0.73	-0.79	-0.85	-1.00	-1.39
43	-1.43	-1.14	-0.99	-1.31	-0.75	-1.11	-1.46	-1.45	-1.49	-1.46	-0.46	-0.58	-0.91	-1.43	0.31	0.22	0.11	-0.38	-0.45	-0.60	-1.31	-0.69	-0.67	-0.73	-0.81	-0.87	-1.05	-1.48
53	-1.39	-1.18	-0.98	-1.23	-0.85	-1.25	-1.45	-1.40	-1.65	-1.20	-0.42	-0.55	-1.11	-1.40	0.41	0.37	0.16	-0.32	-0.40	-0.82	-1.28	-0.66	-0.66	-0.71	-0.78	-0.83	-1.04	-1.47
63	-1.36	-1.17	-1.01	-1.12	-0.98	-1.35	-1.40	-1.37	-1.68	-0.84	-0.44	-0.55	-1.32	-1.39	0.32	0.47	0.20	-0.25	-0.37	-1.12	-1.29	-0.66	-0.63	-0.70	-0.78	-0.83	-1.03	-1.45
73	-1.37	-1.20	-1.01	-0.97	-1.14	-1.38	-1.40	-1.43	-1.36	-0.43	-0.48	-0.85	-1.64	-1.39	0.38	0.45	0.17	-0.22	-0.36	-1.66	-1.26	-0.68	-0.66	-0.71	-0.79	-0.84	-1.02	-1.43
83	-1.43	-1.25	-1.05	-1.14	-1.18	-1.41	-1.45	-1.50	-0.72	-0.53	-0.55	-1.63	-1.72	-1.39	0.23	0.29	0.20	-0.08	-0.61	-1.88	-1.31	-0.73	-0.70	-0.75	-0.79	-0.89	-1.02	-1.45
93	-1.41	-1.22	-1.41	-2.54	-1.14	-1.38	-1.40	-1.51	-0.40	-0.53	-2.17	-2.10	-1.65	-1.40	-0.23	0.23	0.25	-1.14	-2.14	-1.78	-1.26	-0.73	-0.70	-0.73	-0.78	-0.85	-1.02	-1.42

Table A-2. Database for cube building at TI1. Number in the left-hand column is the tapping index.

Elevation	0							15							30							-15						
Azimuth	0	15	30	45	60	75	90	0	15	30	45	60	75	90	0	15	30	45	60	75	90	0	15	30	45	60	75	90
11	-2.05	-1.72	-1.66	-1.56	-1.50	-1.60	-1.68	-2.09	-1.55	-1.65	-1.57	-1.56	-1.60	-1.60	-1.15	-1.42	-1.58	-1.71	-1.50	-1.35	-1.59	-1.63	-1.35	-1.22	-1.39	-1.52	-1.55	-1.66
21	-2.07	-1.75	-1.69	-1.67	-1.70	-1.72	-1.87	-2.14	-1.55	-1.70	-1.74	-1.64	-1.59	-1.69	-1.13	-1.23	-1.38	-1.51	-1.43	-1.31	-1.70	-1.62	-1.37	-1.34	-1.43	-1.50	-1.66	-1.78
31	-2.02	-1.78	-1.83	-1.96	-1.96	-1.81	-1.97	-2.04	-1.76	-1.89	-1.91	-1.80	-1.49	-1.89	-1.06	-1.16	-1.31	-1.37	-1.34	-1.21	-1.95	-1.56	-1.35	-1.34	-1.42	-1.56	-1.89	-1.93
41	-1.93	-1.78	-2.01	-2.08	-2.12	-1.90	-2.13	-1.99	-1.79	-1.98	-2.08	-1.83	-1.62	-2.03	-1.06	-1.07	-1.28	-1.41	-1.31	-1.23	-1.96	-1.45	-1.40	-1.28	-1.39	-1.74	-1.97	-1.99
51	-1.97	-1.97	-2.18	-2.46	-2.40	-1.99	-2.33	-1.89	-1.95	-2.19	-2.33	-2.01	-1.68	-2.24	-1.11	-1.12	-1.33	-1.43	-1.40	-1.21	-2.22	-1.52	-1.41	-1.45	-1.37	-1.72	-2.08	-2.16
61	-1.95	-2.07	-2.25	-2.55	-2.66	-1.98	-2.28	-1.84	-2.12	-2.40	-2.53	-2.20	-1.79	-2.22	-1.11	-1.18	-1.27	-1.42	-1.41	-1.19	-2.27	-1.46	-1.38	-1.36	-1.46	-1.85	-2.06	-2.18
71	-1.94	-2.14	-2.56	-3.26	-2.97	-2.13	-2.30	-1.95	-2.34	-2.74	-2.94	-2.37	-2.05	-2.21	-1.16	-1.17	-1.36	-1.51	-1.48	-1.57	-2.25	-1.64	-1.40	-1.35	-1.46	-1.83	-2.01	-2.21
81	-1.98	-2.26	-2.89	-3.87	-2.96	-2.30	-2.28	-2.12	-2.71	-3.52	-2.79	-2.06	-2.44	-2.16	-1.26	-1.37	-1.61	-1.32	-1.12	-2.36	-2.17	-1.69	-1.48	-1.40	-1.46	-1.83	-1.96	-2.18
91	-2.04	-2.07	-2.65	-2.75	-2.18	-2.15	-2.05	-2.05	-2.88	-1.88	-1.32	-2.29	-2.52	-2.07	-1.30	-1.24	0.30	-0.63	-1.08	-2.58	-2.14	-1.67	-1.43	-1.38	-1.34	-1.59	-1.85	-2.05
12	-2.23	-1.86	-1.88	-1.62	-1.59	-1.55	-1.72	-2.28	-1.71	-1.80	-1.82	-1.91	-1.53	-1.59	-1.19	-1.58	-1.84	-1.86	-1.74	-1.45	-1.69	-1.70	-1.46	-1.39	-1.52	-1.57	-1.55	-1.65
22	-2.20	-1.84	-1.82	-1.79	-1.85	-1.48	-1.79	-2.28	-1.73	-1.81	-1.98	-1.96	-1.30	-1.72	-1.19	-1.35	-1.52	-1.68	-1.55	-1.18	-1.71	-1.62	-1.42	-1.37	-1.50	-1.61	-1.63	-1.77
32	-2.14	-1.89	-1.95	-2.10	-2.18	-1.42	-1.97	-2.15	-1.84	-2.02	-2.22	-1.93	-1.21	-1.81	-1.25	-1.29	-1.46	-1.55	-1.06	-1.08	-1.86	-1.59	-1.47	-1.38	-1.48	-1.67	-1.57	-1.86
42	-2.16	-2.02	-2.12	-2.34	-2.30	-1.59	-2.16	-2.06	-2.03	-2.26	-2.61	-1.60	-1.24	-2.13	-1.25	-1.27	-1.46	-1.42	-0.93	-1.11	-2.12	-1.66	-1.50	-1.47	-1.56	-1.82	-1.67	-2.03
52	-1.98	-2.02	-2.16	-2.47	-2.15	-1.62	-2.15	-1.96	-2.03	-2.47	-2.35	-1.20	-1.20	-2.05	-1.19	-1.14	-1.32	-0.95	-0.88	-0.96	-2.10	-1.53	-1.42	-1.36	-1.43	-1.72	-1.80	-2.06
62	-2.05	-2.06	-2.36	-2.69	-2.16	-1.97	-2.20	-1.91	-2.17	-2.69	-1.60	-1.15	-1.56	-2.19	-1.21	-1.19	-1.19	-0.50	-0.93	-1.07	-2.18	-1.57	-1.45	-1.36	-1.46	-1.78	-1.92	-2.12
72	-2.16	-2.31	-2.74	-2.42	-2.02	-2.31	-2.30	-2.06	-2.53	-2.18	-1.03	-1.22	-2.18	-2.20	-1.26	-1.29	0.27	-0.79	-0.96	-1.93	-2.21	-1.56	-1.48	-1.39	-1.48	-1.79	-2.09	-2.16
82	-2.04	-2.28	-2.54	-2.14	-2.35	-2.36	-2.07	-2.07	-2.55	-0.95	-1.04	-1.80	-2.47	-2.02	-1.17	0.14	0.16	-0.62	-0.84	-2.39	-2.14	-1.59	-1.45	-1.26	-1.34	-1.57	-1.88	-2.03
92	-2.09	-2.23	-2.26	-3.04	-2.66	-2.25	-2.11	-2.16	-2.14	-1.16	-1.12	-3.72	-2.73	-2.05	-1.39	0.25	0.24	-0.72	-2.94	-2.59	-2.06	-1.61	-1.45	-1.35	-1.40	-1.58	-1.79	-2.01
13	-2.29	-1.89	-1.87	-1.60	-1.65	-1.51	-1.68	-2.16	-1.72	-1.84	-1.96	-1.37	-1.40	-1.58	-0.55	-1.08	-1.40	-1.42	-1.40	-1.41	-1.61	-1.61	-1.42	-1.34	-1.43	-1.54	-1.44	-1.63
23	-2.15	-1.83	-1.79	-1.79	-1.70	-1.20	-1.69	-2.17	-1.76	-1.91	-1.88	-1.08	-1.23	-1.68	0.42	-0.97	-1.03	-0.99	-1.10	-1.16	-1.63	-1.67	-1.44	-1.31	-1.40	-1.49	-1.37	-1.65
33	-2.10	-1.78	-1.96	-1.97	-1.52	-1.36	-1.89	-2.20	-1.80	-2.10	-1.47	-1.12	-1.12	-1.76	0.49	-0.92	-0.80	-0.93	-1.09	-1.10	-1.79	-1.55	-1.39	-1.34	-1.45	-1.54	-1.62	-1.82
43	-2.14	-1.97	-2.13	-2.11	-1.42	-1.56	-2.05	-2.16	-2.00	-2.14	-1.02	-1.19	-1.19	-1.98	-0.17	-0.68	-0.44	-0.96	-0.98	-1.05	-2.00	-1.60	-1.46	-1.40	-1.48	-1.66	-1.70	-2.02
53	-2.09	-2.00	-2.30	-1.86	-1.36	-1.73	-2.07	-2.00	-2.14	-1.77	-0.89	-1.07	-1.41	-2.00	-0.02	-0.27	-0.17	-0.83	-0.87	-0.98	-2.05	-1.49	-1.42	-1.38	-1.48	-1.66	-1.80	-2.06
63	-1.91	-2.06	-2.34	-1.70	-1.58	-2.00	-2.14	-2.00	-2.17	-1.28	-0.97	-1.10	-1.75	-2.02	-0.41	0.54	0.31	-0.77	-0.84	-1.33	-2.17	-1.51	-1.43	-1.36	-1.39	-1.60	-1.91	-2.00
73	-1.96	-2.17	-2.22	-1.40	-1.99	-2.21	-2.09	-2.06	-1.94	-0.94	-1.03	-1.18	-2.31	-2.00	0.06	0.38	0.25	-0.77	-0.83	-2.12	-2.06	-1.51	-1.48	-1.27	-1.41	-1.67	-1.97	-2.01
83	-2.13	-2.31	-2.18	-1.93	-2.52	-2.49	-2.16	-2.20	-1.60	-0.98	-1.10	-2.41	-2.73	-2.09	-0.06	0.18	0.03	-0.69	-0.90	-2.61	-2.17	-1.67	-1.54	-1.43	-1.55	-1.76	-1.96	-2.17
93	-2.06	-2.12	-2.81	-3.67	-2.43	-2.33	-2.04	-2.19	-0.89	-1.32	-2.91	-3.28	-2.67	-2.03	-0.76	0.34	0.35	-1.82	-2.96	-2.57	-2.06	-1.70	-1.46	-1.45	-1.39	-1.67	-1.97	-1.98

Table A-3. Database for cube building at TI2. Number in the left-hand column is the tapping index.

Elevation	0							15							30							-15						
Azimuth	0	15	30	45	60	75	90	0	15	30	45	60	75	90	0	15	30	45	60	75	90	0	15	30	45	60	75	90
11	-2.38	-1.90	-1.87	-1.79	-1.75	-1.60	-1.63	-2.13	-1.85	-1.92	-2.01	-1.77	-1.55	-1.64	-1.43	-1.64	-1.86	-1.70	-1.51	-1.47	-1.56	-1.64	-1.50	-1.69	-1.74	-1.67	-1.54	-1.78
21	-2.36	-1.90	-1.94	-1.97	-1.97	-1.70	-1.87	-2.23	-1.85	-1.93	-2.04	-1.86	-1.61	-1.72	-1.39	-1.42	-1.60	-1.59	-1.60	-1.45	-1.66	-1.70	-1.64	-1.76	-1.72	-1.69	-1.78	-1.87
31	-2.16	-1.84	-2.08	-2.23	-2.12	-1.86	-1.94	-2.02	-1.90	-2.10	-2.18	-1.89	-1.61	-1.89	-1.29	-1.35	-1.48	-1.56	-1.48	-1.33	-1.87	-1.65	-1.61	-1.69	-1.80	-1.95	-1.88	-1.98
41	-2.16	-2.03	-2.34	-2.48	-2.34	-1.93	-2.15	-1.95	-1.97	-2.25	-2.28	-2.00	-1.63	-1.98	-1.32	-1.36	-1.40	-1.57	-1.43	-1.41	-1.96	-1.65	-1.64	-1.76	-1.91	-2.23	-1.96	-2.10
51	-2.10	-2.18	-2.59	-2.78	-2.78	-2.11	-2.33	-1.89	-2.18	-2.49	-2.59	-2.18	-1.76	-2.28	-1.29	-1.39	-1.49	-1.69	-1.49	-1.49	-2.25	-1.58	-1.66	-1.88	-2.01	-2.33	-2.12	-2.35
61	-2.06	-2.17	-2.83	-3.06	-3.03	-2.18	-2.36	-1.91	-2.29	-2.70	-2.73	-2.28	-1.84	-2.40	-1.26	-1.30	-1.50	-1.57	-1.50	-1.32	-2.27	-1.57	-1.76	-1.86	-2.11	-2.52	-2.25	-2.44
71	-2.15	-2.48	-3.06	-3.89	-3.57	-2.36	-2.56	-1.95	-2.59	-3.36	-3.29	-2.53	-2.01	-2.44	-1.33	-1.43	-1.61	-1.89	-1.63	-1.77	-2.36	-1.66	-1.79	-1.89	-2.30	-2.67	-2.26	-2.43
81	-2.24	-2.66	-4.05	-4.56	-3.58	-2.60	-2.66	-2.08	-3.14	-4.06	-3.15	-2.18	-2.56	-2.55	-1.47	-1.65	-1.86	-1.78	-1.36	-2.63	-2.42	-1.77	-1.89	-1.93	-2.34	-2.81	-2.30	-2.42
91	-2.26	-2.35	-3.67	-3.02	-3.24	-2.61	-2.49	-2.20	-3.35	-1.83	-1.48	-1.97	-2.99	-2.44	-1.56	-1.63	0.27	-0.89	-1.24	-3.17	-2.30	-1.75	-1.81	-1.84	-2.18	-2.29	-2.15	-2.36
12	-2.51	-2.03	-1.97	-1.88	-1.95	-1.72	-1.71	-2.43	-1.94	-2.11	-2.26	-2.04	-1.63	-1.65	-1.43	-1.80	-2.01	-1.99	-1.85	-1.53	-1.68	-1.73	-1.75	-1.80	-1.91	-1.74	-1.71	-1.73
22	-2.39	-1.93	-1.99	-2.06	-2.21	-1.65	-1.64	-2.37	-1.97	-2.16	-2.32	-2.15	-1.53	-1.66	-1.41	-1.59	-1.66	-1.81	-1.63	-1.18	-1.61	-1.77	-1.68	-1.78	-1.76	-1.84	-1.71	-1.86
32	-2.40	-2.03	-2.32	-2.48	-2.55	-1.59	-1.90	-2.18	-1.98	-2.39	-2.59	-2.25	-1.28	-1.84	-1.36	-1.49	-1.62	-1.83	-1.36	-1.15	-1.84	-1.75	-1.72	-1.72	-1.87	-2.06	-1.79	-1.90
42	-2.27	-2.13	-2.52	-2.84	-2.63	-1.61	-2.03	-2.10	-2.12	-2.60	-2.79	-2.00	-1.26	-2.10	-1.44	-1.46	-1.60	-1.74	-1.13	-1.10	-2.01	-1.70	-1.70	-1.82	-2.00	-2.27	-1.78	-2.10
52	-2.16	-2.11	-2.68	-2.95	-2.27	-1.55	-2.17	-1.96	-2.19	-2.78	-2.52	-1.53	-1.19	-2.17	-1.31	-1.40	-1.58	-1.40	-0.94	-1.10	-2.10	-1.56	-1.69	-1.81	-2.01	-2.29	-1.78	-2.16
62	-2.15	-2.28	-2.92	-3.05	-2.11	-1.85	-2.32	-1.96	-2.44	-3.10	-1.98	-1.15	-1.40	-2.38	-1.37	-1.46	-1.46	-1.04	-1.05	-1.24	-2.28	-1.66	-1.80	-1.93	-2.17	-2.48	-1.99	-2.31
72	-2.27	-2.52	-3.27	-2.55	-1.76	-2.37	-2.61	-2.10	-2.86	-2.40	-1.15	-1.31	-2.17	-2.49	-1.44	-1.56	0.20	-0.84	-1.01	-2.13	-2.40	-1.73	-1.84	-1.93	-2.31	-2.37	-2.30	-2.39
82	-2.31	-2.63	-2.97	-1.70	-2.39	-2.64	-2.47	-2.17	-2.68	-1.02	-1.16	-1.32	-2.63	-2.43	-1.45	-1.18	0.35	-0.72	-0.88	-2.70	-2.33	-1.73	-1.75	-1.89	-2.19	-2.44	-2.36	-2.20
92	-2.39	-2.51	-2.71	-3.02	-4.30	-2.80	-2.38	-2.38	-2.20	-1.18	-1.41	-4.26	-3.29	-2.43	-1.43	0.30	0.38	-0.99	-3.39	-3.29	-2.27	-1.78	-1.86	-1.89	-2.22	-2.57	-2.29	-2.26
13	-2.40	-1.93	-1.85	-2.04	-1.90	-1.41	-1.52	-1.92	-1.98	-2.19	-2.25	-1.52	-1.40	-1.56	-0.37	-1.22	-1.57	-1.54	-1.44	-1.47	-1.60	-1.81	-1.69	-1.78	-1.74	-1.66	-1.39	-1.64
23	-2.34	-1.77	-2.05	-2.17	-1.81	-1.23	-1.61	-2.15	-1.95	-2.25	-2.14	-1.26	-1.17	-1.61	-0.03	-1.15	-1.31	-1.20	-1.14	-1.15	-1.54	-1.75	-1.61	-1.68	-1.75	-1.77	-1.35	-1.66
33	-2.29	-1.97	-2.25	-2.30	-1.52	-1.26	-1.79	-2.17	-2.05	-2.43	-1.67	-1.19	-1.23	-1.86	-0.34	-1.13	-1.13	-0.96	-1.07	-1.13	-1.63	-1.76	-1.59	-1.75	-1.92	-1.90	-1.52	-1.92
43	-2.35	-2.07	-2.55	-2.33	-1.41	-1.51	-2.04	-2.18	-2.29	-2.38	-1.42	-1.21	-1.22	-2.09	-1.06	-1.24	-1.02	-0.91	-1.03	-1.09	-1.98	-1.74	-1.78	-1.86	-2.05	-1.98	-1.69	-2.07
53	-2.21	-2.12	-2.62	-2.03	-1.33	-1.66	-2.06	-2.02	-2.34	-1.91	-0.97	-1.11	-1.36	-2.15	-0.85	-0.83	-0.20	-0.79	-0.95	-1.12	-2.05	-1.55	-1.69	-1.87	-2.02	-1.85	-1.85	-2.11
63	-2.17	-2.18	-2.60	-1.72	-1.36	-1.97	-2.21	-2.00	-2.25	-1.28	-1.01	-1.10	-1.63	-2.21	-0.79	-0.20	0.25	-0.79	-0.87	-1.48	-2.13	-1.52	-1.76	-1.79	-1.94	-1.91	-2.02	-2.18
73	-2.35	-2.44	-2.39	-1.44	-1.85	-2.41	-2.39	-2.13	-1.93	-0.98	-1.07	-1.12	-2.28	-2.39	-0.89	0.31	0.34	-0.79	-0.90	-2.33	-2.24	-1.63	-1.83	-1.88	-2.06	-2.20	-2.20	-2.20
83	-2.36	-2.45	-2.01	-1.62	-2.95	-2.76	-2.46	-2.35	-1.60	-1.11	-1.21	-2.18	-2.97	-2.45	-0.60	0.34	0.25	-0.81	-1.09	-3.02	-2.36	-1.85	-1.96	-1.97	-2.28	-2.58	-2.43	-2.26
93	-2.29	-2.30	-3.00	-4.24	-3.72	-2.64	-2.26	-2.19	-0.90	-1.66	-3.35	-4.07	-2.95	-2.33	-0.73	0.31	0.07	-1.96	-3.18	-2.98	-2.19	-1.86	-1.86	-1.97	-2.33	-2.49	-2.24	-2.18

Table A-4. Database for cube building at TI3. Number in the left-hand column is the tapping index.

Elevation	0							15							30							-15						
Azimuth	0	15	30	45	60	75	90	0	15	30	45	60	75	90	0	15	30	45	60	75	90	0	15	30	45	60	75	90
11	-2.74	-2.43	-2.45	-2.02	-1.82	-1.61	-1.60	-3.13	-2.59	-1.98	-2.14	-1.89	-1.39	-1.59	-1.73	-2.18	-2.02	-2.09	-1.52	-1.46	-1.55	-1.85	-1.76	-2.07	-2.04	-1.88	-1.61	-1.45
21	-2.85	-2.24	-2.29	-2.13	-2.01	-1.76	-1.72	-3.02	-2.43	-2.04	-2.31	-1.98	-1.49	-1.71	-1.73	-1.90	-1.81	-1.89	-1.64	-1.46	-1.67	-1.83	-1.70	-2.02	-2.03	-1.95	-1.81	-1.58
31	-2.56	-2.08	-2.59	-2.61	-2.22	-2.01	-1.99	-2.62	-2.37	-2.10	-2.50	-2.11	-1.62	-1.84	-1.67	-1.70	-1.66	-1.81	-1.55	-1.50	-1.77	-1.86	-1.66	-1.91	-2.05	-2.19	-1.99	-1.67
41	-2.30	-2.13	-2.74	-2.90	-2.51	-2.17	-2.21	-2.39	-2.37	-2.29	-2.74	-2.24	-1.68	-1.96	-1.63	-1.67	-1.73	-1.81	-1.63	-1.59	-2.02	-1.74	-1.69	-2.09	-2.32	-2.43	-2.16	-1.89
51	-2.26	-2.45	-3.16	-3.32	-2.85	-2.49	-2.46	-2.46	-2.50	-2.56	-3.02	-2.43	-1.77	-2.20	-1.58	-1.63	-1.68	-1.94	-1.72	-1.65	-2.21	-1.63	-1.78	-2.28	-2.48	-2.89	-2.34	-2.04
61	-2.29	-2.52	-3.60	-3.82	-3.19	-2.63	-2.59	-2.39	-2.67	-2.85	-3.41	-2.76	-1.97	-2.38	-1.64	-1.69	-1.84	-1.96	-1.78	-1.75	-2.47	-1.64	-1.95	-2.43	-2.90	-3.20	-2.50	-2.23
71	-2.46	-2.84	-4.33	-4.96	-3.76	-3.00	-2.76	-2.58	-3.06	-3.43	-4.13	-3.16	-2.29	-2.66	-1.76	-1.82	-2.05	-2.29	-2.06	-1.99	-2.62	-1.73	-1.94	-2.70	-3.29	-3.74	-2.64	-2.39
81	-2.75	-3.36	-5.48	-6.17	-3.92	-3.14	-2.86	-2.89	-3.84	-4.26	-4.51	-2.92	-2.66	-2.85	-1.93	-2.16	-2.50	-2.38	-2.02	-2.54	-2.76	-1.91	-2.14	-3.05	-3.97	-4.16	-2.90	-2.59
91	-2.78	-3.48	-4.96	-3.87	-4.03	-3.58	-2.73	-3.06	-4.08	-2.52	-1.88	-2.64	-3.51	-2.75	-2.01	-2.17	-0.53	-0.56	-1.45	-3.44	-2.76	-1.86	-2.10	-2.93	-3.62	-3.71	-3.03	-2.45
12	-2.88	-2.23	-2.34	-2.05	-2.09	-1.78	-1.62	-2.86	-2.29	-2.24	-2.42	-2.13	-1.64	-1.58	-1.48	-2.12	-2.26	-2.19	-1.76	-1.61	-1.54	-1.97	-1.81	-2.02	-2.03	-1.84	-1.66	-1.51
22	-2.84	-2.36	-2.43	-2.30	-2.22	-1.91	-1.76	-3.04	-2.42	-2.24	-2.47	-2.29	-1.60	-1.64	-1.60	-1.79	-1.82	-1.97	-1.73	-1.42	-1.58	-1.94	-1.74	-2.02	-1.99	-2.03	-1.72	-1.46
32	-2.66	-2.31	-2.76	-2.94	-2.65	-1.99	-2.00	-2.82	-2.57	-2.52	-2.83	-2.42	-1.48	-1.90	-1.61	-1.72	-1.89	-1.93	-1.72	-1.30	-1.82	-1.93	-1.77	-2.09	-2.23	-2.44	-1.93	-1.68
42	-2.54	-2.35	-3.17	-3.38	-2.78	-2.00	-2.30	-2.61	-2.68	-2.68	-3.17	-2.39	-1.40	-2.09	-1.55	-1.70	-1.88	-1.99	-1.60	-1.20	-2.11	-1.85	-1.88	-2.23	-2.44	-2.70	-2.01	-1.89
52	-2.28	-2.38	-3.48	-3.61	-2.53	-1.84	-2.34	-2.46	-2.58	-2.84	-3.21	-1.99	-1.25	-2.21	-1.50	-1.70	-1.84	-1.76	-1.26	-1.13	-2.13	-1.69	-1.83	-2.32	-2.63	-2.90	-2.01	-1.99
62	-2.35	-2.60	-3.89	-3.77	-2.19	-1.99	-2.49	-2.56	-2.93	-3.20	-2.97	-1.67	-1.49	-2.50	-1.68	-1.77	-1.89	-1.55	-1.01	-1.20	-2.35	-1.70	-1.94	-2.46	-3.00	-3.09	-2.08	-2.17
72	-2.60	-3.05	-4.13	-3.13	-1.72	-2.48	-2.65	-2.80	-3.32	-2.72	-1.32	-1.38	-2.08	-2.71	-1.68	-1.79	-0.82	-0.35	-1.06	-1.94	-2.71	-1.83	-2.02	-2.76	-3.07	-2.76	-2.52	-2.41
82	-2.74	-3.24	-3.52	-2.00	-2.58	-3.24	-2.75	-2.89	-3.34	-1.35	-1.33	-1.56	-2.85	-2.65	-1.60	-1.00	0.44	-0.60	-0.96	-2.78	-2.63	-1.78	-1.95	-2.64	-2.80	-2.95	-2.94	-2.43
92	-2.71	-3.07	-3.14	-4.17	-5.53	-3.94	-2.79	-2.99	-2.71	-1.45	-2.28	-5.43	-3.88	-2.69	-1.65	0.51	0.34	-1.80	-3.68	-4.02	-2.70	-2.00	-2.12	-2.79	-3.88	-4.12	-3.19	-2.39
13	-2.56	-2.04	-2.31	-2.22	-1.92	-1.41	-1.49	-2.37	-2.18	-2.25	-2.45	-1.80	-1.32	-1.41	-0.79	-1.49	-1.81	-1.92	-1.43	-1.42	-1.49	-1.98	-1.76	-1.96	-1.92	-1.84	-1.40	-1.40
23	-2.54	-2.07	-2.55	-2.57	-1.98	-1.34	-1.58	-2.45	-2.19	-2.30	-2.48	-1.61	-1.10	-1.46	-0.83	-1.37	-1.62	-1.56	-1.10	-1.19	-1.52	-1.99	-1.68	-1.88	-1.94	-1.99	-1.42	-1.41
33	-2.52	-2.11	-2.80	-2.72	-1.71	-1.33	-1.87	-2.55	-2.23	-2.32	-2.33	-1.25	-1.16	-1.67	-0.82	-1.31	-1.32	-1.18	-0.99	-1.13	-1.73	-1.92	-1.69	-2.00	-2.27	-2.05	-1.50	-1.53
43	-2.49	-2.32	-3.09	-2.82	-1.45	-1.58	-2.14	-2.52	-2.57	-2.47	-1.95	-1.32	-1.18	-2.13	-1.06	-1.38	-1.26	-1.09	-1.06	-1.14	-2.11	-1.92	-1.87	-2.23	-2.44	-2.12	-1.81	-1.77
53	-2.28	-2.42	-3.16	-2.38	-1.27	-1.70	-2.30	-2.36	-2.55	-2.02	-1.15	-1.20	-1.29	-2.19	-0.90	-1.13	-0.75	-0.91	-0.93	-1.22	-2.21	-1.77	-1.87	-2.34	-2.32	-1.91	-1.96	-1.95
63	-2.36	-2.56	-3.15	-2.05	-1.38	-1.99	-2.43	-2.26	-2.59	-1.71	-1.06	-1.24	-1.55	-2.40	-0.88	-0.77	0.14	-0.74	-0.87	-1.49	-2.26	-1.74	-1.89	-2.31	-2.30	-1.93	-2.14	-2.12
73	-2.54	-2.73	-2.58	-1.52	-1.99	-2.73	-2.58	-2.44	-2.37	-1.06	-1.17	-1.27	-2.36	-2.60	-0.91	0.19	0.42	-0.86	-0.97	-2.35	-2.64	-1.92	-2.07	-2.38	-2.13	-2.38	-2.65	-2.22
83	-2.72	-2.69	-2.09	-1.86	-3.47	-3.47	-2.77	-2.49	-1.91	-1.16	-1.28	-2.72	-3.17	-2.73	-0.63	0.46	0.27	-0.63	-1.68	-3.25	-2.65	-2.07	-2.21	-2.46	-2.78	-3.25	-3.00	-2.43
93	-2.62	-2.63	-3.92	-5.45	-4.58	-3.29	-2.58	-2.32	-1.33	-2.44	-4.05	-4.79	-3.11	-2.55	-0.96	0.50	-1.31	-2.81	-3.71	-3.30	-2.51	-2.06	-2.12	-2.76	-3.69	-3.53	-2.87	-2.26

Table A-5. Database for cube building at TI4. Number in the left-hand column is the tapping index.

Elevation	0							15							30							-15						
Azimuth	0	15	30	45	60	75	90	0	15	30	45	60	75	90	0	15	30	45	60	75	90	0	15	30	45	60	75	90
11	-3.58	-2.81	-2.46	-2.16	-1.85	-1.56	-1.62	-3.68	-3.05	-2.79	-2.20	-1.70	-1.55	-1.75	-2.35	-2.79	-2.66	-2.18	-1.85	-1.59	-1.45	-2.02	-1.89	-2.29	-2.08	-1.84	-1.61	-1.59
21	-3.50	-2.69	-2.48	-2.45	-2.10	-1.68	-1.76	-3.36	-3.09	-2.85	-2.08	-1.75	-1.65	-1.95	-2.19	-2.40	-2.30	-2.14	-1.88	-1.53	-1.60	-2.15	-1.82	-2.22	-2.07	-2.04	-1.82	-1.79
31	-3.04	-2.36	-2.67	-2.67	-2.25	-1.91	-1.95	-2.88	-2.96	-2.77	-2.25	-1.93	-1.75	-2.24	-1.99	-2.37	-2.18	-2.09	-1.82	-1.56	-1.83	-1.91	-1.77	-2.23	-2.31	-2.39	-2.07	-2.05
41	-2.63	-2.31	-2.79	-3.01	-2.57	-2.05	-2.12	-2.65	-2.76	-2.95	-2.39	-2.05	-1.93	-2.27	-0.95	-2.13	-2.02	-2.05	-1.90	-1.62	-2.00	-1.76	-1.83	-2.36	-2.61	-2.69	-2.21	-2.14
51	-2.55	-2.55	-3.16	-3.58	-3.02	-2.31	-2.38	-2.77	-2.64	-3.24	-2.70	-2.34	-2.07	-2.53	-1.24	-2.10	-2.02	-2.13	-1.98	-1.62	-2.16	-1.68	-2.00	-2.66	-2.99	-3.13	-2.49	-2.39
61	-2.53	-2.82	-3.65	-4.07	-3.44	-2.58	-2.62	-2.66	-2.89	-3.72	-3.03	-2.51	-2.27	-2.88	-1.17	-2.02	-2.11	-2.33	-2.23	-1.83	-2.40	-1.70	-2.14	-2.76	-3.31	-3.66	-2.81	-2.55
71	-2.75	-3.22	-4.40	-5.29	-4.25	-2.89	-2.86	-2.86	-3.32	-4.54	-3.72	-2.98	-2.55	-3.30	-1.60	-2.21	-2.38	-2.70	-2.52	-2.18	-2.79	-1.84	-2.33	-3.11	-3.90	-4.40	-3.07	-2.95
81	-3.14	-3.78	-5.76	-7.05	-4.56	-3.46	-3.20	-3.24	-4.15	-5.90	-4.36	-3.10	-3.09	-3.53	-2.06	-2.60	-2.90	-2.79	-2.23	-3.16	-3.09	-1.91	-2.45	-3.86	-5.09	-5.03	-3.29	-3.25
91	-3.19	-3.88	-5.23	-4.56	-4.34	-4.33	-3.34	-3.58	-4.42	-4.28	-1.90	-2.92	-4.18	-3.59	-2.27	-2.58	0.19	0.12	-3.01	-4.58	-3.26	-1.88	-2.41	-3.90	-4.39	-4.45	-3.91	-3.38
12	-3.41	-2.47	-2.38	-2.28	-2.10	-1.67	-1.56	-3.18	-2.77	-2.91	-2.26	-1.88	-1.75	-1.73	-1.62	-2.26	-2.58	-2.36	-1.95	-1.69	-1.55	-2.24	-2.08	-2.41	-2.13	-1.93	-1.71	-1.68
22	-3.47	-2.76	-2.53	-2.56	-2.22	-1.76	-1.67	-3.21	-2.76	-2.79	-2.30	-1.97	-1.74	-1.93	-1.90	-2.20	-2.30	-2.24	-1.89	-1.52	-1.62	-2.14	-1.90	-2.26	-2.19	-2.18	-1.90	-1.74
32	-3.23	-2.49	-2.81	-3.13	-2.72	-1.85	-1.99	-2.94	-2.75	-3.12	-2.58	-2.33	-1.78	-2.26	-1.87	-2.01	-2.13	-2.15	-1.93	-1.37	-1.84	-1.96	-1.89	-2.30	-2.53	-2.64	-2.07	-1.97
42	-2.94	-2.53	-3.15	-3.57	-2.89	-1.89	-2.14	-2.81	-2.71	-3.49	-2.80	-2.42	-1.80	-2.34	-1.84	-2.01	-2.17	-2.15	-1.71	-1.33	-2.01	-1.93	-2.08	-2.54	-2.87	-3.08	-2.23	-2.18
52	-2.69	-2.56	-3.51	-3.92	-2.84	-1.87	-2.27	-2.63	-2.68	-3.68	-2.87	-2.12	-1.53	-2.52	-1.60	-1.87	-2.00	-2.03	-1.47	-1.25	-2.14	-1.77	-2.09	-2.66	-3.07	-3.08	-2.16	-2.32
62	-2.70	-2.92	-3.98	-4.30	-2.74	-2.18	-2.69	-2.73	-3.12	-3.98	-2.92	-1.95	-1.69	-2.94	-1.14	-2.01	-2.06	-2.05	-1.28	-1.56	-2.38	-1.72	-2.21	-2.91	-3.38	-3.20	-2.25	-2.55
72	-2.95	-3.28	-4.03	-3.79	-1.81	-2.66	-3.09	-2.98	-3.50	-3.91	-1.77	-1.28	-2.26	-3.34	-1.74	-2.13	0.01	0.08	-1.18	-2.48	-2.77	-1.87	-2.48	-3.29	-3.52	-2.88	-2.62	-3.01
82	-3.05	-3.64	-3.47	-2.61	-2.74	-3.48	-3.23	-3.08	-3.37	-2.20	-1.37	-1.71	-3.48	-3.53	-1.69	-0.81	0.82	0.55	-1.34	-3.69	-3.06	-1.89	-2.38	-3.10	-3.05	-3.05	-3.30	-3.23
92	-3.27	-3.44	-3.52	-4.61	-6.09	-4.67	-3.40	-3.19	-2.82	-1.77	-3.62	-5.12	-5.05	-3.49	-1.76	0.11	1.10	-2.80	-5.77	-5.08	-3.33	-2.08	-2.54	-3.51	-4.88	-4.92	-4.03	-3.41
13	-2.94	-2.32	-2.30	-2.40	-1.89	-1.35	-1.46	-2.49	-2.31	-2.72	-2.18	-1.75	-1.46	-1.76	0.33	-1.78	-1.99	-1.97	-1.71	-1.44	-1.48	-2.25	-2.04	-2.24	-2.10	-2.04	-1.49	-1.54
23	-3.00	-2.35	-2.42	-2.66	-2.06	-1.25	-1.55	-2.54	-2.36	-2.81	-2.21	-1.61	-1.25	-1.73	0.38	-1.48	-1.73	-1.72	-1.34	-1.16	-1.47	-2.10	-1.98	-2.03	-2.24	-2.11	-1.48	-1.56
33	-3.02	-2.26	-2.80	-2.93	-1.86	-1.29	-1.73	-2.49	-2.31	-2.88	-2.08	-1.40	-1.18	-2.04	-0.54	-1.46	-1.57	-1.52	-1.08	-1.10	-1.65	-2.02	-1.85	-2.28	-2.49	-2.13	-1.52	-1.78
43	-3.06	-2.42	-3.10	-3.08	-1.91	-1.64	-2.12	-2.56	-2.65	-3.09	-1.97	-1.34	-1.34	-2.28	-0.72	-1.32	-1.54	-1.38	-1.14	-1.23	-1.93	-1.99	-2.05	-2.46	-2.76	-2.23	-1.79	-2.23
53	-2.79	-2.71	-3.10	-2.89	-1.44	-1.93	-2.40	-2.41	-2.68	-2.81	-1.43	-1.14	-1.50	-2.61	-0.65	-0.70	-0.08	-0.85	-0.93	-1.46	-2.10	-1.88	-2.06	-2.61	-2.73	-1.88	-2.00	-2.33
63	-2.65	-2.81	-2.95	-2.48	-1.40	-2.16	-2.57	-2.49	-2.63	-2.37	-1.15	-1.02	-1.69	-2.78	-0.47	-0.35	0.49	0.23	-0.95	-1.83	-2.33	-1.77	-2.14	-2.67	-2.56	-1.93	-2.14	-2.52
73	-3.00	-3.04	-2.67	-1.85	-2.13	-2.98	-3.04	-2.49	-2.53	-1.45	-1.14	-1.19	-2.74	-3.24	-0.80	0.42	0.97	-0.02	-0.98	-2.94	-2.77	-1.88	-2.32	-2.76	-2.26	-2.49	-2.96	-2.96
83	-2.99	-3.04	-2.12	-2.31	-3.86	-3.73	-3.21	-2.53	-2.17	-1.32	-1.38	-2.86	-3.79	-3.42	-0.54	0.78	0.84	-0.26	-3.14	-4.06	-3.09	-2.11	-2.51	-2.75	-2.88	-3.61	-3.50	-3.27
93	-3.10	-2.68	-4.55	-5.91	-5.20	-3.60	-2.96	-2.48	-1.64	-2.82	-4.09	-4.43	-3.82	-3.18	-1.04	0.67	0.15	-3.17	-4.87	-3.88	-2.91	-2.17	-2.34	-3.47	-4.63	-3.95	-3.31	-3.04

Table A-6. Database for cube building at TI5. Number in the left-hand column is the tapping index.

Elevation	0							15							30							-15						
Azimuth	0	15	30	45	60	75	90	0	15	30	45	60	75	90	0	15	30	45	60	75	90	0	15	30	45	60	75	90
11	-3.85	-3.40	-2.90	-2.53	-1.97	-1.62	-1.57	-4.25	-3.60	-3.23	-2.54	-2.14	-1.71	-1.60	-2.80	-3.03	-3.13	-2.69	-1.78	-1.63	-1.36	-2.14	-2.03	-2.50	-2.48	-1.80	-1.57	-1.88
21	-3.76	-3.34	-2.83	-2.46	-2.23	-1.87	-1.67	-3.79	-3.50	-3.25	-2.71	-2.29	-1.73	-1.79	-2.56	-2.61	-2.79	-2.51	-1.89	-1.79	-1.65	-2.17	-2.07	-2.40	-2.38	-1.97	-1.74	-2.20
31	-3.17	-2.98	-2.79	-2.78	-2.63	-2.09	-1.97	-3.16	-3.17	-3.15	-2.92	-2.54	-1.94	-2.25	-1.52	-2.26	-2.59	-2.39	-2.02	-1.85	-1.95	-2.05	-1.90	-2.29	-2.56	-2.26	-1.99	-2.54
41	-2.92	-2.95	-3.05	-3.09	-2.84	-2.14	-2.15	-2.95	-3.00	-3.19	-2.90	-2.67	-2.15	-2.46	-1.04	-2.18	-2.49	-2.41	-2.12	-1.88	-2.05	-1.99	-2.00	-2.46	-2.93	-2.61	-2.18	-2.78
51	-2.84	-3.23	-3.34	-3.49	-3.22	-2.43	-2.33	-2.97	-3.17	-3.42	-3.37	-3.09	-2.34	-2.57	-1.56	-2.27	-2.59	-2.60	-2.39	-2.07	-2.31	-1.74	-2.21	-2.65	-3.52	-2.90	-2.43	-2.90
61	-2.87	-3.41	-3.76	-4.04	-3.73	-2.59	-2.62	-2.83	-3.38	-3.76	-3.78	-3.51	-2.52	-2.91	-1.97	-2.36	-2.71	-2.73	-2.62	-2.31	-2.47	-1.68	-2.33	-2.95	-3.88	-3.45	-2.66	-3.03
71	-3.17	-3.94	-4.73	-5.26	-4.86	-3.00	-2.92	-3.11	-4.07	-4.65	-4.75	-4.42	-3.04	-3.59	-2.50	-2.67	-3.18	-3.22	-3.23	-2.70	-2.64	-1.88	-2.42	-3.43	-4.98	-4.18	-3.06	-3.57
81	-3.70	-4.86	-6.12	-6.37	-5.73	-3.75	-3.47	-3.46	-5.01	-6.04	-5.96	-4.70	-3.66	-3.98	-2.70	-3.17	-3.79	-3.69	-3.48	-3.07	-3.10	-2.17	-2.60	-4.09	-6.47	-4.92	-3.27	-3.99
91	-3.96	-5.35	-6.00	-4.15	-4.37	-5.08	-3.78	-3.90	-5.13	-5.04	-3.23	-3.98	-5.51	-4.35	-3.08	-3.37	-2.88	-0.52	-2.52	-4.91	-3.41	-2.15	-2.55	-4.39	-5.50	-4.43	-3.98	-4.21
12	-3.85	-2.85	-2.52	-2.64	-2.12	-1.72	-1.50	-3.23	-3.16	-2.78	-2.59	-2.18	-1.83	-1.59	-2.21	-2.67	-2.90	-2.52	-1.91	-1.73	-1.41	-2.57	-2.09	-2.45	-2.28	-1.88	-1.69	-1.88
22	-3.78	-3.29	-2.76	-2.63	-2.35	-1.82	-1.61	-3.53	-3.33	-3.09	-2.66	-2.48	-1.82	-1.77	-2.37	-2.45	-2.50	-2.34	-1.87	-1.73	-1.58	-2.25	-2.05	-2.41	-2.39	-2.06	-1.77	-1.98
32	-3.39	-3.05	-2.97	-3.03	-2.90	-1.98	-1.77	-3.09	-2.93	-2.97	-2.88	-2.72	-1.83	-1.96	-2.28	-2.27	-2.35	-2.49	-2.09	-1.77	-1.75	-2.21	-2.00	-2.30	-2.74	-2.56	-1.96	-2.26
42	-2.96	-3.24	-3.30	-3.48	-3.19	-2.22	-2.01	-2.86	-3.12	-3.33	-3.28	-2.97	-1.92	-2.38	-2.27	-2.28	-2.51	-2.53	-2.29	-1.68	-2.12	-2.00	-2.18	-2.57	-3.27	-2.81	-2.14	-2.61
52	-2.93	-3.27	-3.50	-3.59	-3.32	-1.99	-2.14	-2.74	-3.22	-3.54	-3.60	-2.87	-1.79	-2.52	-1.77	-2.25	-2.47	-2.45	-2.20	-1.64	-2.12	-1.84	-2.07	-2.76	-3.63	-3.00	-2.19	-2.77
62	-3.02	-3.68	-4.05	-3.77	-3.46	-2.28	-2.60	-2.80	-3.56	-4.09	-3.83	-2.74	-1.93	-2.96	-2.10	-2.37	-2.60	-2.45	-2.15	-1.64	-2.41	-1.84	-2.28	-3.08	-4.00	-3.11	-2.41	-3.10
72	-3.41	-4.15	-4.53	-3.12	-2.52	-2.96	-3.04	-3.15	-4.11	-4.06	-2.97	-1.84	-2.76	-3.70	-2.30	-2.61	-1.52	-1.07	-1.40	-2.38	-2.76	-2.10	-2.45	-3.48	-3.76	-2.65	-2.56	-3.66
82	-3.59	-4.35	-4.20	-2.41	-2.31	-4.07	-3.55	-3.36	-3.68	-3.15	-1.70	-2.15	-4.04	-3.90	-2.35	-2.25	0.33	0.66	-1.50	-3.62	-2.99	-2.16	-2.51	-3.48	-3.44	-2.89	-3.16	-3.93
92	-3.70	-4.04	-3.71	-6.59	-6.11	-5.23	-3.82	-3.35	-3.25	-2.21	-3.73	-6.46	-6.24	-4.56	-2.32	-2.06	1.05	-3.64	-4.37	-5.34	-3.37	-2.35	-2.61	-4.06	-5.83	-5.36	-4.26	-4.12
13	-3.33	-2.63	-2.41	-2.40	-1.97	-1.46	-1.56	-2.28	-2.69	-2.50	-2.35	-1.93	-1.49	-1.54	-1.16	-2.31	-2.28	-2.25	-1.68	-1.45	-1.31	-2.50	-2.15	-2.24	-2.21	-1.83	-1.47	-1.71
23	-3.24	-2.67	-2.55	-2.41	-2.14	-1.43	-1.55	-2.54	-2.56	-2.53	-2.42	-2.02	-1.30	-1.55	-1.41	-1.97	-1.98	-1.96	-1.68	-1.22	-1.35	-2.31	-2.01	-2.09	-2.33	-2.00	-1.47	-1.80
33	-3.28	-2.86	-2.93	-2.56	-2.30	-1.54	-1.76	-2.96	-2.78	-2.88	-2.60	-1.99	-1.25	-1.87	-0.98	-1.90	-1.93	-1.84	-1.52	-1.22	-1.65	-2.23	-2.04	-2.37	-2.62	-2.12	-1.59	-2.21
43	-3.11	-2.97	-3.23	-2.58	-2.28	-1.75	-2.07	-2.60	-2.95	-2.98	-2.56	-1.82	-1.43	-2.31	-1.23	-1.99	-1.95	-1.65	-1.49	-1.22	-1.88	-2.10	-2.20	-2.68	-2.85	-2.25	-1.73	-2.52
53	-2.83	-3.18	-3.31	-2.29	-1.83	-2.04	-2.23	-2.43	-3.00	-3.06	-2.26	-1.38	-1.72	-2.71	-1.09	-1.98	-0.46	-0.54	-1.13	-1.37	-2.11	-1.86	-2.12	-2.71	-2.76	-1.92	-1.87	-2.72
63	-2.85	-3.47	-3.53	-2.01	-1.58	-2.42	-2.50	-2.48	-2.95	-2.74	-1.83	-1.30	-2.06	-3.05	-1.72	-1.68	0.59	0.08	-1.02	-1.75	-2.32	-1.82	-2.16	-2.87	-2.69	-1.80	-2.12	-3.08
73	-3.24	-3.59	-3.12	-1.80	-1.78	-3.29	-3.07	-2.71	-2.92	-2.21	-1.35	-1.62	-3.23	-3.41	-1.72	-1.42	1.26	0.32	-1.18	-2.75	-2.62	-2.17	-2.29	-2.86	-2.48	-2.35	-2.65	-3.57
83	-3.42	-3.34	-2.54	-2.94	-3.46	-4.28	-3.32	-2.82	-2.48	-1.61	-1.71	-3.58	-4.70	-3.80	-1.89	-0.51	1.18	-0.39	-2.53	-4.16	-3.07	-2.48	-2.61	-2.88	-3.49	-3.70	-3.56	-3.78
93	-3.28	-3.09	-4.45	-6.31	-5.15	-4.08	-3.36	-2.71	-1.89	-2.94	-4.69	-6.03	-4.93	-3.78	-1.76	0.14	-1.83	-4.43	-4.11	-4.28	-2.97	-2.46	-2.56	-3.92	-5.31	-4.44	-3.50	-3.65

Table A-7. Database for portal building at TI0. Number in the left-hand column is the tapping index.

Elevation	0							15							30							-15						
Azimuth	0	15	30	45	60	75	90	0	15	30	45	60	75	90	0	15	30	45	60	75	90	0	15	30	45	60	75	90
11	-0.68	-1.25	-1.35	-1.22	-0.55	-0.57	-0.65	-2.49	-2.36	-1.40	-0.64	-0.56	-0.52	-0.63	-0.80	-0.68	-0.59	-0.62	-0.58	-0.44	-0.60	-0.62	-0.71	-0.76	-1.29	-0.93	-1.03	-0.71
21	-0.63	-0.92	-0.96	-0.93	-0.76	-0.77	-0.88	-1.86	-1.56	-1.01	-0.69	-0.70	-0.56	-0.87	-0.57	-0.51	-0.48	-0.51	-0.48	-0.36	-0.82	-0.57	-0.60	-0.62	-0.94	-0.71	-0.89	-0.95
31	-0.61	-0.79	-0.79	-0.73	-0.96	-0.90	-1.02	-1.46	-1.22	-0.89	-0.80	-0.80	-0.63	-1.02	-0.58	-0.50	-0.52	-0.50	-0.49	-0.40	-1.00	-0.59	-0.60	-0.61	-0.74	-0.79	-0.96	-1.04
41	-0.62	-0.75	-0.73	-0.69	-1.15	-0.98	-1.14	-1.30	-1.16	-0.98	-0.95	-0.84	-0.67	-1.10	-0.57	-0.51	-0.49	-0.49	-0.45	-0.39	-1.11	-0.57	-0.60	-0.58	-0.68	-0.96	-1.01	-1.15
51	-0.65	-0.73	-0.70	-0.73	-1.33	-1.04	-1.15	-1.32	-1.20	-1.10	-1.11	-0.95	-0.75	-1.10	-0.57	-0.49	-0.51	-0.49	-0.49	-0.41	-1.15	-0.59	-0.61	-0.60	-0.68	-1.11	-1.03	-1.10
61	-0.60	-0.66	-0.67	-0.83	-1.47	-1.06	-1.02	-1.30	-1.31	-1.17	-1.23	-0.98	-0.71	-1.00	-0.54	-0.48	-0.44	-0.45	-0.44	-0.35	-1.01	-0.55	-0.59	-0.58	-0.63	-1.25	-0.97	-1.05
71	-0.61	-0.70	-0.69	-1.10	-1.57	-1.03	-0.90	-1.44	-1.40	-1.40	-1.35	-1.05	-0.82	-0.90	-0.57	-0.44	-0.44	-0.47	-0.47	-0.40	-0.95	-0.59	-0.62	-0.62	-0.65	-1.34	-0.84	-0.89
81	-0.62	-0.73	-0.69	-1.55	-1.78	-0.87	-0.87	-1.81	-1.73	-1.83	-1.71	-1.24	-0.98	-0.86	-0.58	-0.45	-0.45	-0.42	-0.30	-0.96	-0.87	-0.58	-0.63	-0.60	-0.64	-1.27	-0.79	-0.84
91	-0.72	-0.83	-0.70	-1.38	-0.80	-0.85	-0.88	-2.11	-2.24	-0.38	-0.39	-1.31	-0.91	-0.90	-0.72	-0.49	0.61	0.33	-0.31	-1.09	-0.86	-0.62	-0.68	-0.59	-0.65	-0.85	-0.78	-0.84
12	-0.71	-1.11	-1.22	-1.18	-0.61	-0.64	-0.59	-0.91	-1.15	-1.16	-0.66	-0.60	-0.56	-0.63	-0.28	-0.44	-0.51	-0.57	-0.58	-0.43	-0.59	-0.66	-0.75	-0.79	-1.18	-0.90	-0.69	-0.66
22	-0.65	-0.94	-0.95	-0.90	-0.78	-0.73	-0.68	-1.84	-1.48	-1.01	-0.68	-0.75	-0.47	-0.72	-0.24	-0.45	-0.52	-0.49	-0.45	-0.29	-0.65	-0.58	-0.61	-0.64	-0.94	-0.73	-0.78	-0.76
32	-0.66	-0.80	-0.83	-0.76	-1.14	-0.77	-0.93	-1.46	-1.22	-0.94	-0.86	-0.98	-0.48	-0.88	-0.51	-0.51	-0.54	-0.54	-0.46	-0.34	-0.83	-0.60	-0.61	-0.62	-0.82	-0.85	-0.90	-0.95
42	-0.65	-0.75	-0.75	-0.71	-1.51	-0.78	-1.04	-1.34	-1.21	-0.99	-1.08	-1.12	-0.41	-1.00	-0.57	-0.52	-0.53	-0.49	-0.38	-0.30	-1.00	-0.59	-0.61	-0.60	-0.70	-1.05	-0.96	-1.09
52	-0.62	-0.71	-0.69	-0.71	-1.75	-0.78	-1.06	-1.30	-1.19	-1.05	-1.41	-1.13	-0.40	-1.05	-0.54	-0.50	-0.50	-0.43	-0.23	-0.28	-1.04	-1.46	-1.46	-1.46	-1.55	-1.52	-1.50	-1.50
62	-0.63	-0.72	-0.68	-0.88	-1.52	-0.84	-1.01	-1.36	-1.30	-1.32	-1.80	-0.77	-0.54	-0.99	-0.56	-0.48	-0.43	-0.32	-0.21	-0.29	-1.00	-1.79	-1.80	-1.80	-1.83	-1.85	-1.84	-1.84
72	-0.61	-0.69	-0.69	-1.25	-0.68	-0.87	-0.89	-1.45	-1.49	-1.99	-0.60	-0.30	-0.80	-0.87	-0.48	-0.15	0.37	0.27	-0.12	-0.55	-0.89	-1.50	-1.51	-1.51	-1.53	-1.57	-1.55	-1.56
82	-0.63	-0.72	-0.70	-1.22	-0.72	-0.88	-0.85	-1.79	-1.94	0.51	-0.28	-0.46	-1.02	-0.85	-0.37	0.51	0.48	0.20	-0.18	-1.10	-0.87	-1.44	-1.44	-1.44	-1.46	-1.49	-1.48	-1.48
92	-0.67	-0.83	-0.70	-1.47	-0.82	-0.83	-0.82	-1.00	-0.54	-0.19	-0.27	-2.00	-1.00	-0.83	0.23	0.36	0.53	0.55	-1.99	-1.16	-0.84	-1.49	-1.49	-1.49	-1.50	-1.53	-1.53	-1.52
13	-0.79	-1.12	-1.19	-1.21	-0.68	-0.56	-0.59	-0.74	-0.83	-1.03	-0.63	-0.72	-0.48	-0.59	-0.36	-0.31	-0.46	-0.50	-0.51	-0.43	-0.55	-1.51	-1.51	-1.51	-1.53	-1.56	-1.56	-1.56
23	-0.68	-0.95	-0.99	-0.90	-0.93	-0.46	-0.66	-1.36	-1.33	-0.98	-0.69	-0.72	-0.34	-0.68	0.25	0.15	-0.28	-0.24	-0.28	-0.30	-0.62	-1.54	-1.55	-1.54	-1.89	-1.54	-1.53	-1.54
33	-0.64	-0.80	-0.83	-0.75	-1.15	-0.49	-0.85	-1.51	-1.22	-0.90	-1.05	-0.72	-0.39	-0.82	0.27	0.22	-0.22	-0.26	-0.29	-0.32	-0.80	-1.48	-1.48	-1.50	-1.47	-1.50	-1.48	-1.49
43	-0.62	-0.77	-0.70	-0.68	-0.72	-0.57	-0.97	-1.36	-1.20	-0.94	-1.15	-0.30	-0.33	-0.97	0.28	0.25	0.20	-0.03	-0.22	-0.25	-0.94	-0.56	-0.58	-0.57	-0.67	-1.18	-0.82	-0.99
53	-0.61	-0.73	-0.72	-0.74	-0.43	-0.71	-1.04	-1.37	-1.24	-1.18	-0.88	-0.31	-0.42	-1.01	0.14	0.27	0.14	0.07	-0.27	-0.31	-1.03	-0.60	-0.63	-0.62	-0.65	-1.26	-0.89	-1.00
63	-0.60	-0.70	-0.68	-0.92	-0.45	-0.79	-1.00	-1.34	-1.29	-1.34	0.10	-0.33	-0.57	-0.97	0.21	0.30	0.29	0.12	-0.21	-0.29	-0.97	-0.55	-0.59	-0.57	-0.62	-1.12	-0.83	-0.93
73	-0.62	-0.72	-0.71	-0.95	-0.62	-0.91	-0.91	-1.47	-1.52	-0.44	-0.33	-0.39	-0.90	-0.93	0.18	0.32	0.20	0.13	-0.23	-0.75	-0.93	-0.59	-0.62	-0.60	-0.65	-1.01	-0.81	-0.84
83	-0.63	-0.73	-0.74	-0.63	-0.86	-0.91	-0.85	-1.44	-0.96	-0.29	-0.37	-0.45	-1.07	-0.86	0.24	0.34	0.33	0.21	-0.21	-1.12	-0.87	-0.56	-0.60	-0.58	-0.67	-0.90	-0.76	-0.81
93	-0.70	-0.87	-0.75	-2.24	-0.80	-0.84	-0.81	-0.70	-0.32	-0.19	-1.47	-1.44	-1.04	-0.82	-0.21	0.28	0.48	-0.44	-1.45	-1.04	-0.81	-0.59	-0.72	-0.65	-0.69	-0.82	-0.75	-0.77

Table A-8. Database for portal building at TI1. Number in the left-hand column is the tapping index.

Elevation	0							15							30							-15						
Azimuth	0	15	30	45	60	75	90	0	15	30	45	60	75	90	0	15	30	45	60	75	90	0	15	30	45	60	75	90
11	-1.12	-1.67	-1.91	-1.87	-1.02	-0.95	-0.94	-2.92	-2.60	-2.06	-1.23	-0.99	-0.90	-0.89	-1.41	-1.23	-1.05	-1.07	-0.99	-0.84	-0.80	-1.03	-1.10	-1.31	-1.79	-1.43	-1.27	-0.88
21	-1.19	-1.46	-1.59	-1.41	-1.16	-1.13	-0.95	-2.35	-2.13	-1.48	-1.29	-1.19	-1.03	-0.91	-1.18	-1.18	-1.01	-1.03	-0.99	-0.87	-0.97	-1.08	-1.03	-1.10	-1.65	-1.20	-1.35	-1.01
31	-1.10	-1.32	-1.30	-1.22	-1.42	-1.28	-1.10	-2.00	-1.73	-1.45	-1.32	-1.25	-1.01	-1.07	-1.14	-1.08	-1.01	-0.94	-0.98	-0.80	-0.97	-1.01	-1.01	-1.01	-1.26	-1.24	-1.49	-1.09
41	-1.07	-1.20	-1.28	-1.29	-1.67	-1.31	-1.33	-1.88	-1.76	-1.55	-1.50	-1.30	-1.02	-1.32	-1.12	-1.09	-1.03	-0.96	-1.00	-0.86	-1.26	-1.08	-0.99	-1.08	-1.24	-1.51	-1.56	-1.42
51	-1.16	-1.24	-1.33	-1.40	-1.85	-1.43	-1.61	-1.89	-1.79	-1.66	-1.63	-1.39	-1.10	-1.45	-1.12	-1.08	-1.09	-0.97	-0.94	-0.82	-1.38	-1.12	-1.14	-1.11	-1.24	-1.69	-1.70	-1.50
61	-1.15	-1.15	-1.30	-1.55	-1.92	-1.52	-1.47	-1.81	-1.77	-1.66	-1.64	-1.42	-1.14	-1.53	-1.08	-0.99	-0.91	-0.97	-0.93	-0.83	-1.49	-1.04	-1.02	-1.07	-1.25	-1.83	-1.68	-1.53
71	-1.09	-1.25	-1.43	-1.85	-2.18	-1.71	-1.57	-1.97	-1.92	-1.89	-1.83	-1.47	-1.19	-1.53	-1.09	-0.98	-1.01	-0.90	-0.91	-0.77	-1.53	-1.00	-1.05	-1.16	-1.35	-2.12	-1.71	-1.54
81	-1.16	-1.31	-1.65	-2.62	-2.80	-1.76	-1.38	-2.38	-2.12	-2.33	-2.11	-1.70	-1.60	-1.43	-1.15	-0.99	-0.98	-0.89	-0.86	-1.16	-1.44	-1.02	-1.03	-1.12	-1.39	-2.17	-1.60	-1.39
91	-1.25	-1.49	-1.64	-1.54	-2.53	-1.70	-1.40	-2.66	-2.81	-0.85	-0.77	-1.18	-1.87	-1.38	-1.40	-1.00	0.57	0.47	-0.10	-1.98	-1.39	-1.18	-1.22	-1.21	-1.36	-1.39	-1.52	-1.38
12	-1.29	-1.66	-1.77	-1.79	-1.10	-1.08	-0.91	-1.75	-1.67	-1.75	-1.23	-1.16	-1.06	-0.91	-0.91	-1.00	-1.08	-1.07	-1.13	-0.92	-0.85	-1.22	-1.18	-1.34	-1.84	-1.35	-1.10	-0.93
22	-1.13	-1.47	-1.63	-1.51	-1.23	-1.17	-0.84	-2.47	-2.07	-1.54	-1.20	-1.20	-0.94	-0.80	-0.95	-1.01	-1.05	-0.98	-0.93	-0.70	-0.79	-1.10	-1.08	-1.12	-1.57	-1.20	-1.24	-0.96
32	-1.13	-1.34	-1.38	-1.33	-1.53	-1.22	-1.03	-2.09	-1.78	-1.50	-1.33	-1.34	-0.94	-1.00	-1.07	-1.05	-1.06	-1.01	-0.94	-0.73	-1.00	-1.11	-1.06	-1.07	-1.32	-1.31	-1.51	-1.06
42	-1.15	-1.27	-1.37	-1.36	-1.82	-1.26	-1.28	-1.95	-1.87	-1.61	-1.59	-1.41	-0.90	-1.15	-1.15	-1.16	-1.11	-1.00	-0.90	-0.80	-1.22	-1.08	-1.10	-1.13	-1.28	-1.58	-1.50	-1.33
52	-1.07	-1.14	-1.23	-1.33	-1.95	-1.11	-1.30	-1.84	-1.65	-1.51	-1.61	-1.41	-0.74	-1.26	-1.06	-1.02	-0.99	-0.85	-0.70	-0.58	-1.26	-1.03	-0.97	-1.00	-1.19	-1.74	-1.43	-1.37
62	-1.11	-1.27	-1.39	-1.60	-2.26	-1.16	-1.51	-1.91	-1.79	-1.82	-2.02	-1.48	-0.75	-1.48	-1.10	-0.98	-1.01	-0.89	-0.63	-0.67	-1.51	-1.06	-1.09	-1.12	-1.28	-2.23	-1.50	-1.60
72	-1.01	-1.26	-1.41	-2.11	-1.06	-1.20	-1.49	-1.98	-1.97	-2.41	-1.64	-0.67	-0.78	-1.45	-1.00	-0.91	0.19	0.34	-0.23	-0.60	-1.43	-1.02	-1.04	-1.09	-1.31	-2.16	-1.44	-1.45
82	-1.07	-1.26	-1.67	-1.64	-1.05	-1.56	-1.39	-2.24	-2.30	0.04	-0.49	-0.81	-1.49	-1.38	-0.85	0.60	0.55	0.36	-0.58	-1.38	-1.35	-1.02	-1.05	-1.13	-1.34	-1.69	-1.49	-1.39
92	-1.11	-1.35	-1.46	-1.73	-2.22	-1.79	-1.34	-1.72	-1.22	-0.52	-0.94	-3.14	-1.90	-1.32	-0.70	0.49	0.60	0.51	-2.40	-1.98	-1.43	-1.01	-1.15	-1.13	-1.49	-1.37	-1.48	-1.32
13	-1.33	-1.65	-1.75	-1.82	-1.12	-1.00	-0.87	-1.28	-1.37	-1.50	-1.14	-1.18	-0.97	-0.91	-0.90	-0.86	-0.97	-1.00	-1.03	-0.87	-0.91	-1.27	-1.21	-1.27	-1.72	-1.31	-1.07	-0.90
23	-1.11	-1.52	-1.67	-1.55	-1.28	-0.84	-0.84	-1.83	-1.73	-1.47	-1.22	-1.19	-0.72	-0.78	0.24	-0.05	-0.75	-0.72	-0.74	-0.71	-0.83	-1.08	-1.05	-1.07	-1.62	-1.11	-1.13	-0.90
33	-1.14	-1.27	-1.38	-1.27	-1.67	-0.85	-0.94	-2.06	-1.79	-1.43	-1.54	-1.26	-0.79	-0.89	-0.09	-0.30	-0.74	-0.55	-0.76	-0.72	-0.93	-0.99	-0.99	-0.99	-1.28	-1.32	-1.06	-0.93
43	-1.10	-1.27	-1.27	-1.26	-1.67	-0.82	-1.13	-1.93	-1.70	-1.48	-1.60	-0.99	-0.71	-1.08	-0.04	-0.16	-0.55	-0.31	-0.63	-0.71	-1.08	-1.10	-1.05	-1.01	-1.22	-1.58	-1.17	-1.13
53	-1.14	-1.26	-1.43	-1.48	-1.18	-0.92	-1.41	-2.02	-1.88	-1.82	-1.52	-0.84	-0.83	-1.42	-0.15	-0.22	-0.05	-0.04	-0.66	-0.74	-1.39	-0.98	-1.05	-1.10	-1.35	-1.78	-1.23	-1.38
63	-1.10	-1.20	-1.39	-1.61	-0.79	-0.95	-1.39	-1.99	-1.90	-1.88	-0.72	-0.73	-0.76	-1.50	-0.37	0.18	0.18	-0.01	-0.69	-0.68	-1.43	-0.99	-1.04	-1.03	-1.26	-1.57	-1.30	-1.47
73	-1.14	-1.29	-1.47	-1.49	-0.95	-1.27	-1.51	-2.01	-2.02	-0.89	-0.64	-0.79	-1.05	-1.51	0.16	0.43	0.32	0.26	-0.42	-0.80	-1.46	-1.17	-1.10	-1.11	-1.38	-1.52	-1.46	-1.57
83	-1.10	-1.31	-1.52	-0.92	-1.11	-1.68	-1.33	-1.79	-1.38	-0.65	-0.68	-0.77	-1.56	-1.34	0.06	0.38	0.38	0.29	-0.44	-1.53	-1.37	-1.10	-1.04	-1.04	-1.33	-1.48	-1.56	-1.28
93	-1.18	-1.56	-1.57	-2.55	-1.83	-1.68	-1.32	-1.15	-0.63	-0.64	-1.81	-2.38	-1.73	-1.26	-0.70	0.32	0.53	-0.82	-1.95	-1.71	-1.28	-1.08	-1.18	-1.11	-1.60	-1.33	-1.50	-1.25

Table A-9. Database for portal building at TI2. Number in the left-hand column is the tapping index.

Elevation	0							15							30							-15						
Azimuth	0	15	30	45	60	75	90	0	15	30	45	60	75	90	0	15	30	45	60	75	90	0	15	30	45	60	75	90
11	-1.79	-2.60	-2.68	-2.40	-1.16	-1.07	-0.99	-3.41	-2.96	-2.34	-1.52	-1.11	-0.95	-0.79	-1.84	-1.38	-1.23	-1.11	-1.10	-0.92	-0.89	-1.15	-1.21	-1.59	-2.16	-1.44	-1.12	-0.92
21	-1.49	-2.11	-2.08	-1.74	-1.29	-1.13	-1.20	-2.64	-2.14	-1.74	-1.45	-1.23	-1.06	-0.96	-1.27	-1.26	-1.23	-1.14	-1.10	-0.89	-1.05	-1.07	-1.11	-1.29	-1.77	-1.27	-1.30	-1.06
31	-1.40	-1.74	-1.73	-1.55	-1.56	-1.19	-1.17	-2.14	-1.86	-1.63	-1.43	-1.30	-1.07	-0.94	-1.32	-1.24	-1.15	-1.06	-1.02	-0.91	-0.96	-1.05	-1.04	-1.26	-1.49	-1.39	-1.41	-1.12
41	-1.38	-1.57	-1.68	-1.57	-1.74	-1.31	-1.37	-2.15	-1.89	-1.75	-1.63	-1.43	-1.09	-1.24	-1.29	-1.17	-1.18	-1.09	-1.06	-0.90	-1.23	-1.08	-1.13	-1.31	-1.52	-1.69	-1.61	-1.33
51	-1.33	-1.53	-1.64	-1.73	-1.86	-1.46	-1.48	-2.15	-1.90	-1.77	-1.71	-1.52	-1.19	-1.43	-1.26	-1.26	-1.14	-1.05	-1.02	-0.90	-1.41	-1.12	-1.11	-1.30	-1.50	-1.85	-1.70	-1.51
61	-1.39	-1.59	-1.73	-1.87	-2.07	-1.50	-1.53	-2.10	-1.95	-1.86	-1.80	-1.44	-1.11	-1.63	-1.26	-1.11	-1.07	-0.99	-0.99	-0.90	-1.53	-1.06	-1.12	-1.31	-1.57	-2.11	-1.73	-1.57
71	-1.38	-1.63	-2.06	-2.33	-2.28	-1.76	-1.71	-2.13	-2.01	-2.08	-2.03	-1.62	-1.32	-1.78	-1.37	-1.23	-1.08	-1.05	-1.05	-0.94	-2.04	-1.10	-1.18	-1.48	-1.90	-2.65	-1.98	-1.77
81	-1.34	-1.78	-2.50	-3.33	-2.93	-2.00	-1.65	-2.53	-2.32	-2.71	-2.49	-1.91	-1.64	-1.69	-1.40	-1.18	-1.15	-1.11	-1.10	-1.13	-1.71	-1.07	-1.18	-1.62	-2.32	-3.22	-1.98	-1.72
91	-1.65	-1.93	-3.04	-1.54	-2.80	-2.20	-1.54	-3.04	-3.26	-1.30	-0.89	-1.37	-2.66	-1.50	-1.77	-1.29	0.65	0.52	-0.99	-3.09	-1.57	-1.21	-1.32	-1.62	-2.59	-2.28	-1.86	-1.50
12	-1.71	-2.09	-2.05	-1.95	-1.25	-1.12	-0.97	-2.21	-1.88	-1.71	-1.34	-1.21	-1.07	-0.90	-1.05	-1.16	-1.13	-1.19	-1.14	-1.00	-0.92	-1.28	-1.26	-1.65	-2.00	-1.52	-1.16	-0.98
22	-1.48	-2.20	-2.11	-1.76	-1.37	-1.13	-0.91	-2.75	-2.18	-1.74	-1.32	-1.27	-0.92	-0.82	-0.89	-1.14	-1.09	-1.07	-0.94	-0.80	-0.85	-1.07	-1.16	-1.28	-1.91	-1.26	-1.27	-0.93
32	-1.49	-1.81	-1.88	-1.59	-1.69	-1.27	-1.00	-2.31	-2.02	-1.69	-1.53	-1.48	-0.99	-0.94	-1.31	-1.24	-1.19	-1.13	-1.04	-0.80	-0.94	-1.08	-1.12	-1.24	-1.61	-1.41	-1.47	-1.03
42	-1.45	-1.64	-1.78	-1.54	-1.96	-1.29	-1.09	-2.20	-2.05	-1.84	-1.80	-1.53	-1.03	-1.17	-1.40	-1.24	-1.22	-1.14	-1.06	-0.81	-1.17	-1.13	-1.15	-1.25	-1.59	-1.76	-1.55	-1.23
52	-1.37	-1.52	-1.63	-1.58	-2.08	-1.19	-1.16	-2.12	-1.89	-1.85	-1.84	-1.45	-0.86	-1.31	-1.27	-1.12	-1.09	-1.04	-0.87	-0.69	-1.18	-0.91	-1.01	-1.15	-1.50	-2.00	-1.52	-1.27
62	-1.41	-1.64	-1.76	-2.23	-2.48	-1.21	-1.52	-2.20	-2.08	-2.21	-2.18	-1.65	-0.86	-1.57	-1.31	-1.21	-1.18	-1.06	-0.83	-0.72	-1.46	-1.03	-1.12	-1.24	-1.65	-2.48	-1.53	-1.51
72	-1.32	-1.62	-2.07	-2.77	-1.59	-1.13	-1.70	-2.31	-2.26	-2.54	-2.04	-0.96	-0.81	-1.68	-1.26	-1.05	-0.30	-0.23	-0.13	-0.69	-1.72	-1.09	-1.08	-1.47	-1.88	-2.64	-1.62	-1.69
82	-1.32	-1.82	-2.48	-1.31	-1.05	-1.70	-1.58	-2.54	-2.59	-1.60	-0.56	-0.79	-1.61	-1.55	-1.16	-0.11	0.60	0.44	0.25	-1.23	-1.72	-1.01	-1.08	-1.51	-2.03	-2.05	-1.70	-1.53
92	-1.56	-1.90	-1.80	-2.22	-3.28	-2.16	-1.52	-2.19	-1.17	-0.56	-1.65	-3.48	-2.45	-1.44	-0.98	0.48	0.65	-0.81	-2.58	-2.67	-1.51	-1.16	-1.26	-1.64	-2.80	-2.20	-1.89	-1.49
13	-1.70	-1.93	-1.85	-1.82	-1.23	-1.07	-0.91	-1.55	-1.51	-1.58	-1.32	-1.20	-0.98	-0.80	-0.82	-1.03	-1.12	-1.07	-1.02	-0.98	-0.85	-1.30	-1.28	-1.56	-1.88	-1.46	-1.13	-1.02
23	-1.50	-1.98	-2.00	-1.67	-1.52	-0.96	-0.85	-2.08	-1.81	-1.62	-1.35	-1.26	-0.80	-0.62	0.28	-0.16	-0.87	-0.93	-0.85	-0.78	-0.78	-1.16	-1.14	-1.34	-1.85	-1.26	-1.11	-0.87
33	-1.40	-1.77	-1.80	-1.51	-1.76	-0.87	-0.88	-2.23	-1.86	-1.62	-1.50	-1.37	-0.78	-0.84	0.00	-0.19	-0.86	-0.84	-0.79	-0.75	-0.87	-1.05	-1.07	-1.19	-1.55	-1.54	-1.18	-0.92
43	-1.42	-1.64	-1.82	-1.53	-1.86	-0.84	-0.99	-2.21	-1.92	-1.74	-1.72	-1.30	-0.71	-1.10	-0.84	-0.64	-0.87	-0.80	-0.67	-0.71	-1.04	-1.11	-1.06	-1.16	-1.57	-1.75	-1.17	-1.13
53	-1.43	-1.77	-1.78	-1.89	-1.57	-0.93	-1.29	-2.29	-2.11	-1.96	-1.87	-1.09	-0.78	-1.33	-0.85	-0.40	-0.93	-0.50	-0.59	-0.79	-1.32	-1.14	-1.13	-1.33	-1.74	-2.03	-1.32	-1.38
63	-1.36	-1.62	-1.73	-1.93	-0.88	-0.89	-1.43	-2.20	-2.03	-1.96	-1.34	-0.76	-0.77	-1.40	-0.92	-0.61	0.09	0.20	-0.65	-0.72	-1.43	-1.12	-1.11	-1.35	-1.69	-1.65	-1.24	-1.52
73	-1.44	-1.79	-2.14	-1.48	-1.02	-1.28	-1.65	-2.33	-2.16	-1.41	-0.72	-0.86	-1.01	-1.63	-0.23	0.36	0.28	0.20	-0.36	-0.75	-1.73	-1.02	-1.13	-1.36	-1.76	-1.36	-1.41	-1.64
83	-1.34	-1.85	-1.76	-1.00	-1.06	-1.78	-1.62	-2.02	-1.45	-0.67	-0.74	-0.76	-1.77	-1.49	-0.17	0.40	0.45	0.32	-0.18	-1.73	-1.62	-0.98	-1.13	-1.40	-1.59	-1.71	-1.70	-1.54
93	-1.58	-1.87	-2.10	-3.00	-2.55	-2.04	-1.46	-1.49	-0.69	-0.81	-2.15	-2.75	-2.12	-1.45	-0.83	0.32	0.58	-1.13	-2.05	-2.20	-1.54	-1.15	-1.28	-1.60	-2.31	-1.92	-1.79	-1.36

Table A-10. Database for portal building at TI3. Number in the left-hand column is the tapping index.

Elevation	0							15							30							-15						
Azimuth	0	15	30	45	60	75	90	0	15	30	45	60	75	90	0	15	30	45	60	75	90	0	15	30	45	60	75	90
11	-3.15	-3.08	-2.99	-2.50	-1.73	-1.10	-0.78	-3.60	-3.22	-2.60	-1.82	-1.31	-1.01	-0.89	-2.41	-1.71	-1.52	-1.27	-1.18	-0.93	-0.92	-1.43	-1.60	-2.28	-2.61	-1.85	-1.24	-0.94
21	-2.91	-2.95	-2.36	-2.06	-1.55	-1.35	-0.91	-2.82	-2.79	-2.20	-1.81	-1.41	-1.23	-0.93	-1.87	-1.81	-1.56	-1.37	-1.30	-0.90	-0.95	-1.32	-1.38	-1.79	-2.06	-1.53	-1.40	-1.14
31	-2.31	-2.19	-2.17	-1.84	-1.72	-1.40	-1.03	-2.65	-2.65	-2.20	-1.80	-1.42	-1.12	-1.09	-1.75	-1.77	-1.51	-1.37	-1.21	-1.03	-1.17	-1.24	-1.31	-1.52	-1.82	-1.57	-1.46	-1.11
41	-2.13	-2.17	-2.12	-1.90	-1.87	-1.51	-1.20	-2.75	-2.52	-2.05	-1.86	-1.45	-1.21	-1.28	-1.67	-1.65	-1.50	-1.41	-1.23	-1.03	-1.21	-1.19	-1.25	-1.59	-1.76	-1.89	-1.63	-1.32
51	-2.04	-2.19	-2.11	-1.98	-2.07	-1.65	-1.37	-2.70	-2.60	-2.11	-1.96	-1.59	-1.30	-1.34	-1.71	-1.73	-1.52	-1.34	-1.27	-1.09	-1.57	-1.23	-1.30	-1.67	-1.81	-2.12	-1.76	-1.58
61	-2.08	-2.16	-2.15	-2.42	-2.24	-1.60	-1.76	-2.80	-2.49	-2.16	-1.99	-1.48	-1.17	-1.59	-1.62	-1.63	-1.40	-1.28	-1.23	-1.07	-1.74	-1.17	-1.20	-1.56	-1.83	-2.43	-1.95	-1.72
71	-2.29	-2.25	-2.54	-2.96	-2.54	-1.95	-2.04	-2.79	-2.63	-2.36	-2.25	-1.72	-1.47	-1.86	-1.77	-1.58	-1.42	-1.30	-1.30	-1.21	-2.14	-1.20	-1.29	-1.71	-2.33	-3.00	-2.11	-1.97
81	-2.78	-2.51	-3.55	-4.17	-3.47	-2.45	-2.21	-3.02	-2.74	-3.06	-2.80	-2.09	-1.90	-2.05	-1.84	-1.06	-1.52	-1.44	-1.49	-1.58	-2.21	-1.23	-1.35	-2.03	-3.45	-4.08	-2.50	-2.25
91	-3.08	-3.32	-3.06	-1.87	-2.89	-4.04	-1.96	-3.63	-4.06	-2.02	-1.22	-2.78	-4.09	-1.95	-2.27	-1.74	-0.20	0.64	-2.05	-4.30	-2.15	-1.51	-1.54	-2.53	-3.42	-3.43	-2.87	-2.13
12	-2.67	-2.43	-2.21	-1.97	-1.51	-1.18	-0.96	-2.49	-2.06	-1.77	-1.45	-1.20	-1.16	-0.90	-1.59	-1.46	-1.31	-1.19	-1.19	-0.99	-0.97	-1.57	-1.71	-1.96	-2.15	-1.61	-1.15	-0.97
22	-2.99	-3.03	-2.52	-2.01	-1.58	-1.25	-0.96	-3.02	-2.73	-1.91	-1.60	-1.40	-1.10	-0.92	-1.46	-1.54	-1.44	-1.27	-1.08	-0.87	-0.97	-1.26	-1.36	-1.82	-2.22	-1.41	-1.33	-1.01
32	-2.46	-2.33	-2.36	-1.90	-1.85	-1.43	-1.02	-2.83	-2.64	-1.98	-1.85	-1.57	-1.17	-1.00	-1.60	-1.54	-1.48	-1.28	-1.22	-0.95	-1.09	-1.25	-1.37	-1.68	-1.99	-1.68	-1.61	-1.06
42	-2.30	-2.34	-2.29	-1.96	-2.09	-1.56	-1.12	-2.90	-2.67	-2.13	-1.98	-1.55	-1.20	-1.20	-1.55	-1.32	-1.50	-1.33	-1.24	-0.99	-1.14	-1.31	-1.38	-1.63	-1.80	-2.08	-1.62	-1.21
52	-2.18	-2.22	-2.10	-2.31	-2.29	-1.49	-1.24	-2.76	-2.65	-2.19	-2.02	-1.46	-1.16	-1.22	-1.51	-1.44	-1.36	-1.29	-1.09	-0.83	-1.18	-1.12	-1.18	-1.57	-1.77	-2.42	-1.60	-1.34
62	-2.30	-2.32	-2.29	-2.93	-2.57	-1.57	-1.55	-2.99	-2.85	-2.48	-2.33	-1.69	-1.26	-1.46	-1.55	-0.99	-1.41	-1.28	-1.16	-0.88	-1.57	-1.21	-1.34	-1.61	-1.98	-2.96	-1.78	-1.64
72	-2.39	-2.35	-2.95	-3.34	-2.54	-1.38	-1.88	-3.05	-2.63	-2.78	-2.19	-1.40	-1.09	-1.71	-1.55	-0.86	-1.32	-1.07	-0.88	-0.81	-1.96	-1.20	-1.32	-1.67	-2.70	-3.02	-1.62	-2.00
82	-3.01	-2.66	-3.48	-1.50	-1.26	-1.89	-2.09	-3.07	-2.91	-2.23	-0.76	-0.87	-1.43	-1.96	-1.41	-0.08	-0.15	0.46	-0.63	-1.52	-2.15	-1.22	-1.36	-2.06	-2.74	-2.14	-2.01	-2.09
92	-2.59	-2.74	-2.02	-4.01	-4.14	-3.34	-1.88	-2.42	-1.74	-1.15	-2.68	-3.92	-3.64	-1.83	-1.30	0.67	0.68	-1.57	-3.14	-3.46	-1.95	-1.39	-1.53	-2.13	-3.76	-2.86	-2.63	-1.97
13	-2.57	-2.31	-2.04	-1.91	-1.39	-1.12	-0.99	-1.91	-1.74	-1.57	-1.43	-1.21	-0.99	-0.91	-1.09	-1.26	-1.29	-1.22	-1.10	-1.00	-0.95	-1.69	-1.70	-2.07	-2.03	-1.49	-1.07	-0.93
23	-2.50	-2.34	-2.32	-1.84	-1.47	-1.06	-0.89	-2.36	-2.08	-1.62	-1.41	-1.16	-0.86	-0.71	-0.90	-0.32	-1.04	-1.05	-0.89	-0.82	-0.83	-1.32	-1.41	-1.84	-2.07	-1.37	-1.10	-0.86
33	-2.52	-2.27	-2.11	-1.75	-1.79	-1.06	-1.01	-2.54	-2.22	-1.77	-1.63	-1.29	-1.01	-0.81	-1.02	-0.76	-1.17	-1.04	-1.00	-0.78	-0.91	-1.26	-1.31	-1.76	-1.78	-1.67	-1.11	-1.07
43	-2.62	-2.35	-2.20	-1.94	-2.00	-1.15	-1.07	-2.71	-2.33	-1.98	-1.80	-1.43	-0.98	-1.05	-1.14	-0.54	-1.01	-1.03	-0.97	-0.76	-1.11	-1.25	-1.28	-1.71	-1.66	-2.04	-1.20	-1.03
53	-2.43	-2.43	-2.20	-2.36	-2.08	-1.08	-1.30	-2.68	-2.39	-2.07	-1.91	-1.31	-0.99	-1.17	-1.16	-0.67	-1.18	-0.95	-0.96	-0.86	-1.32	-1.35	-1.30	-1.70	-1.87	-2.38	-1.25	-1.38
63	-2.37	-2.35	-2.44	-2.30	-1.46	-1.02	-1.60	-2.57	-2.32	-2.06	-1.56	-0.87	-0.81	-1.44	-1.10	-0.35	-0.88	-0.39	-0.68	-0.74	-1.51	-1.23	-1.30	-1.64	-2.05	-1.87	-1.23	-1.53
73	-2.55	-2.52	-2.64	-1.49	-1.02	-1.19	-1.87	-2.56	-2.53	-1.70	-1.01	-0.85	-0.92	-1.82	-0.87	0.28	0.08	0.27	-0.48	-0.66	-1.93	-1.28	-1.35	-1.81	-2.10	-1.54	-1.56	-2.01
83	-2.66	-2.67	-1.77	-1.19	-1.28	-2.12	-2.03	-2.18	-1.96	-0.81	-0.87	-0.90	-1.76	-1.86	0.04	0.64	0.53	0.12	-0.77	-1.91	-2.06	-1.32	-1.37	-1.85	-1.57	-1.87	-2.21	-2.15
93	-2.30	-2.12	-2.81	-3.69	-3.15	-2.64	-1.88	-1.73	-0.95	-1.38	-2.67	-3.12	-2.75	-1.75	-0.89	0.54	0.72	-1.44	-2.62	-2.74	-1.92	-1.49	-1.62	-1.99	-3.26	-2.39	-2.28	-1.95

Table A-11. Database for portal building at TI4. Number in the left-hand column is the tapping index.

Elevation	0							15							30							-15						
Azimuth	0	15	30	45	60	75	90	0	15	30	45	60	75	90	0	15	30	45	60	75	90	0	15	30	45	60	75	90
11	-4.28	-3.89	-3.89	-2.85	-1.72	-1.04	-0.82	-3.76	-3.53	-2.63	-2.14	-1.40	-1.05	-0.81	-2.34	-2.09	-1.65	-1.36	-1.24	-0.88	-0.88	-1.61	-1.63	-2.72	-2.82	-2.07	-1.22	-0.85
21	-3.40	-3.62	-3.18	-2.43	-1.75	-1.29	-0.95	-3.18	-3.06	-2.25	-2.31	-1.53	-1.23	-1.12	-1.09	-0.58	-1.84	-1.57	-1.39	-0.93	-1.12	-1.58	-1.36	-2.46	-2.48	-1.63	-1.38	-0.99
31	-2.75	-2.75	-2.74	-2.15	-1.73	-1.37	-0.99	-3.10	-2.90	-2.13	-2.37	-1.62	-1.14	-1.16	-1.71	-0.98	-1.72	-1.29	-1.33	-0.91	-1.03	-1.46	-1.35	-1.92	-2.04	-1.74	-1.48	-0.89
41	-2.93	-2.56	-2.80	-2.32	-1.87	-1.41	-1.16	-3.11	-3.03	-2.43	-2.47	-1.56	-1.23	-1.35	-1.45	-0.08	-1.68	-1.48	-1.31	-1.01	-1.30	-1.45	-1.36	-1.81	-1.99	-1.98	-1.63	-1.11
51	-2.92	-2.76	-2.62	-2.48	-2.06	-1.58	-1.43	-3.22	-2.98	-2.30	-2.32	-1.59	-1.28	-1.58	-1.83	0.32	-1.68	-1.41	-1.33	-1.00	-1.44	-1.43	-1.38	-1.93	-2.13	-2.36	-1.81	-1.30
61	-2.79	-2.61	-2.59	-2.59	-2.15	-1.57	-1.54	-3.05	-2.91	-2.33	-2.31	-1.57	-1.24	-1.84	-1.51	0.25	-1.26	-1.24	-1.21	-0.98	-1.64	-1.30	-1.35	-1.89	-2.20	-2.66	-1.89	-1.45
71	-2.74	-2.75	-2.98	-3.27	-2.40	-1.82	-2.17	-3.38	-3.09	-2.61	-2.44	-1.83	-1.55	-2.51	-1.43	0.95	-1.49	-1.43	-1.40	-1.20	-2.17	-1.45	-1.38	-2.10	-2.70	-3.24	-2.23	-2.00
81	-3.37	-3.28	-4.23	-4.44	-3.19	-2.38	-2.63	-3.28	-3.25	-3.04	-3.00	-2.15	-2.12	-2.85	0.40	-0.01	-1.32	0.09	-1.54	-1.72	-2.45	-1.55	-1.49	-2.42	-4.09	-4.44	-2.74	-2.21
91	-3.70	-4.47	-4.54	-1.96	-4.04	-4.42	-2.91	-4.03	-4.32	-2.26	-1.12	-2.89	-5.38	-2.79	-2.35	-1.83	-0.49	1.15	-2.72	-4.69	-2.66	-1.67	-1.76	-3.12	-3.30	-4.15	-4.15	-2.32
12	-3.30	-2.76	-2.65	-2.07	-1.41	-1.18	-0.88	-2.92	-2.35	-1.90	-1.64	-1.32	-1.06	-0.94	-1.15	-1.58	-1.46	-1.27	-1.11	-0.94	-1.01	-1.89	-1.73	-2.19	-2.32	-1.73	-1.25	-0.83
22	-3.45	-3.91	-3.31	-2.14	-1.59	-1.24	-0.30	-3.15	-2.78	-1.98	-1.87	-1.37	-0.97	-0.68	-0.09	0.74	-1.50	-1.18	-1.26	-0.85	-0.93	-1.57	-1.43	-2.40	-2.43	-1.64	-1.42	-0.83
32	-2.96	-3.17	-2.92	-2.28	-1.86	-1.41	-1.01	-3.25	-2.89	-2.25	-2.00	-1.51	-1.10	-1.07	-1.18	0.46	-1.64	-1.26	-1.21	-0.83	-0.99	-1.54	-1.45	-2.07	-2.22	-1.83	-1.56	-0.93
42	-3.16	-2.86	-2.99	-2.42	-2.06	-1.57	-1.00	-3.21	-3.01	-2.35	-2.23	-1.55	-1.15	-1.24	-0.31	0.74	-1.59	-1.22	-1.14	-0.94	-1.19	-1.56	-1.43	-2.04	-2.16	-2.24	-1.60	-1.04
52	-2.99	-2.89	-2.69	-2.61	-2.13	-1.49	-1.14	-3.23	-2.80	-2.48	-2.28	-1.53	-1.08	-1.30	-1.02	0.89	-1.47	-1.16	-1.08	-0.82	-1.27	-1.32	-1.38	-1.83	-2.00	-2.45	-1.72	-1.00
62	-3.06	-2.92	-2.76	-3.11	-2.44	-1.67	-1.51	-3.27	-2.96	-2.64	-2.54	-1.74	-1.06	-1.85	-0.06	0.74	-1.52	-0.61	-1.25	-0.90	-1.61	-1.43	-1.39	-1.94	-2.29	-3.09	-1.82	-1.36
72	-2.91	-2.94	-3.48	-3.52	-2.32	-1.47	-1.99	-3.13	-3.08	-2.79	-2.57	-1.51	-0.97	-2.22	0.37	0.86	-1.51	0.05	-0.95	-0.87	-1.98	-1.44	-1.41	-2.00	-3.02	-3.20	-1.78	-1.73
82	-3.55	-3.53	-3.74	-2.12	-1.06	-1.43	-2.60	-3.14	-2.92	-2.10	-1.38	-0.82	-1.91	-2.66	0.49	0.96	0.17	0.85	0.51	-1.74	-2.42	-1.47	-1.49	-2.45	-2.79	-1.62	-2.08	-2.22
92	-3.01	-3.13	-2.51	-4.18	-4.93	-4.41	-2.58	-2.85	-1.97	-1.24	-2.81	-4.33	-4.50	-2.46	-0.75	0.98	0.97	0.00	-3.55	-3.97	-2.43	-1.72	-1.81	-2.74	-4.33	-4.02	-3.35	-2.10
13	-2.83	-2.53	-2.40	-2.01	-1.36	-1.03	-0.70	-2.03	-2.11	-1.69	-1.49	-1.16	-0.99	-0.86	-0.62	-1.35	-1.24	-1.08	-1.14	-0.90	-0.90	-2.12	-1.96	-2.01	-2.16	-1.51	-1.10	-0.88
23	-2.91	-2.77	-2.75	-1.92	-1.49	-1.15	-0.83	-2.37	-2.11	-1.72	-1.53	-1.22	-0.81	-0.79	0.91	0.79	-1.23	-0.93	-1.00	-0.78	-0.88	-1.70	-1.53	-2.05	-2.09	-1.50	-1.20	-0.75
33	-2.91	-2.95	-2.60	-2.05	-1.71	-1.17	-0.51	-2.52	-2.45	-1.82	-1.69	-1.21	-0.83	-0.71	0.64	0.97	-0.96	-0.47	-0.95	-0.68	-0.87	-1.52	-1.42	-1.94	-2.05	-1.83	-1.28	-0.68
43	-2.99	-2.96	-2.82	-2.30	-1.84	-1.24	-0.85	-2.82	-2.52	-2.06	-1.82	-1.31	-0.89	-1.12	0.12	0.99	-1.21	-0.65	-0.98	-0.70	-1.04	-1.59	-1.44	-1.96	-1.98	-2.13	-1.43	-0.98
53	-3.17	-3.00	-2.69	-2.62	-1.90	-1.24	-1.20	-3.04	-2.52	-2.28	-2.05	-1.40	-0.91	-1.30	1.15	0.89	-1.12	0.04	-0.69	-0.25	-1.34	-1.58	-1.62	-2.09	-2.07	-2.38	-1.42	-1.10
63	-3.01	-2.89	-2.85	-2.55	-1.49	-0.92	-1.50	-2.76	-2.46	-2.20	-1.82	-1.14	-0.80	-1.65	1.15	0.95	-0.51	0.28	0.09	-0.66	-1.49	-1.47	-1.50	-1.89	-2.31	-1.92	-1.19	-1.33
73	-3.05	-2.93	-3.00	-1.89	-1.04	-0.97	-1.98	-2.66	-2.44	-1.65	-1.16	-0.75	-1.02	-2.18	1.37	0.90	0.36	0.46	0.17	-0.93	-1.83	-1.56	-1.55	-2.08	-2.36	-1.27	-1.44	-1.69
83	-2.81	-3.14	-2.37	-1.01	-1.14	-1.75	-2.37	-2.52	-1.95	-0.69	-0.77	-0.75	-2.19	-2.49	1.18	0.93	0.73	0.71	0.38	-1.96	-2.31	-1.51	-1.54	-2.09	-1.54	-1.65	-2.28	-2.04
93	-2.63	-2.30	-2.53	-3.95	-3.64	-3.05	-2.27	-1.94	-0.14	-1.74	-2.59	-3.31	-3.25	-2.19	0.00	0.84	0.91	0.48	-2.87	-3.15	-2.19	-1.82	-1.83	-2.46	-3.81	-2.98	-2.64	-1.93

Table A-12. Database for portal building at TI5. Number in the left-hand column is the tapping index.

Elevation	0							15							30							-15						
Azimuth	0	15	30	45	60	75	90	0	15	30	45	60	75	90	0	15	30	45	60	75	90	0	15	30	45	60	75	90
11	-5.24	-4.12	-3.84	-3.21	-1.54	-1.21	-0.86	-4.12	-3.90	-3.09	-2.04	-1.62	-1.10	-0.89	-2.67	-2.73	-2.02	-1.71	-1.24	-1.01	-0.89	-1.84	-2.02	-2.90	-3.13	-2.02	-1.21	-0.89
21	-4.35	-3.96	-3.42	-2.81	-1.86	-1.65	-0.96	-3.50	-4.07	-3.45	-2.11	-1.83	-1.34	-0.99	-0.97	-1.26	-2.18	-1.66	-1.43	-1.14	-1.02	-1.67	-1.58	-2.52	-2.68	-1.92	-1.46	-1.06
31	-3.67	-3.37	-3.09	-2.89	-1.97	-1.59	-1.09	-3.21	-3.72	-3.47	-2.20	-1.78	-1.25	-1.09	-0.81	-0.53	-2.06	-1.80	-1.41	-1.05	-1.04	-1.49	-1.55	-2.21	-2.55	-1.99	-1.62	-1.15
41	-3.62	-3.30	-3.10	-2.92	-2.07	-1.76	-1.25	-3.30	-4.02	-3.43	-2.21	-1.83	-1.41	-1.46	-1.91	-2.21	-2.06	-1.52	-1.41	-1.16	-1.17	-1.67	-1.55	-2.31	-2.58	-2.19	-1.82	-1.30
51	-3.41	-3.38	-3.01	-2.94	-2.25	-1.92	-1.62	-3.91	-3.56	-3.43	-2.20	-1.81	-1.40	-1.58	-2.25	-1.49	-2.01	-1.87	-1.49	-1.19	-1.37	-1.65	-1.70	-2.22	-2.64	-2.48	-1.96	-1.54
61	-3.43	-3.26	-3.14	-2.77	-2.25	-1.80	-1.71	-4.00	-3.50	-3.28	-2.22	-1.73	-1.48	-1.75	-1.27	-2.49	-1.96	-1.22	-1.39	-1.11	-1.57	-1.51	-1.57	-2.19	-2.68	-2.71	-2.09	-1.88
71	-3.36	-3.16	-3.55	-3.43	-2.48	-2.13	-2.14	-3.90	-3.55	-3.19	-2.46	-1.90	-1.63	-2.39	0.00	-2.56	-2.04	-1.45	-1.37	-1.45	-2.06	-1.61	-1.69	-2.53	-3.46	-3.32	-2.59	-2.40
81	-3.56	-3.77	-4.39	-4.47	-3.23	-2.75	-2.64	-3.99	-3.59	-3.51	-3.22	-2.47	-2.27	-3.20	0.07	-2.41	-2.05	-1.61	-1.46	-1.85	-2.64	-1.82	-1.95	-3.01	-5.58	-4.78	-3.05	-2.90
91	-4.00	-5.29	-4.81	-2.59	-5.39	-4.89	-3.65	-4.44	-4.23	-3.67	-1.81	-3.59	-4.80	-3.81	-2.76	-2.72	-1.13	0.58	-3.71	-5.18	-3.77	-2.08	-2.51	-3.60	-3.74	-4.53	-5.35	-3.67
12	-3.78	-3.11	-2.77	-2.37	-1.46	-1.25	-0.98	-3.10	-2.58	-2.27	-1.73	-1.48	-1.06	-0.96	-1.89	-2.15	-1.63	-1.52	-1.19	-0.94	-0.92	-2.12	-2.11	-2.32	-2.37	-1.67	-1.16	-0.91
22	-4.38	-4.32	-3.22	-2.51	-1.61	-1.41	-0.88	-3.10	-3.28	-2.65	-1.90	-1.55	-1.15	-0.98	0.95	-0.61	-1.69	-1.65	-1.18	-0.91	-0.86	-1.68	-1.69	-2.66	-2.51	-1.74	-1.42	-0.95
32	-3.96	-3.41	-3.05	-2.63	-1.95	-1.53	-0.94	-3.38	-3.48	-2.92	-2.06	-1.75	-1.23	-0.87	-0.21	-0.53	-1.88	-1.65	-1.02	-0.94	-1.02	-1.64	-1.70	-2.41	-2.43	-2.15	-1.59	-1.08
42	-3.72	-3.62	-3.19	-2.87	-2.11	-1.62	-1.14	-3.57	-3.51	-3.08	-2.11	-1.73	-1.23	-1.26	-1.45	-0.63	-1.86	-1.52	-1.30	-1.01	-1.12	-1.80	-1.69	-2.47	-2.51	-2.44	-1.82	-1.26
52	-3.61	-3.47	-2.96	-2.95	-2.14	-1.70	-1.26	-3.63	-3.34	-3.10	-2.13	-1.73	-1.13	-1.28	-1.61	-0.33	-1.71	-1.45	-0.81	-0.93	-1.15	-1.65	-1.71	-2.35	-2.59	-2.65	-1.87	-1.28
62	-3.27	-3.42	-3.12	-3.12	-2.38	-1.95	-1.52	-3.69	-3.30	-3.00	-2.40	-1.89	-1.26	-1.68	-1.06	-1.08	-1.86	-1.40	-0.77	-0.94	-1.48	-1.71	-1.73	-2.15	-3.20	-3.19	-1.91	-1.69
72	-3.28	-3.39	-3.90	-3.82	-2.42	-1.97	-1.91	-3.57	-3.27	-3.29	-2.70	-1.99	-1.45	-2.30	0.82	-1.72	-1.08	-1.26	-0.73	-1.04	-1.86	-1.74	-1.80	-2.44	-4.09	-3.43	-1.95	-2.22
82	-3.91	-3.83	-4.02	-2.94	-1.42	-1.69	-2.67	-3.55	-2.97	-2.99	-1.69	-1.08	-1.84	-3.09	2.09	-0.34	-0.93	-0.45	0.46	-1.76	-2.56	-1.83	-1.96	-2.96	-3.20	-1.63	-2.52	-3.01
92	-3.50	-3.40	-2.90	-4.19	-5.72	-4.62	-3.13	-3.16	-2.45	-1.45	-3.71	-4.46	-4.14	-3.31	-1.12	-0.86	0.81	-1.65	-4.07	-4.50	-3.17	-2.18	-2.44	-3.33	-5.50	-4.74	-4.34	-3.18
13	-3.09	-2.83	-2.38	-2.27	-1.36	-1.02	-0.94	-2.44	-2.12	-1.83	-1.51	-1.25	-0.97	-0.94	0.67	-1.64	-1.43	-1.38	-1.16	-0.94	-0.89	-2.16	-2.10	-2.13	-2.18	-1.56	-1.12	-0.82
23	-3.45	-3.10	-2.83	-2.16	-1.57	-1.13	-0.86	-2.45	-2.40	-1.99	-1.58	-1.31	-1.01	-0.91	1.17	1.17	-0.90	-0.92	-0.54	-0.64	-0.64	-1.88	-1.82	-2.18	-2.18	-1.59	-1.18	-0.93
33	-3.42	-3.20	-2.72	-2.26	-1.81	-1.28	-0.71	-2.77	-2.72	-2.24	-1.76	-1.47	-0.98	-0.55	0.90	1.85	-1.12	-0.95	-0.61	-0.23	-0.72	-1.72	-1.69	-2.15	-2.16	-2.01	-1.31	-0.99
43	-3.36	-3.25	-2.72	-2.44	-1.85	-1.40	-0.83	-2.83	-2.75	-2.45	-1.87	-1.56	-1.06	-1.18	0.49	1.53	-1.51	-0.95	-0.49	-0.53	-1.08	-1.77	-1.77	-2.42	-2.30	-2.21	-1.34	-1.18
53	-3.48	-3.35	-3.07	-2.69	-1.95	-1.44	-1.35	-3.02	-2.88	-2.64	-2.04	-1.73	-1.15	-1.46	0.35	1.02	-1.15	-1.08	0.04	-0.65	-1.33	-1.92	-1.90	-2.30	-2.74	-2.62	-1.47	-1.45
63	-3.17	-3.05	-3.08	-2.78	-1.70	-1.17	-1.36	-3.03	-2.51	-2.52	-1.95	-1.50	-1.01	-1.51	0.75	1.00	-0.90	-0.67	-0.08	-0.45	-1.45	-1.78	-1.74	-2.08	-2.88	-2.27	-1.37	-1.66
73	-3.20	-3.22	-3.17	-2.58	-1.16	-1.23	-1.98	-2.73	-2.57	-2.29	-1.49	-0.97	-1.03	-2.16	1.23	0.52	-0.11	-0.45	0.12	-0.79	-1.91	-1.88	-1.88	-2.47	-2.59	-1.36	-1.74	-2.21
83	-3.26	-3.22	-2.46	-1.39	-1.72	-1.91	-2.50	-2.43	-2.29	-1.72	-0.53	-0.90	-1.95	-2.89	1.84	0.65	0.88	0.83	0.05	-1.94	-2.59	-1.91	-2.08	-2.33	-1.54	-1.73	-2.73	-2.97
93	-3.04	-2.74	-2.81	-3.71	-4.01	-3.47	-2.68	-2.06	-1.54	-1.51	-3.11	-3.59	-3.25	-3.05	1.20	0.90	0.51	-1.22	-3.14	-3.44	-2.68	-2.22	-2.17	-3.20	-4.52	-3.44	-3.50	-2.80

Appendix B Surface roughness categories from ASCE

Table B-1. Surface roughness categories from ASCE7 (2013).

Surface roughness category	Characteristics
Surface Roughness B	Urban and suburban areas, wooded areas or other terrain with numerous closely spaced obstructions having the size of single-family dwellings or larger.
Surface Roughness C	Open terrain with scattered obstructions having heights generally less than 30 ft (9.1 m). This category includes flat open country, grasslands, and all water surfaces in hurricane-prone regions.
Surface Roughness D	Flat, unobstructed areas and water surfaces outside hurricane-prone regions. This category includes smooth mud flats, salt flats, and unbroken ice.

Table B-2. Adjustment factor for building height and exposure (ASCE7, 2013).

Mean roof height (ft)	Exposure		
	B	C	D
15	1.00	1.21	1.47
20	1.00	1.29	1.55
25	1.00	1.35	1.61
30	1.00	1.40	1.66
35	1.05	1.45	1.70
40	1.09	1.49	1.74
45	1.12	1.53	1.78
50	1.16	1.56	1.81
55	1.19	1.59	1.84
60	1.22	1.62	1.87

Appendix C Terrain categories from Eurocode 1-4

The terrain category defined in Eurocode (2010) is illustrated in Table C-1. z_0 is the roughness length and z_{min} is the minimum height. The defined ratio (C_e) of the peak dynamic pressure to mean dynamic pressure with variable terrain categories and heights is stated in Figure C-1.

Table C-1. Terrain category and terrain parameters (Eurocode, 2010).

Terrain category	**z_0 (m)**	**z_{min} (m)**
0 Sea or coastal area exposed to the open sea	0.003	1
I Lakes or flat and horizontal area with negligible vegetation and without obstacles	0.01	1
II Area with low vegetation such as grass and isolated obstacles (trees, buildings) with separations of at least 20 obstacle heights	0.05	2
III Area with regular cover of vegetation or buildings or with isolated obstacles with separations of maximum 20 obstacle heights (such as villages, suburban terrain, permanent forest)	0.3	5
IV Area in which at least 15% of the surface is covered with buildings and their average height exceeds 15 m	1	10

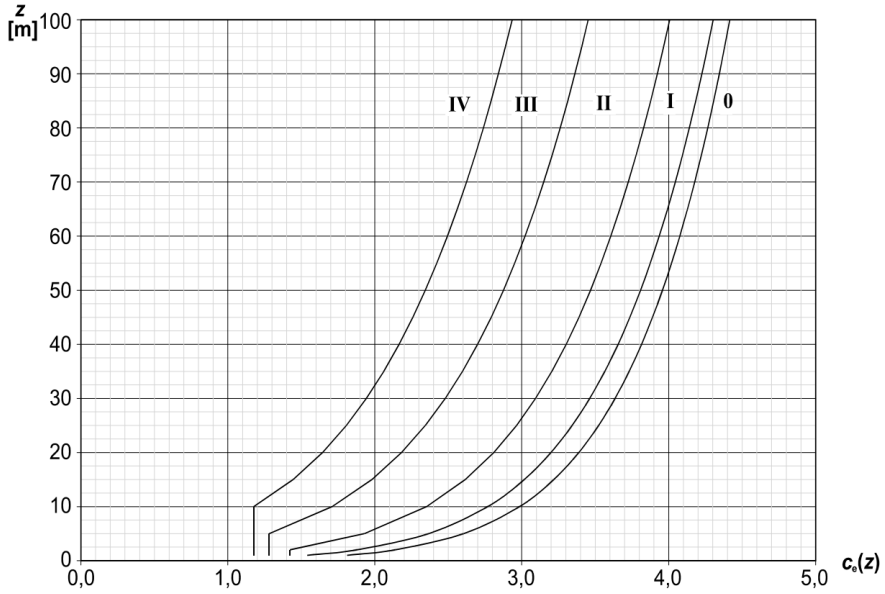


Figure C-1. Ratio of the peak dynamic pressure to mean dynamic pressure based on different heights and terrain categories (Eurocode, 2010).

Appendix D Publications

This appendix contains author's publication list and abstracts. These are:

(1) Song, J., Martinez-Vazquez, P., & Skalomenos, K. A. (2021). A framework on the dynamic response of tall structures to non-stationary wind using design spectrum. 8th ECCOMAS Thematic Conference on Computational Methods in Structural Dynamics and Earthquake Engineering, Athens, Greece.

(2) Song, J., Martinez-Vazquez, P., & Skalomenos, K. A. (2021). Generalisation for thunderstorm downburst wind design spectra. The 2021 World Congress on Advances in Structural Engineering and Mechanics (ASEM21) GECE, Seoul, Korea, August 23-26, 2021.

(3) Song, J., Skalomenos, K., Martinez-Vazquez, P., & Kastiza, P. (2022). "A computational method for determining combined ductility demands on structures under sequential hazards." 3rd International Conference on Natural Hazards & Infrastructure, 5-7 July 2022, Athens, Greece.

COMPDYN 2021
8th ECCOMAS Thematic Conference on
Computational Methods in Structural Dynamics and Earthquake Engineering
M. Papadrakakis, M. Fragiadakis (eds.)
Streamed from Athens, Greece, 27–30 June 2021

A FRAMEWORK ON THE DYNAMIC RESPONSE OF TALL STRUCTURES TO NON-STATIONARY WIND USING DESIGN SPECTRUM

Jing Song[1], Pedro Martinez-Vazquez[2], Konstantinos A. Skalomenos[3]

Department of Civil Engineering, University of Birmingham, Birmingham, B15 2TT, UK

Abstract

The use of design spectra is common practice in earthquake engineering design as opposed to wind-resisting design. Nonetheless, previous research has identified ways to map such technique to study wind effects on structures. The present investigation introduces a novel framework to deal with the dynamic performance of infrastructure subject to thunderstorm downbursts. It builds on recent developments that demonstrate that spectral analysis is applicable to wind engineering given various equivalences developed to quantify random loading generated through non-synoptic wind environment. The new framework is tested on a benchmark building via a simplified model, which demonstrates its validity. In this framework, the dynamic response of the multi-degree-of-freedom (MDOF) system subjected to non-stationary wind can be obtained assuming that the first mode of vibration is dominant when the mechanical properties of the structure and aerodynamic characteristics of the thunderstorm downburst are identified.

Keywords: Wind design spectrum, Wind-excited response, Thunderstorm downburst, Non-stationary wind, Multi-degree-of-freedom system

ICONHIC2022
3rd International Conference on Natural Hazards & Infrastructure
5-7 July 2022, Athens, Greece

A computational method for determining combined ductility demands on steel structures subject to multi-hazards

Jing Song, Konstantinos Skalomenos, Pedro Martinez-Vazquez, Pelagia Kastiza
Department of Civil Engineering, Edgbaston, Birmingham, B15 2TT, University of Birmingham

ABSTRACT

This paper presents a computational method for investigating the ductility demands induced by thunderstorm downbursts to steel building structures that have been previously damaged during a strong hazard event of any nature (earthquakes, strong winds). The proposed computational method synchronizes the finite element (FE) analysis software ABAQUS and MATLAB reverse optimization subroutines. A nonlinear static pushover analysis is initially performed to induce the ductility demands of the first hazard event and identify the relationship between the base shear force and lateral roof drift up to a target plastic deformation. The method uses the pushover analysis in order to bring the structure at a pre-defined ductility level, including the descending branch of the load-deformation curve, thus allowing for a direct control of the initially imposed damage. The transient non-stationary wind loads are then subsequently applied as an externally applied dynamic loading and the revised displacement ductility demand is directly determined. The method is applied on a tall steel building subject to several initial damage stages and three subsequent thunderstorm downburst synthetic records. The results demonstrate the non-negligible effects of such wind events on the total ductility demands. The method can successfully quantify the increased ductility demands on structures subjected to multi-hazards.

Keywords: Thunderstorm downburst, Ductility demand, Sequential hazards, Non-linear analysis